Ville Laitinen

LASER POWDER BED FUSION FOR THE MANUFACTURE OF Ni-Mn-Ga MAGNETIC SHAPE MEMORY ALLOY ACTUATORS

Ville Laitinen

LASER POWDER BED FUSION FOR THE MANUFACTURE OF Ni-Mn-Ga MAGNETIC SHAPE MEMORY ALLOY ACTUATORS

Dissertation for the degree of Doctor of Science (Technology) to be presented with due permission for public examination and criticism in the Auditorium 1314 at Lappeenranta-Lahti University of Technology LUT, Lappeenranta, Finland on the 3rd of December, 2021, at noon.

Acta Universitatis
Lappeenrantaensis 995

Supervisors   Professor Kari Ullakko
              LUT School of Engineering Science
              Lappeenranta-Lahti University of Technology LUT
              Finland

              Professor Antti Salminen
              Department of Mechanical Engineering
              University of Turku
              Finland

Reviewers   Professor Ilkka Tittonen
              Department of Electronics and Nanoengineering
              Aalto University
              Finland

              Professor Inigo Flores Ituarte
              Faculty of Engineering and Natural Sciences
              Tampere University
              Finland

Opponents   Professor Ilkka Tittonen
              Department of Electronics and Nanoengineering
              Aalto University
              Finland

              Professor Inigo Flores Ituarte
              Faculty of Engineering and Natural Sciences
              Tampere University
              Finland

Abstract

The ability of the magnetic shape memory (MSM) alloy Ni-Mn-Ga to exhibit large magnetic-field-induced strain (MFIS) of 6-12% makes it a promising actuation material for small devices in which traditional mechanisms and piezoelectric materials are impractical. As the grain boundaries in fine-grained polycrystalline material significantly hinder twin boundary motion, large MFIS is almost exclusively obtained in oriented single crystals. However, a moderate MFIS of ~1-4% can be obtained in bulk polycrystalline Ni-Mn-Ga after a sufficient reduction of the grain boundary constraints and the introduction of a strong crystallographic texture. The drawbacks of conventionally manufactured single crystals and polycrystalline Ni-Mn-Ga, e.g. low geometric freedom and high production costs, currently limit the development of novel functional MSM devices. Therefore, additive manufacturing (AM) is attracting increasing attention as a promising method for manufacturing polycrystalline Ni-Mn-Ga, especially as it allows realization of complex geometries or device structures.

Here, a laser powder bed fusion (L-PBF) AM process and a subsequent heat-treatment process were developed for the manufacture of coarse-grained polycrystalline Ni-Mn-Ga samples. It is shown that the chemical composition and resulting MSM-related properties of the L-PBF-built Ni-Mn-Ga can be precisely changed in-situ by adjusting the applied L-PBF process parameters to control the selective evaporation of Mn. A repeatable and fully reversible MFIS of 5.8% is demonstrated for a single crystalline grain of an L-PBF-built Ni-Mn-Ga exhibiting a five-layered modulated martensitic structure at ambient temperature. The obtained MFIS is two orders of magnitude larger than the 0.01% MFIS previously reported for additively manufactured Ni-Mn-Ga and is similar to that of conventional single crystals exhibiting the same crystal structure.

The results indicate that L-PBF can be used to manufacture functional polycrystalline Ni-Mn-Ga, facilitating a new generation of fast and simple digital components with integrated MSM alloy sections that can be actuated by an external magnetic field. Practically, the reported results will permit the exploration of polycrystalline-MSM-based devices with a geometric freedom that has thus far been impossible with conventional manufacturing methods.

Keywords: additive manufacturing, 4D printing, laser powder bed fusion, Ni-Mn-Ga, magnetic shape memory, magnetic-field-induced strain, twinning

Acknowledgements

The research presented in this dissertation was carried out in the Material Physics Laboratory of the School of Engineering Science at Lappeenranta-Lahti University of Technology LUT, Lappeenranta, Finland, between 2018 and 2021.

Ville Laitinen
September 2021
Lappeenranta, Finland

To my family and friends

Contents

Abstract

Acknowledgements

Contents

List of publications

This dissertation is based on the following papers. The rights have been granted by publishers to include the papers in dissertation.

I. Laitinen, V., Merabtene, M., Stevens, E., Chmielus, M., Van Humbeeck, J., and Ullakko, K. (2020). Additive manufacturing from the point of view of materials research. Chapter. In: Collan M, Michelsen K-E. (Eds.). *Technical, Economic and Societal Effects of Manufacturing 4.0*, pp. 43-83. Switzerland. Palgrave Macmillan, Cham.
II. Laitinen, V., Salminen, A., and Ullakko, K. (2019). First investigation on processing parameters for laser powder bed fusion of Ni-Mn-Ga magnetic shape memory alloy. *Journal of Laser Applications* 31, p.022303.
III. Laitinen, V., Sozinov, A., Saren, A., Salminen, A., and Ullakko, K. (2019). Laser powder bed fusion of Ni-Mn-Ga magnetic shape memory alloy. *Additive Manufacturing* 30, p.100891.
IV. Laitinen, V., Sozinov, A., Saren, A., Chmielus, M., and Ullakko, K. (2021). Characterization of as-built and heat-treated Ni-Mn-Ga magnetic shape memory alloy manufactured via laser powder bed fusion. *Additive Manufacturing* 39, p.101854.
V. Laitinen, V., Saren, A., Sozinov, A., and Ullakko, K. (2022). Giant 5.8% magnetic-field-induced strain in additive manufactured Ni-Mn-Ga magnetic shape memory alloy. *Scripta Materialia* 208, p.114324.

Author's contribution

Ville Laitinen is the principal author and researcher in **publications I–V**. He conceived the initial research ideas and strategies, designed and conducted the experiments, interpreted the results, and wrote the manuscripts. He developed and assembled the heat treatment apparatus used in **publications IV and V**. Mr Mahdi Merabtene, Ms Erica Stevens (currently, PhD), Prof. Markus Chmielus and Prof. emerit. Jan Van Humbeeck participated to the literature review and manuscript writing in **Publication I.** Prof. Markus Chmielus provided access to DSC and VSM equipment and participated in the preparation of the manuscript in **publication IV**. Dr Andrey Saren designed and carried out the AFM/MFM experiments in **publications III–V** and MFIS characterization in **publication V**. Dr Alexei Sozinov designed and carried out the XRD experiments in **publication III** and participated in the analysis of the XRD results in **publications IV-V**. The research was conducted under the supervision and guidance of Prof. Antti Salminen (**publications I-III**) and Prof. Kari Ullakko (**publications I-V**), who also acquired the financial support.

Nomenclature

List of symbols

γ	monoclinic crystallographic unit cell angle	º
ε	maximum transformation strain of a crystal	-
2Θ	the angle between the incident X-ray and the diffracted X-ray	º
λ	wavelegth	nm
a, b, c	crystal lattice parameters	Å
$Adj\ SS$	adjusted sum of squares	-
$Adj\ MS$	adjusted mean squares	-
c/a	crystal tetragonality ratio	-
DF	degrees of freedom	-
$F\text{-}value$	a value on the Snedecor's F-Distribution	-
H	magnetic field strength	T
h	hatch spacing	μm
P	laser power	W
P_{avg}	average laser power	W
$P\text{-}value$	statistical significance value	-
R^2	coefficient of determination	-
$RMSE$	root mean square error	-
T	temperature	°C
t	layer thickness	μm
T_{AS}	martensite to austenite transformation start temperature	°C
T_{AF}	martensite to austenite transformation finish temperature	°C
T_C	Curie temperature	°C
T_h	homogenization temperature	°C
t_h	homogenization time	h
T_{MS}	austenite to martensite transformation start temperature	°C
T_{MF}	austenite to martensite transformation finish temperature	°C
T_o	atomic ordering temperature	°C
t_o	atomic ordering time	h
ΔT_M	witdth of the austenite-martensite transformation	°C
t	layer thickness	μm
v	scanning speed	mm/s
VED	volume energy density	J/mm³
Vol	crystal unit cell volume	Å³

Abbreviations

2D	two-dimensional
3D	three-dimensional
10M	modulated five-layered martensite (also referred to as 5M)
14M	modulated seven-layered martensite (also referred to as 7M)
AC	alernating current

AFM	atomic force microscopy
AM	additive manufacturing
ANOVA	analysis of variance
B2′	disordered cubic crystal structure
BD	build direction
DSC	differential scanning calorimetry
EDS	energy-dispersive spectroscopy
HT	heat treatment
L2_1	ordered cubic crystal structure
LDV	laser Doppler vibrometer
LFMS	low-field AC magnetic susceptibility
L-PBF	laser powder bed fusion
MFIS	magnetic-field-induced strain
MFM	magnetic force microscopy
MSM	magnetic shape memory
NM	non-modulated martensite
SEM	scanning electron microscopy
TB	twin boundary
VSM	vibrating sample magnetometry
XRD	X-ray diffraction
XRF	X-ray fluorescence

1 Introduction

1.1 Background and motivation

Ni-Mn-Ga-based magnetic shape memory (MSM) alloys can exhibit giant magnetic-field-induced strain (MFIS). This straining phenomenon, called the MSM effect, occurs when the crystal lattice of the alloy's martensitic phase reorientates in response to magnetic-field-induced stress (Ullakko et al., 1996; Ullakko et al., 1997). The strain can be recovered by reorienting the applied magnetic field or by mechanical loading. Large MFIS is almost exclusively obtained in oriented single crystals because twin boundary (TB) motion is significantly hindered by the grain boundaries in fine-grained randomly textured polycrystalline Ni-Mn-Ga. A sufficient reduction of these constraints and the introduction of a strong crystallographic texture enable polycrystalline Ni-Mn-Ga to develop moderate MFIS: ~1-4% in coarse-grained bulk Ni-Mn-Ga (Ullakko et al., 2001; Gaitzsch et al., 2009) and up to ~8.7% in Ni-Mn-Ga foams (Chmielus et al., 2009).

The drawbacks of conventionally manufactured single crystals and polycrystalline Ni-Mn-Ga, including low geometric freedom and high production costs, currently limit the development of novel functional MSM devices. Hence, additive manufacturing (AM) is attracting increased attention as a promising method for manufacturing polycrystalline Ni-Mn-Ga, especially as it allows complex geometries or device structures to be incorporated.

However, a severe shortcoming presented in recent research is that additively manufactured Ni-Mn-Ga shows maximum strains of only 0.01% (Caputo et al., 2018; Ullakko et al., 2018). There are numerous reasons for the lack of large MFIS, including process-induced internal defects, metallurgical characteristics, e.g. a lack or randomness of the crystallographic texture, or large grain boundary constraints.

1.2 Objectives of the dissertation

The overall aim of the research presented here is to determine whether laser powder bed fusion (L-PBF) can be used to manufacture functional polycrystalline Ni-Mn-Ga-based MSM alloys that can be actuated by an external magnetic field.

Publication I contains a review of the studies on the AM of stimuli-responsive materials, such as Ni-Mn-Ga-based MSM alloys or magnetocaloric materials, conducted around the time the second experimental investigation was published. The experimental part of the research is presented in **publications II-V**.

The first objective of the research was to experimentally determine whether Ni-Mn-Ga alloys can be manufactured via L-PBF and to understand the laser–material interactions in the L-PBF of Ni-Mn-Ga. **Publications II and III** report on the successful use of the technique and reveal how the applied process parameters affect the composition and

relative density of L-PBF-built Ni-Mn-Ga. **Publication III** also identifies the optimal processing conditions for obtaining high-density samples with minimal Mn loss. These findings enabled the development of new gas atomized Ni-Mn-Ga powders with excess Mn, allowing the experimental research to fulfil the next research objective.

The second objective of the research was to experimentally determine whether the initial composition-dependent material properties can be retained via post-process heat treatment and to understand the other effects of the applied heat-treatment conditions. **Publication IV** reveals the optimal heat-treatment conditions for the improvement of functional properties and grain growth, which are critical for achieving large MFIS in bulk polycrystalline Ni-Mn-Ga manufactured via L-PBF.

The third objective of the research was to demonstrate the MSM effect in additively manufactured Ni-Mn-Ga. **Publication V** reveals that L-PBF-built Ni-Mn-Ga can develop giant fully reversible MFIS of 5.8%. Furthermore, selective Mn evaporation during the process can be used to control the chemical composition and resulting properties of the built material.

1.3   Scope and limitations

This dissertation exclusively focuses on the Ni-Mn-Ga alloy to examine the specific compositions known to exhibit modulated martensite crystal structures. The aim was to identify properties significant to the development of the material for actuation purposes. The potential magnetocaloric properties of the used materials were disregarded. Moreover, the focus was also exclusively on the L-PBF process. Other prospective AM processes, such as 3D ink printing, binder jetting or directed energy deposition, were disregarded as these have been extensively discussed elsewhere in the context of additively manufacturing Ni-Mn-Ga – see **publication I** for reference. The main reasons for choosing L-PBF were threefold: 1) It offers the highest geometric freedom among the mentioned AM processes; 2) unlike 3D ink printing or binder jetting, it does not require liquid binding agents, allowing greater control over the built samples' chemical composition; and 3) L-PBF-built materials typically develop a crystallographic texture due to the solidification conditions within the process. This was considered a benefit because crystallographic texture enhances the occurrence of MFIS in polycrystalline Ni-Mn-Ga.

Due to the limited number of samples produced in each study, the dissertation does not majorly address the statistical aspects of L-PBF process optimization. Additionally, the experiments within the dissertation were conducted for relatively simple sample geometries to ease the sample preparation and characterization. Consequently, the experimental findings are principally applicable for similar experimental setups. However, the use of more complex sample geometries, different Ni-Mn-Ga powders, different L-PBF devices, or different process temperatures will require the subsequent re-adjustment of the applied processing parameters, which may influence the obtained sample properties. In addition, the dissertation investigates the produced Ni-Mn-Ga alloys

in both as-built and post-process heat-treated conditions. Other post-process treatments, such as hot isostatic pressing or thermomechanical and magnetic treatments, are not addressed here. Nevertheless, as similar samples with corresponding properties can potentially also be produced with other laser or electron beam-based AM processes, the concepts and general results presented here are not limited to L-PBF processes.

1.4   Structure of the dissertation

The dissertation comprises five chapters. Chapter 1 introduces background, motivation, and objectives of the dissertation and defines the scope and limitations of the conducted research. Chapter 2 gives a short introduction into the Ni-Mn-Ga-based magnetic shape memory alloys and the general principles of the laser powder bed fusion process. Chapter 3 provides an overview of the scientific methods, experimental setups and materials that were used in the dissertation. Chapter 4 presents and discusses the original results obtained in the dissertation. Chapter 5 provides the conclusions of the dissertation and summarizes the scientific contribution and future research objectives.

2 State of the art

This chapter provides a background to the results discussed in this dissertation by presenting general information about Ni-Mn-Ga-based MSM alloys and the general principles of the L-PBF process.

Apart from the research presented in this dissertation and the original publications, only the studies of Ullakko et al. (2018), Laitinen et al. (2019), Nilsén et al. (2019), and Maziarz et al. (2021) focused on the L-PBF of Ni-Mn-Ga. Recent developments in the AM of Ni-Mn-Ga-based MSM alloys and magnetocaloric materials were extensively reviewed and discussed in **publication I** and are therefore excluded from this chapter.

2.1 Ni-Mn-Ga-based magnetic shape memory alloys

2.1.1 Crystal structure of Ni-Mn-Ga

The crystal structure and phase transformation temperatures of Ni-Mn-Ga are strongly composition-dependent (Jin et al., 2002; Takeuchi et al., 2003; Lanska et al., 2004). Upon cooling from liquid, a stoichiometric $Ni_{50}Mn_{25}Ga_{25}$ alloy undergoes a phase transition sequence from a disordered cubic B2′ to an ordered cubic $L2_1$ phase – also known as austenite (Overholser et al., 1999). This alloy exhibits a cubic $L2_1$ crystal structure at ambient temperature with a typical lattice parameter a ≈ 5.82 Å. Figure 2.1 shows the $L2_1$ structure of the austenitic phase, wherein Ga atoms (black) occupy the unit cell corners and the centre of each facet, Mn atoms (green) occupy the centre of the unit cell and the middle of each edge, and Ni atoms (red) occupy the centre of each of the eight cubic sub-unit cells.
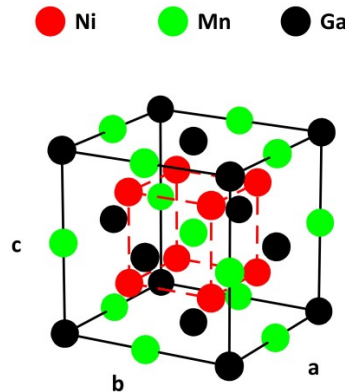

Figure 2.1: The $L2_1$ structure of the austenitic phase of $Ni_{50}Mn_{25}Ga_{25}$.

When a Ni-Mn-Ga alloy with a suitable off-stoichiometric composition is cooled to ambient temperature, it experiences a diffusionless phase transformation – known as martensitic transformation – from the $L2_1$ phase into a low-symmetric martensite phase (Vasil'ev et al., 1999; Richard et al., 2006; Yang et al., 2012). Ni-Mn-Ga alloys exhibit three distinct martensitic phases: non-modulated (NM) martensite, five-layered modulated (10M, also known as 5M) martensite, and seven-layered modulated (14M, also known as 7M) martensite (Pons et al., 2000; Heczko et al., 2009). The crystallographic lattices of these martensites are often described using the coordinate system of the cubic parent $L2_1$ phase. In this coordinate system, NM martensite is described by a tetragonal unit cell with a = b and c > a, 10M martensite is described by a pseudo-tetragonal unit cell with the lattice parameters a ≈ b, c < a and γ > 90º, whereas 14M martensite is described by a pseudo-orthorhombic unit cell with a > b > c, and γ > 90º. Each of the modulated martensites exhibit lattice modulation over (220) atomic planes (10M – 10 planes, 14M – 14 planes) along the $[\bar{1}10]$ direction. The alternative names (5M, 7M) for each modulated martensite are obtained if the modulation layers are counted in 'unit cells', instead of using atomic planes. Some Ni-Mn-Ga compositions can also exhibit intermartensitic transformations (Martynov & Kokorin, 1992; Straka et al., 2013).

2.1.2 Twinning

Twinning is a mechanism for crystal deformation, in which individual atoms can move distances that are less than their interatomic spacing. In Ni-Mn-Ga martensites, twin boundaries (TBs) are the reflection planes or axis of rotation that separate twin variants – new crystallographic orientations – from the parent crystal (Jaswon & Dove, 1960; Saren et al., 2016). An Ni-Mn-Ga alloy with a 10M martensite structure has been observed to exhibit two crystallographically different types of TBs: type 1 with a rational twinning plane and an irrational shear direction, and type 2 with an irrational twinning plane and a rational shear direction (Sozinov et al., 2011; Straka et al., 2011). Different TB types exhibit different projections with respect to the facets of a single crystal sample that is perfectly cut along the {100} lattice planes of the austenite. Both TB types exhibit the same ~45° projections on the two facets along the (010) lattice plane of the martensitic phase; see Figure 2.2. The slight surface kink angle (typically ~3.7° with the 10M structure) on the side face originates from the difference in spatial orientation between each variant – see the figure inset. However, perpendicular to this plane, the type 1 boundary is almost parallel to the [010] direction of the crystal, whereas the type 2 TB is inclined by ~6°.

2.1.3 Magnetic shape memory effect

The mechanism behind the MSM effect and the large MFIS observed in Ni-Mn-Ga is the magnetically induced reorientation of the crystal lattice through TB motion (Ullakko et al., 1996; Heczko et al., 2009). Figure 2.2 schematically illustrates the MSM effect, wherein the TBs separate the twin variants with a different – by around 86° – orientation of the c-axis. When the field reaches the minimum value, the martensitic twin variants

with the shorter crystallographic *c*-axis, which is the axis of easy magnetization, oriented along the applied magnetic field (*H*) grow at the expense of other variants with different orientations. The reorientation of the *c*-axis along the applied field and the subsequent 'expansion' of the corresponding twin variant cause the sample to physically contract along the field direction; see Figure 2.2b.

The minimum field value depends on multiple factors, including chemical composition, crystal quality and TB type (Straka et al., 2012). The maximum strain, which ideally results in a single variant structure, is achieved when the applied magnetic field saturates the material. During saturation, all magnetic moments in each twin variant are aligned with the applied magnetic field, and the corresponding magnetic field-induced stress for TB motion reaches its maximum value. As a result, any increase in the applied magnetic field beyond the saturation field value provides no further increase in the magnetic driving force for TB motion (Saren et al., 2016). The sample retains its shape after the magnetic field is removed. A reverse transformation can be induced by applying a transverse magnetic field or by mechanical force.
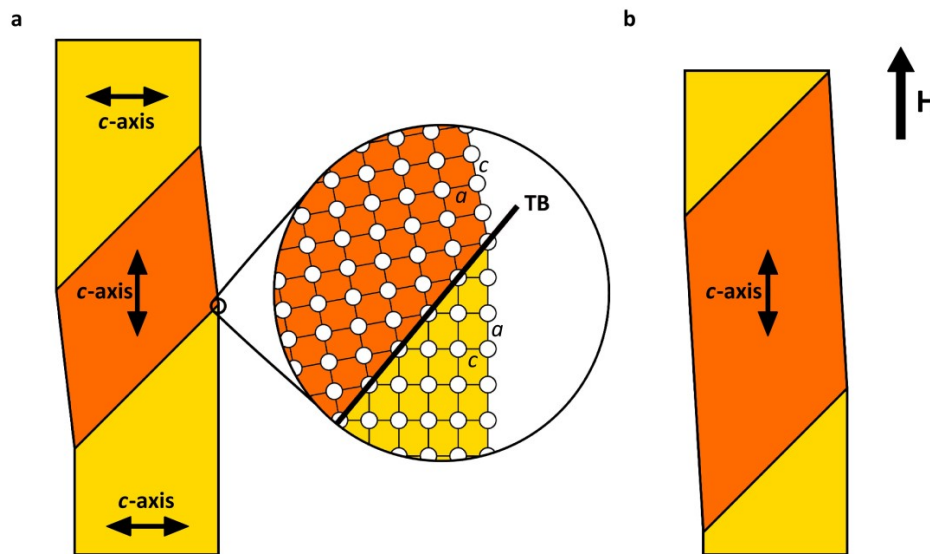
Figure 2.2: A schematic illustration of the magnetic shape memory effect in a single crystalline Ni-Mn-Ga sample exhibiting a microstructure with two parallel TBs: Yellow variants with the *c*-axis in the horizontal direction, and an orange variant with the *c*-axis in a vertical direction. The *b*-axis is oriented normal to the plane of view. The inset contains a magnified image showing the orientation of the unit cell on each side of the TB. (a) The sample before applying the magnetic field. (b) The same sample after magnetic field (*H*) application in the direction pointed by the arrow.

Multiple factors determine whether a Ni-Mn-Ga alloy can exhibit large MFIS. The foremost requirement is the crystal structure, which must be martensitic at the intended actuation temperature – typically ambient temperature. Additionally, to exhibit the MSM effect, the alloy must have high magnetic anisotropy compared to the energy needed to move the TBs – the magnetic-field-induced stress should be higher than the twinning stress, which defines the minimum stress needed to move an existing TB.

The theoretical maximum strain (ε) for the martensitic crystal lattice can be calculated using the following equation:

$$\varepsilon = 1 - \frac{c}{a} \tag{2.1}$$

where c (Å) and a (Å) correspond to the lattice parameters of the martensite unit cell (Söderberg et al., 2005).

The largest MFIS at ambient temperature was observed in oriented Ni-Mn-Ga single crystals exhibiting modulated martensite structures: up to 6% for 10M martensite (Murray et al., 2000) and up to 9.5% for 14M martensite (Sozinov et al., 2002). Among the modulated Ni-Mn-Ga martensites, the 10M is the most studied structure, mostly because it has relatively low twinning stress and high work output while still maintaining a large MFIS. Overall, the observed maximum strains are approximately two orders of magnitude larger than the ~0.1 % strains obtained in competing giant magnetostrictive materials (Engdahl, 2000). Additionally, Ni-Mn-Ga can exhibit high strain accelerations of up to 1.6×10^6 m/s^2 (Smith et al., 2014), and its fatigue life can exceed 2×10^9 cycles (Aaltio et al., 2010). Although 12% MFIS has been obtained in a doped alloy exhibiting an NM structure (Sozinov et al., 2013), a typical non-doped alloy with an NM martensite structure has a twinning stress that is much greater than its maximum magnetic-field-induced stress; therefore, it does not typically exhibit large MFIS (Likhachev et al., 2006; Chernenko et al., 2009).

The twinning stresses (in 10M martensite) of TB type 1 have been experimentally determined as ~1 MPa at ambient temperature, whereas TB type 2 exhibits a drastically different value of ~0.05-0.3 MPa (Sozinov et al., 2011; Straka et al., 2011). Additionally, TB type 1 exhibits a large increase in twinning stress when temperature is decreased (Straka et al., 2012), which is the reason why most functional Ni-Mn-Ga compositions have been tailored to start the martensite to austenite transformation at ~40-50 °C. However, TB type 2 shows considerably lower twinning stress temperature dependency (Heczko et al., 2013). The stress required for the nucleation of another variant and the formation of a completely new TB is typically higher than the twinning stress (Aaltio et al., 2010b). There is also the concept of dynamic twinning stress, which describes the twinning stress of the TB as a function of TB velocity (Saren & Ullakko, 2017).

Crystal quality is also a limiting factor in the MSM effect because TB mobility can be affected by internal defects (e.g. crystal defects or particle/phase inclusions) and surface

defects (Chmielus et al., 2011). These defects can result in the formation of pinning obstacles and residual twin variants, which restrict TB motion. For example, the motion of TBs is significantly hindered by the grain boundaries, which is the major reason why large MFIS in Ni-Mn-Ga is almost exclusively observed in oriented single crystals, while polycrystalline alloys typically do not exhibit large strains. In polycrystalline Ni-Mn-Ga, some of these constraints can be removed by increasing the grain size and applying training (Gaitzsch et al., 2011; Hürrich et al., 2011) or by inducing a 'bamboo-grained' structure with a crystallographic texture (Chmielus et al., 2009). Additionally, applying a magnetic field and/or mechanical stress can help remove the complex self-accommodated twin microstructure, composed of multiple twin variants, which appears during cooling from austenite into martensite.

2.1.4   Applications

As MSM-based technologies are relatively underdeveloped compared to competing piezo ceramics and giant magnetostrictive materials, the commercial applications of Ni-Mn-Ga remain rather limited. However, Ni-Mn-Ga-based MSM alloys show the highest potential for applications where the use of traditional mechanisms and piezoelectric materials is impractical, as exemplified in the following:

- The MSM effect can be used in unidirectional or bidirectional linear actuators (Tellinen et al., 2002) and strain/displacement sensors (Hobza et al., 2018). Additionally, twin variant redistribution during actuation changes the magnetic permeability of the MSM element, which can be used for actuator self-sensing and control (Hubert et al., 2012). The strain characteristically remains unchanged in MSM materials after the magnetic field has been switched off. This produces significant energy savings for many applications, especially on-off valves, because magnetic field energy is only needed during the brief time when the shape of the MSM element is changing.
- TB movement can be used for mechanical damping (Nilsén et al., 2018)
- A locally applied external inhomogeneous magnetic field can be used to generate a local shrinkage of the MSM material. When the MSM element is embedded into a casing, this shrinkage can carry fluid or gas, similar to a peristaltic pump (Ullakko et al., 2012; Smith et al., 2015). This can be used for medical drug delivery (Barker et al., 2016) or integrated into microfluidic circuits and microreactors for life science and chemistry applications (Saren et al., 2018)
- MSM materials can be used in microactuators to produce movement in adaptronic devices (Kohl et al., 2014; Musiienko et al., 2018). Such microactuators can theoretically exhibit working frequencies up to 100 kHz (Musiienko et al., 2019)
- MSM materials can be used to generate electrical energy from mechanical vibrations (Saren et al., 2015; Lindquist et al., 2018).
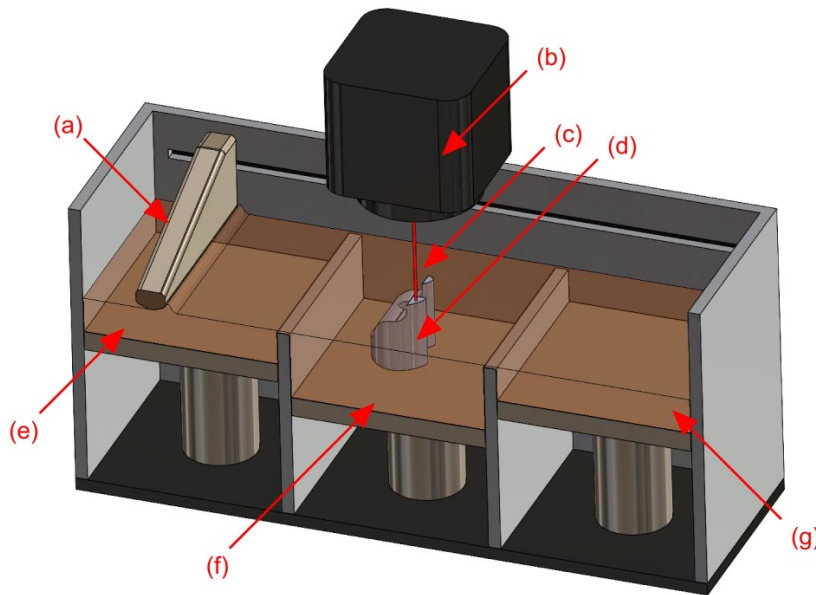
Figure 2.3: Schematic of a general L-PBF process. (a) powder recoater blade, (b) a galvanometric scanner and focusing optics, (c) laser beam, (d) an L-PBF-built object, (e) primary powder reservoir, (f) build platform, and (g) secondary powder reservoir.

2.2   Laser powder bed fusion

Laser powder bed fusion (L-PBF), also known by the commercial names 'Direct Metal Laser Sintering' or 'Selective Laser Melting', is an AM process in which a focused laser beam melts and fuses selected regions of a powder bed layer-by-layer, forming a three-dimensional (3D) object. This chapter focuses exclusively on the aspects relating to the L-PBF of metals and disregards other materials, such as plastics and ceramics.

Figure 2.3 presents a schematic of a general L-PBF process. The main heat source for melting in L-PBF is typically a focused laser beam produced by a single-mode fibre laser emitting continuous wave radiation with a near-infrared wavelength of 1060-1080 nm (Lee at al., 2017). Laser beam movement is typically achieved using a galvanometric scanner. Typical L-PBF devices employ a build chamber integrated with a powder delivery system, such as a hopper or reservoir located next to the work area, with a roller or blade that spreads the powder evenly on top of the build platform (Van der Schueren & Kruth, 1995; Lee at al., 2017). The build platform itself is connected to a piston or other mechanism, allowing precise up/down motion in the build direction. Most L-PBF systems use an inert gas atmosphere or partial vacuum in the build chamber to prevent the processed material from reacting with oxygen during melting. The general principle of the L-PBF process is as follows:

- First, a 3D computer model of the manufactured object is prepared, including the nesting and generation of the support structures. This is converted into object cross-sections that correspond to the two-dimensional (2D) projections of the manufactured object in the build direction. Lattice-like support structures anchor the built object to the build platform during melting and provide heat dissipation to prevent thermal distortion by lowering thermal gradients. They can also support horizontally oriented structures and overhanging surfaces (DebRoy et al., 2018).
- The powder delivery system is manually or automatically loaded with the metal powder.
- After the process environment has been prepared, the system spreads a thin layer of powder across the build platform (metallic plate, typically compositionally similar to the manufactured material). Next, the laser beam selectively melts the spread metal powder layer based on the prepared 2D cross-sectional data and the set hatch pattern. The use of hatched scan patterns ensure control over individual laser scan track lengths and helps to maintain the overall consistency of the melting conditions. The temperature in the laser–material interaction zone increases above the material's melting temperature, completely melting and fusing the exposed material with the substrate and adjacent scan tracks.
- Subsequently, the build platform is incrementally lowered according to the set powder layer thickness, and another thin layer of powder is spread on top of the previous layer. The selective melting is then repeated based on the 2D cross-sectional data corresponding to the new layer. This process is repeated layer by layer until the build job is complete and all layers have melted and fused.
- At the end of the build operation, the manufactured object remains buried inside the powder. Required post-processing steps include de-powdering, detaching the manufactured object from the build plate, and removing the support structures.

2.2.1 Defect generation and microstructural characteristics

In general, L-PBF allows the realization of complex geometries, facilitating high geometrical design freedom. However, the non-equilibrium conditions, rapid heating and cooling, and complex laser–material interactions (Wang et al., 2002) during the layer-by-layer melting in L-PBF can cause several defects and produce certain microstructural characteristics within the processed material.

Although L-PBF-built materials are often comparable with their conventionally processed counterparts (Mower & Long, 2016), the applied process parameters have a substantial effect on the properties of the manufactured materials. For example, grain structure, crystal structure and chemical composition can vary locally within the built material. During L-PBF, the melt pool dissipates heat into the substrate (previous layers), creating a curved melt pool shape that is influenced by the applied processing parameters, such as the applied laser power and scanning speed, and the thermo-physical properties of the built material. Subsequently, the geometric features of the melt pool influence grain growth and crystallographic texture (Vecchiato et al., 2020; Sanchez et al., 2021). The

resulting grain structure is spatially highly anisotropic, often containing columnar grains spanning from the substrate towards the top of the built object.

Defect formation in L-PBF is a complex phenomenon that can be influenced by multiple different factors, including faults in the initial 3D model, the L-PBF equipment itself, the processed feedstock powder, and the applied process parameters. Some of the formed defects, such as large thermal distortions (Douellou et al., 2019) or the staircase effect, are directly observable as they result in the failure of the L-PBF build or the large dimensional inaccuracy of the built object. Defects that do not necessarily influence the build itself include surface oxidation and roughness, loss of alloying elements (Mukherjee et al., 2016), different types of material defects (such as particle inclusions or impurities) (Young et al., 2020), keyhole porosity (Kamath et al., 2014; King et al., 2014) and large lack-of-fusion defects (Tang et al. 2017). Additionally, the L-PBF process exhibits large thermal gradients, resulting in the formation of residual stresses within the built object, ranging in size from macroscopic to atomic lattice (Li et al., 2018; Bartlett & Li, 2019). Residual stress formation is highly dependent on the applied process parameters and the chemical composition of the processed material and can lead to the cracking or delamination of individual layers (Louvis et al., 2011). Additionally, cracks can have a significant impact on the fatigue characteristics and crack propagation behaviour of the built objects.

3 Methods

This chapter provides an overview of the scientific methods, materials and experimental setups used in this dissertation.

3.1 Materials

In the course of the research, three different patches of Ni-Mn-Ga powders were developed and used. The chemical composition, volume-weighted particle size distribution and particle morphology (SEM image) of each patch are summarized in Figure 3.1. All Ni-Mn-Ga powders were prepared at the Technical Research Centre of Finland via an argon gas atomization process using high purity Ni (99.95%), Mn (99.99%) and Ga (99.99%). The first patch (**publications II and III**) was pre-alloyed to correspond approximately to the typical 10M martensite composition. In between publications, new gas atomized Ni-Mn-Ga powders were developed, which were alloyed with excess Mn to compensate for the expected evaporation of Mn during L-PBF. The pre-alloyed amount of 'excess Mn' compared to the reference composition was approximately ~0.6 at.% for the second patch (**publication IV**) and approximately ~2.2 at.% for the third patch (**publication V**).

Each patch was mechanically sieved to obtain a <80 μm particle size. The volume-weighted particle size distributions were determined using the Malvern Panalytical Morphologi G3S automated optical particle analyser. The powders were further evaluated using a Hitachi SU3500 Scanning Electron Microscope (SEM), which showed that each patch mainly comprised spherical particles with only a minor amount of irregularly shaped satellites and spatters observable within each patch. Before use in the L-PBF process, the powders were kept at ~80 °C for 3 hours to remove excess moisture.

The compositions of the substrate materials used in **publications II-V** are summarized in Table 3.1. The initial investigations into the single-track formation and the development of the L-PBF process for Ni-Mn-Ga presented in **publication II** were conducted using stainless steel 316L and Incoloy 825 substrate pieces, which were laser-cut from standard pre-alloyed sheets and subsequently ground to the final dimensions of $10 \times 30 \times 5$ mm^3. The Ni-Mn-Ga cuboid samples in **publication II** were manufactured on an Incoloy 825 substrate, whereas the extended process optimization presented in **publication III** was conducted using stainless steel substrates. These substrate materials were used because they provided a cost-effective approach for the initial parameter optimization. Later, to minimize the risk of contaminating the built Ni-Mn-Ga with the alloying elements of the substrate, we used other substrate materials that had higher chemical compatibilities with Ni-Mn-Ga. In **publication III**, the optimized process parameters were used to build samples on compositionally similar Ni-Mn-Ga substrate disks (Ø 22 mm, thickness ~4.1 mm) cut from an oriented single-crystalline bar prepared by AdaptaMat Ltd. In **publications IV and V**, the samples were built on Ø 45×~6.1 mm^2 high-purity Ni substrates.
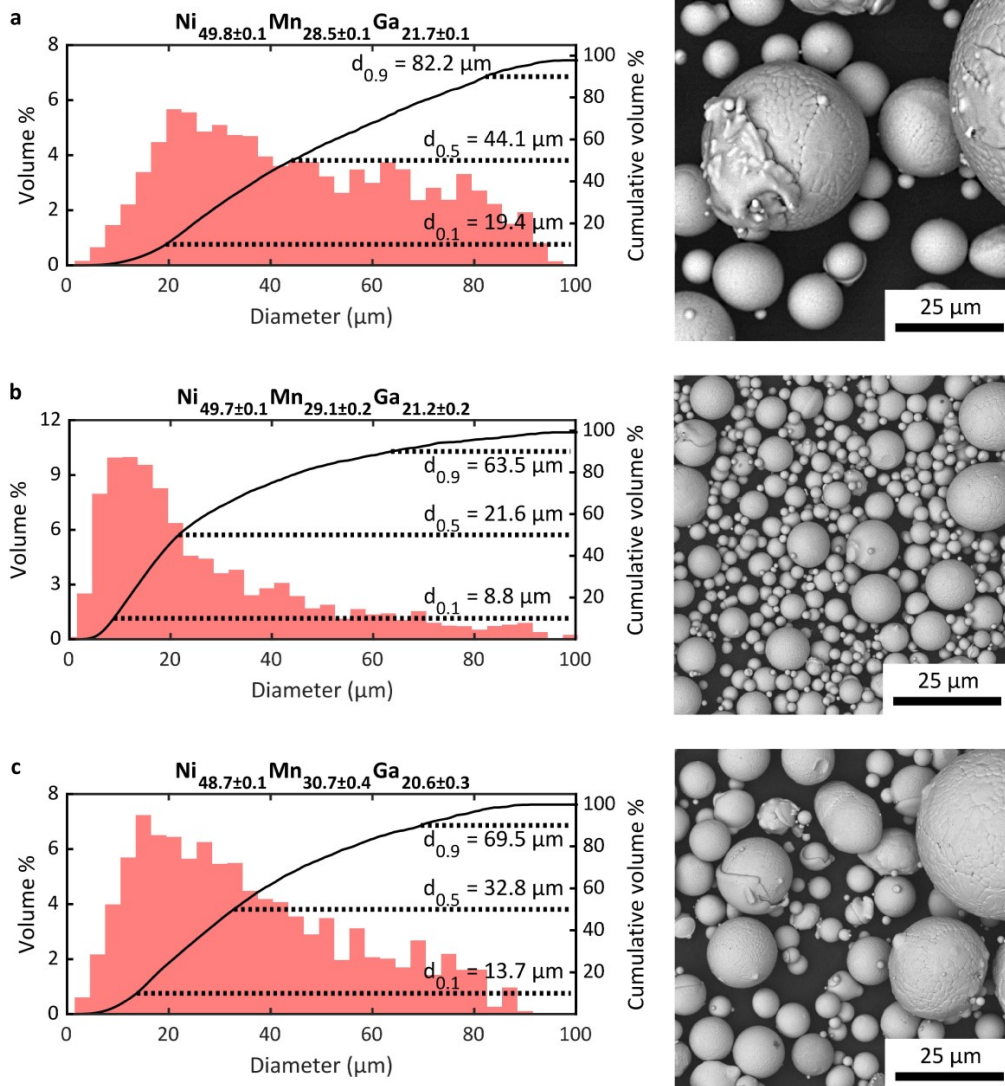
Figure 3.1: Chemical compositions (at.%), volume-weighted particle size distributions and particle morphologies (SEM image) of the Ni-Mn-Ga powders used in: (a) publications II and III, (b) publication IV, and (c) publication V. The shown errors correspond to the measured standard deviations in the chemical composition. (*Modified from* **publications II-V**.)

Table 3.1: Compositions (at. %) of the substrates used in **publications II-V**.

Material	Al	Si	Ti	Cr	Mn	Fe	Ni	Cu	Ga	Mo
316L	0.7	1.1	-	20.9	1.7	68.1	7.1	-	-	0.2
Incoloy 825	1.0	0.8	1.1	26.1	0.8	32.1	34.2	1.9	-	1.8
Ni-Mn-Ga	-	-	-	-	26.0	-	50.1	-	23.9	-
Ni	-	-	-	-	-	-	>99.5	-	-	-
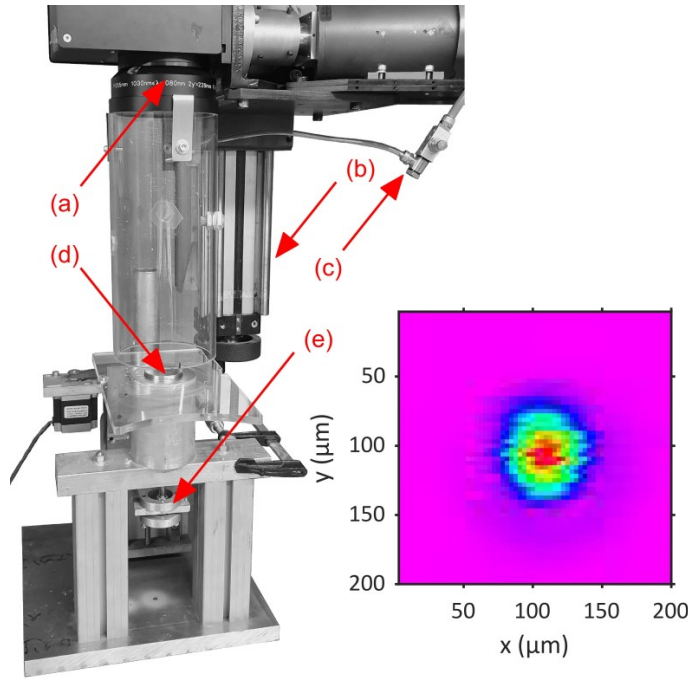
Figure 3.2: The in-house-developed L-PBF system used in **publications II-V**. (a) a galvanometric scanner and focusing optics, (b) adjustment of the focal point position in the z-direction (equal to the build direction), (c) argon inlet, (d) build platform with a detachable high-purity Ni substrate, and (e) motorized mechanism for the adjustment of the substrate position in the z-direction. The powder recoater system is absent in the image. The inset shows the measurement of the used laser beam (at focal point) by a Primes MicroSpotMonitor.

3.2   Sample manufacture

3.2.1   Laser powder bed fusion

All samples in **publications II-V** were built using the L-PBF system shown in Figure 3.2, which was developed and built in-house for material experimentation and testing. The system was equipped with an IPG YLS-200-SM-WC continuous-wave single-mode ytterbium fibre laser (λ = 1075 nm, maximum P_{avg} = 200 W), a SCANLAB intelliSCAN 10 galvanometric scanner head, and an F-theta lens. Both the laser and the scan head were controlled externally using SCAPS SAMLight scanner software with 3D functionality. A measurement with a Primes MicroSpotMonitor showed that this setup produced a laser beam with near-Gaussian power distribution, a ~82 μm focal point diameter, a Rayleigh length of 3.24 mm, and a beam parameter product of 0.53 mm mrad. The system was equipped with a build platform system with a slot for detachable substrate pieces and a maximum substrate size of Ø 46×10 mm^2. The build platform was connected to an

externally controlled stepper motor, which allowed precise control of the applied powder layer thickness from layer to layer. The repeatability of the powder layer deposition from patch to patch during the experiments was ensured by a delicate mechanical calibration of the re-coater blade of the system with each substrate before melting the samples. The build chamber of the system consisted of a Ø 120 mm (wall thickness of 5 mm) plexiglass tube attached to the used focusing optics. The shielding gas (high-purity argon) tube was directly connected to the chamber, and the gas was released into the chamber during the L-PBF process with a constant flow of ~3 l/min. The system can also be operated without the build chamber or with other build platform setups, as in Laitinen et al. (2019b), in which case the shielding gas can be delivered directly through a welding gas nozzle.

The experiments in this dissertation were implemented in three separate stages:

1) **Publications II and III**: Development and optimization of the L-PBF process for the manufacture of solid polycrystalline Ni-Mn-Ga samples. Investigation into the main effects of the applied process parameters on the chemical composition and relative density of the built material.

2) **Publications III and IV**: Development of a heat-treatment process for chemical homogenization and grain growth. Characterization of the produced material in as-built and heat-treated conditions.

3) **Publication V**: Demonstration of the MSM effect in L-PBF-built Ni-Mn-Ga.

Single-track and hatch distance experiments

Before manufacturing the 3D samples, the single-track formation in the L-PBF of Ni-Mn-Ga and the optimization of hatch distance values were investigated to enable the estimation and determination of the initial process parameters for the manufacture of solid Ni-Mn-Ga samples. The L-PBF process parameters and their increments (in parentheses) used in the single track and hatch distance experiments in **publication II** are summarized in Table 3.2. The length of the melted single tracks was 7 mm, and they were manufactured in batches of 20 tracks (160 samples in total, with 80 samples for each substrate material). A 1 mm wide gap was left between each track to avoid thermal interaction between adjacent tracks. The experiments were repeated twice for each parameter combination in randomized order. A bidirectional scanning strategy without a contour scan was used for the hatch distance experiments. The size of the hatched areas was 4×4 mm^2.

Table 3.2: Summary of the applied process parameters for the single-track and hatch distance experiments in **publication II**.

Parameter	Single track experiments	Hatch distance experiments
Powder layer thickness (μm)	50	50
Laser power (W)	80 → 200 (40)	200
Scanning speed (mm/s)	100 → 1000 (100)	100 → 700 (200)
Hatch distance (μm)	-	50 → 275 (25)
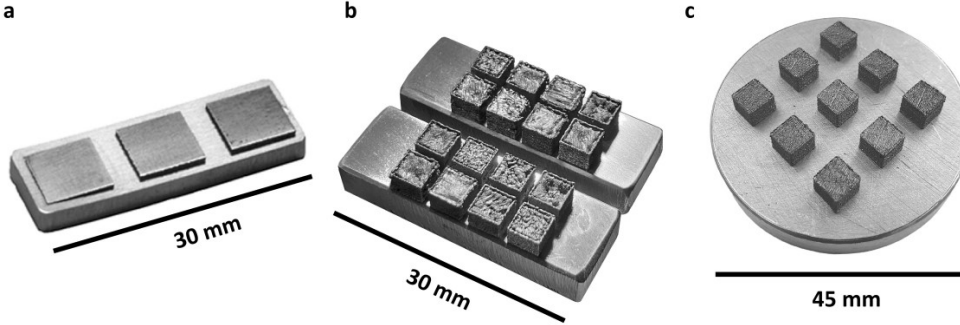
Figure 3.3: Ni-Mn-Ga samples built via L-PBF in: (a) publication II, (b) publication III, and (c) publication IV. (*Modified from* **publications II-IV**.)

Experiments involving the manufacture of 3D samples

The process parameters used for the manufacture of the 3D samples in **publications II-V** are summarized in Table 3.3. The samples have been renamed based on their respective publication and sample number to facilitate comparison and to avoid confusion between samples from different publications. The presented values of volume energy density (*VED*, J/mm^3) were calculated using the following equation:

$$VED = \frac{P}{v \, h \, t} \tag{3.1}$$

where P is the laser power (W), v is the scanning speed (mm/s), h is the hatch distance (mm), and t is the powder layer thickness (mm).

Figure 3.3 shows the Ni-Mn-Ga samples (on substrates) built via L-PBF in **publications II-IV**. All samples in **publications II-V** were built in an inert high-purity argon atmosphere at ambient temperature (~22 °C) without substrate preheating. Powder layer thicknesses were kept constant, at 50 μm for the samples in **publication II** and 60 μm for the samples in **publications III-V**. The laser beam was focused on the surface of the powder bed during sample manufacture. All samples were manufactured using a bidirectional single-pass scanning strategy and a single contour scan with 90% overlap with the hatched area. The same combinations of process parameters were used for both the hatched and contour scans of the samples. The rotation of the scanning direction from layer to layer was different in each publication; see Table 3.3 for the exact values. In **publications II and III**, the built samples were oriented on the substrates so that the x-y hatch directions of the L-PBF system were aligned with the side faces of the cuboids. This approach was implemented due to the geometrical constraints set by the used substrates. In **publications IV and V**, the samples were oriented on the substrates so that the side faces of the walls were aligned at a 45° angle compared to the x-y hatch directions of the used L-PBF system. This sample orientation enabled a smooth operation of the

recoater blade along the x-direction of the platform and minimized the risk of recoater collision with the built samples.

In **publication III**, the selection of the varied process parameters for the initial process optimization was carried out using two partially overlapping Box–Behnken-based experimental designs with three predetermined levels for each of the three varied parameters of laser power, scanning speed, and hatch distance. The samples were deposited in patches of eight samples (2×4 matrix, with a 1.2 mm gap between each sample) on four substrates using a randomized sample order. Some parameter combinations were repeated to allow the sample deposition reliability to be estimated. A short delay of 60 s was set between melting the same layer of each sample to minimize the thermal interaction between samples during the L-PBF. These samples were used to investigate the effect of the applied process parameters on the relative density and chemical composition of the built samples. After determining the optimized processing parameters, a single patch of four samples (2×2 matrix, with a 5 mm gap between each sample) was deposited onto the Ni-Mn-Ga substrate. These samples were used for the initial characterization of the built material.

The applied L-PBF process parameters in **publication IV** were selected and adjusted for the excess Mn within the used powder based on the L-PBF process optimization presented in **publication III**. The samples were built in two patches of nine samples (3×3 matrix) with a 5 mm gap between each sample within the same patch. These samples were used to investigate the effects of the applied heat-treatment parameters on the properties of the built samples and to perform a more thorough characterization of L-PBF-built Ni-Mn-Ga.

In **publication V**, the applied parameters were selected so that the produced samples would have high relative densities above 98.0% while exhibiting different volume energy densities to produce different levels of Mn evaporation during the L-PBF. Each parameter combination was used for two separate samples to facilitate comparison and reliability estimation. The samples were built on the substrate in a single patch of a 2×6 matrix with ~4 mm distance between each sample. These samples were used to investigate the possibility of using Mn evaporation to control the crystal structure and phase transformation temperatures of the L-PBF built material. Additionally, the sample geometry was chosen to enable actuation experiments to be performed to demonstrate the MFIS in L-PBF-built Ni-Mn-Ga.

The applied heat-treatment parameters in **publications IV and V** are summarized in Table 3.3 and Table 3.4, while the heat-treatment procedure itself is discussed in the following subsection.

Table 3.3: L-PBF process parameters and heat-treatment parameters used in **publications II-V**.

Publication Sample	Sample size (mm³)	L-PBF process					Heat-treatment			
		P (W)	v (mm/s)	h (µm)	VED (J/mm³)	Scan dir. rotation (°)	T_h (°C)	t_h (h)	T_o (°C)	t_o (h)
II-1	7×7×1	200	300	100	133	90	-	-	-	-
II-2	7×7×1	200	500	100	80	90	-	-	-	-
II-3	7×7×1	200	700	100	57	90	-	-	-	-
III-1	3.5×3.5×3.5	50	125	50	133	60	-	-	-	-
III-2	3.5×3.5×3.5	85	50	50	567	60	-	-	-	-
III-3	3.5×3.5×3.5	85	200	50	142	60	-	-	-	-
III-4	3.5×3.5×3.5	100	300	50	111	60	-	-	-	-
III-5	3.5×3.5×3.5	120	125	50	320	60	-	-	-	-
III-6	3.5×3.5×3.5	150	150	50	333	60	-	-	-	-
III-7	3.5×3.5×3.5	150	450	50	111	60	-	-	-	-
III-8	3.5×3.5×3.5	200	300	50	222	60	-	-	-	-
III-9	3.5×3.5×3.5	50	50	75	222	60	-	-	-	-
III-10	3.5×3.5×3.5	50	200	75	56	60	-	-	-	-
III-11	3.5×3.5×3.5	85	125	75	151	60	-	-	-	-
III-12	3.5×3.5×3.5	100	150	75	148	60	-	-	-	-
III-13	3.5×3.5×3.5	100	450	75	49	60	-	-	-	-
III-14	3.5×3.5×3.5	120	50	75	533	60	-	-	-	-
III-15	3.5×3.5×3.5	120	200	75	133	60	-	-	-	-
III-16	3.5×3.5×3.5	150	300	75	111	60	-	-	-	-
III-17	3.5×3.5×3.5	200	150	75	296	60	-	-	-	-
III-18	3.5×3.5×3.5	200	450	75	99	60	-	-	-	-
III-19	3.5×3.5×3.5	50	125	100	67	60	-	-	-	-
III-20	3.5×3.5×3.5	85	50	100	283	60	-	-	-	-
III-21	3.5×3.5×3.5	85	200	100	71	60	-	-	-	-
III-22	3.5×3.5×3.5	100	300	100	56	60	-	-	-	-
III-23	3.5×3.5×3.5	120	125	100	160	60	-	-	-	-
III-24	3.5×3.5×3.5	150	150	100	167	60	-	-	-	-
III-25	3.5×3.5×3.5	150	450	100	56	60	-	-	-	-
III-26	3.5×3.5×3.5	200	300	100	111	60	-	-	-	-
III-OPT	3.5×3.5×3.5	200	450	100	74	60	-	-	-	-
IV-1	3.5×3.5×3.5	200	750	100	44	60	-	-	-	-
IV-2	3.5×3.5×3.5	200	750	100	44	60	-	-	800	4
IV-3	3.5×3.5×3.5	200	750	100	44	60	1000	6	800	4
IV-4	3.5×3.5×3.5	200	750	100	44	60	1000	12	800	4
IV-5	3.5×3.5×3.5	200	750	100	44	60	1000	24	800	4
IV-6	3.5×3.5×3.5	200	750	100	44	60	1040	6	800	4
IV-7	3.5×3.5×3.5	200	750	100	44	60	1040	12	800	4
IV-8	3.5×3.5×3.5	200	750	100	44	60	1040	24	800	4
IV-9	3.5×3.5×3.5	200	750	100	44	60	1080	6	800	4
IV-10	3.5×3.5×3.5	200	750	100	44	60	1080	12	800	4
IV-11	3.5×3.5×3.5	200	750	100	44	60	1080	24	800	4
V-1, V-7	10×0.8×5	200	1300	75	34	0	1090	24	800	4
V-2, V-8	10×0.8×5	200	1000	75	44	0	1090	24	800	4
V-3, V-9	10×0.8×5	200	700	75	64	0	1090	24	800	4
V-4, V-10	10×0.8×5	190	500	75	84	0	1090	24	800	4
V-5, V-11	10×0.8×5	180	375	75	107	0	1090	24	800	4
V-6, V-12	10×0.8×5	160	250	75	142	0	1090	24	800	4
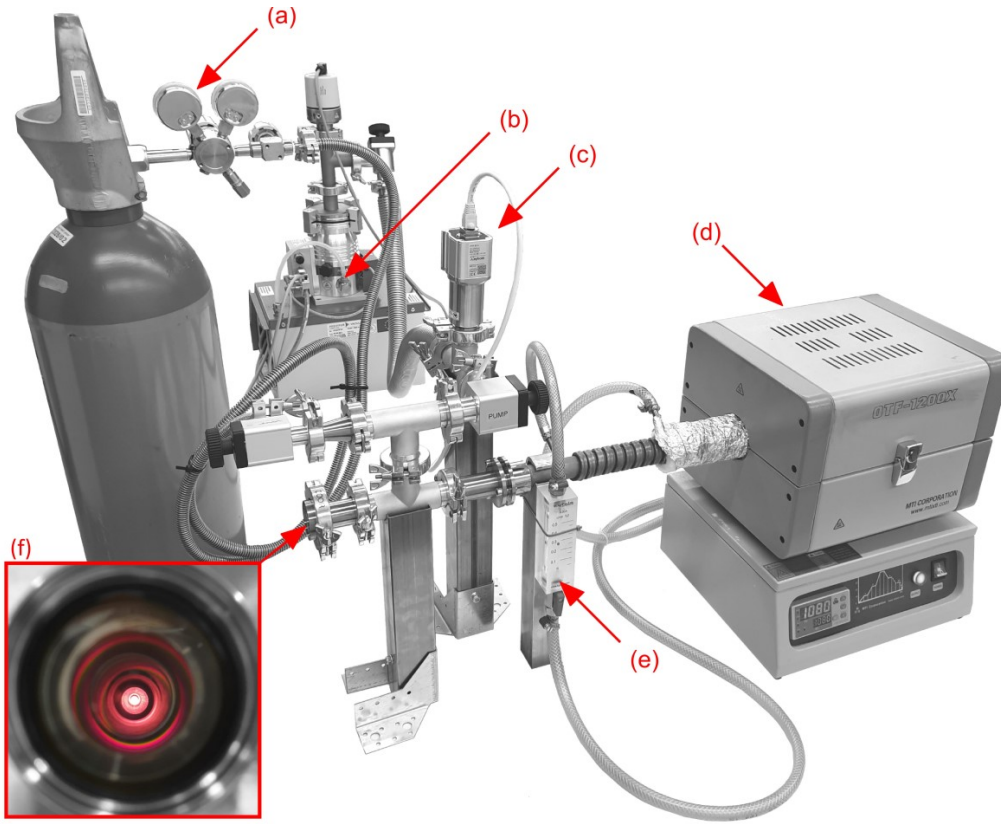
Figure 3.4: The in-house-developed heat-treatment system used in **publications IV and V**. (a) high-purity argon inlet, (b) turbopump, (c) vacuum meter, (d) heat-treatment furnace, (e) coolant flow meter, and (f) access to the main tube of the heat-treatment system with a vacuum window allowing direct observation of the heat-treated samples.

Table 3.4: Heat-treatment parameters used in **publications IV-V**.

Parameter	Value
Heating rate 20°C $\rightarrow T_h$ (°C/h)	250
Homogenization temperature, T_h (°C)	sample specific, see *Table 4.3*
Homogenization time, t_o (h)	sample specific, see *Table 4.3*
Cooling rate $T_h \rightarrow T_o$ (°C/h)	100
Ordering temperature, T_o (°C)	800
Ordering time, t_o (h)	4
Cooling rate $T_o \rightarrow 20$°C (°C/h)	Furnace cooling

3.2.2   Heat treatment

The L-PBF-built samples in **publications IV and V** underwent heat treatment using an in-house developed system based on an MTI OTF-1200X furnace, as shown in Figure 3.4. The system holds a temperature ±1 °C from the set-point temperature within the active length (~60 mm) of the main tube. The used heat-treatment procedure is presented below:

- Prior to the heat treatment, the samples manufactured via L-PBF were separated from the substrate using a Princeton Scientific Corporation WS-25 high-precision wire saw. The sample surfaces were ground and electropolished, after which possible surface contaminants were removed with acetone. The samples were subsequently washed in an ultrasonic bath of 2-propanol to remove any remaining contaminated acetone.
- The samples were placed on a high-purity alumina boat/sample holder with a titanium oxygen-getter, which were subsequently placed inside the main tube of the heat-treatment system.
- The main tube was then sealed and sequentially vacated using a Pfeiffer vacuum MVP 015-4 diaphragm pump and a Pfeiffer vacuum HiCube 80 Eco turbopump (switched on at ~2 mbar) until a high vacuum was achieved. The exact pressure within the main tube was monitored using an Oerlikon Leybold Vacuum PTR 90 N vacuum meter.
- To prevent possible Mn evaporation during heat treatment, the main tube was flooded with pure argon. The argon pressure within the main tube of the system was adjusted to ~300 mbar at ambient temperature, thus taking into consideration the thermal expansion of argon and the resulting increase of pressure during the heat-treatment sequence.
- The samples were first homogenized at a higher temperature; this was then decreased for the ordering treatment. Subsequently, the samples were furnace-cooled to ambient temperature. The heat-treatment parameters used in **publications IV and V** are summarized in Table 3.3 and Table 3.4, respectively.

The solidus temperature (~1110 °C) and $L2_1 \rightarrow B2'$ transition temperature (~765 °C), corresponding to the compositions of the as-built samples in **publications IV and V**, were approximated based on the available literature (Aaltio et al., 2009; Schlagel et al., 2000) and used to determine the corresponding critical temperatures for the heat treatment. In **publication IV**, the samples were treated one by one in a randomized sample order, and some treatments were repeated for secondary samples to permit reliability estimation. Additionally, two reference samples – one without heat treatment (IV-1) and one with the ordering treatment without prior homogenization (IV-2) – were produced to enable a comparison. In **publication V**, all samples were homogenized in a single patch using the same heat-treatment parameters. Before heat treatment, the edges of each sample were cut off and ground to ensure a sample size (resulting sample size ~6×0.6×3 mm^3) compatible with the used alumina sample holders and to allow all samples to be simultaneously heat-treated in a single patch.

3.3   Sample preparation

The samples in **publications II-V** were separated from the substrates and cut using a WS-22 high precision wire saw from Princeton Scientific Corp, equipped with a WSG-02 goniometer. A boron carbide (B_4C) 1:2 slurry mixed with 60% glycerol and cutting wires with 40 and 60 μm diameters were used during the cutting.

The manufactured samples were incrementally wet-ground using SiC abrasives with particle sizes ranging from 25 to 5 μm. The samples were mechanically polished using an EQ-Unipol-1202 (MTI Corporation) equipped with a napless cloth and diamond paste with 3 and 0.04 μm grain sizes.

Additionally, some of the samples in **publications III-V** were electropolished using a constant voltage of 12 V at -20 °C in an electrolyte solution containing a 3:1 volumetric ratio of ethanol to 60% HNO_3, held in an externally cooled beaker. Constant voltage was applied between the sample holder (anode) and the acid-resistant stainless-steel spiral (cathode) immersed in the solution. The solution was mixed continuously via an externally controlled magnetic chemical stirrer, which allowed the sample to be washed by a constant flux of the electropolishing liquid and removed etching products from its surface.

A Meiji Techno stereo microscope equipped with an EMZ-5TR microscope head, MA502 eyepieces, and PKL-1 SCS pole stand was used for observation of the samples during the gluing and cleaning processes.

3.4   Sample characterization

The data processing and preparation of the illustrations for **publications II-IV** were performed using the MathWorks Inc. MATLAB programming and numeric computing platform.

In **publication III**, response surface methodology (2nd degree quadratic polynomial model) was used for the approximation and visualization of the effects of the varied process parameters on the relative density and chemical composition (Mn content, at.%) of the as-built samples.

Additionally, analysis of variance (ANOVA) was used to investigate the effects of the applied processing parameters (L-PBF and heat treatment) on the selected material properties in **publications III and IV**. In **publication III**, factors with a p-value < 0.01 were considered statistically significant, whereas those exceeding this threshold were considered statistically insignificant. In **publication IV**, the cut-off value for statistical significance was < 0.05. However, special consideration should be made when interpreting the p-values due to the relatively low number of samples used in these studies.

3.4.1 Relative density

The relative densities of the as-built and heat-treated samples in **publications III and IV** were determined by averaging the area fraction of pores on the top surface of each sample. The measurements were performed using a customized optical microscope (Zeiss Axio Scope.A1) combined with the open-source image processing software ImageJ. The results were averaged from three consecutive cycles of sample preparation and measurement. In between measurements, ~0.5 mm (**publication III**) or ~0.25 mm (**publication IV**) of material was removed in the build direction of the sample. The contour scan area of each sample, ~200 μm from the sample edge toward the centre of the sample, was ignored during the measurement. For more specific details, the reader is referred to the original publications.

3.4.2 Chemical composition

The average chemical compositions of the initial powder and the manufactured samples in **publications II-V** were determined by averaging multiple measurements obtained via X-ray fluorescence (XRF) using an Oxford Instruments X-Strata 960 with a Ø 300 μm collimator. The XRF system was calibrated with a Ni-Mn-Ga reference sample of known composition. The absolute accuracy of the XRF measurements was 0.3 at.%. Additionally, in **publication III** the chemical homogeneity and distributions of the atomic elements in the sample-substrate interfaces of the as-built samples were studied via energy-dispersive spectroscopy (EDS) using a Hitachi SU3500 equipped with an EDS detector. The relative accuracy of the EDS measurement from point to point was ~1%. For more specific details, the reader is referred to the original publications.

3.4.3 Microstructure

A Meiji Techno MT7000 trinocular metallurgical microscope equipped with polarised light contrast lenses was used for the initial inspections of the twinned microstructures in the studied Ni-Mn-Ga samples. The high-quality optical images presented in **publications IV and V** were produced using a customised configuration of a Zeiss Axio Scope.A1 microscope equipped with a CoolLED pE-4000 light source. The optical image, shown in **publication IV**, was obtained with a long exposure due to the lower overall contrast of the twins in comparison to standard 10M Ni-Mn-Ga single crystalline samples.

SEM (Hitachi SU3500) was used for the microstructural characterization of the samples in **publications III and IV**. Prior to each measurement, the samples were incrementally ground using SiC abrasives, then mechanically polished and subsequently electropolished to ensure smooth surface quality and remove possible surface defects that would have influenced the measurement. The SEM images presented in the original publications and in the 'Results and discussion' section were obtained with relatively low magnifications of 200x and 400x using a backscattered electron detector and a relatively low acceleration voltage of 3 kV to increase the channelling contrast. This approach provided a high grain

contrast but was not ideal for observing individual twins that were generally too narrow to be imaged via the used pixel resolution.

The volume-weighted distributions and average grain sizes of the as-built and heat-treated samples in **publications III and IV** were determined with a linear intercept method using a combination of the ImageJ software package and the MATLAB-based program originally developed in Lehto et al. (2014). Prior to each measurement, the grain boundaries were manually traced using the obtained SEM image.

3.4.4 Crystal structure

Prior to the measurement, the samples were electropolished to ensure smooth surface quality and to remove possible surface stresses that might have influenced the measurement. All samples were first inspected at elevated temperatures, where they exhibited an austenitic crystal structure. Upon cooling, the corresponding austenite peaks disappeared, and a new pattern emerged. Hence, the diffraction peaks at ambient temperature must have originated from one or several martensite phases.

The crystal structure of the as-built sample and the initial powder in **publication III** were studied using a PANalytical Empyrean diffractometer (Co tube, λ=0.17890 nm) equipped with a hybrid monochromator and a PIXcel3D-Medipix3 detector. Additionally, a heating stage was used to inspect the samples in the cubic phase above the martensite transformation temperature. To increase the ratio of the peak intensities against the background level, 2D detectors in scanning line mode and low background single-crystal Si-111 were used to record the pattern for the as-built sample (III-OPT) at ambient temperature.

For later investigations, presented in **publications IV and V**, we used an upgraded setup, which included a PANalytical Empyrean 3 diffractometer (Cu tube, λ=0.15406 nm) equipped with poly-capillary optics, a PIXcel3D-Medipix3 detector, and a Si-510 zero background holder. A heating stage was used to inspect the samples in the cubic phase above the martensite transformation temperature and to perform a stepwise in-situ XRD measurement of a heat-treated sample with heating and cooling of the sample over martensitic transformation. While the scans were typically performed over a 2θ range of 24–140°, the applied generator voltage and current were varied throughout the research based on the sample- and equipment-related limitations.

The obtained diffraction data in **publications III-V** were processed using the PANalytical Data Viewer and a combination of in-house-developed Excel and MATLAB software, which enabled the precise estimation of the lattice parameters of the studied samples. Only the main diffraction peaks were considered in calculating the lattice parameters. Additionally, the lattice parameters in **publication IV** were refined using the Bruker TOPAS software.

Dr Alexei Sozinov designed and carried out the XRD experiments in **publication III** and participated in the analysis of the XRD results in **publications IV-V**.

3.4.5 Phase transformations

The phase transformation and Curie temperatures of the samples built in **publications III-V** were determined using an in-house developed low-field AC magnetic susceptibility (LFMS) device. The LFMS measurements were conducted across a temperature range of ~30-120 °C. Additionally, differential scanning calorimetry (DSC) was used to determine the phase transformation temperatures of the as-built samples and selected heat-treated samples in **publications III and IV**. The DSC system used in **publication III** was a PerkinElmer DSC4000, whereas the system used in **publication IV** was a TA Instruments DSC250 coupled with an autosampler and an RCS90 two-stage refrigeration system. The author acknowledges the assistance provided by Ms Erica Stevens (currently, PhD) in the DSC measurements for **publication IV**.

3.4.6 Magnetic properties

The magnetostructural characterization of the observed martensitic twins within the as-built and heat-treated samples in **publications III-V** was performed by Dr Andrey Saren via atomic force microscopy (AFM) and magnetic force microscopy (MFM) using a Park Systems XE7. Prior to each measurement, the samples were electropolished to ensure smooth surface quality and remove possible surface defects that would have influenced the measurement.

Vibrating sample magnetometry (VSM) was used to perform the magnetic characterization of the samples in **publication IV**. The measurements were done using a LakeShore model 7407 with applied magnetic fields of up to 1.2 T. Each sample was secured to the VSM sample holder using Teflon tape. The author acknowledges the assistance provided by Mr Jakub Toman in these measurements.

3.4.7 Actuation experiments

D.Sc. Andrey Saren designed and carried out the AFM/MFM and LDV experiments and the MFIS characterization in **publication V**. The author manufactured the samples and prepared the actuated sample.

For the magnetic actuation experiments in **publication V**, the surface of the selected sample (V-2, 10M martensite structure) was inspected using a Meiji Techno MT7100 polarized light optical microscope to identify suitable grains. The selected grains were marked and cut using a WS-25 high-precision wire saw (Princeton Scientific Corporation). The extracted sample was incrementally ground using SiC abrasive papers with 10 and 5 μm grain sizes, and subsequently electropolished using the aforementioned setup. The resulting sample was a ~4.0×1.1×0.4 mm^3 polycrystalline cuboid that

contained a large single crystalline grain, about 1.7×1.1×0.4 mm^3 in size, at one end of the sample. The other end of the sample was fixed to a 3 mm diameter sapphire rod using an epoxy adhesive.

In the first experiment, a homogeneous 0.8 T magnetic field, created by an EMU-75 electromagnet (SES Instruments Pvt. Ltd.), was used to reorient the easy c-axis in the active part of the sample. A Zeiss Axio Scope.A1 polarized optical light microscope was used to determine the c-axis orientation from the sample's front side, and a Park Systems AFM/MFM microscope XE7 was utilized to follow the c-axis rotation at the TB on the top side. In the next experiment, a laser Doppler vibrometer (LDV) based setup, previously described in Saren et al. (2016), was used to examine the fast actuation of the sample under sub-ms magnetic field pulses. In the present setup, a miniature solenoid (with an inner diameter of 4.3 mm, a length of 16.3 mm, and comprising 140 turns of insulated copper wire 0.2 mm in diameter, wound in 2 layers) was connected to a high-voltage pulse generator (EMC, Transient 1000) in series, with an additional coil (with 1.86 mH inductance and 0.83 Ohm resistance) providing a current pulse duration of ~250 μs. The sample, fixed to the sapphire rod, was placed inside the solenoid. The actuation velocity and displacement of the sample's free end were measured using an LDV from Polytec (OFV-5000 and OFV-534). The solenoid current was calculated based on the voltage drop on a wire resistor of 0.2 Ohm connected in series with the solenoid. The transient velocity and displacement signals from the LDV as well as the solenoid current were recorded using a 200 MHz oscilloscope (Metrix Scopix III OX 7204). The magnetic field was calculated from the measured current using the solenoid parameters.

4 Results and discussion

This chapter presents and discusses the original results obtained in this dissertation. It is divided into subsections based on the research approach and the stages of experiments presented in Chapter 3.

4.1 Process development and optimization

This section reveals and discusses the results of the first stage in our experimental research, namely developing and optimizing the L-PBF process for manufacturing solid polycrystalline Ni-Mn-Ga samples and investigating the main effects of the applied process parameters on the chemical composition and relative density of the built material. This section discusses the results obtained using stainless steel 316L substrates since the more advanced process optimization in **publication III** was performed exclusively using this substrate material. Incoloy 825 was only used in the initial investigations presented in **publication II**.

4.1.1 Single-track and hatch distance experiments

Figure 4.1 shows the primary results of the single-track and hatch distance experiments, conducted using stainless steel 316L substrates in **publication II**. As single-track formation and the use of hatching distance in L-PBF are well-understood phenomena, this section reflects on the selection of processing parameters for Ni-Mn-Ga. Overall, there were only minor differences in the parameter combinations that produced continuous tracks between the two different substrate materials. However, the tracks melted on the Incoloy substrates exhibited a greater propensity toward irregularity and balling, further observable as larger track widths with a shallower penetration of the substrate. The possible reasons for the observed differences range from variations in the thickness of the spread powder layers and surface oxide films on the used substrates to different chemical compositions and the resulting substrate properties; these are discussed in more detail in the original publication. The analysis of the cross-sections of the produced single tracks, shown in Figure 4.1a, demonstrates that both track width and substrate penetration increase with increasing laser power or decreasing scanning speed. The abrupt increase in the substrate penetration with high laser power and low scanning speed was previously linked to keyhole formation in L-PBF (King et al., 2014); this is further discussed in the following section. Based on the results of the single-track experiments, a constant laser power of 200 W was selected for the hatch spacing experiments.

A critical requirement for a stable L-PBF process is the thickness of the spread powder layer, which should remain nearly constant from layer to layer throughout the process. This criterion is fulfilled only when each melted layer is consistently thick and has a reasonably smooth top surface, allowing it to act as a substrate for the following layers. The main aim of this experiment was to determine which combinations of the applied process parameters fulfil this criterion. The analysis was qualitative and was conducted

visually by dividing the surfaces into four different groups, as shown in Figure 4.1b. The observed changes in the quality of the produced surface directly relate to the applied hatch distance and scanning speed. With a constant scanning speed of 100 mm/s, low hatch spacing values of 50 and 75 µm produced continuous surfaces that exhibit irregularity and spattering (1st group), likely caused by excessive heat input during the process. Increasing the hatch spacing value to 100-150 µm reduced these effects and yielded smooth continuous surfaces (2nd group). This group is considered ideal for the development of a stable L-PBF process. A further increase of hatch spacing values reduced the spatial overlap between consecutive melted tracks, subsequently yielding visibly rougher surfaces (3rd group) or surfaces without overlap between consecutive tracks (4th group). An increase in the scanning speed (constant laser power) caused a leftward shift of the optimal processing zone (2nd group) towards lower hatch distance values due to the reduction in the width of the melted tracks. This was expected because narrower tracks require smaller hatch distance values to achieve sufficient overlap between consecutive tracks.
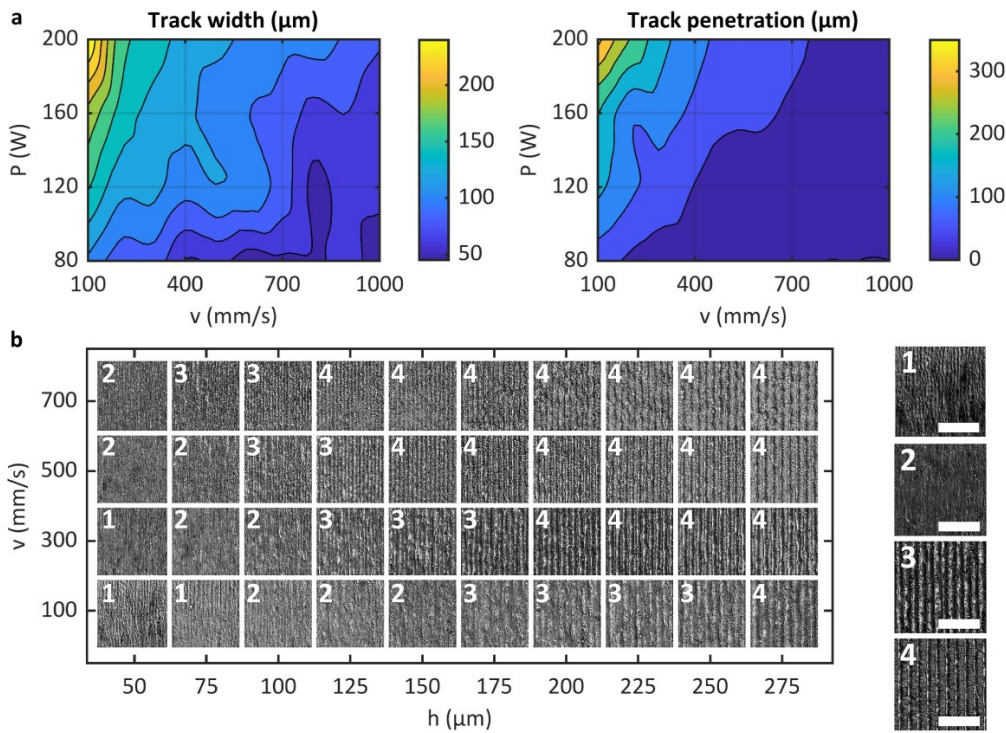
Figure 4.1: Results of the single-track and hatch distance experiments conducted using stainless steel 316L substrates. (a) Evolution of the width and penetration depth of the melted single tracks as a function of applied laser power and scanning speed. (b) Results of the hatch distance experiments. The produced surfaces were categorized as follows: (1) continuous surface with spattering and irregularity, (2) continuous surface with no apparent defects, (3) uneven continuous surface, and (4) non-continuous surface. The scale bar is 1 mm. (*Modified from* **publication II**.)

Table 4.1: Chemical compositions, relative densities and average grain sizes of the samples manufactured via L-PBF in **publications II-V**. (*Modified from* **publications II-V**.)

Publication Sample	Chemical composition			Density	Grain size
	Ni (at.%)	Mn (at.%)	Ga (at.%)	(%)	(µm)
II-1	52.21±0.71	26.93±0.99	20.86±0.35	96.8±0.7	-
II-2	50.99±0.26	27.23±0.33	21.78±0.12	94.9±1.3	-
II-3	50.84±0.18	27.41±0.22	21.75±0.15	93.5±1.8	-
III-1	51.64±0.71	27.13±0.85	21.23±0.30	75.2±4.8	-
III-2	64.57±2.67	19.14±3.93	16.28±1.55	86.2±2.8	-
III-3	51.25±1.01	27.42±1.29	21.33±0.42	87.7±1.6	-
III-4	51.89±1.33	26.70±1.68	21.41±0.54	79.4±2.1	-
III-5	58.69±1.50	20.97±2.51	20.35±1.13	95.2±0.9	-
III-6	59.14±0.83	19.87±0.83	20.98±0.20	92.7±2.1	-
III-7	51.66±0.44	26.47±0.48	21.87±0.11	93.7±0.4	-
III-8	56.76±0.81	21.82±0.78	21.43±0.08	96.2±0.5	-
III-9	52.66±0.92	26.57±1.21	20.77±0.60	81.0±3.2	-
III-10	50.29±0.29	27.92±0.42	21.79±0.17	72.6±5.2	-
III-11	52.57±1.50	26.26±1.58	21.17±0.50	91.2±1.5	-
III-12	53.57±1.24	25.00±1.33	21.43±0.24	94.9±0.6	-
III-13	50.82±0.38	27.38±0.38	21.80±0.10	83.1±3.7	-
III-14	64.24±1.71	17.20±2.06	18.56±1.09	92.6±0.5	-
III-15	52.47±0.67	26.13±0.70	21.40±0.14	97.8±0.3	-
III-16	51.90±0.86	26.43±0.99	21.67±0.24	91.8±2.4	-
III-17	58.34±1.00	20.63±0.96	21.03±0.13	93.7±0.9	-
III-18	51.56±0.44	26.72±0.49	21.72±0.12	98.7±0.5	-
III-19	50.00±0.62	28.05±0.59	21.96±0.58	76.0±2.7	-
III-20	56.19±1.96	24.43±2.96	19.38±1.24	93.5±0.9	-
III-21	50.33±0.56	28.07±0.71	21.59±0.30	93.9±2.3	-
III-22	50.84±0.43	27.38±0.41	21.79±0.13	84.2±1.8	-
III-23	53.66±1.18	25.41±1.35	20.93±0.44	96.8±0.6	-
III-24	53.40±0.77	25.19±0.89	21.41±0.26	94.2±1.1	-
III-25	50.63±0.24	27.55±0.27	21.82±0.09	94.8±1.1	-
III-26	51.73±0.58	26.69±0.75	21.58±0.19	98.5±0.3	-
III-OPT	50.92±0.43	27.43±0.46	21.65±0.12	98.3±0.3	16.6±5.1
IV-1	50.47±0.20	27.50±0.32	22.03±0.24	98.6±0.3	13.5±3.5
IV-2	50.66±0.29	27.27±0.29	22.06±0.14	98.2±0.2	22.2±6.2
IV-3	50.57±0.22	27.36±0.28	22.07±0.15	98.4±0.4	22.1±5.8
IV-4	50.62±0.15	27.46±0.27	21.92±0.14	97.9±0.3	24.2±7.4
IV-5	50.76±0.27	27.22±0.30	22.02±0.15	98.3±0.3	34.8±9.9
IV-6	50.52±0.26	27.70±0.31	21.78±0.24	98.4±0.3	23.2±6.9
IV-7	50.57±0.19	27.54±0.26	21.89±0.13	98.8±0.3	24.5±7.2
IV-8	50.78±0.08	27.08±0.17	22.14±0.13	98.2±0.3	38.0±10.8
IV-9	50.60±0.21	27.40±0.25	22.00±0.14	98.1±0.4	25.4±7.5
IV-10	50.66±0.18	27.34±0.08	22.00±0.15	98.2±0.4	55.5±14.8
IV-11	50.72±0.10	27.21±0.09	22.07±0.09	98.8±0.2	66.2±16.7
V-1, V-7	49.38±0.09	29.38±0.12	21.25±0.07	>98	-
V-2, V-8	49.71±0.09	28.92±0.12	21.37±0.07	>98	-
V-3, V-9	50.08±0.12	28.37±0.22	21.55±0.12	>98	-
V-4, V-10	50.47±0.11	27.79±0.15	21.73±0.14	>98	-
V-5, V-11	50.79±0.16	27.57±0.27	21.64±0.13	>98	-
V-6, V-12	51.91±0.21	26.72±0.26	21.37±0.14	>98	-
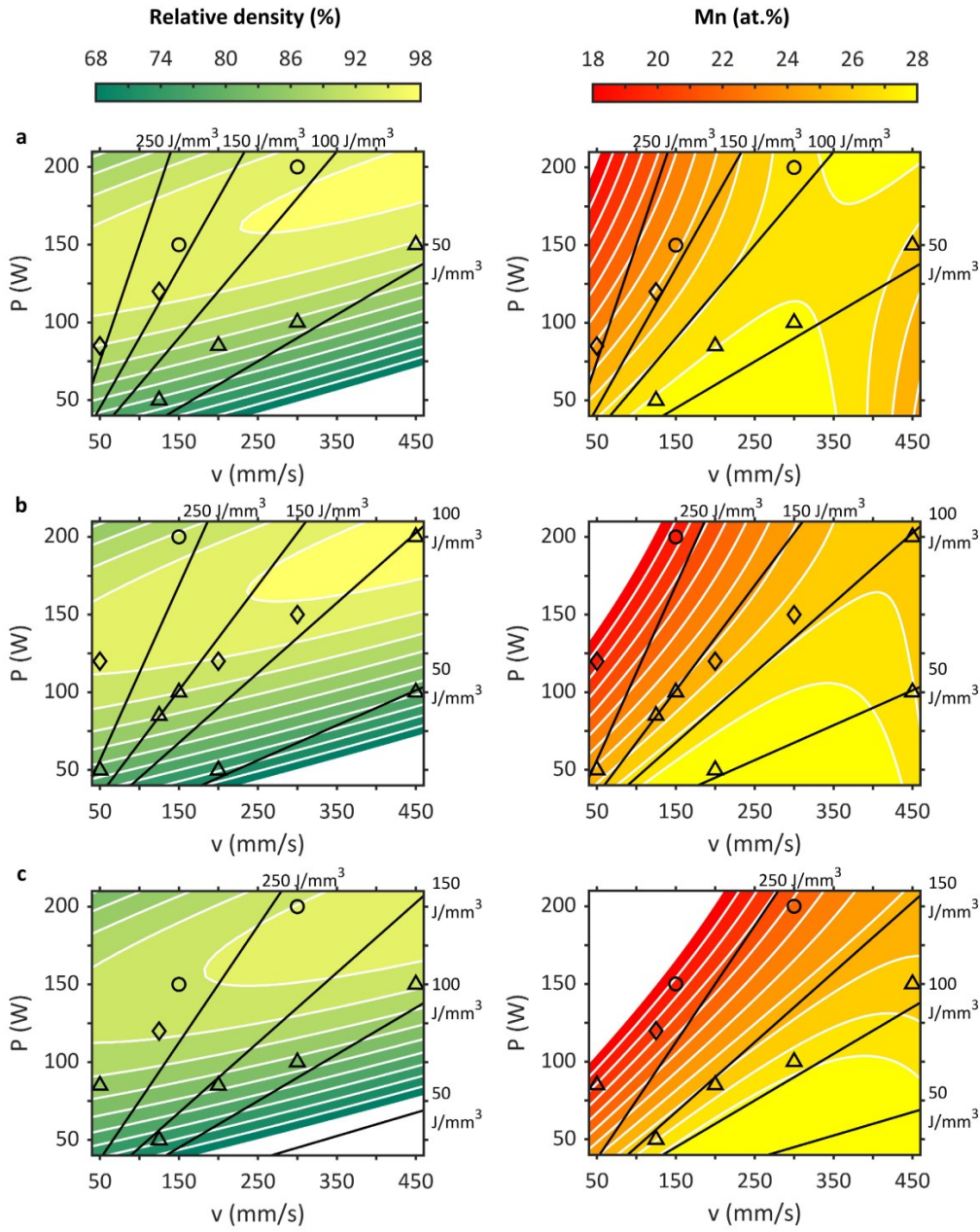
Figure 4.2: Effect of the applied laser power and scanning speed on relative density ($R^2 = 0.855$, $RMSE = 2.86$) and Mn content ($R^2 = 0.927$, $RMSE = 0.82$) of the as-built samples. (a) $h = 100$ µm; (b) $h = 75$ µm; (c) and $h = 50$ µm. The locations of four selected VED levels are marked using black lines. Sample locations are marked with symbols that correspond to the type of porosity observed within the sample: ○ gas porosity, △ irregularly shaped lack-of-fusion pores, and ◇ a combination of the two. For reference, see Figure 4.3. (*Modified from* **publication III**.)

Table 4.2: ANOVA for the quadratic polynomial models fitted for the relative density and Mn content of the as-built samples in **publication III**. (*Modified from* **publication III**.)

		Relative density (%)					Mn content (at.%)			
Source	DF	Adj SS	Adj MS	F-value	P-value	DF	Adj SS	Adj MS	F-value	P-value
Model	9	1257.04	139.67	10.49	0.000	9	223.485	24.832	22.73	0.000
P	1	1024.75	1024.75	76.93	0.000	1	62.910	62.910	57.58	0.000
h	1	32.37	32.37	2.43	0.139	1	25.094	25.094	22.97	0.000
v	1	97.48	97.48	7.32	0.016	1	119.637	119.637	109.50	0.000
P^2	1	314.14	314.14	23.58	0.000	1	0.187	0.187	0.17	0.685
h^2	1	8.07	8.07	0.61	0.448	1	0.260	0.260	0.24	0.632
v^2	1	12.57	12.57	0.94	0.346	1	29.358	29.358	26.87	0.000
$P*h$	1	1.20	1.20	0.09	0.768	1	12.374	12.374	11.33	0.004
$P*v$	1	116.81	116.81	8.77	0.009	1	10.756	10.756	9.85	0.006
$h*v$	1	0.39	0.39	0.03	0.866	1	12.088	12.088	11.06	0.004
Error	16	213.12	13.32	-	-	16	17.481	1.093	-	-
Total	25	1470.16	-	-	-	25	240.965	-	-	-

4.1.2 Process optimization for the manufacture of 3D samples

The chemical compositions, relative densities and average grain sizes of the samples manufactured via L-PBF in **publications II-V** are summarized in Table 4.1. The shown errors correspond to the standard deviations of the measurement. For the corresponding L-PBF process parameters, the reader is referred to Table 3.3, presented in Chapter 3. Figure 4.2 shows the contour plots of the two fitted quadratic polynomial models, visualizing the effects of applied laser power, scanning speed and hatch distance on the relative density and Mn content of the as-built Ni-Mn-Ga samples in **publication III**. Both models have relatively high correlation coefficients (see figure caption), which indicates moderate consistency between the experimental and predicted values. Additionally, the ANOVA in Table 4.2 shows that both models are statistically significant; thus, they can provide an adequate approximation and offer a good basis for further process optimization within the applied range of parameters.

The contour plots of the model fitted for relative density, shown in Figure 4.2a, reveal that for each used value of hatch distance, there exists a clear area of optimum processing conditions where the highest relative densities are achieved. Variation of the processing parameters toward low *VED* or high *VED* conditions results in a decrease in the relative density. The p-values presented in Table 4.2 show that relative density appears to be mainly affected by the applied laser power and its product with scanning speed, whereas the other parameters are not statistically significant. The effect of hatch distance is mainly noticeable as a shift of the area of high relative density towards lower values of scanning speed with increasing hatch distance; see Figure 4.2a. Here, *VED* is used merely as a reference as it is essentially a thermodynamic parameter that does not well describe the complex physical phenomena connected with densification in L-PBF. Additionally, the lack of high relative density samples at parameter combinations with low laser power and scanning speed values implies that the parameter spacing in the used experimental design may have been too large in this region.
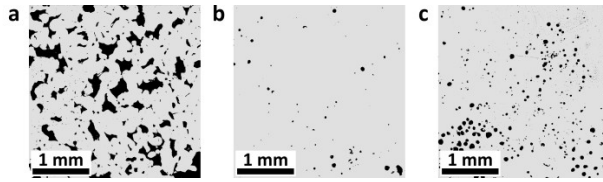
Figure 4.3: Examples of sample sections with different porosities observed by an optical microscope. (a) a sample with irregularly shaped lack-of-fusion pores ($P = 50$ W, $v = 125$ mm/s, $h = 100$ μm), (b) a high-density sample with a low amount of gas pores ($P = 200$ W, $v = 300$ mm/s, $h = 100$ μm), and (c) a lower-density sample with an increased amount of gas pores ($P = 150$ W, $v = 150$ mm/s, $h = 50$ μm). (*Modified from* **publication III**.)

As mentioned above, the highest relative densities for the built material in L-PBF were achieved when the melted tracks exhibited adequate metallic bonding with the underlying material and sufficient spatial overlap between consecutive parallel tracks, yielding layers with reasonably smooth top surfaces and consistent thicknesses, and when these processing conditions remained stable throughout the layer-by-layer melting. A variation of the process parameters from these optimum conditions toward low *VED* conditions led to the formation of lack-of-fusion pores with irregular morphologies (see the sample sections exemplified in Figure 4.3) as the applied process parameters failed to fulfil the above criteria. Additionally, balling and other phenomena linked to the instability of single-track formation likely contributed to pore formation. The observed lack-of-fusion pores were up to several hundred μm in diameter and possessed a highly irregular morphology, which might explain the larger standard deviations in relative density obtained for the lower-density samples. Meanwhile, a variation of the process parameters toward high *VED* conditions led to the formation of small spherical pores with observed diameters generally below ~70 μm. This was expected as high *VED* conditions (high laser power, low scanning speed) may shift the process from conduction mode melting to keyhole melting (Kamath et al., 2014; King et al., 2014), resulting in gas entrapment. Additionally, some samples with intermediate parameter combinations exhibited pores of both morphologies.

The initial results obtained in **publication II** showed that the selective evaporation of Mn and Ga may occur during the laser–material interaction in the L-PBF of Ni-Mn-Ga. This effect was further studied in **publication III**. The p-values in Table 4.2 reveal that most of the applied process parameters are statistically significant for the obtained Mn content. Furthermore, Figure 4.2 shows that the effects of the applied process parameters on relative density and Mn content are overall remarkably different. The slight decrease in Mn content with *VED* values below ~50 J/mm^3 occurs due to the model's inaccuracy as this area is located outside the applied range of parameters. Additionally, the marked levels of *VED* are almost parallel to the contour lines of Mn content, implying that *VED* can be effectively used as an explanatory parameter to visualize the effect of the process parameters on chemical composition within the applied range of parameters; see Figure 4.4.
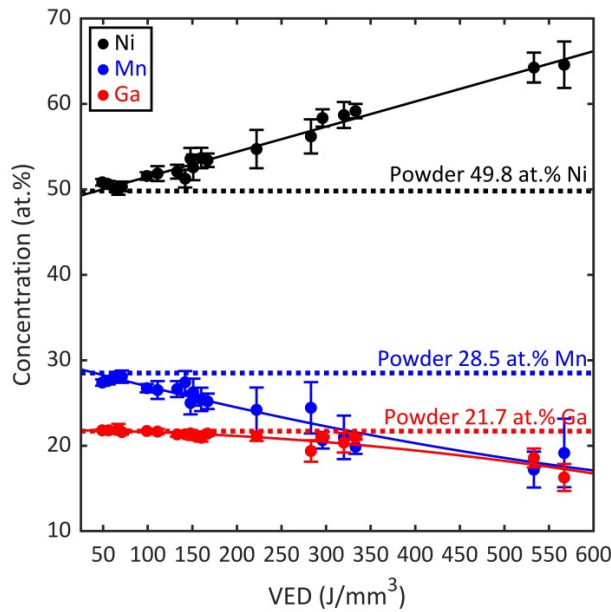
Figure 4.4: Effect of the applied *VED* on the chemical composition of the as-built Ni-Mn-Ga samples. (*Modified from* **publication III**.)

The samples with low *VED* values exhibited only a ~0.5-1.0 at.% decrease in the fraction of Mn in comparison to the initial powder. Additionally, these samples exhibited standard deviations of composition (shown in Table 4.1) approximately within the absolute measurement accuracy of the used XRF device. A distinctive decrease in the fraction of Mn and a corresponding increase in the fraction of Ni occurred when *VED* was increased above ~75-100 J/mm^3. Additionally, a decrease in the fraction of Ga was observed when VED was increased above ~200 250 J/mm^3. Notably, standard deviations of the compositions increased toward the high *VED* samples, which may be linked to localized segregation or the selective evaporation of certain elements on a smaller scale when *VED* was increased (Schönrath et al., 2019). Here, compositional variations in the size scales below the diameter of the used XRF collimator (300 μm) were undetectable. Selective evaporation of Mn was expected because it has the lowest absolute boiling temperature at ~2061 °C (Haynes et al., 2017) among the elements in Ni-Mn-Ga. The absolute boiling temperature of Ga is ~2204 °C, which explains the selective evaporation of Ga at higher *VED* values. The boiling temperature of Ni is ~2913 °C (Haynes et al., 2017), making it unlikely that it will evaporate in large quantities without the simultaneous loss of Mn and Ga. The obtained results are in good agreement with those obtained in **publication II** and by Nielsen et al. (2019) and suggest that, with the used L-PBF system, high-density Ni-Mn-Ga samples can be deposited with the controlled loss of Mn. However, an over-alloying of Mn into the initial powder is required to counteract the evaporation of Mn.

Table 4.3: ANOVA tables for relative density and Mn content, including homogenization temperature (T_h) and time (t_h) as continuous predictors. (*Modified from* **publication IV**.)

Source		Relative density (%)					Mn content (at.%)			
	DF	Adj SS	Adj MS	F-value	P-value	DF	Adj SS	Adj MS	F-value	P-value
T_h	1	0.063	0.063	0.43	0.558	1	0.001	0.001	0.05	0.832
t_h	1	0.027	0.027	0.18	0.699	1	0.151	0.151	5.89	0.094
T_h^2	1	0.067	0.067	0.46	0.547	1	0.024	0.024	0.92	0.408
t_h^2	1	0.004	0.004	0.03	0.882	1	0.008	0.008	0.30	0.620
T_h*t_h	1	0.138	0.138	0.94	0.404	1	0.000	0.000	0.01	0.935
Error	3	0.440	0.147	-	-	3	0.077	0.026	-	-
Total	8	0.722	-	-	-	8	0.280	-	-	-

4.2   Characterization of as-built and heat-treated samples

This section reveals and discusses the results of the second stage in our experimental research, namely the development of a heat-treatment process for chemical homogenization and grain growth and the characterization of the produced material in as-built and heat-treated conditions. The results presented here were obtained in **publications III and IV**.

4.2.1   Relative density and chemical composition

Table 4.3 shows the ANOVA obtained in **publication IV** for relative density and Mn content, including homogenization temperature (T_h) and time (t_h) as continuous predictors. Overall, the results demonstrate the high repeatability of L-PBF for manufacturing high-density polycrystalline Ni-Mn-Ga with a consistent and predictable composition. All samples in **publication IV** were highly dense (average ~98.4%) with only minor between-sample variation and standard deviations in the range of ±0.15–0.41% for all samples. The ANOVA does not show any dependency between applied homogenization treatment and observed density. Considerable density changes were not expected during the heat treatment because the density of the as-built samples was relatively high.

The optimized sample in **publication III** exhibited a ~1.1 at.% decrease in the fraction of Mn and a corresponding increase in the fraction of Ni compared to the initial powder, with no clear change in the fraction of Ga. This was expected based on the parameter optimization conducted earlier in the same publication. The as-built samples in **publication IV** exhibited a ~1.6 at.% decrease on average in the fraction of Mn compared to the initial powder. Consequently, the fractions of Ni and Ga each increased by ~0.8 at.%. Using a lower *VED* value (44.4 J/mm^3) in **publication IV** than in **publication III** likely led to the reduced evaporation of Ga during L-PBF, which explains this observation. Additionally, the studies were conducted using different Ni-Mn-Ga powders and substrates, further contributing to the observed differences. The ANOVA in Table 4.3 shows that the heat treatment did not influence the samples' chemical composition. The

observed compositional differences between samples (see Table 4.1) were not large enough to impact their magneto-structural properties.

The XRF measurements did not reveal any distinct change of composition within each sample in each publication. The EDS analysis conducted on a section along the build direction of a sample (III-OPT) in **publication III** did not show any segregation or scattering of the chemical elements. The composition of the sample was moderately homogenous, with only a minor variation that could not be reliably distinguished from the noise and uncertainty of the measurement itself. Importantly, the samples in both publications exhibited standard deviations of the measured compositions approximately within the measurement accuracy. In **publication IV**, the standard deviations of the measured compositions were smaller in samples with longer homogenization times or higher homogenization temperatures, implying an increase in chemical homogeneity.
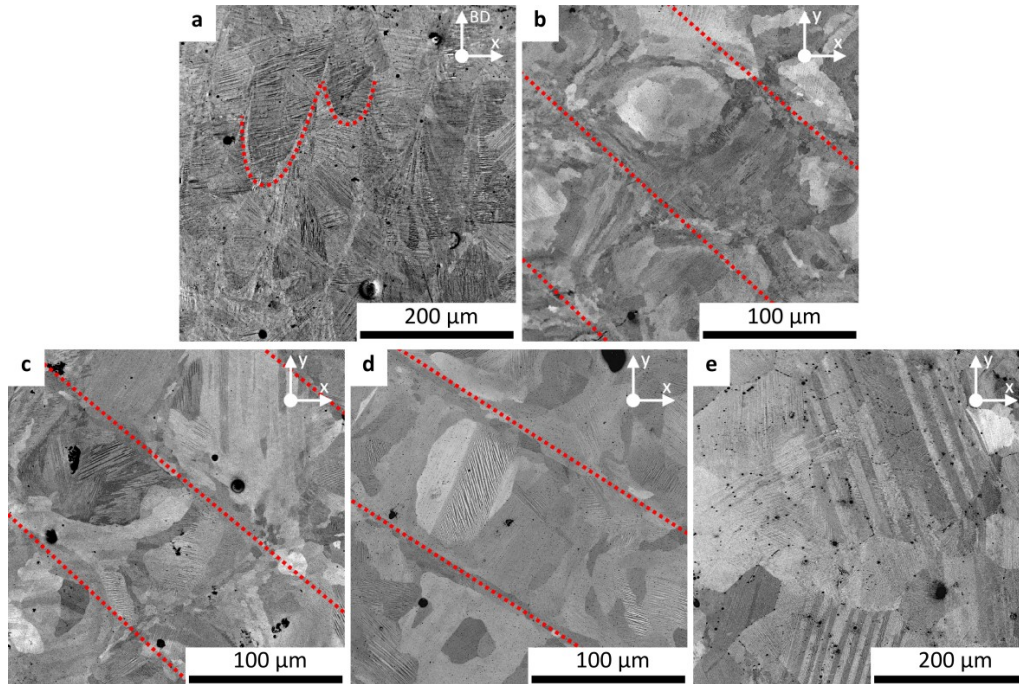

Figure 4.5: SEM images of the microstructure obtained from: (a) a section of an as-built sample (III-OPT) along the build direction; sections perpendicular to the build direction: (b) as-built sample (IV-1), (c) a sample ordered at 800 °C for 4 hours (IV-2), (d) a sample homogenized at 1040 °C for 6 h (IV-6), and (e) a sample homogenized at 1080 °C for 24 h (IV-11). The dotted red lines indicate observed boundaries between adjacent laser-scanning tracks. (Modified from **publications III and IV**.)

4.2.2   Microstructure

Figure 4.5 shows the SEM images obtained from a section of the as-built sample III-OPT along the build direction and sections of the as-built sample IV-1 and selected heat-treated samples (IV-2, IV-6, and IV-11) perpendicular to the build direction. Some of the observed boundaries between adjacent laser scanning tracks are marked with red dotted lines. The reader is advised to note the composition difference between the sample produced in **publication III** and the samples produced in **publication IV**.

The microstructures of the as-built samples, shown in Figure 4.5a-b, are highly anisotropic, with the boundaries and profiles of each deposited track clearly distinguishable in the SEM images. Both samples exhibit a columnar grain structure without the presence of dendritic cooling structures that are sometimes observed with L-PBF-built materials. Some finer grains are located between the relatively larger columnar grains at the boundaries between adjacent laser-scanning tracks. This grain texture develops when columnar grains grow along the normal direction to the edges of melt pools induced by the large directional thermal gradients during L-PBF manufacture. Additionally, martensitic twin variants, observable as a parallel stripe-like surface relief with contrasting areas, can be observed throughout the SEM image of sample III-OPT in Figure 4.5a. Some of the observed twins cross the boundaries between adjacent tracks and consecutive deposition layers. The orientation and width of the twins vary from grain to grain. The twins are not as visible in the SEM images of the samples produced in **publication IV**, mostly because the used SEM parameters were selected to enable high grain contrast for grain size measurements; see the section about SEM in Chapter 3. Figure 4.5e shows that the sample homogenized at 1080 °C for 24 h displayed considerable recrystallization, exhibiting a microstructure that predominantly consists of large equiaxed grains. The boundaries between adjacent laser-scanning tracks are no longer observable. The SEM images of intermediate samples, shown in Figure 4.5c-d, demonstrate the gradual change from the columnar grain structure of the as-built samples to the equiaxed grain structure of the sample homogenized at 1080 °C for 24 h.

Some intergranular cracking was observed within the built samples in **publication IV**, which was expected based on the results obtained earlier in **publication II**. The location, size, number and distribution of the observed cracks appeared to be random. Overall, Ni-Mn-Ga based MSM alloys possess low deformability (Wei et al., 2018), which makes them brittle and highly susceptible to cracking in response to internal stresses accumulated in L-PBF or during cutting and grinding in sample preparation. Cracking was not observed with the as-built sample (III-OPT) in **publication III**, possibly due to its different chemical composition and the different L-PBF processing conditions in comparison to the samples in **publication IV**.

In **publication III**, the volume-weighted average grain size of the as-built sample was determined as 16.6 μm. A similar value, 13.5 μm, was obtained for the as-built sample in **publication IV** despite the obvious compositional difference between the two samples. Overall, the average grain sizes of the as-built samples can be considered small but are

within the typical range for L-PFF-manufactured materials (DebRoy et al., 2018). Figure 4.6 shows the effect of the applied heat-treatment parameters on the volume-weighted average grain sizes of the samples built in **publication IV**. All heat-treated samples exhibited grain growth in comparison to the as-built material. The ANOVA in Table 4.4 shows a statistically significant dependency between the observed grain size and the applied homogenization temperature and time. The most significant average grain size increase was observed for samples homogenized at 1080 °C for 12 and 24 h. The observed grain growth was overall equal throughout the volume of each sample, although some singular larger grains formed near the edges of these samples. For example, the sample homogenized at 1080 °C for 24 h exhibited a large quantity of grains exceeding 300 µm in diameter; see the SEM image in Figure 4.5e and the polarized light optical image in Figure 4.7e.
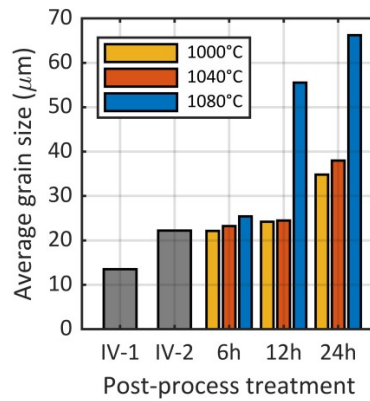

Figure 4.6: Effect of the applied heat-treatment on the average grain size of the L-PBF-built samples, as measured and averaged from multiple sections of each sample perpendicular to the build direction. (*Modified from* **publication IV**.)

Table 4.4: ANOVA table for the volume-weighted average grain size, including homogenization temperature (T_h) and time (t_h) as continuous predictors. (*Modified from* **publication IV**.)

Source	DF	Average grain size (µm)			
		Adj SS	Adj MS	F-value	P-value
T_h	1	803.610	803.610	12.38	0.039
t_h	1	776.410	776.410	11.96	0.041
T_h^2	1	180.620	180.620	2.78	0.194
t_h^2	1	24.510	24.510	0.38	0.582
T_h*t_h	1	150.690	150.690	2.32	0.225
Error	3	194.770	64.920	-	-
Total	8	2029.410	-	-	-

4.2.3   Magneto-structure

We conducted a series of combined AFM/MFM measurements to study the magnetic properties of the martensitic twins in as-built and heat-treated Ni-Mn-Ga samples in **publications III and IV**. To allow a comparison, a heat-treated and electropolished single-crystalline sample with a 10M martensite structure (40° $Ni_{50}Mn_{28.5}Ga_{21.5}$ alloy by AdaptaMat Ltd.) was heated to ~80 °C and then cooled to ambient temperature to create a random twin structure.

Figure 4.7a shows the MFM image of the 10M sample (two-variant structure) with the *a*- and *c*-axes perpendicular to the plane of view. A labyrinth-like magnetic domain structure is observable in the variants, with the *c*-axis perpendicular to the image plane. On this scale, the TBs appear as clearly distinguishable straight lines, and the twin variants with widths as low as ~1-2 μm exhibit a clear MFM contrast between the different twin variants. Figure 4.7b shows the MFM image of the 10M sample with the *c*-axis oriented approximately to the plane of view. A slight relief between the two variants visible in the corresponding AFM image – see **publication III** – indicates that the sample was not cut precisely along {001} lattice plane.

Figure 4.7c-d shows the MFM scans obtained from two sections of an as-built sample in **publication III**. The MSM scans show very narrow stripes, below 1 μm in width, exhibiting magnetic anisotropy (MFM contrast) that is considerably weaker compared to the 10M reference sample. Additionally, there is minor variation between the MFM contrasts between measurements, possibly due to minor compositional variation effects, L-PBF-induced internal stresses, or the differences in MFM contrast between different variants at different angles depending on the localized crystalline orientation of each grain.

Figure 4.7e shows a polarized light image of a top surface section of the sample homogenized at 1080 °C for 24 h in **publication IV**. A few areas of the sample with the largest features attributed to the twins were chosen for MFM scanning. The specified locations corresponding to the MFM images A1 and A2 are outlined with white squares. The optical image shows martensitic twins with widths at the limit of the optical resolution and their orientation varying from grain to grain. This parallel stripe-like surface relief with contrasting cannot be observed in some areas, possibly due to the twins' thickness lying under the optical resolution limit. Overall, the heat-treated sample exhibits drastically improved MFM contrast in comparison to the as-built sample. The MFM images reveal thick bands that correspond to the optical image and thinner bands with thicknesses down to the nanoscale. Hence, the thicker bands are composed of very narrow bands, which, in combination with the differences in MFM contrast between different variants at different angles, explains the unusually weak contrast obtained for the optical images; see Chapter 3 for reference. Additionally, the MFM image A1 shows visible signs of branching in the central band. Overall, the observed twin structure is consistent with polycrystalline Ni-Mn-Ga 14M martensites (Li et al., 2016), as also confirmed by the XRD measurement.
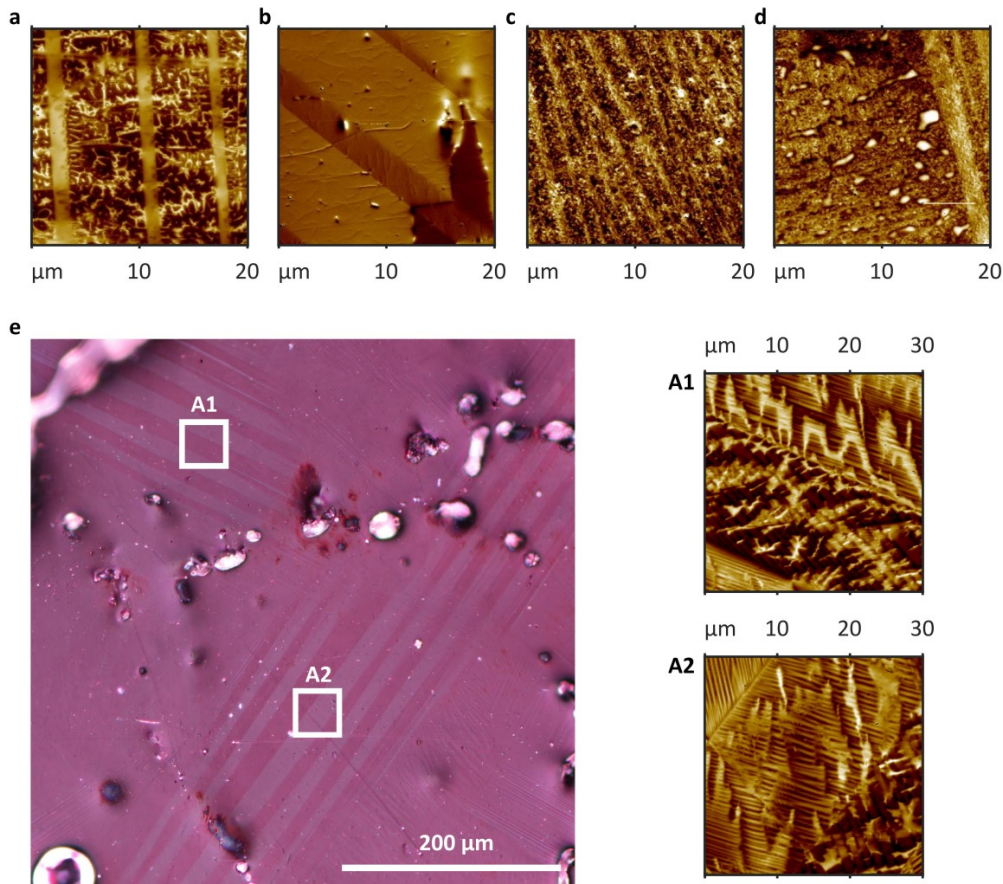
Figure 4.7: MFM images obtained from: (a) a section of a single-crystalline 10M martensite reference sample showing a two-variant microstructure with the *a*- and *c*-axes perpendicular to the plane of view; (b) a section of the 10M sample with the *c*-axis oriented in the plane of view; and (c-d) two sections of an as-built L-PBF sample (III-OPT) perpendicular to the build direction. (e) Optical image (left) with polarized light contrast of an L-PBF sample homogenized at 1080°C for 24 h (IV-11). The image was taken perpendicular to the build direction. Areas A1 and A2 correspond to the locations of the two MFM scans shown on the right. (Modified from **publications III and IV**.)

Table 4.5: Critical phase transformation temperatures and martensite lattice parameters, corresponding to the 14M, 10M and NM martensites, obtained for each sample in **publications III-V**. The corresponding X-ray diffractograms were collected at ambient temperature. The lattice parameters are presented in the cubic coordinate system of the parent austenite unit cell with an approximate accuracy of $\pm$ 0.01 Å and $\pm$ 0.01**°**. (*Modified from* **publications III-V**.)

Publication Sample	Phase	Martensite lattice parameters at 22 °C						Transformation temperatures				
		a (Å)	b (Å)	c (Å)	γ (º)	Vol (Å^3)	c/a (-)	T_{AS} (°C)	T_{AF} (°C)	T_{MS} (°C)	T_{MF} (°C)	T_C (°C)
III-OPT	14M	6.21	5.82	5.52	90.5	199.3	0.89	103	135	122	97	52
	NM	5.38	5.38	6.65	-	192.5	1.24					
IV-1	14M	6.10	5.85	5.55	90.47	198.2	0.91	22	64	57	16	73
	10M	5.97	5.97	5.57	90.32	198.6	0.93					
IV-2	14M	6.10	5.85	5.55	90.48	198.2	0.91	46	58	54	42	90
	10M	5.98	5.98	5.57	90.34	199.0	0.93					
IV-3	14M	6.1	5.85	5.56	90.53	198.3	0.91	49	62	58	45	89
	10M	5.98	5.98	5.56	90.29	198.9	0.93					
IV-4	14M	6.10	5.85	5.55	90.50	198.2	0.91	46	57	54	43	90
	10M	5.98	5.98	5.57	90.34	199.5	0.93					
IV-5	14M	6.10	5.85	5.55	90.51	198.0	0.91	46	57	54	42	89
	10M	5.98	5.98	5.55	90.32	198.2	0.93					
IV-6	14M	6.11	5.85	5.55	90.51	198.2	0.91	50	60	57	46	89
IV-7	14M	6.09	5.85	5.55	90.49	198.0	0.91	50	60	57	47	89
IV-8	14M	6.10	5.85	5.55	90.46	198.1	0.91	51	60	57	48	89
IV-9	14M	6.11	5.85	5.55	90.51	198.3	0.91	49	58	54	45	90
IV-10	14M	6.10	5.85	5.55	90.50	198.2	0.91	47	56	52	44	90
IV-11	14M	6.10	5.85	5.55	90.52	197.8	0.91	48	56	52	45	92
V-1, V-7	10M	5.97	5.90	5.57	90.34	196.4	0.93	52	59	50	45	98
V-2, V-8	10M	5.96	5.89	5.59	90.39	196.0	0.94	47	55	46	40	99
V-3, V-9	10M	5.95	5.89	5.58	90.32	195.8	0.94	46	54	47	40	96
V-4, V-10	14M	6.11	5.84	5.54	90.51	197.4	0.91	53	58	51	46	99
V-5, V-11	14M	6.11	5.84	5.54	90.47	197.5	0.91	57	66	62	53	92
V-6, V-12	NM	5.37	5.37	6.68	-	192.5	1.25	59	71	67	56	83

4.2.4   Crystal structure

The approximate martensite lattice parameters obtained for the samples manufactured via L-PBF in **publications III-V** are summarized in Table 4.5. All lattice parameters are presented in the cubic coordinate system of the parent austenite unit cell. For the corresponding L-PBF process parameters and other properties, the reader is referred to Table 3.3 and Table 4.1. Figure 4.8 shows the X-ray diffractograms obtained for each sample in **publication IV** at ambient temperature. The identified peaks, corresponding to the 10M and 14M martensites, are indexed relative to the coordinate system of the parent austenite unit cell. The unindexed diffraction peaks originate from the modulated superstructure. Overall, the samples produced in **publication IV** showed very little lattice parameter variation from sample to sample, which was expected because the average compositions of these samples were nearly the same; see Table 4.1 for reference.
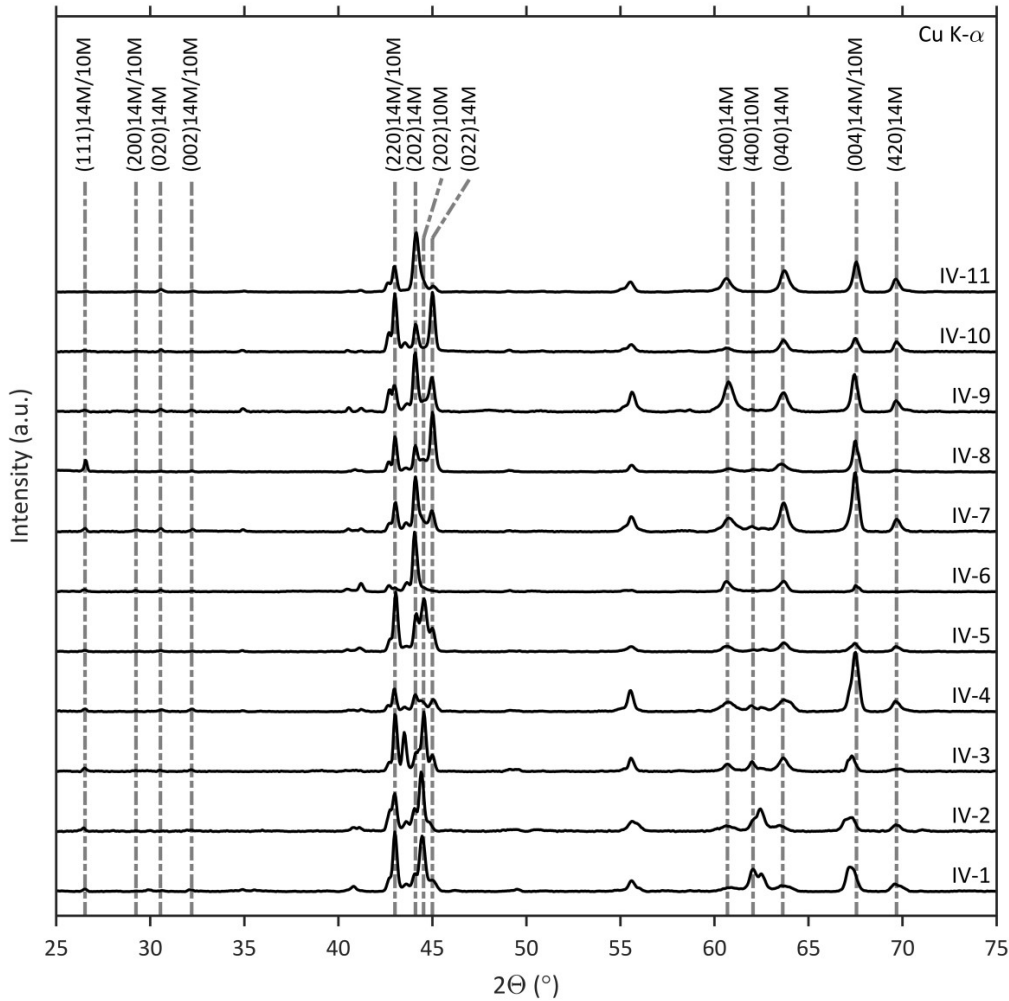
Figure 4.8: XRD patterns obtained for each sample at ambient temperature in **publication IV**. Intensities have been scaled and the baseline is offset. Recognized peaks of the 14M and 10M martensites are marked with grey dashed lines and indexed relative to the coordinate system of the parent austenite unit cell. (*Modified from* **publication IV**.)

The as-built sample IV-1 and the heat-treated sample IV-2 (atomic ordering treatment, no prior homogenization) showed a mixed crystal structure of 14M and 10M martensites with moderately high intensities of the 10M peaks at the angles of ~62.0° and ~62.5°. This was expected as the as-built sample (III-OPT) in **publication III** also exhibited a mixed structure of 14M and NM martensites at ambient temperature. Additionally, the diffraction lines obtained for the as-built samples in both publications were generally broader and exhibited lower diffraction intensities in comparison to the heat-treated

samples. In **publication III**, it was suggested that these observations were likely caused by a localized variation of the lattice parameters, possibly due to the inhomogeneity of the chemical composition typically present in the anisotropic microstructures developed during L-PBF combined with L-PBF-induced internal stresses. This is supported by the fact that the samples' chemical compositions do not correspond to those (Chernenko, 1999) that would typically exhibit co-existing martensite phases at ambient temperature. Homogenization at temperatures above 1040 °C leads to chemical homogenization, which increases the stability of the 14M martensite at the cost of the 10M martensite. Consequently, the intensity of the 10M lines is considerably reduced for all homogenized samples, and thus, the lattice parameters of the 10M martensite could only be obtained for samples IV-1 → IV-5. Finally, the samples homogenized at 1080 °C for 12–24 h showed only the diffraction peaks originating from 14M martensite at ambient temperature. Moreover, the variation and distribution of peak intensities within the measured samples suggested the presence of a crystallographic texture. However, the complex nature of the diffraction patterns produced by modulated martensites in multivariant polycrystalline samples, as produced by L-PBF in these publications, made a more thorough analysis of the crystallographic texture in **publications III-IV** unfeasible.

4.2.5   **Phase transformations and magnetic properties**

The phase transformation and Curie temperatures of the samples produced in **publications II-V** are summarized in Table 4.5. The LFMS and DSC curves obtained for the as-built sample (IV-1) and the heat-treated sample (IV-11) in **publication IV** are shown in Figure 4.9a-b. Here, two phase transformations are observed upon heating: the first-order structural transformation from 14M martensite to cubic, and the second-order phase transformation from cubic ferromagnetic to cubic paramagnetic. The reverse transformations are observed upon cooling.

The phase transformations of the as-built samples (III-OPT and IV-1) in **publications III and IV** were broad, in the range of ~20–40 °C, and exhibited a large deviation from the values obtained for similar alloy compositions in the scientific literature. It was suggested in **publication III** that the observed shift and broadening of the phase transformations could correspond to minor compositional variations, lattice strains, or the presence of multiple phases or martensite structures.
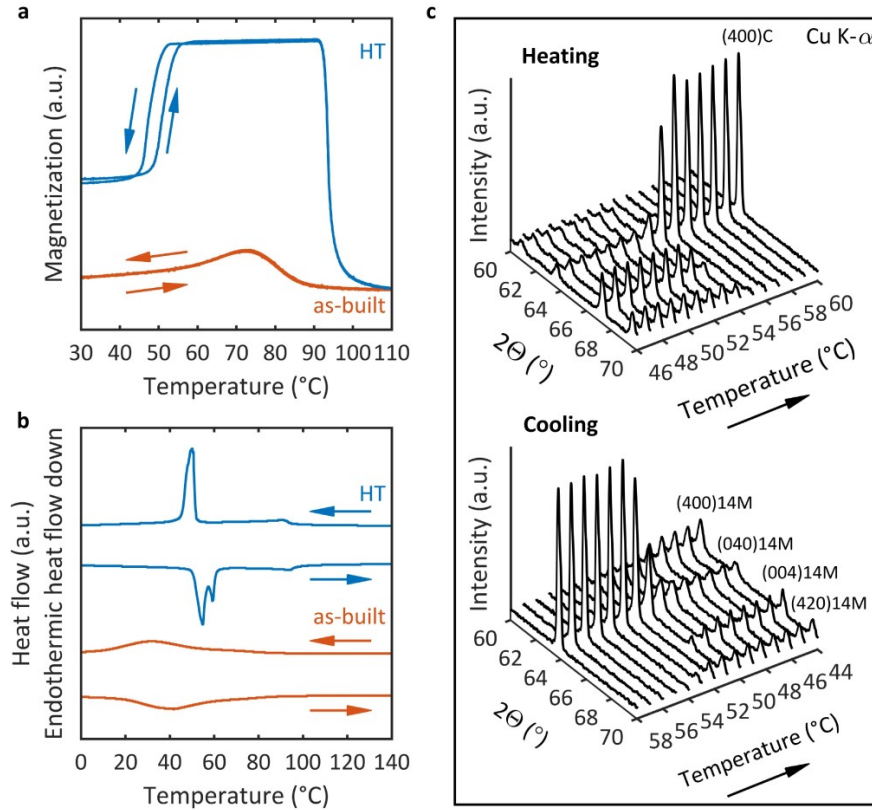
Figure 4.9: The phase transformations of an as-built sample (IV-1) and a heat-treated sample (HT, IV-11). (a) LFMS measurement. Zero-magnetization level corresponds to the magnetization of paramagnetic austenite. (b) DSC measurement. (c) The X-ray diffractograms obtained for the heat-treated sample (IV-11) upon heating and cooling over the martensite transformation temperature. Intensities have been scaled and the baseline is used as an offset for each measurement. Recognized peaks are indexed relative to the coordinate system of the parent austenite unit cell. (*Modified from* **publication IV**.)

Table 4.6: ANOVA table for the width of the austenite-martensite transformation (ΔT_M), including homogenization temperature (T_h) and time (t_h) as continuous predictors. (*Modified from* **publication IV**.)

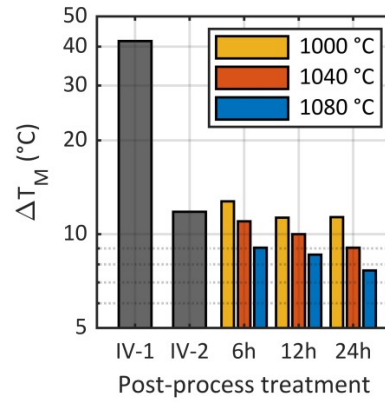| | | ΔT_M (°C) | | | |
Source	DF	Adj SS	Adj MS	F-value	P-value
T_h	1	16.822	16.822	113.47	0.002
t_h	1	3.760	3.760	25.36	0.015
T_h^2	1	0.020	0.020	0.13	0.738
t_h^2	1	0.372	0.372	2.51	0.212
$T_h * t_h$	1	0.012	0.012	0.08	0.795
Error	3	0.445	0.148	-	-
Total	8	21.300	-	-	-

Figure 4.10: Effect of the applied heat-treatment on the width of the austenite-martensite transformation. (*Modified from* **publication IV**.)

All homogenized samples in **publication IV** showed a recovery of the typical magneto-structural properties and reversible martensitic transformations in relation to the chemical composition of each sample. Notably, the sample annealed at 800°C for 4 h without homogenization at a higher temperature also showed a recovery of the typical properties. This implies that the untypical magneto-structural properties of as-built Ni-Mn-Ga are mostly related to the atomic disorder and quenched-in stress from the L-PBF process, as low-temperature annealing itself is not expected to induce a large chemical homogeneity increase. The observed variations in the phase transformation temperatures between samples were small and likely relate to the small differences in the exact chemical compositions of the samples. The ANOVA in Table 4.6 and Figure 4.10 show that increasing either the homogenization temperature or time resulted in a decrease in the width of the austenite-martensite transformation (ΔT_M). This change was suggested to attribute to the general homogeneity increase and the gradual dissolving of the 10M martensite phase. However, the observed transitions are wider than the transitions observed in conventional Ni-Mn-Ga single crystals.

Figure 4.9c shows the results of an additional XRD experiment performed on the sample homogenized at 1080 °C for 24 h to investigate the anomaly (two transformation peaks) observed upon heating during the DSC measurement of the same sample; see Figure 4.9b for reference. The observed peak splitting may relate to intermartensitic transformation in Ni-Mn-Ga. The X-ray diffraction patterns were collected from 60–70° angles during heating and cooling of the sample over martensitic and reverse martensitic transformations. The diffraction data revealed the absence of intermediate phases during these transformations; hence, it was suggested that the splitting of the transformation peak upon heating observed in the DSC measurements occurred due to the presence of structural defects such as pores or cracks. The observed anomaly was not observed upon cooling in DSC, which supports this argument.
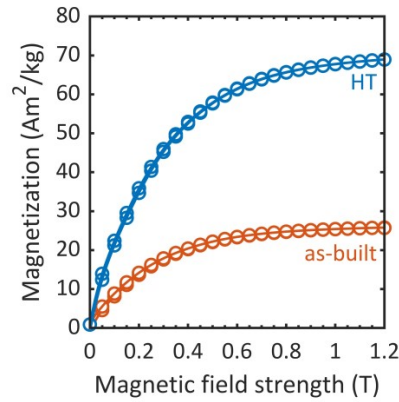
Figure 4.11: The VSM magnetization curves obtained for the as-built sample IV-1 and a sample homogenized at 1080 °C for 24 h (HT, IV-11). (*Modified from* **publication IV**.)

Figure 4.11 shows the VSM hysteresis loops obtained for the as-built sample IV-1 and the heat-treated samples (exemplified by IV-11) in **publication IV**. The measured saturation magnetization of the as-built sample was 25 Am^2/kg. All heat-treated samples exhibited a clear magnetization value increase of nearly ~170% in comparison to the as-built sample. Additionally, the saturation magnetization values obtained for the heat-treated samples were nearly identical, averaging ~68±1 Am^2/kg, which was expected because all samples exhibited mostly the same crystal structure and were equally dense. Additionally, the obtained value is in agreement with the values previously reported in the literature for Ni-Mn-Ga alloys with the same electron concentrations (Heczko & Straka, 2004). The coercive field of the as-built sample was ~31 mT, which was relatively high compared to the values of ~8 mT and ~4–5 mT obtained for the annealed sample (IV-2) and the homogenized samples (IV-3→IV-11), respectively. Each heat-treated sample exhibited a saturation field in the approximate range of 0.6–0.8 T.

4.3   Actuation experiments

This section reveals and discusses the results of the third stage in our experimental research, namely the demonstration of the MSM effect in L-PBF-built Ni-Mn-Ga.

In **publication V**, polycrystalline Ni-Mn-Ga samples were manufactured via L-PBF and subsequently heat-treated near the melting temperature to increase the chemical homogeneity and degree of atomic ordering and to induce a coarse grain structure. The applied L-PBF and heat-treatment parameters and the corresponding sample properties are summarized in Table 3.3, Table 4.1, and Table 4.5, respectively. Figure 4.12a shows a photo of the as-built samples on a high-purity Ni substrate. The samples were built using different combinations of process parameters so that they would exhibit different values of *VED*, thus inducing different amounts of Mn evaporation. Subsequently, the heat-

treated samples exhibited different chemical compositions with corresponding crystal structures; see Figure 4.12b. Notably, the samples with the largest amount of Mn evaporation also exhibited the largest standard deviations in composition after the heat treatment. The results presented here are consistent with those obtained earlier in **publication III**, showing that the evaporation of Mn during L-PBF increases with increasing *VED*. The XRD patterns obtained for the heat-treated samples are displayed in Figure 4.12c. Peaks belonging to the 10M, 14M, and NM martensites are indexed relative to the cubic coordinate system. The unindexed peaks originate from the modulated superstructure. Importantly, each sample exhibited a single martensite phase structure, which implies that the heat treatment near the melting temperature effectively increased the chemical homogeneity and reduced the L-PBF-induced internal stresses. The samples exhibited different phase transformation temperatures, corresponding to the chemical composition and crystal structure of each sample, with a clear increase in the martensite transformation temperature and a decrease in the Curie temperature observable from the sample with the largest amount of Mn (V-1) to that with the least (V-6).
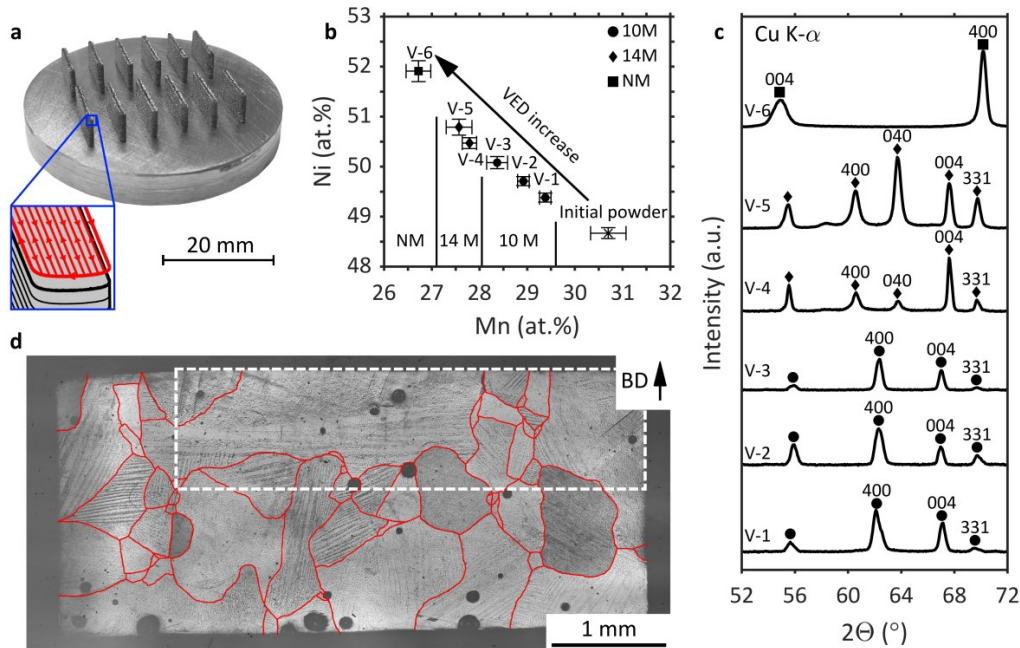

Figure 4.12: General characterization of the Ni-Mn-Ga samples manufactured via L-PBF in **publication V**. (a) Photo of the samples as-built on a high-purity Ni substrate. The inset shows the applied scanning strategy. (b) Chemical composition (error bars correspond to standard measurement deviations) and the corresponding martensitic crystal structure at ambient temperature for the heat-treated samples. (c) A set of XRD patterns obtained for heat-treated samples at ambient temperature. (d) Optical polarized light image of the heat-treated and polished sample V-2, revealing large grains (outlined with red lines) with twins. BD notes the build direction. The white rectangle marks the part of the sample containing the largest grain, which was further investigated in the magnetic actuation experiments. (*Modified from* **publication V**.)

Figure 4.12d shows an optical polarized light image of the sample V-2, revealing a coarse grain structure with martensitic twins ranging from a few micrometres to hundreds of micrometres in width. The spherical pores visible in the figure may have formed due to gas entrapment during the L-PBF manufacture; see the discussion of the results obtained in **publication III**. No crack formation was observed in the produced samples, possibly due to the reduction of the L-PBF-induced internal stresses enabled by the smaller thickness of the samples compared to the thicker samples in **publications II-IV**.

4.3.1 Giant magnetic-field-induced strain

For the magnetic field actuation experiments, a section about $4 \times 1.1 \times 0.35$ mm^3 in size (outline marked in Figure 4.12d) containing a large grain was cut from sample V-2. The aim of this approach was to create a sample with so-called 'bamboo grains', wherein each unconstrained grain behaved like a single crystal, allowing free motion of the TBs and a large MFIS (Chmielus et al., 2009). The cut sample was polished mechanically and electrolytically to remove possible cutting-process-induced surface defects that may have inhibited TB motion and thus suppressed MFIS (Chmielus et al., 2011). The large grain was freed from possible constraints at one end of the prepared sample, while the other end was glued to a sapphire rod, which functioned as a sample holder.

In the first actuation experiment, the sample was placed in a homogeneous 0.8 T magnetic field at different angles. It was observed that the field caused the sample to elongate or contract, depending on the field direction. Figure 4.13a-b shows two polarized light images of the sample taken after the magnetic field application perpendicular (a) and parallel (b) to the sample length. The white arrows mark the final positions of the TBs that moved during the transformation. The TBs did not completely disappear after the field application, which indicates that the TB motion was restricted from both sides of the sample by surface defects and/or grain boundaries. However, a large part of the sample, measuring 1.65 mm along the sample length, was transformed during the magnetic field application. The ~45° inclination angle of the TBs on this facet indicates that the crystallographic axes are oriented nearly parallel to the top facet in the transformed region. Figure 4.13c presents an optical image taken from the top facet of the sample in its elongated state, with the TB located near the free end of the sample. The red circle marks the area wherein the AFM/MFM scans were conducted to ensure c-axis orientation in the different variants. The MFM scan presented in Figure 4.13d demonstrates that the c-axis changed its orientation at the TB on this facet. The left variant shows the characteristic magnetic domain pattern for the out-of-plane c-axis orientation (REF '22'), thus indicating a c-axis orientation perpendicular to the sample surface. The right variant does not show any remarkable MFM contrast because the c-axis is almost parallel to the surface and the magnetic lines do not cross the sample surface. Additionally, the 3D rendered AFM scan in Figure 4.13e shows that the sample surface kinking angle at the TB location is ~3.9°, which is in good agreement with the value of 3.7° calculated using the measured lattice parameters; see Table 4.5. The observed inclination of TB on the top facet indicates that the c-axis in the right variant deviates by ~20° from the front facet (Figure 4.13a-b).
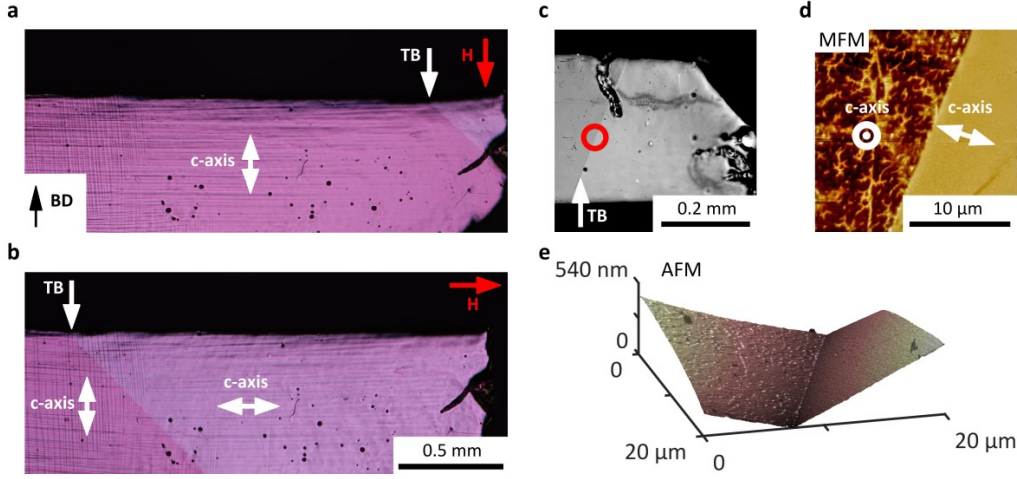
Figure 4.13: (a-b) Optical polarized light images of the magnetically actuated sample (front view) in its (a) elongated and (b) contracted states, obtained after application of a homogeneous 0.8 T magnetic field in different directions. BD notes the build direction. The red arrows indicate the field direction. The white arrows show the final location of the observed TB after the field application. The double-ended arrows show the orientation of the easy magnetization *c*-axis in different twin variants. (c) Optical image obtained from the top side of the sample in the elongated state, showing a TB trace. The red circle marks the location of the AFM/MFM scan. (d) MFM image revealing the change in the *c*-axis orientation in the adjacent twin variants at the TB site. (e) 3D rendered image of the AFM scan showing a kink angle of ~3.9° at the TB site. (*Modified from* **publication V**.)

In the second actuation experiment, LDV was employed to precisely characterize the response of the sample to a pulsed magnetic field. The actuated sample was placed inside a solenoid (see the schematic in Figure 4.14a) connected to a generator that produced a sub-millisecond-ranged current pulse providing a magnetic field amplitude above the anisotropy field level of 0.7 T to fully magnetize the sample. The LDV measured the displacement of the free end of the sample in relation to its fixed end. Prior to each LDV measurement, the sample was elongated by applying a homogeneous 0.8 T magnetic field in the transverse direction. The results of three sequential LDV measurements are presented in Figure 4.14b. All measurements showed identical results: The sample contracted by 96±1 μm within ~135 μs with an average actuation speed of 0.7 m/s and a maximum speed of ~1.2 m/s. This is comparable with the actuation speeds of ~2 m/s observed in 10M Ni-Mn-Ga single crystals (Saren et al., 2016b; Saren & Ullakko, 2017), indicating a low-defect crystal structure that does not hinder TB motion in the L-PBF-built sample. The MFIS, which was calculated using the measured displacement and the length (1.65 mm) of the active section of the sample, reached a value of 5.8%. The measured MFIS agrees well with the maximum transformation strain of 5.7% calculated using Equation 2.1 based on the lattice parameters of the original sample (V-2).
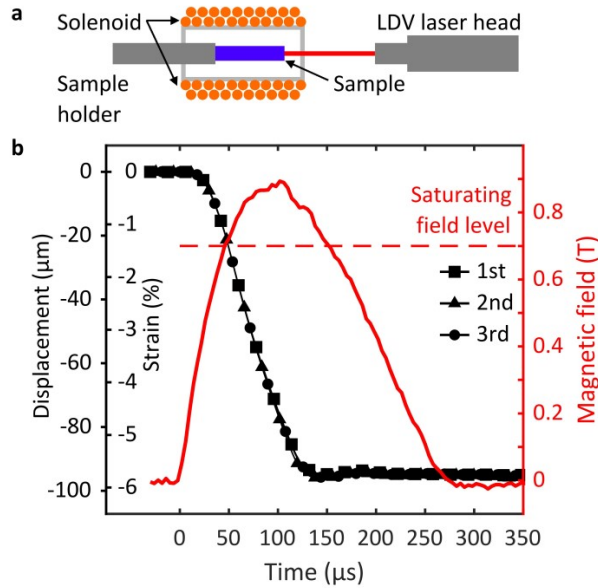
Figure 4.14: (a) Schematic representation of the LDV experimental setup for the pulsed magnetic field actuation of Ni-Mn-Ga. A magnetic field created inside the solenoid is applied along the length of the sample, thereby contracting it. During the magnetic field pulse, the LDV measures the displacement of the free end of the sample in relation to its fixed part. (b) Dependencies of the applied magnetic field (red line, right axis), and the measured displacement and strain versus time (black lines, left axis) for three sequential measurements. Before each measurement, the sample with the holder was placed in a transversal homogeneous 0.8 T magnetic field to elongate the sample. Saturating field level refers to a typical value of the anisotropy field needed to fully magnetically saturate 10M Ni-Mn-Ga. The magnetic field was calculated from the measured solenoid current. The strain was calculated by dividing the displacement by the length (1.65 mm) of the transformed part of the sample. (*Modified from* **publication V**.)

5 Conclusions

This dissertation presented a new approach for the manufacture of functional Ni-Mn-Ga-based magnetic shape memory (MSM) alloys. A systematic experimental approach was used to develop and optimize a laser powder bed fusion (L-PBF) additive manufacturing (AM) process to produce bulk polycrystalline Ni-Mn-Ga. In a later stage, a stepwise chemical homogenization and atomic ordering heat-treatment process was developed to increase chemical homogeneity, induce grain growth, and improve the magneto-structural properties of the L-PBF-built material. The following conclusions can be drawn from the results presented in this dissertation and the attached original publications:

- Overall, the results offer an increased understanding of the laser–material interactions in the L-PBF of Ni-Mn-Ga. It was experimentally revealed in **publications II and III** that the L-PBF of Ni-Mn-Ga is characterized by the selective evaporation of Mn and the corresponding concentration of Ni during the process. Increasing the applied volume energy density (*VED*) increased the observed Mn loss, whereas a loss of Ga was observed when excessive *VED* was applied. Future applications using L-PBF will require a minor over-alloying of Mn in the initial Ni-Mn-Ga powder to counteract the selective evaporation.

- The experimental investigations into the properties of as-built Ni-Mn-Ga in **publications III and IV** demonstrated the feasibility and high repeatability of L-PBF for the manufacture of highly dense (~98.5%) Ni-Mn-Ga. The samples built using the same combination of process parameters and the same Ni-Mn-Ga powder showed only minor between-sample variation in relative density and chemical composition. The crystal structure of the as-built material at ambient temperature in each publication was a mixture of two martensites, whereas the microstructure consisted of layered columnar grains with martensitic twins – a structure typical for L-PBF-built materials. Additionally, the samples showed a weak MFM contrast, which can be attributed to the magnetic anisotropy of the twinned martensite. The as-built Ni-Mn-Ga exhibited relatively low saturation magnetization and broad first-order structural transformations from martensite to austenite, and vice versa.

- It was shown experimentally in **publication IV** that post-process heat treatment can considerably improve the magneto-structural properties of Ni-Mn-Ga built via L-PBF. Notably, annealing at 800 °C for 4 h without homogenization at a higher temperature was enough for the recovery of the typical, composition-dependent, narrow phase transformations and magneto-structural properties. This suggests that the atomic disorder and quenched-in stress from the L-PBF process are the primary factors influencing the atypical magneto-structural properties of the as-built Ni-Mn-Ga. Additionally, it was observed that homogenization treatment near melting temperature at 1080 °C effectively stabilized a single martensite structure (14M) at ambient temperature, resulting in considerable grain growth with moderately short homogenization times of 12–24 h. Consequently, the microstructure of these samples consisted of large equiaxed grains exhibiting

martensitic twins with stronger MFM contrast compared to the as-built samples. Overall, the obtained results highlight the importance of post-process heat treatment for improving the MSM-related properties of the L-PBF-built Ni-Mn-Ga.

- It was shown experimentally in **publication V** that the composition of Ni-Mn-Ga can be precisely changed in-situ by controlling the selective evaporation of Mn during manufacture by adjusting the applied L-PBF processing parameters. This approach requires the use of Ni-Mn-Ga powders with excess Mn. After homogenization treatment near the melting temperature at 1090 °C for 24 h, the built samples exhibited different crystal structures and phase transformation temperatures corresponding to the chemical composition of each sample

- In **publication V**, an mm-sized single crystalline grain, extracted from an L-PBF-built polycrystalline 10M Ni-Mn-Ga sample, exhibited a giant repeatable MFIS of 5.8%. The obtained MFIS is similar to that of conventionally grown single crystals exhibiting the 10M crystal structure (Murray et al., 2000), which is more than two orders of magnitude larger than the MFIS of 0.01% previously reported by Caputo et al. (2018) and Ullakko et al. (2018) for additive manufactured Ni-Mn-Ga. The result demonstrates that L-PBF-built Ni-Mn-Ga can exhibit a low-defect crystal structure that does not hinder TB motion, consequently enabling large MFIS.

5.1   Scientific contribution

Prior to the experimental research conducted in this dissertation, the existing knowledge on the laser-based additive manufacturing of Ni-Mn-Ga was sparse to non-existent. The reported results are an important step towards the additive manufacture of entire MSM devices with integrated actuating sections. Practically, the reported results will permit the explorative development of polycrystalline-MSM-based devices with a geometric freedom that has thus far not been possible with conventional manufacturing methods. Example applications include fast optical and electrical switches, digital pneumatic valves, microfluidic pumps, micromanipulators, and soft robotic grippers. Additionally, the chemical composition tuning facilitated by the selective evaporation of Mn subsequently enables the in-situ control of the crystal structure, thereby opening up the possibility of additively manufactured functional MSM devices with tailored or localized (within the device itself) functional properties, while retaining the high relative densities of the built material.

5.2   Future research topics

The first problem that requires solving is the crystallographic texture of Ni-Mn-Ga polycrystals manufactured via L-PBF. This is considered important because the occurrence of MFIS in polycrystalline material is enhanced by increasing texture and is in fact critical for obtaining giant MFIS. Future efforts should focus on a systematic analysis of the crystallographic texture and its dependencies on the applied process

parameters via electron backscatter diffraction. Additionally, this research could benefit from the use of in-situ measurements, such as synchrotron-based operando X-ray diffraction, during the melting in L-PBF.

The second problem that is the utilization of this technique in complex geometries. The typical bulk samples produced in **publications II-V** exhibited grain boundary constraints that hindered the development of macroscopic MFIS. Therefore, future efforts should focus on the systematic development of the L-PBF process towards manufacturing 'bamboo-grained' lattice structures, in which neighbouring grains are less constrained and pose fewer obstacles to TB motion.

The third problem is the grain size. Obtaining large grains in L-PBF-built Ni-Mn-Ga is considered beneficial for the manufacture of bamboo-grained Ni-Mn-Ga structures using the aforementioned approach. Future investigations should foremost focus on alloying Ni-Mn-Ga with small quantities of additive elements to enhance grain growth. The creation of single crystals using L-PBF or similar methods remains a challenge, but as this problem has been partially solved for Ni-base single crystal superalloys, any principal obstacles are not envisioned in this regard.

References

Aaltio, I., Söderberg, O., Friman, M., Glavatskyy, I., Ge, Y., Glavatska, N. and Hannula, S.-P. (2009). Determining the liquidus and ordering temperatures of the ternary Ni-Mn-Ga and quaternary Ni-Mn-Ga-Fe/Cu alloys. 8th European Symposium on Martensitic Transformations, p. 04001.

Aaltio, I., Soroka, A., Ge, Y., Söderberg, O. and Hannula, S. (2010). High-cycle fatigue of 10M Ni–Mn–Ga magnetic shape memory alloy in reversed mechanical loading. Smart Materials and Structures, 19(7), p.075014.

Aaltio, I., Söderberg, O., Ge, Y., Hannula, S.-P. (2010b). Twin boundary nucleation and motion in Ni–Mn–Ga magnetic shape memory material with a low twinning stress. Scripta Materialia, 62, pp.9-12.

Barker, S., Rhoads, E., Lindquist, P., Vreugdenhil, M. and Müllner, P. (2016). Magnetic Shape Memory Micropump for Submicroliter Intracranial Drug Delivery in Rats. Journal of Medical Devices, 10(4).

Bartlett, J. and Li, X. (2019). An overview of residual stresses in metal powder bed fusion. Additive Manufacturing, 27, pp.131-149.

Caputo, M., Berkowitz, A., Armstrong, A., Müllner, P. and Solomon, C. (2018). 4D printing of net shape parts made from Ni-Mn-Ga magnetic shape-memory alloys. Additive Manufacturing, 21, pp.579-588.

Chernenko, V. (1999). Compositional instability of β-phase in Ni-Mn-Ga alloys. Scripta Materialia, 40(5), pp.523-527.

Chernenko, V., Chmielus, M. and Müllner, P. (2009). Large magnetic-field-induced strains in Ni–Mn–Ga nonmodulated martensite. Applied Physics Letters, 95(10), p.104103.

Chmielus, M., Zhang, X., Witherspoon, C., Dunand, D. and Müllner, P. (2009). Giant magnetic-field-induced strains in polycrystalline Ni–Mn–Ga foams. Nature Materials, 8(11), pp.863-866.

Chmielus, M., Witherspoon, C., Ullakko, K., Müllner, P., and Schneider, R. (2011). Effects of surface damage on twinning stress and the stability of twin microstructures of magnetic shape memory alloys. Acta Materialia, 59(8), pp. 2948–2956.

DebRoy, T., Wei, H., Zuback, J., Mukherjee, T., Elmer, J., Milewski, J., Beese, A., Wilson-Heid, A., De, A. and Zhang, W. (2018). Additive manufacturing of metallic components – Process, structure and properties. Progress in Materials Science, 92, pp.112-224.

Douellou, C., Balandraud, X. and Duc, E. (2019). Assessment of geometrical defects caused by thermal distortions in laser-beam-melting additive manufacturing: a simulation approach. Rapid Prototyping Journal, 25(5), pp.939-950.

Engdahl, G. (2000). Handbook of giant magnetostrictive materials. San Diego, CA: Academic Press. 386 p.

Gaitzsch, U., Pötschke, M., Roth, S., Rellinghaus, B. and Schultz, L. (2009). A 1% magnetostrain in polycrystalline 5M Ni–Mn–Ga. Acta Materialia, 57(2), pp.365-370.

Gaitzsch, U., Romberg, J., Pötschke, M., Roth, S. and Müllner, P. (2011). Stable magnetic-field-induced strain above 1% in polycrystalline Ni–Mn–Ga. Scripta Materialia, 65(8), pp.679-682.

Haynes, W., Lide, D. and Bruno, T. (2017). CRC handbook of chemistry and physics. 97th ed. Boca Raton, FL: Taylor & Francis Group, p.5652.

Heczko, O. and Straka, L. (2004). Compositional dependence of structure, magnetization and magnetic anisotropy in Ni–Mn–Ga magnetic shape memory alloys. Journal of Magnetism and Magnetic Materials, 272-276, pp.2045-2046.

Heczko, O., Scheerbaum, N., and Gutfleisch, O. (2009). Magnetic Shape Memory Phenomena. In: Nanoscale Magnetic Materials and Applications, pp. 399–439. Springer, Boston, MA. ISBN 9780387855981.

Heczko, O., Kopecký, V., Sozinov, A. and Straka, L. (2013). Magnetic shape memory effect at 1.7 K. Applied Physics Letters, 103(7), p.072405.

Hobza, A., Patrick, C., Ullakko, K., Rafla, N., Lindquist, P. and Müllner, P. (2018). Sensing strain with Ni-Mn-Ga. Sensors and Actuators A: Physical, 269, pp.137-144.

Hubert, A., Calchand, N., Le Gorrec, Y., and Gauthier, J.Y. (2012). Magnetic shape memory alloys as smart materials for micro-positioning devices. Advanced electromagnetics, 1(2), pp. 75–84.

Hürrich, C., Roth, S., Wendrock, H., Pötschke, M., Cong, D., Rellinghaus, B. and Schultz, L. (2011). Influence of grain size and training temperature on strain of polycrystalline Ni50Mn29Ga21samples. Journal of Physics: Conference Series, 303, p.012080.

Jaswon, M. and Dove, D. (1960). The crystallography of deformation twinning. Acta Crystallographica, 13(3), pp. 232–240.

Jin, X., Marioni, M., Bono, D., Allen, S., O'Handley, R. and Hsu, T. (2002). Empirical mapping of Ni–Mn–Ga properties with composition and valence electron concentration. Journal of Applied Physics, 91(10), p.8222.

Kamath, C., El-dasher, B., Gallegos, G., King, W. and Sisto, A. (2014). Density of additively-manufactured, 316L SS parts using laser powder-bed fusion at powers up to 400 W. The International Journal of Advanced Manufacturing Technology, 74(1-4), pp.65-78.

King, W., Barth, H., Castillo, V., Gallegos, G., Gibbs, J., Hahn, D., Kamath, C. and Rubenchik, A. (2014). Observation of keyhole-mode laser melting in laser powder-bed fusion additive manufacturing. Journal of Materials Processing Technology, 214(12), pp.2915-2925.

Kohl, M., Gueltig, M., Pinneker, V., Yin, R., Wendler, F., and Krevet, B. (2014). Magnetic shape memory microactuators. Micromachines, 5(4), pp. 1135–1160.

Laitinen, V., Sozinov, A., Saren, A. and Ullakko, K. (2019). Laser based 4D printing of Ni-Mn-Ga MSM alloy. The 6th International Conference on Ferromagnetic Shape Memory Alloys: book of abstracts, ISBN 978-80-905962-9-0, pp. 156-157.

Laitinen, V., Piili, H., Nyamekye, P., Ullakko, K. and Salminen, A. (2019b). Effect of process parameters on the formation of single track in pulsed laser powder bed fusion. Procedia Manufacturing, 36, pp.176-183.

Lanska, N., Söderberg, O., Sozinov, A., Ge, Y., Ullakko, K. and Lindroos, V. (2004). Composition and temperature dependence of the crystal structure of Ni–Mn–Ga alloys. Journal of Applied Physics, 95(12), pp.8074-8078.

Lee, H., Lim, C., Low, M., Tham, N., Murukeshan, V. and Kim, Y. (2017). Lasers in additive manufacturing: A review. International Journal of Precision Engineering and Manufacturing-Green Technology, 4(3), pp.307-322.

Lehto, P., Remes, H., Saukkonen, T., Hänninen, H. and Romanoff, J. (2014). Influence of grain size distribution on the Hall–Petch relationship of welded structural steel. Materials Science and Engineering: A, 592, pp.28-39.

Li, Z., Jiang, Y., Li, Z., Yang, Y., Yang, B., Zhang, Y., Esling, C., Zhao, X. and Zuo, L. (2016). Texture inheritance from austenite to 7 M martensite in Ni–Mn–Ga melt-spun ribbons. Results in Physics, 6, pp.428-433.

Li, C., Liu, Z., Fang, X. and Guo, Y. (2018). Residual Stress in Metal Additive Manufacturing. Procedia CIRP, 71, pp.348-353.

Likhachev, A., Sozinov, A. and Ullakko, K. (2006). Modeling the strain response, magneto-mechanical cycling under the external stress, work output and energy losses in Ni–Mn–Ga. Mechanics of Materials, 38(5-6), pp.551-563.

Lindquist, P., Hobza, T., Patrick, C. and Müllner, P. (2018). Efficiency of Energy Harvesting in Ni–Mn–Ga Shape Memory Alloys. Shape Memory and Superelasticity, 4(1), pp.93-101.

Louvis, E., Fox, P. and Sutcliffe, C. (2011). Selective laser melting of aluminium components. Journal of Materials Processing Technology, 211(2), pp.275-284.

Martynov, V., Kokorin, V. (1992). The crystal structure of thermally- and stress-induced Martensites in Ni2MnGa single crystals. Journal de Physique III, 2(5), pp.739-749.

Maziarz, W., Czaja, P., Chulist, R., Wójcik, A., Żrodowski, Ł., Morończyk, B., Wróblewski, R. and Kowalczyk, M. (2021). Microstructure and Magnetic Properties of Selected Laser Melted Ni-Mn-Ga and Ni-Mn-Ga-Fe Powders Derived from as Melt-Spun Ribbons Precursors. Metals, 11(6), p.903.

Mower, T. and Long, M. (2016). Mechanical behavior of additive manufactured, powder-bed laser-fused materials. Materials Science and Engineering: A, 651, pp.198-213.

Mukherjee, T., Zuback, J., De, A. and DebRoy, T. (2016). Printability of alloys for additive manufacturing. Scientific Reports, 6(1). p.19717.

Murray, S., Marioni, M., Allen, S., O'Handley, R. and Lograsso, T. (2000). 6% magnetic-field-induced strain by twin-boundary motion in ferromagnetic Ni–Mn–Ga. Applied Physics Letters, 77(6), pp.886-888.

Musiienko, D., Straka, L., Klimša, L., Saren, A., Sozinov, A., Heczko, O. and Ullakko, K. (2018). Giant magnetic-field-induced strain in Ni-Mn-Ga micropillars. Scripta Materialia, 150, pp.173-176.

Musiienko, D., Saren, A., Straka, L., Vronka, M., Kopeček, J., Heczko, O., Sozinov, A. and Ullakko, K. (2019). Ultrafast actuation of Ni-Mn-Ga micropillars by pulsed magnetic field. Scripta Materialia, 162, pp.482-485.

Nilsén, F., Aaltio, I., and Hannula, S.P. (2018). Comparison of magnetic field controlled damping properties of single crystal Ni-Mn-Ga and Ni-Mn-Ga polymer hybrid composite structures. Composites Science and Technology, 160, pp. 138–144.

Nilsén, F., Ituarte, I., Salmi, M., Partanen, J. and Hannula, S. (2019). Effect of process parameters on non-modulated Ni-Mn-Ga alloy manufactured using powder bed fusion. Additive Manufacturing, 28, pp.464-474.

Overholser, R., Wuttig, M. and Neumann, D. (1999). Chemical ordering in Ni-Mn-Ga Heusler alloys. Scripta Materialia, 40(10), pp.1095-1102.

Pons, J., Chernenko, V., Santamarta, R. and Cesari, E. (2000). Crystal structure of martensitic phases in Ni–Mn–Ga shape memory alloys. Acta Materialia, 48(12), pp.3027-3038.

Richard, M., Feuchtwanger, J., Schlagel, D., Lograsso, T., Allen, S. and O'Handley, R. (2006). Crystal structure and transformation behavior of Ni–Mn–Ga martensites. Scripta Materialia, 54(10), pp.1797-1801.

Sanchez, S., Smith, P., Xu, Z., Gaspard, G., Hyde, C., Wits, W., Ashcroft, I., Chen, H. and Clare, A. (2021). Powder Bed Fusion of nickel-based superalloys: A review. International Journal of Machine Tools and Manufacture, 165, p.103729.

Saren, A., Musiienko, D., Smith, A., Tellinen, J., and Ullakko, K. (2015). Modeling and design of a vibration energy harvester using the magnetic shape memory effect. Smart Materials and Structures, 24(9), p. 095002.

Saren, A., Musiienko, D., Smith, A. and Ullakko, K. (2016). Pulsed magnetic field-induced single twin boundary motion in Ni–Mn–Ga 5M martensite: A laser vibrometry characterization. Scripta Materialia, 113, pp.154-157.

Saren, A., Nicholls, T., Tellinen, J. and Ullakko, K. (2016b). Direct observation of fast-moving twin boundaries in magnetic shape memory alloy Ni–Mn–Ga 5 M martensite. Scripta Materialia, 123, pp.9-12.

Saren, A. and Ullakko, K. (2017). Dynamic twinning stress and viscous-like damping of twin boundary motion in magnetic shape memory alloy Ni-Mn-Ga. Scripta Materialia, 139, pp.126-129.

Saren, A., Smith, A. and Ullakko, K. (2018). Integratable magnetic shape memory micropump for high-pressure, precision microfluidic applications. Microfluidics and Nanofluidics, 22(4).

Schlagel, D., Wu, Y., Zhang, W. and Lograsso, T. (2000). Chemical segregation during bulk single crystal preparation of Ni–Mn–Ga ferromagnetic shape memory alloys. Journal of Alloys and Compounds, 312(1-2), pp.77-85.

Schönrath, H., Spasova, M., Kilian, S., Meckenstock, R., Witt, G., Sehrt, J. and Farle, M. (2019). Additive manufacturing of soft magnetic permalloy from Fe and Ni powders: Control of magnetic anisotropy. Journal of Magnetism and Magnetic Materials, 478, pp.274-278.

Smith, A., Tellinen, J. and Ullakko, K. (2014). Rapid actuation and response of Ni–Mn–Ga to magnetic-field-induced stress. Acta Materialia, 80, pp.373-379.

Smith, A., Saren, A., Järvinen, J. and Ullakko, K. (2015). Characterization of a high-resolution solid-state micropump that can be integrated into microfluidic systems. Microfluidics and Nanofluidics, 18(5-6), pp.1255-1263.

Sozinov, A., Likhachev, A., Lanska, N. and Ullakko, K. (2002). Giant magnetic-field-induced strain in NiMnGa seven-layered martensitic phase. Applied Physics Letters, 80(10), pp.1746-1748.

Sozinov, A., Lanska, N., Soroka, A., and Straka, L. (2011). Highly mobile type II twin boundary in Ni-Mn-Ga five-layered martensite. Applied Physics Letters, 99(12), p. 124103.

Sozinov, A., Lanska, N., Soroka, A. and Zou, W. (2013). 12% magnetic field-induced strain in Ni-Mn-Ga-based non-modulated martensite. Applied Physics Letters, 102(2), p.021902.

Straka, L., Heczko, O., Seiner, H., Lanska, N., Drahokoupil, J., Soroka, A., Fähler, S., Hänninen, H., Sozinov A. (2011). Highly mobile twinned interface in 10 M modulated Ni−Mn−Ga martensite. Acta Materialia, 59, pp.7450-7463.

Straka, L., Soroka, A., Seiner, H., Hänninen, H., Sozinov, A. (2012). Temperature dependence of twinning stress of type I and type II twins in 10 M modulated Ni−Mn−Ga martensite. Scripta Materialia, 67, pp.25-28.

Straka, L., Sozinov, A., Drahokoupil, J., Kopecký, V., Hänninen, H., Heczko, O. (2013). Effect of intermartensite transformation on twinning stress in Ni-Mn-Ga 10M martensite. Journal of Applied Physics, 114, 063504.

Söderberg, O., Ge, Y., Sozinov, A., Hannula, S., and Lindroos, V. (2005). Recent breakthrough development of the magnetic shape memory effect in Ni–Mn–Ga alloys. Smart Materials and Structures, 14(5), p. S223.

Takeuchi, I., Famodu, O., Read, J., Aronova, M., Chang, K., Craciunescu, C., Lofland, S., Wuttig, M., Wellstood, F., Knauss, L. and Orozco, A. (2003). Identification of novel compositions of ferromagnetic shape-memory alloys using composition spreads. Nature Materials, 2(3), pp.180-184.

Tang, M., Pistorius, P. and Beuth, J. (2017). Prediction of lack-of-fusion porosity for powder bed fusion. Additive Manufacturing, 14, pp.39-48.

Tellinen, J., Suorsa, I., Jääskeläinen, A., Aaltio, I., Ullakko, K. (2002). Basic properties of magnetic shape memory actuators. In: Borgmann, H. (Ed.), Proceedings of 8th International Conference on New Actuators, Actuator 2002. Bremen: Messe Bremen GmbH, pp. 566–569.

Ullakko, K., Huang, J., Kantner, C., O'Handley, R. and Kokorin, V. (1996). Large magnetic-field-induced strains in Ni2MnGa single crystals. Applied Physics Letters, 69(13), pp.1966-1968.

Ullakko, K., Huang, J., Kokorin, V. and O'Handley, R. (1997). Magnetically controlled shape memory effect in Ni2MnGa intermetallics. Scripta Materialia, 36(10), pp.1133-1138.

Ullakko, K., Ezer, Y., Sozinov, A., Kimmel, G., Yakovenko, P. and Lindroos, V. (2001). Magnetic-field-induced strains in polycrystalline Ni-Mn-Ga at room temperature. Scripta Materialia, 44(3), pp.475-480.

Ullakko, K., Wendell, L., Smith, A., Müllner, P., and Hampikian, G. (2012). A magnetic shape memory micropump: contact-free, and compatible with PCR and human DNA profiling. Smart Materials and Structures, 21(11), p. 115020.

Ullakko, K., Laitinen, V., Saren, A., Sozinov, A., Musiienko, D., Chmielus, M. and Salminen, A. (2018). Ni-Mn-Ga actuating elements manufactured using 3D printing. 11th European Symposium on Martensitic Transformations, Metz, 27-31 August 2018.

Van der Schueren, B. and Kruth, J. (1995). Powder deposition in selective metal powder sintering. Rapid Prototyping Journal, 1(3), pp.23-31.

Vasil'ev, A., Bozhko, A., Khovailo, V., Dikshtein, I., Shavrov, V., Seletskii, S. and Buchelnikov, V. (1999). Structural and magnetic phase transitions in shape memory alloys Ni2 + XMn1 −XGa. Journal of Magnetism and Magnetic Materials, 196-197, pp.837-839.

Vecchiato, F., de Winton, H., Hooper, P. and Wenman, M. (2020). Melt pool microstructure and morphology from single exposures in laser powder bed fusion of 316L stainless steel. Additive Manufacturing, 36, p.101401.

Wang, X., Laoui, T., Bonse, J., Kruth, J., Lauwers, B. and Froyen, L. (2002). Direct Selective Laser Sintering of Hard Metal Powders: Experimental Study and Simulation. The International Journal of Advanced Manufacturing Technology, 19(5), pp.351-357.

Wei, L., Zhang, X., Qian, M., Martin, P., Geng, L., Scott, T. and Peng, H. (2018). Compressive deformation of polycrystalline Ni-Mn-Ga alloys near chemical ordering transition temperature. Materials & Design, 142, pp.329-339.

Yang, S., Wang, C. and Liu, X. (2012). Phase equilibria and composition dependence of martensitic transformation in Ni–Mn–Ga ternary system. Intermetallics, 25, pp.101-108.

Young, Z., Guo, Q., Parab, N., Zhao, C., Qu, M., Escano, L., Fezzaa, K., Everhart, W., Sun, T. and Chen, L. (2020). Types of spatter and their features and formation mechanisms in laser powder bed fusion additive manufacturing process. Additive Manufacturing, 36, p.101438.

Publication I

Laitinen, V., Merabtene, M., Stevens, E., Chmielus, M., Van Humbeeck, J., and
Ullakko, K.
Additive manufacturing from the point of view of materials research

Additive Manufacturing from the Point of View of Materials Research

Ville Laitinen, Mahdi Merabtene, Erica Stevens,
Markus Chmielus, Jan Van Humbeeck, and Kari Ullakko

1 Introduction

Over the course of history, there have been three major industrial revolutions, each of them powered by the technological advances of the time and characterized by an increased productivity of industrial processes. Industry 1.0 incorporated the use of hydropower, steam power, and the

V. Laitinen (✉) • M. Merabtene • K. Ullakko
Material Physics Laboratory, Lappeenranta-Lahti University of Technology LUT, Lappeenranta, Finland
e-mail: ville.laitinen@lut.fi; mahdi.merabtene@student.lut.fi; kari.ullakko@lut.fi

E. Stevens • M. Chmielus
Department of Mechanical Engineering and Materials Science, University of Pittsburgh, Pittsburgh, PA, USA
e-mail: ericastevens@pitt.edu; chmielus@pitt.edu

J. Van Humbeeck
Department of Materials Engineering, KU Leuven, Leuven, Belgium
e-mail: jan.vanhumbeeck@kuleuven.be

43

development of machine tools that enabled the mechanization of manufacturing processes; Industry 2.0 introduced mass production assembly lines that were powered by electrical energy; and Industry 3.0 introduced production automation, robots, and computer systems [1, 2]. The key aspect of the ongoing industrial revolution, Industry 4.0, relates to the cyber-physical production systems that consist of physical machines controlled and interconnected by collaborating computational elements. In fact, Industry 4.0 is strongly influenced by our ability to process data, which has phenomenally increased over the past 15 years. In parallel with Industry 4.0, there also exists the concept of Materials 4.0 (or big data materials informatics), which incorporates the tools of cyber-physical space and materials informatics to enhance the design of materials and devices with targeted functionalities in a virtual environment through computational synthesis or reverse engineering from existing knowledge on materials [3, 4]. This approach aims at a higher efficiency in synthesizing and testing novel material compositions and allows shorter lead times from conceptualization to production. However, as the concept of Materials 4.0 has been extensively reviewed in a recent article by [3], it is not discussed further in this chapter. Instead, we focus on the emerging topic of the additive manufacturing (AM) of metal-based stimuli-responsive materials and emphasize possible future directions for the additive manufacturing of metallic materials in general.

'Smart manufacturing' (later Manufacturing 4.0) is one of the primary concepts under Industry 4.0, and it can be described as an adaptable manufacturing system where production processes can adjust automatically for multiple types of products or changing conditions [1]. Manufacturing 4.0 incorporates a large group of base technologies, such as robots and other manufacturing automation, artificial intelligence, the internet of things, analytics and big data [2]. Additive manufacturing, also known as 3D printing, is without a doubt one of the key technologies empowering manufacturing under Industry 4.0. Additive manufacturing is a general term for technologies that are based on the layer-by-layer deposition of material according to a digital model of the object to be manufactured. Additive manufacturing offers many advantages, such as mass customization, reduced tooling costs, on-demand manufacturing, shorter lead times, reduced material waste, and the application-oriented optimization of geometries. In principle, additive manufacturing facilitates a greater freedom of design compared to traditional manufacturing technologies, which has opened up new ways to conduct engineering design. One of the central aspects in this development has been design for additive

manufacturing (DFAM), which is a method that aims to consider additive manufacturing processes and material-related constraints in the design of components for additive manufacturing [5].

Besides freedom of design and enhanced shape complexity, another advantage of additive manufacturing relates to the materials themselves. Additive manufacturing is already today suitable for realizing complex geometries using several engineering materials, such as polymers, metals, ceramics, and composites [5–8]. Additive manufacturing has proven to be feasible for the processing of metallic materials, such as tungsten, which have been considered difficult to work with using conventional methods because of their high hardness and low ductility. In fact, for the last few years, pure tungsten has been commercially available for use in additive manufacturing systems made by EOS GmbH. Additionally, some additive manufacturing processes may introduce new options for metallic materials and enable the engineering and manufacturing of materials that are difficult or nearly impossible to synthesize using conventional methods. A good example of such materials are the so-called functionally graded materials, in which tailored properties can be obtained through a spatial gradation of chemical composition (gradient materials) and/or a 3D structure (hierarchical metamaterials). In addition, the size of these compositional or structural features can span multiple orders of magnitude. Furthermore, the introduction of new materials allows an expansion of the design space for additive manufacturing, which is interconnected with another interesting concept under Industry 4.0: the so-called 'smart materials' [9, 10].

Because materials themselves cannot be smart but can rather only exhibit certain intrinsic characteristics, the expressions 'smart materials' or 'intelligent materials' are typically (but not exclusively) used as an analogy to stimuli-responsive materials that can change their physical properties in response to external stimuli, such as a temperature change, mechanical stress, a magnetic field or an electrical current. In the scientific literature, stimuli-responsive materials are often divided into different classes based on their responses to an applied stimulus. Here, we entertain a similar approach and divide the stimuli-responsive materials into the four classes listed below.

- *Stimuli-responsive actuator materials*—materials that produce strain in response to the applied stimuli.
- *Stimuli-responsive energy conversion materials*—materials that exhibit an electric current, electrical resistance, magnetic field or temperature change as a primary response to the applied stimuli.

- *Stimuli-responsive optical materials*—materials that exhibit an optical response, such as light emission or a change in optical properties, as a response to the applied stimuli.
- *Stimuli-responsive state-changing materials*—materials that alter their physical properties, such as viscosity, in response to the applied stimuli.

Examples of stimuli-responsive materials and some of their applications are listed in Table 1, based on research by [11–88]. Applications of stimuli-responsive materials under Industry 4.0 range from small actuators, sensors, and signalization devices all the way to photovoltaic materials used in the production of electricity from sunlight. In general, stimuli-responsive materials may yield a multitude of enhanced capabilities and functionalities for many products as these allow an active response to be achieved in a product that would otherwise lack it. Some examples of applications for stimuli-responsive materials under Manufacturing 4.0 are listed below; refer to Table 1 for specific examples and references.

- Materials that can generate significant mechanical motion with almost no other components besides the material itself have a high potential for replacing traditional mechanical components, such as the gears, shafts, and pulleys that are used to **generate motion** in conventional machines. Some of these materials, such as thermally activated shape memory alloys (SMAs) or magnetic shape memory alloys (MSMAs), can still produce motion below the size threshold where mechanical components or traditional mechanisms can no longer be used, thus offering a feasible application in different types of **microelectromechanical systems**. Additionally, some of these materials, such as the shape memory alloy Ni-Ti or some of the shape memory polymers, are highly appreciated due to their biocompatibility for medical applications. Stimuli-responsive actuators can also be practical in any **soft robotics** that may be required for the handling of delicate or brittle materials or even living organisms.
- Some stimuli-responsive materials, such as magnetorheological liquids or the magnetic shape memory alloy Ni-Mn-Ga, may be practically useful in **shock absorption** and **active vibration damping,** for example in high-precision devices.
- Shape memory polymers can be used in **active disassembly** systems that are triggered at specific temperatures.
- Magnetocaloric materials can be used for high-efficiency **magnetic cooling and refrigeration** systems.

Table 1 Classification of different types of stimuli-responsive materials and examples of their applications

Class	Group	Stimulus	Response	Example materials	Example applications
Stimuli-responsive actuator materials	Chemomechanical polymers	Chemical reaction	Strain	Hydrogels [11]	Delivery of drugs such as insulin, artificial muscles, tissue engineering [11]
	Electroactive polymers	Electric current	Strain	Polyaniline, Nafion, polythiophenes, poly(vinyl alcohol) gel with dimethyl sulfoxide, poly(acrylonitrile) with conductive fibers [12], polypyrrole, poly(3,4-ethylene dioxythiophene) [12, 13]	Robotic applications, space applications, biomimetic applications [12], wearable sensors, prosthetic applications, haptic sensing, pulse rate monitoring, muscle movement detectors [13]
	Electrostrictive	Electric current	Strain	Lead magnesium niobite [14, 15], barium titanate [16]	Piezo-actuator applications [14, 15], actuators, transducers, energy harvesters [17]
	Magnetostrictive	Magnetic field	Strain	Metglas, Terfenol-D [18–20]	Microwave devices, sensors, transducers [18], sonar, ultrasonic cleaning [20]
	Photostrictive	Light	Strain	PLZT [21, 22]	Non-contact actuation [21], wireless remote control [21, 22]
	Shape memory alloys	Shape memory effect Temperature	Strain	Ni-Ti [23, 24], Fe-Mn-Si, Cu-Zn-Al, Cu-Al-Ni [23]	Thermal actuators, couplings [23], dental implants, artificial heart valves [23, 24], active disassembly [25, 26]
	Shape memory polymer	Shape memory effect Temperature, electric current, light	Strain	Polyurethane [27–29]	Active disassembly [30], ocular implants, vascular stents, sutures [27], self-tightening sutures [28], autochoke elements, intravenous cannula [29]
	Magnetic shape memory alloys	Shape memory effect Magnetic shape memory effect Magnetic field	Strain	Fe-Pd [31, 32], Ni-Mn-Ga [33–35], Ni-Mn-Al [36],	Micropumps [33], magnetic sensors, energy harvesters [32, 35, 37], actuators [34, 36, 38]

Table 1 (continued)

Class	Group	Stimulus	Response	Example materials	Example applications
Stimuli-responsive energy conversion materials	Magnetoelectric	Magnetic field	Electric current	Multiferroics [39, 40]	Information storage [40], energy harvesting, resonators [42] optoelectronics, transducers, radioelectronics [43] microwaves [44], sensors, optical components [45, 46], spintronics and medicine [46]
		Electric current	Magnetic field	Cr2O3 [41, 42]	
	Photovoltaic	Light	Electric current	Silicon [47], gallium arsenide [48], Chalcogenide [49]	PV solar applications [47]
	Magnetocaloric	Magnetic field	Temperature change	Ni-Co-Mn-Sn [50]	Magnetic refrigeration [50]
	Pyroelectric	Temperature	Electric current	Barium strontium titanate [51]	Infrared detector [51]
	Piezoelectric	Mechanical stress	Electric current	Gallium arsenide [52], lead-zirconate-titanate [53]	Microactuators [52], biosensors [54]
	Piezoresistive	Mechanical stress	Electrical resistance	Silicon [55, 56]	Pressure sensors [55] accelerometers [56]
	Thermoelectric	Temperature	Electric current	Silicon/SiGe [57], bismuth telluride, PbTe, SrTiO3 [58]	Engines, refrigeration, air conditioning [57], automotive HVAC [58]

Stimuli-responsive optical materials	Electrochromic/Electroreflective	Electric current	Color/optical property change	Poly(indole-6-carboxylic acid) [59], polyacrylate [60], 3,4-ethylenedioxythiophene [61, 62]	Energy-saving, light control [59] supercapacitors, transistors, diodes [60], switchable mirrors [63], optical devices [61], optical recordings, forensics, smart windows [62]
	Chemochromic	Chemical reaction	Color change	Tungsten oxide [64, 65]	Hydrogen gas detectors/sensors [64, 65]
	Photochromic/photorefractive	Light	Color change	Azobenzene, dithienylethene [66] spiropyrane [67, 68] LiNbO3:Mn [69] BaTiO3 [70]	Optical data storage, optical switching [66], drug delivery systems [67], gel-glasses [68], holographic storage [69], image processing, laser resonators [70]
	Thermochromic	Temperature	Color change	Vanadium dioxide [71, 72] titanium nitride [72]	Energy saving [71, 72]
	Mechanochromic	Mechanical stress	Color change	Poly(1,4-butylene succinate) [73], polydiacetylenes, spiropyrans [74]	Healthcare [73], protective helmets, biosensors [74]
	Photoluminescent	Light	Light emission	Strontium aluminate [75, 76], zinc sulfide [76]	Warning signs, dial plates, escape routes [75], footpaths, lanes [76]
	Thermoluminescent	Temperature	Light emission	Lithium borate, beryllium oxide, lithium fluoride, calcium sulphate [77]	Medical dosimetry [77]
	Electroluminescent	Electric current	Light emission	Zinc sulfide doped with terbium or manganese [78], zinc sulfide doped with copper [79]	Emergency signage, lighting, backlights [78, 79], detection of electric/magnetic fields [80]
	Mechanoluminescent	Mechanical stress	Light emission	Zinc sulfide doped with copper, zinc sulfide doped with manganese [80]	Dynamic pressure mapping, stress sensing [80], optoelectronic devices, security papers [81]

Table 1 (continued)

Class	Group	Stimulus	Response	Example materials	Example applications
Stimuli-responsive state changing materials	Shear-thickening	Mechanical stress	State change (fluid/solid)	Silica particles in a polyethylene glycol solution [82, 83], amphiphilic polymer, hydrophilic particles and polyethylene-oxide [82]	Adaptive stiffness, damping, smart structures [82], protective equipment, seismic isolation of buildings/bridges, shock loading applications [83]
	Electrorheological	Electric current	State change (fluid/solid)	Aluminosilicate, biopolymers (silicone oil/hydrocarbon), oxides (surfactant) and TiO2, mineral oil, water [84, 85], zeolite and silicone oil [84]	Damping devices (shock absorbers, bearing dampers), clutches, mechanical polishers [84], haptic sensors, force feedback systems, anti-lock braking systems [85]
	Magnetorheological	Magnetic field	State change (fluid/solid)	Carbonyl iron particles and carrier liquids (silicone oils, polyesters, synthetic hydrocarbons) [86] hydrocarbon-based magneto-rheological [87]	Biomedical applications (prosthetic knees) [87], shock absorbers and dampers, brakes, clutches [86–88]

- Stimuli-responsive materials also have a high potential in different types of signalization devices, such as **displays** or **haptic** (sense of touch) technologies. In fact, haptic devices provide a unique interface between humans and machines, allowing remote distance operators to receive force feedback from the operated machines. For example, operators could receive information about the weight or resistance of lifted objects or be alerted when there is an issue with the operated machine.
- Another group of applications for stimuli-responsive materials under Industry 4.0 are different types of **sensors**, such as the ones used for failure detection and predictive maintenance in manufacturing systems. Additionally, **wearable sensors** are a prominent group of applications for many stimuli-responsive materials.

2 Additive Manufacturing of Stimuli-Responsive Materials

When it comes to stimuli-responsive materials, additive manufacturing is often referred to as 4D printing, which may refer to either the stimuli-responsive properties of the additively manufactured material in general or the ability of some of the materials (stimuli-responsive actuator materials) to change their physical shape in response to an applied stimulus. However, here we employ the term 'additive manufacturing of stimuli-responsive materials' instead of 4D printing as the usage of the former aligns better with the existing standardized terminology for additive manufacturing.

The additive manufacturing of different stimuli-responsive materials has gained significant interest in the past few years as this technology could facilitate a higher freedom of design concerning the stimuli-responsive properties of the manufactured objects. Tremendous advantages can be gained when devices can be optimized to fulfill the requirements of the intended application, instead of designing within the limits of the used manufacturing process. Thus, additive manufacturing may also accelerate the adoption of stimuli-responsive materials or expand their possible applications. Additionally, a combination of structural and stimuli-responsive materials under a single additive manufacturing process could enable the manufacturing of entire devices with integrated stimuli-responsive sections. In this case, certain functional characteristics or properties would be obtained locally in certain sections of the additively manufactured device. For example, in the case of stimuli-responsive actuator materials, the stimuli-responsive material would replace the traditional mechanisms within the manufactured device. These 'active regions' of the device could be

actuated using a passive source of energy, such as a magnetic field in the case of magnetic shape memory alloys or heat in the case of thermally activated shape memory alloys. Additionally, additive manufacturing could allow a localized tailoring of properties (as in Fig. 1) within a single device,
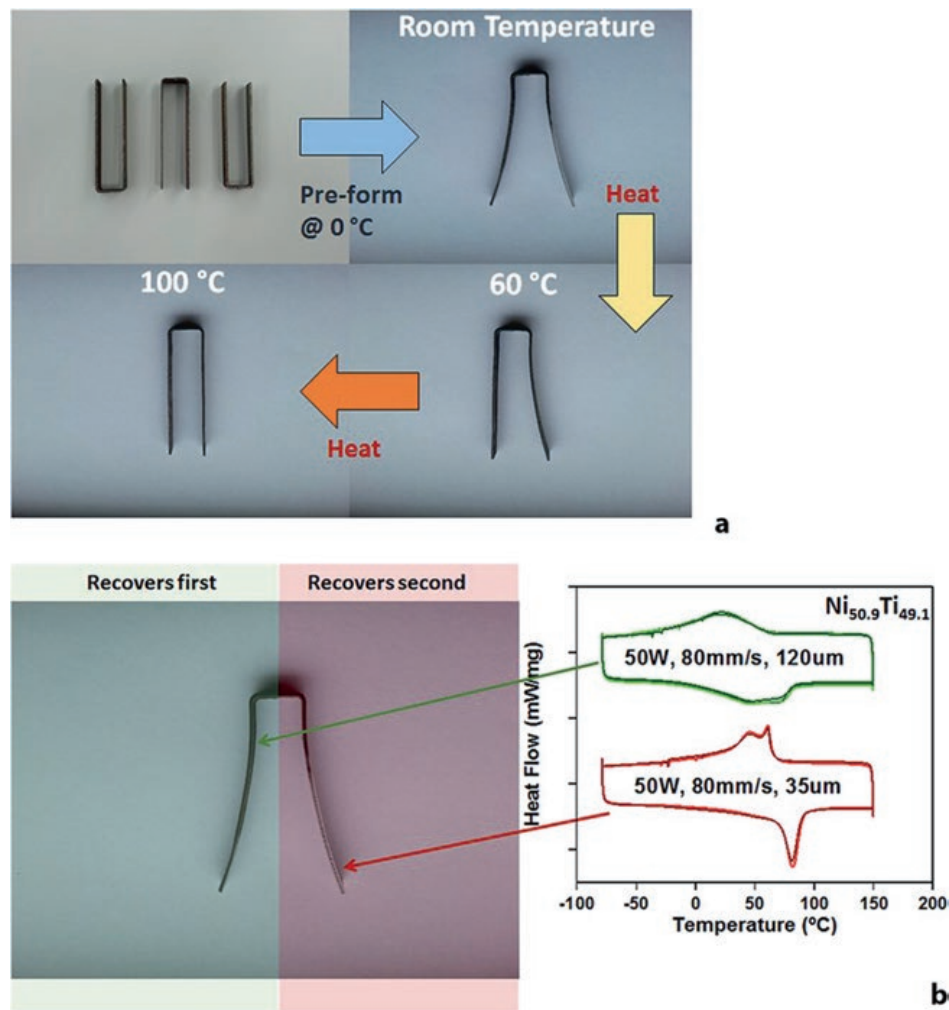

Fig. 1 (a) A location-dependent active response generated by temperature-dependent multi-stage shape recovery in a U-shaped Ni-Ti component deposited using L-PBF; (b) effect of the L-PBF process parameters on the transformation temperatures and active responses at different sections of the build. Reproduced from [151] under Creative Commons Attribution 4.0 International License

for example by inducing local differences in composition or microstructure in the processed stimuli-responsive material. Overall, these developments could facilitate the additive manufacturing of entire devices with embedded actuators or sensors, which could act as functional parts in existing systems, such as in soft robotics or pneumatics.

The majority of the published reviews on the additive manufacturing of stimuli-responsive materials have focused on shape memory polymers [152–161], while a few articles [162–167] have discussed aspects of expanding the DFAM method towards the adoption of these materials in additively manufactured components. Although some reviews have also discussed the additive manufacturing of thermally activated shape memory alloys, reviews concerning other metal-based stimuli-responsive materials, such as magnetic shape memory alloys or magnetocaloric materials, are sparse to non-existent. The popularity of polymer-based materials is expected because they are more feasible for low-cost additive manufacturing in comparison to metal-based materials, which are more difficult to manufacture additively without defects. Hence, this chapter concentrates on the additive manufacturing of thermally activated shape memory alloys, magnetic shape memory alloys, and magnetocaloric alloys. A brief overview of the state of the art in the additive manufacturing of these materials is presented in Table 2, based on the research results from [89–150]. An overview of the main additive manufacturing process categories (compared to the additive manufacturing processes in Table 2) for metal-based stimuli-responsive materials is presented below, following the definitions given in standard SFS-EN ISO/ASTM 52900:2017.

- *Material extrusion*—"An additive manufacturing process in which material is selectively dispensed through a nozzle or orifice"; an example process for metals is 3D ink printing, whereby metal powder is dispensed in a mixture with a bonding agent.
- *Powder bed fusion*—"An additive manufacturing process in which thermal energy selectively fuses regions of a powder bed"; the applied thermal energy can be either a laser (L-PBF) or an electron beam (E-PBF).
- *Binder jetting*—"An additive manufacturing process in which a liquid bonding agent is selectively deposited to join powder materials".
- *Directed energy deposition*—"An additive manufacturing process in which focused thermal energy is used to fuse materials by melting as they are being deposited"; example processes include laser-based directed energy deposition of powder material (L-DED), plasma arc deposition (PAD), and wire and arc additive manufacturing (WAAM).

Table 2 A brief overview of state of the art in the additive manufacturing of metal-based stimuli-responsive materials

Group	Alloy	Process	Feedstock	Observations
SMA	Ni-Ti	L-DED	Pre-alloyed powder	Retention and finer grain sizes proved to have a higher hardness values due to a high temperature austenite phase [89, 90]
				Ni-rich Ni-Ti alloys required aging treatment [91]
			Mechanically produced powder	Solutionized and aged Ni-Ti had a better shape memory response [92]
				Ni-rich Ni-Ti showed superelastic behavior [93]
				Shape memory effect recovery and unstable oriented/de-twinned martensite [94]
			Gas atomized powder	NiTi50 showed excellent mechanical properties as compared to NiTi45 and NiTi55 [95]
				Using low scanning speed reduced the obtained shape memory effect [96]
				Superelastic behavior [96]
				Loss of nickel in the process [97]
		L-PBF		High relative density (>97%) and hardness reported [98, 99]
				Excellent compression fatigue resistance [100] with an irreversible stain behavior [99]
				Wider hatch distance decreased relative density [101]
				Superelastic response (95%) [102–108]
				Shape memory effect [94, 105, 109, 110]
				Recovery above 5.5% [106–108, 111]
				Desired stiffness was achieved by regulating the level of porosity and stiffness reduced from 69 GPa to 20.5 GPa for 58% porosity [112]
				Loss of nickel in the process [113, 114]
				Wider hatch spacing led to a highly irrecoverable strain [114]
				Microstructure influenced the shape memory response and mechanical behavior [109, 115]
				Martensite twins were formed easily after annealing process [116]
				Heat treatment above 400 °C decreased the shape recovery and transformation strain [117]
				Tensile strain recovery was 1.5 times larger than in compression [111]

Alloy	Process	Feedstock	Findings
		Plasma atomized	Reversible martensitic transformation. Processing parameters, Ni evaporation and oxygen content of the processing atmosphere (oxidation) impacted martensite transformation. Solution treatment resulted in sharpened transformation peaks and undid the influence of dissolvable Ni-Ti precipitates [118].
	Micro L-PBF	Mechanically produced powder	Mechanical shape memory functionality was proven with a force range of 10–100 mN [119] Quality of deposited Ni-Ti was improved by increasing the scanning speed [120]
	E-PBF	PREP atomized powder	No visible shape memory and pseudoplastic effect seen [121] The authors did not recommend E-PBF for Ni-Ti alloys. Preheating was required [97] E-PBF process resulted in better tensile properties than L-DED and L-PBF [97, 122]
	PAD	Pre-alloyed powder	Linear superelasticity [123] Quasi-linear superelasticity with narrow hysteresis [123, 124]
	WAAM	Wire	High hardness and tensile strength [125]
Cu-Al-Ni Cu-Al-Ni-Mn	L-PBF	Elemental powders	High aluminum content led to dendrites and high hardness [126]
		Gas atomized powder	High relative density (>92%) achieved [127–129] Reversible martensitic transformation with the formation of $\beta_1{}'$-martensite [127–129] Large strain recovery after unloading (up to 18%) [127] Strong distribution of pores produced by the L-PBF sample [127, 128] Additional re-melting led to smaller grain size and yielded a deformability of 14% [129] Higher strength and improved plasticity was observed for both samples (Cu-Al-Ni-Mn and Cu-Al-Ni-Mn-Zr) [128–130] For the Cu-Al-Ni-Mn-Zr sample, Zr-rich phase was found to precipitate at the grain boundaries during the annealing process [130]
Cu-Al-Ni-Mn-Zr Cu-Al-Ni-Ti Fe-Mn-Al-Ni			Copper alloy with Ti addition had a high hardness of about 280 HV due to the grain refinement. The relative density exceeded 99% [131] Reversible martensitic transformation and pseudo-elastic effect [132]

Table 2 (continued)

Group	Alloy	Process	Feedstock	Observations
MSMA	Ni-Mn-Ga	3D ink printing	Ink with elemental powders	Reversible martensitic transformation [133]
				Martensitic twins [134]
		Binder jetting	Mechanically produced powder	Martensitic twins and reversible martensitic transformation after post-processing [135, 136] Binder jetting produced a complex-shaped porous Ni-Mn-Ga geometry with a reversible martensitic transformation [137–139]
				Sintering of Ni-Mn-Ga powder was shown to produce net-shaped porous structures [136, 138, 139]
				Minor loss of nickel seen in sintered Ni-Mn-Ga in comparison to the initial powders [140]
		L-DED	Gas atomized powder	Narrow hysteresis and increase in saturation magnetization [141]
		L-PBF		Ni-Mn-Ga could be deposited on compositionally dissimilar materials [142, 143]
				Complex geometries [143, 144]
				High relative density of 98.3% [143]
				Martensitic twins and reversible martensitic transformation [143–146]
				Loss of Mn in process [143, 145, 146]
				Susceptibility to cracking [145]
Magnetocaloric	Ni-Co-Mn-Sn	L-DED	Mechanically produced powder	Reduction of Sn was observed at the subgrain boundaries [147]
				'Properly built' samples of Ni-Co-Mn-Sn exhibited better magnetic properties than 'overbuilt' samples [148]
				Heat-treatment promoted martensite growth and increased twinning [149]
	Ni-Mn-Cu-Ga	Binder jetting		Larger grain growth and Mn-O particles were observed at samples sintered at 1080 °C as compared 1050 °C and 1070 °C [150]

3   ADDITIVE MANUFACTURING OF SHAPE MEMORY ALLOYS

Shape memory alloys are alloys that can recover a limited applied strain of less than 10% either thermally or mechanically [168]. This property finds its origin in a thermoelastic martensitic transformation in some particular alloys. This transformation is characterized by its transformation temperatures (M_s, M_f during cooling reaching the martensitic phase, A_s, A_f during heating reaching the beta phase), exhibiting a relatively small hysteresis of about 10–40 K compared to the well-known martensitic transformation in many steels exhibiting a hysteresis of several 100 K. When a strain, limited to 10%, is applied in the martensitic state, this strain can be recovered by heating above the transformation temperature into the beta phase. This is called the thermal recovery or shape memory effect. When a strain of less than 10% is applied in the beta phase, above M_s, the strain is mechanically recovered upon releasing the applied stress, which is called superelasticity. Complete thermal or mechanical recovery can only be obtained in a limited temperature window around the martensitic transformation. The thermally activated shape memory effect occurs in some Cu-based alloys and Fe-based alloys, but it is mostly associated with Ni-Ti alloys. Ni-Ti is superior compared to other shape memory alloys for many reasons, including its high ductility, high strength, and very fine grain size. These properties enable the production of very thin devices (wires with a diameter down to 25 μm). Additionally, it is biocompatible, which is why more than 80% of the products made of Ni-Ti are medically related [169]. Besides their use in medical applications, shape memory alloys can convert heat into a high force or work output, which makes these alloys useful in the actuators of stress-creating components [23, 170].

From the perspective of conventional manufacturing processes, a major problem of Ni-Ti is its poor machinability, primarily due to the strong strain hardening effect. Thus, wire and tube drawing are the most common applied forming techniques used in the production of devices such as guise wires, stents, and actuators based on springs. This sets many limitations on the shape complexity of the manufactured devices. Therefore, additive manufacturing of Ni-Ti has gained the attention of designers of medical and other devices. As shown in Table 2, laser-based processes, especially L-PBF, are the most typical approach for the additive manufacturing of Ni-Ti. The same observation applies to Cu- and Fe-based alloys, although little scientific literature is available on the additive

manufacturing of these materials. In fact, the future for Cu-based SMAs does not look bright as the majority of research on additive manufacturing of SMAs concentrates on Ni-Ti. However, the additive manufacturing of Ni-Ti represents only a small fraction of the medical applications produced by metal-based additive manufacturing, and only a handful of studies on the additive manufacturing of Ni-Ti consider its stimuli-responsive properties, such as the very low stiffness (very low E-modulus), and its functional properties, such as superelasticity and the shape memory effect. However, a fair amount of research on the laser additive manufacturing (LAM) of Ni-Ti shape memory alloys has been conducted [23, 115, 171–174]. Therefore, we summarize here the most important observations of Ni-Ti deposited using L-PBF, as previously discussed by [173] and briefly overviewed in Table 2.

- Although Ni-Ti can be processed at a high density crack-free, the mechanical and functional properties of the processed material are on average inferior compared to the wrought material. However, using repetitive laser scanning in the process may allow improvement of the functional properties of deposited Ni-Ti.
- Controlling the transformation temperatures of the processed material is difficult, mainly due to the evaporation of Ni and precipitation based on impurities. Hence, the composition and transformation temperatures of the processed material are strongly dependent on the processing parameters and, therefore, the transformation temperatures of the final product are not necessarily the transformation temperatures of the initial powder.
- Additionally, the processing environment should be controlled to prevent oxygen and/or nitrogen pick-up that may lead to an increased density of impurities, which may influence the transformation temperatures and the mechanical properties of the processed material.
- The surface roughness of the final product should be considered in relation to potential wear or for the difficulties it causes in sterilization, which is required for biomedical applications.

4 ADDITIVE MANUFACTURING OF MAGNETIC SHAPE MEMORY ALLOYS

Besides the thermally activated shape memory effect, magnetic shape memory (MSM) alloys may also exhibit a straining phenomenon when the magnetic moments of the martensitic twin variants of the alloy align with the applied magnetic field [38, 175, 176]. This straining phenomenon is called the magnetic shape memory effect. The Ni-Mn-Ga system, which is the most studied class of MSM materials, has been shown to exhibit outstanding characteristics, such as magnetic-field-induced strains (MFIS) of 12% [176], which is a hundred times larger than the magnetically induced strains obtained in competing materials. In addition, the efficiency (mechanical work output / magnetic field energy) of the MSM effect can be over 95% and its fatigue life can exceed 2×10^9 cycles [177]. Characteristic of the MSM materials is that the strain remains unchanged after the magnetic field has been switched off (the strain can be recovered by applying a magnetic field in transversal direction or by force). This results in significant energy savings in many applications, especially on-off valves, because magnetic field energy is needed only during the brief time when the shape of the MSM element is changed. Additionally, Ni-Mn-Ga can exhibit high strain accelerations of 1.6×10^6 m/s^2 [178], which is assumed to be the highest acceleration of all actuator materials. These characteristics may be beneficial in several applications, such as in robotics, biomedical applications and optics. For instance, fast actuators/sensors [34, 176], micropumps [33], and vibration energy harvesters [35] have been identified as potential applications for MSM materials. However, commercial applications of MSM materials are still limited, possibly due to the relatively young age of the technology itself compared to competing piezo ceramics or giant magnetostrictive materials.

Typically, bulk polycrystalline Ni-Mn-Ga does not exhibit limited MFIS due to grain boundary constraints that effectively block twin boundary motion in the material. However, directionally solidified (textured) polycrystalline Ni-Mn-Ga has been shown to exhibit up to 1.0% strain [179], whereas polycrystalline Ni-Mn-Ga foam has been shown to exhibit up to 8.7% recoverable strain [180]. A smaller force output and brittleness are disadvantages of foamy polycrystalline compared to more conventional single-crystalline material. From a manufacturing perspective, the use of additive manufacturing offers better freedom of design, especially compared to typical single-crystalline material. Thus, the additive

manufacturing of MSM alloys aims at obtaining parts with controlled porosity while facilitating the possibility to manufacture complex geometries. Additionally, additive manufacturing places fewer limitations on the size of the manufactured object. Other advantages that may be potentially gained through additive manufacturing relate to the possibility to produce compositional gradients that allow for the tailoring of the properties for specific applications.

Compared to the additive manufacturing of Ni-Ti based thermally activated shape memory alloys, additive manufacturing of magnetic shape memory alloys is still in its infancy. All the scientific literature available at the time focuses on the additive manufacturing of Ni-Mn-Ga-based MSMAs. The most common approaches on additive manufacturing of Ni-Mn-Ga have concentrated on 3D ink printing [133, 134] and binder jetting [135–140]. However, also a few investigations into manufacturing of polycrystalline Ni-Mn-Ga using L-DED [141] and L-PBF [142–146] have recently been published. Each of the aforementioned processes have their own advantages and disadvantages concerning the manufacture of a material that exhibits MFIS. Nevertheless, a common aspect for all of the processes is the aim to obtain controlled composition, microstructure and porosity, which is essential for obtaining MFIS in polycrystalline Ni-Mn-Ga. Especially, assuring the chemical integrity of the manufactured material is also important because of the high susceptibility of the crystal structure of Ni-Mn-Ga to compositional variation and impurities.

In general, both 3D ink printing and binder jetting processes have been proven to be feasible for producing Ni-Mn-Ga with complex geometries. However, binder-based processes face a challenge regarding the control of the composition and microstructure because the consistent removal of binder elements post-processing is difficult and some oxidation and Mn evaporation may occur during the sintering process [139]. LAM processes base on melting the material, thus enabling the use of binders to be avoided. However, previous studies on the L-PBF of Ni-Mn-Ga show that some Mn is lost in the process and that this Mn loss is strongly influenced by the used process parameters [143–145]. In fact, loss of Mn during the L-PBF process is expected due to the high vapor pressure and low boiling temperature of Mn in comparison to the other elements in the alloy. Thus, control over the processing parameters and the thermal cycle that the processed material undergoes is critical for obtaining a controlled composition. This may also be an advantage, as the composition could be controlled through an adjustment of the process parameters, which could potentially

allow for the adjustment of the microstructure and stimuli-responsive properties of the processed material. However, excessive over-alloying of Mn into the used powder would be required for this approach to be feasible.

The control of the porosity in the additive manufacturing of Ni-Mn-Ga has typically based on manufacturing different types of lattice structures [133, 137, 142] or foam-like materials [134, 138]. Additionally, the sintering process used in binder-based additive manufacturing processes can also be adjusted to control the density of the processed material [140]. The processed material undergoes a repetitive cycle of heating and cooling in LAM processes as the heat from melting is conducted through the prior layers of deposited material. As a result, the processed material may exhibit regions with different thermal histories, which also affects the local microstructures. This has been observed as broad ferromagnetic hysteresis and wide phase transitions in as-deposited material [141, 143]. Additionally, Ni-Mn-Ga processed by L-PBF may exhibit cracking [145]. Post-process heat-treatment is required to retain the typical ferromagnetic behavior and material properties in the deposited material [141, 143, 144]. However, laser-based processes typically produce a microstructural texture [181], which is considered beneficial for obtaining MFIS.

Although additive manufacturing shows high potential for facilitating greater design freedom for MSM based devices, so far the functional properties of the additively manufactured material are inferior compared to the conventional oriented single crystals or textured polycrystalline material. By so far, Ni-Mn-Ga processed by binder jetting [136] and L-PBF [142] have been shown to develop a magnetically induced strains up to 0.01%, which are significantly lower than the 8.7% achieved in Ni-Mn-Ga based foams [180]. In conclusion, more research on additive manufacturing of MSM alloys is required for understanding relationships between the applied process parameters and the resulting functional properties.

5 ADDITIVE MANUFACTURING OF MAGNETOCALORIC MATERIALS

Some materials experience a change in entropy (Δs_T) when exposed to a magnetic field in an isothermal environment due to a phase change of either the first or second thermodynamic order [182–184]. When placed in an adiabatic environment instead, this magnetic-field-induced phase

change produces a temperature change (ΔT_{ad}) in the material, leading to the common designation of this phenomenon as the magnetocaloric effect [185]. The magnetocaloric effect can be observed in both first- and second-order materials, with the order parameter of magnetization. In a first-order material, the change in magnetization is discontinuous at the transformation, whereas the change in magnetization for a second-order material is gradual and continuous over the transformation. In the case of a second-order material, this magnetization change is caused by an alignment of magnetic moments around the Curie temperature (demagnetization temperature), reducing the magnetic entropy with increasing magnetic field and causing a corresponding increase in the thermal entropy. The entropy trade-off concept remains for first-order materials, but with the addition of a magnetostructural (or magnetoelastic) phase transformation that causes the direction of the entropy change with the addition of an applied field to be less straightforward. Near the transformation temperature, an applied magnetic field will stabilize the more magnetic phase, which could be either the high-temperature or the low-temperature phase. If the high-temperature phase is stabilized, the application of a magnetic field shifts the transition to lower temperatures and leads to a decrease in the temperature of the material—called the negative (or inverse) magnetocaloric effect. If the low-temperature phase is stabilized, the application of a magnetic field shifts the transition to higher temperatures and leads to an increase in the temperature of the material—the positive magnetocaloric effect.

Recently, the magnetocaloric effect has been researched for leverage in heat pumps, particularly for cooling in applications such as solid-state-based magnetic refrigeration requiring no harmful refrigerants and in localized hypothermia therapy to treat cancer [186, 187]. For the most common application of refrigeration, any magnetocaloric effect-exhibiting material that is to be considered a viable option as a heat exchanger within a heat pump must be formed with a high surface-to-volume ratio and must allow satisfactory fluid flow [188, 189]. Thus, the following two requirements are placed upon the heat exchanger [190]:

1. Maximize the volume fraction of the magnetocaloric effect material while maintaining a large surface area.
2. Minimize the pressure drop in the fluid across the heat exchanger.

Common methods for producing heat exchanger devices from magnetocaloric effect materials are [190]: packed powder beds [191–193], parallel plates [194–197], and microchannel systems [198]. Packed powder beds, though cheap and simple, have a high pressure drop across the device due to the presence of turbulent flow. Microchannels, though inducing only a low drop in fluid pressure, have a high manufacturing cost (if they can be currently manufactured at all for the given material). Parallel plate devices are a median between the two extremes, allowing for a fluid flow that is not as turbulent as in packed powder beds and a production that is not quite as expensive as with microchannels.

With an abundance of requirements on both the feedstock material and the final magnetocaloric-effect-based heat exchanger, fabrication complications are an inescapable challenge. For example, first-order phase transition materials tend to be brittle, which limits the ability to machine them into desired geometries [199]. Difficulties with fabrication can leave promising alloys showing only a modest magnetocaloric effect after device fabrication due to changes in microstructure or atomic ordering and defects [200, 201]. In addition, first-order phase transition magnetocaloric effect materials have narrow operating temperature windows [200, 202]. For ideally efficient operation, a heat exchanger using the first-order phase transition magnetocaloric effect must have stages or a gradient of material transformation temperatures [198]. With a transformation temperature gradient, the fluid will heat (or cool) as it passes through the series of materials, at each point existing within the operating temperature for the magnetocaloric effect material that it is currently in contact with. Second-order phase transition materials are less difficult to shape and have a wider operating temperature range, but the most promising material (Gd) is a 'critical material' as it is costly, has a high environmental impact, and its use in a large number of cooling applications would lead to demand far exceeding supply [190, 199, 203].

As a manufacturing method, additive manufacturing may allow for the inclusion of designed, multi-scale porosity; complicated geometries impossible with other methods; the processing of brittle materials that cannot be machined; and gradient or layered materials with gradient or staged material transformation temperatures. This combination of benefits can grant the ability to fulfill both heat exchanger requirements with no trade-offs: a minimal pressure drop across a material that has a high surface-to-volume ratio with a maximized volume of functional material present to produce a large temperature change across a wide temperature range.

Additive manufacturing for magnetocaloric materials is in its relative infancy, although it is increasingly being recognized as a potential production avenue for magnetocaloric effect materials. In 2013, [204] used selective laser melting to create heat exchangers from La(Fe, Co, Si)$_{13}$. Meanwhile, [137, 139, 147, 148, 150] conducted experiments with Ni-Mn-based Heusler alloys fabricated using L-DED and powder bed binder jet 3D printing. L-DED, with a laser as the energy source, required a heat treatment to homogenize the microstructure before promising properties were observed [147, 148]. Binder jet printing, since it requires no heat input that would change the feedstock powder's microstructure, showed a magnetocaloric response in the as-sintered state [150] [133]. used inkjet printing to deposit a mixture containing elemental Ni, Mn, and Ga powders, then sintered them to create final lattice structures with 73–75% porosity in the micro-trusses. Published experimental studies are scarce compared to the literature on the additive manufacturing of structural metals. Nevertheless, as discussed here and in [190, 199], with the proper attention to tailoring the processing to maintain the functional properties and with measures taken to balance cost and effectiveness, additive manufacturing is a promising technology to address current manufacturing and design issues while at the same time improving the overall performance of magnetocaloric structures.

6   FUTURE ASPECTS OF ADDITIVE MANUFACTURING FOR NOVEL METALLIC MATERIALS

Besides enabling advances in freedom of design and the processing of stimuli-responsive alloys, additive manufacturing may allow the development and manufacturing of customized, application-specific materials and could thus enable the expansion of the exciting material box of different metal alloys. For example, recent developments have been made in the additive manufacturing of metal matrix composites and high-entropy alloys [8], which are favored for their outstanding mechanical properties. Additionally, significant progress has been made in engineering and manufacturing functionally graded materials, such as gradient materials or metamaterials [205–209]. A common additive manufacturing process for the fabrication of compositional gradient materials is DED, which offers unique capabilities, such as the deposition of more than one material simultaneously or the changing of the deposited material from layer to

layer. A second advantage of DED is that the build process itself is not limited, compared to PBF, where deposition is only possible in successive horizontal layers. This makes the DED process suitable for depositing material on 3D substrates, such as existing parts. In fact, repairing a worn part or tool represents a typical industrial application for this process. In principle, this type of additive manufacturing process allows a precise small-scale synthesis of materials during the manufacturing process itself, thus enabling the manufacturing of materials that are difficult to synthesize on a larger scale using conventional methods. Besides potentially allowing the creation of new alloys, this also enables the application-specific tailoring of the materials of the manufacturing process itself, which could be practical for on-demand manufacturing [210]. Additionally, LAM enables the composition and microstructures to be adjusted via the process parameters, which allows the integration of information within the processed material [211]. This could be used to enhance the traceability of the used materials or processes or of the 'smart products' themselves.

7   SUMMARY

In this chapter, we discussed how additive manufacturing could contribute to metal-based stimuli-responsive materials and material science in general. Although the future looks bright, substantial research is still required to extend the range of 'printable' materials and to achieve appropriate stimuli-responsive properties in additively manufactured metal-based materials. The complexity of the production and the material parameters create large challenges in producing dense, defect-free materials using the associated additive manufacturing processes. Indeed, specific processing conditions of metal additive manufacturing are challenging, and many material systems still suffer from cracks, unwanted porosity, high internal stresses, bad surface quality, and mechanical properties below the required levels. In many cases, this creates the need for post-processing, such as hot isostatic pressing (HIP), stress relieving, thermal treatments or polishing. However, additive manufacturing facilitates a great amount of design freedom for complex geometries and in some cases may enable the tailoring of compositional properties of the processed materials to an extent that is almost impossible to achieve using conventional manufacturing methods. Hence, additive manufacturing has a high potential for the development of novel types of stimuli-responsive devices.

References

1. Frank A, Dalenogare L, and Ayala N (2019) Industry 4.0 technologies: Implementation patterns in manufacturing companies. Int J Prod Econ 210:15–26. https://doi.org/10.1016/j.ijpe.2019.01.004.

2. Alcácer V, Cruz-Machado V (2019) Scanning the Industry 4.0: A Literature Review on Technologies for Manufacturing Systems. Eng Sci Technol Int J 22(3):899–919. https://doi.org/10.1016/j.jestch.2019.01.006.

3. Jose R, Ramakrishna S (2018) Materials 4.0: Materials big data enabled materials discovery Appl Mater Today 10:27–132. https://doi.org/10.1016/j.apmt.2017.12.015.

4. Ramakrishna S, Zhang T, Lu W, Qian Q, Low J, Yune J, Tan D, Bressan S, Sanvito S, Kalidindi S (2018) Materials informatics. J Intell Manuf 30(6):2307–2326. https://doi.org/10.1007/s10845-018-1392-0.

5. Thompson M, Moroni G, Vaneker T, Fadel G, Campbell R, Gibson I, Bernard A, Schulz J, Graf P, Ahuja B, Martina F (2016) Design for Additive Manufacturing: Trends, opportunities, considerations, and constraints. CIRP Ann 65(2):737–760. https://doi.org/10.1016/j.cirp.2016.05.004.

6. Gibson I, Rosen D, Stucker B (2015) Additive Manufacturing Technologies: 3D Printing, Rapid Prototyping, and Direct Digital Manufacturing. Springer, New York.

7. Bourell D, Kruth J, Leu M, Levy G, Rosen D, Beese A, Clare A (2017) CIRP Ann 66(2):659–681. https://doi.org/10.1016/j.cirp.2017.05.009.

8. Li N, Huang S, Zhang G, Qin R, Liu W, Xiong H, Shi G, Blackburn J (2019) Progress in additive manufacturing on new materials: A review. J Mater Sci Technol 35(2):242–269. https://doi.org/10.1016/j.jmst.2018.09.002.

9. Mittal S, Khan M, Romero D, Wuest T (2017) Smart manufacturing: Characteristics, technologies and enabling factors. Journal of Engineering Manufacture 233(5):1342–1361. https://doi.org/10.1177/0954405417736547.

10. Dilberoglu U, Gharehpapagh B, Yaman U, Dolen M (2017) The Role of Additive Manufacturing in the Era of Industry 4.0. Procedia Manuf 11:545–554. https://doi.org/10.1016/j.promfg.2017.07.148.

11. Schneider H-J, Kato K, Strongin R.M. (2007) Chemomechanical Polymers as Sensors and Actuators for Biological and Medicinal Applications. J Sens 7(8):1578–1611. https://doi.org/10.3390/s7081578.

12. Bar-Cohen Y, Zhang Q (2008) Electroactive Polymer Actuators and Sensors. MRS Bull 33(3):173–181. https://doi.org/10.1557/mrs2008.42.

13. Wang T, Farajollahi M, Choi YS, Lin I-T, Marshall JE, Thompson NM, Kar-Narayan S, Madden JDW, Smoukov SK (2016) Electroactive polymers for sensing. Interface Focus 6:20160026. https://doi.org/10.1098/rsfs.2016.0026.

14. Blackwood G, Ealey M (1993) Electrostrictive behavior in lead magnesium niobate (PMN) actuators. I. Materials perspective. Smart Mater Struct 2(2):124–133. https://doi.org/10.1088/0964-1726/2/2/008.

15. Kumar P, Singh S, Thakur O, Prakash C, Goel T (2004) Study of Lead Magnesium Niobate–Lead Titanate Ceramics for Piezo-Actuator Applications. Jpn J Appl Phys 43(4A):1501–1506. https://doi.org/10.1143/jjap.43.1501.

16. Burcsu E, Ravichandran G, Bhattacharya K (2004) Large electrostrictive actuation of barium titanate single crystals. J Mech Phys Solids, 52(4):823–846. https://doi.org/10.1016/j.jmps.2003.08.001.

17. Baraskar B, Kambale R, James A, Mahesh M, Ramana C, Kolekar Y (2017) Ferroelectric, piezoelectric and electrostrictive properties of Sn4+−modified Ba0.7Ca0.3TiO3 lead-free electroceramics. J Am Ceram Soc 100(12):5755–5765. https://doi.org/10.1111/jace.15073.

18. Nan C, Bichurin M.I, Dong S, Viehland D, Srinivasan G (2008) Multiferroic magnetoelectric composites: Historical perspective, status, and future directions. J Appl Phys 103:031101. https://doi.org/10.1063/1.2836410.

19. Olabi AG, Grunwald A (2008) Design and application of magnetostrictive materials. Mater Des 29(2):469–483. https://doi.org/10.1016/j.matdes.2006.12.016.

20. Priya S, Islam R, Dong S, Viehland D (2007) Recent advancements in magnetoelectric particulate and laminate composites. J Electroceram 19(1):147–164. https://doi.org/10.1007/s10832-007-9042-5.

21. Rahman M, Ahmed M, Nawaz M, Molina G, Rahman A (2017) Experimental Investigation of Photostrictive Materials for MEMS Application. OALib Journal 4:e3856. https://doi.org/10.4236/oalib.1103856.

22. Sun D, Tong L (2007) Modeling of wireless remote shape control for beams using nonlinear photostrictive actuators. Int J Solids Struct 44(2):672–684. https://doi.org/10.1016/j.ijsolstr.2006.05.013.

23. Mohd Jani J, Leary M, Subic A, Gibson M (2014) A review of shape memory alloy research, applications and opportunities. Mater Des 1980–2015 56:1078–1113. https://doi.org/10.1016/j.matdes.2013.11.084.

24. Mishnaevsky L, Levashov E, Valiev R, Segurado J, Sabirov I, Enikeev N, Prokoshkin S, Solov'yov A, Korotitskiy A, Gutmanas E, Gotman I, Rabkin E, Psakh'e S, Dluhoš L, Seefeldt M, Smolin A (2014) Nanostructured titanium-based materials for medical implants: Modeling and development. Mater Sci Eng R Rep 81:1–19. https://doi.org/10.1016/j.mser.2014.04.002.

25. Chiodo J, Jones N (2012) Smart materials use in active disassembly. Assembly Autom 32(1):8–24. https://doi.org/10.1108/01445151211198683.

26. Chiodo J, Jones N, Billett E (2002) WITHDRAWN: Shape memory alloy actuators for active disassembly using 'smart' materials of consumer electronic products. Mater Des https://doi.org/10.1016/s0261-3069(02)00016-x.

27. Fu Y, Huang W, Luo J, Lu H (2015) Polyurethane shape-memory polymers for biomedical applications. In: L'Hocine Y (ed) Shape Memory Polymers for Biomedical Applications. Woodhead Publishing, Cambridge, p 167–195. https://doi.org/10.1016/B978-0-85709-698-2.00009-X.

28. Lendlein A, Langer R (2002) Biodegradable, elastic shape-memory polymers for potential biomedical applications. Science, 296(5573):1673–1676. https://doi.org/10.1038/news020422-18.

29. Tobushi H, Hayashi S, Hoshio K, Ejiri Y (2008) Shape recovery and irrecoverable strain control in polyurethane shape-memory polymer. Sci Technol Adv Mat 9(1):015009. https://doi.org/10.1088/1468-6996/9/1/015009.

30. Santo L, Quadrini F, Bellisario D, Iorio L (2019) Applications of Shape-Memory Polymers, and Their Blends and Composites. In: Parameswaranpillai J, Siengchin S, George J, Jose S (ed) Shape Memory Polymers, Blends and Composites. Advanced Structured Materials vol 115. Springer, Singapore, p 311–329. https://doi.org/10.1007/978-981-13-8574-2_13.

31. Kakeshita T, Ullakko K (2002) Giant magnetostriction in ferromagnetic shape-memory alloys. MRS Bull 27(2):105–109. https://doi.org/10.1557/mrs2002.45.

32. Sánchez-Alarcos V, Recarte V, Pérez-Landazábal JI, González MA, Rodríguez-Velamazán JA (2009) Effect of Mn addition on the structural and magnetic properties of Fe-Pd ferromagnetic shape memory alloys. Acta Mater 57(14):4224–4232. https://doi.org/10.4028/www.scientific.net/MSF.635.103.

33. Ullakko K, Wendell L, Smith A, Müllner P, Hampikian G (2012) A magnetic shape memory micropump: Contact-free, and compatible with PCR and human DNA profiling. Smart Mater Struct 21:11. https://doi.org/10.1088/0964-1726/21/11/115020.

34. Smith AR, Tellinen J, Ullakko K (2014) Rapid actuation and response of Ni-Mn-Ga to magnetic-field-induced stress. Acta Mater 80:373–379. https://doi.org/10.1016/j.actamat.2014.06.054.

35. Saren A, Musiienko D, Smith A, Tellinen J, Ullakko K (2015) Modeling and design of a vibration energy harvester using the magnetic shape memory effect. Smart Mater Struct 24(9):095002. https://doi.org/10.1088/0964-1726/24/9/095002.

36. Büsgen T, Feydt J, Hassdorf R, Thienhaus S, Moske M, Boese M, Zayak A, Entel P (2004) Ab initio calculations of structure and lattice dynamics in Ni-Mn-Al shape memory alloys. Phys. Rev B 70(1):014111-1–014111-8. https://doi.org/10.1103/PhysRevB.70.014111.

37. Bruno NM, Ciocanel C, Feigenbaum HP, Waldauer A (2012) A theoretical and experimental investigation of power harvesting using the NiMnGa martensite reorientation mechanism. Smart Mater Struct 21:9 https://doi.org/10.1088/0964-1726/21/9/094018.

38. Ullakko K (1996) Magnetically controlled shape memory alloys: A new class of actuator materials. J Mater Eng Perform 5(3):405–409. https://doi.org/10.1007/BF02649344.

39. Ortega N, Kumar A, Scott J.F., Katiyar R.S. (2015) Multifunctional magnetoelectric materials for device applications. J Condens Matter Phys 27:50. https://doi.org/10.1088/0953-8984/27/50/504002.

40. Ma J, Hu J, Li Z and Nan C (2011) Recent Progress in Multiferroic Magnetoelectric Composites: from Bulk to Thin Films. Adv Mater 23(9):1062–1087. https://doi.org/10.1002/adma.201003636.

41. Meier QN, Fechner M, Nozaki T, Sahashi M, Salman Z, Prokscha T, Suter A, Schoenherr P, Lilienblum M, Borisov P, Dzyaloshinskii IE, Fiebig M, Luetkens H, Spaldin NA (2019) Search for the Magnetic Monopole at a Magnetoelectric Surface. Phys Rev X 9(1):011011. https://doi.org/10.1103/PhysRevX.9.011011.

42. Yokota T, Ichikawa K, Gomi M (2013) Epitaxial growth and magnetoelectric properties of magnetoelectric multilayers: Cr2o3/linbo3/cr2o 3 thin films. e-J Surf Sci Nanotech 11:89–92. https://doi.org/10.1380/ejssnt.2013.89.

43. Ce Wen Nan, Li M, Huang JH (2001) Calculations of giant magnetoelectric effects in ferroic composites of rare-earth-iron alloys and ferroelectric polymers. Phys. Rev B 63(14):1444151–1444159. https://doi.org/10.1103/PhysRevB.63.144415.

44. Kamenetskii EO, Sigalov M, Shavit R (2008) Magnetoelectric effect for novel microwave device applications. In: Proceedings of IEEE Convention of Electrical and Electronics Engineers in Israel, p 599. https://doi.org/10.1109/EEEI.2008.4736601.

45. Yoo I, Ahn C, Cho K (2018) 15-Mode piezoelectric composite and its application in a magnetoelectric laminate structure. J Alloys Compd 767:61–67. https://doi.org/10.1016/j.jallcom.2018.07.084.

46. Fuentes-Cobas LE, Matutes-Aquino JA, Botello-Zubiate ME, González-Vázquez A, Fuentes-Montero ME, Chateigner D (2015) Advances in Magnetoelectric Materials and Their Application, Handbook of Magnetic Materials 24:237–322. https://doi.org/10.1016/bs.hmm.2015.10.001.

47. Pizzini S (2012) Advanced Silicon Materials for Photovoltaic Applications. John Wiley & Sons, Chichester.

48. Czaban JA, Thompson DA, LaPierre RR (2009) GaAs core-shell nanowires for photovoltaic applications. Nano Lett 9(1):148–154. https://doi.org/10.1021/nl802700u.

49. Scheer R, Schock H (2011) Chalcogenide Photovoltaics: Physics, Technologies, and Thin Film Devices. Wiley-VCH, Singapore.

50. Qu YH, Cong DY, Sun XM, Nie ZH, Gui WY, Li RG, Ren Y, Wang YD (2017) Giant and reversible room-temperature magnetocaloric effect in Ti-doped Ni-Co-Mn-Sn magnetic shape memory alloys. Acta Mater 134:236–248. https://doi.org/10.1016/j.actamat.2017.06.010.

51. Cheng J, Tang J, Zhang A, Meng X, Chu J (2000) Sol-gel-derived pyro-electric barium strontium titanate thin films for infrared detector applications. Appl Phys A-Mater 71(6):667–670. https://doi.org/10.1080/00150190108016271.

52. Grudkowski TW, Montress GK, Gilden M, Black JF (1981) Integrated Circuit Compatible Surface Acoustic Wave Devices on Gallium Arsenide. IEEE Trans. Microw. Theory Tech 29(12):1348–1356. https://doi.org/10.1109/TMTT.1981.1130564.

53. Mescher M, Abe T, Brunett B, Metla H, Schlesinger TE, Reed M (1995) Piezoelectric lead-zirconate-titanate actuator films for microelectromechanical systems applications. In: Proceedings of the IEEE Micro Electro Mechanical Systems, p 261. https://doi.org/10.1109/MEMSYS.1995.472537.

54. Parton E, Bartic C, Campitelli A (2004) Micro-system platforms/new materials for biosensor applications. Solid State Technol 47(4):s1–s2.

55. Zhao Y, Fang X, Jiang Z, Zhao L (2010) An ultra-high pressure sensor based on SOI piezoresistive material. Journal of Mech Sci Technol 24(8):1655–1660. https://doi.org/10.1007/s12206-010-0515-0.

56. Tschan T, de Rooij N, Bezinge A (1992) Damping of piezoresistive silicon accelerometers. Sensor Actuat A-Phys, 32(1–3):375–379. https://doi.org/10.1016/0924-4247(92)80015-U.

57. Jovanovic V, Ghamaty S, Bass JC (2012) New thermoelectric materials and applications. In: Proceedings of InterSociety Conference on Thermal and Thermomechanical Phenomena in Electronic Systems, p 1159. https://doi.org/10.1109/ITHERM.2012.6231554.

58. Yang J, Stabler FR (2009) Automotive applications of thermoelectric materials. J Electron Mater 38(7):1245–1251. https://doi.org/10.1007/s11664-009-0680-z.

59. Kuo C, Wu T, Fan S (2018) Applications of Poly(indole-6-carboxylic acid-co-2,2′-bithiophene) Films in High-Contrast Electrochromic Devices. Coatings 8(3):102. https://doi.org/10.3390/coatings8030102.

60. Lin K, Zhang S, Liu H, Zhao Y, Wang Z, Xu J (2015) Effects on the electrochemical and electrochromic properties of 3 linked polythiophene derivative by the introduction of polyacrylate. Int J Electrochem Sci 10(9):7720–7731.

61. Fabre-Francke I, Aubert P, Alfonsi S, Vidal F, Sauques L, Chevrot C (2012) Electropolymerization of 3,4-ethylenedioxythiophene within an insulating nitrile butadiene rubber network: Application to electroreflective surfaces and devices. Sol Energy Mater Sol Cells 99:109–115. https://doi.org/10.1016/j.solmat.2011.07.004.

62. Granqvist C (2014) Electrochromics for smart windows: Oxide-based thin films and devices. Thin Solid Films 564:1–38. https://doi.org/10.1016/j.tsf.2014.02.002.

63. Tajima K, Yamada Y, Bao S, Okada M, Yoshimura K (2008) Flexible all-solid-state switchable mirror on plastic sheet. Appl Phys Lett 92(4):041912. https://doi.org/10.1063/1.2839298.

64. Smith II RD, Benson DK, Maroef I, Olson DL, Wildeman TR (2001) The determination of hydrogen distribution in high-strength steel weldments. Part 2: Opto-electronic diffusible hydrogen sensor. Weld J 80(5):122s–125s.

65. Benson, D.K., Tracy, C.E., Hishmeh, G.A., Ciszek, P.E., Lee, S. & Haberman, D.P. (1999). In: Proceedings of SPIE—The International Society for Optical Engineering 3535, p 185–202. https://doi.org/10.1117/12.337465.

66. Shirota Y, Utsumi H, Ujike T, Yoshikawa S, Moriwaki K, Nagahama D, Nakano H (2003) Photochromic amorphous molecular materials and their applications. Opt Mater 21(1–3):249–254. https://doi.org/10.1016/S0925-3467(02)00145-3.

67. Tangso KJ, Fong W-K, Darwish T, Kirby N, Boyd BJ, Hanley TL (2013) Novel spiropyran amphiphiles and their application as light-responsive liquid crystalline components. J Phys Chem B 117(35):10203–10210. https://doi.org/10.1021/jp403840m.

68. Levy D (1997) Recent applications of photochromic sol-gel materials. Mol Cryst Liq Cryst Sci Tech 297–298:31–39. https://doi.org/10.1080/10587259708036100.

69. Yang Y, Psaltis D, Luennemann M, Berben D, Hartwig U, Buse K (2003) Photorefractive properties of lithium niobate crystals doped with manganese. J Opt Soc Am B 20(7):1491. https://doi.org/10.1364/josab.20.001491.

70. Ducharme S, Feinberg J (1986) Altering the photorefractive properties of BaTiO_3 by reduction and oxidation at 650°C. J Opt Soc Am B 3(2):283. https://doi.org/10.1364/josab.3.000283.

71. Li Y, Ji S, Gao Y, Luo H, Kanehira M (2013) Core-shell VO2 @TiO2 nanorods that combine thermochromic and photocatalytic properties for application as energy-saving smart coatings. Sci Rep 3:1370 https://doi.org/10.1038/srep01370.

72. Hao Q, Li W, Xu H, Wang J, Yin Y, Wang H, Ma L, Ma F, Jiang X, Schmidt OG, Chu PK (2018) VO 2 /TiN Plasmonic Thermochromic Smart Coatings for Room-Temperature Applications. Adv Mater 30(10):1705421. https://doi.org/10.1002/adma.201705421.

73. Pucci A, Ruggeri G (2011) Mechanochromic polymer blends. J Mater Chem 21(23):8282. https://doi.org/10.1039/C0JM03653F.

74. Jiang Y (2014) An outlook review: Mechanochromic materials and their potential for biological and healthcare applications. Mater Sci Eng: C 45:682–689. https://doi.org/10.1016/j.msec.2014.08.027.

75. Gao F, Xiong Z, Xue H, Liu Y (2009) Improved performance of strontium aluminate luminous coating on the ceramic surface. J Phys 152:012082. https://doi.org/10.1088/1742-6596/152/1/012082.

76. Giuliani F, Autelitano F (2014) Photoluminescent road surface dressing: A first laboratory experimental investigation. Mater Tech 102(6–7):603. https://doi.org/10.1051/mattech/2014030.

77. Azorin J (2014) Preparation methods of thermoluminescent materials for dosimetric applications: An overview. Appl Radiat Isot 83:187–191. https://doi.org/10.1016/j.apradiso.2013.04.031.

78. Tang W, Cameron DC (1996) Electroluminescent zinc sulphide devices produced by sol-gel processing. Thin Solid Films 280(1–2):221–226. https://doi.org/10.1016/0040-6090(95)08198-4.

79. Smet P, Moreels I, Hens Z, Poelman D (2010) Luminescence in Sulfides: A Rich History and a Bright Future. Mater 3(4):2834–2883. https://doi.org/10.3390/ma3042834.

80. Feng A, Smet P (2018) A Review of Mechanoluminescence in Inorganic Solids: Compounds, Mechanisms, Models and Applications. Mater 11(4):484. https://doi.org/10.3390/ma11040484.

81. Di B, Chen Y (2018) Recent progress in organic mechanoluminescent materials. Chin Chem Lett 29(2):245–251. https://doi.org/10.1016/j.cclet.2017.08.043.

82. Ding J, Li W, SZ Shen (2011) Research and Applications of Shear Thickening Fluids. Recent Pat Mater Sci 4(1):43–49. https://doi.org/10.2174/1874464811104010043.

83. Gürgen S, Kushan M, Li W (2017) Shear thickening fluids in protective applications: A review. Prog Polym Sci 75:48–72. https://doi.org/10.1016/j.progpolymsci.2017.07.003.

84. Hao T (2002) Electrorheological suspensions. Adv Colloid Interface Sci 97(1–3):1–35. https://doi.org/10.1016/S0001-8686(01)00045-8.

85. Agafonov, A. and Zakharov, A. (2010) Electrorheological fluids. Russ J Gen Chem 80:567–575. https://doi.org/10.1134/S1070363210030382.

86. de Vicente J, Klingenberg D, Hidalgo-Alvarez R (2011) Magnetorheological fluids: a review. Soft Matter 7(8):3701. https://doi.org/10.1039/C0SM01221A.

87. Spaggiari A (2012) Properties and applications of Magnetorheological fluids. Frattura ed Integrità Strutturale 7(23):48–61. https://doi.org/10.3221/IGF-ESIS.23.06

88. Kostamo E, Kostamo J, Kajaste J, Pietola M (2012) Magnetorheological valve in servo applications. J Intel Mater Syst Str 23(9):1001–1010. https://doi.org/10.1177/1045389X12436732.

89. Krishna B, Bose S, Bandyopadhyay A (2007) Laser Processing of Net-Shape NiTi Shape Memory Alloy. Metallurgical and Materials Transactions A 38(5):1096–1103. https://doi.org/10.1007/s11661-007-9127-4.

90. Marattukalam J, Singh A, Datta S, Das M, Balla V, Bontha S, Kalpathy S (2015) Microstructure and corrosion behavior of laser processed NiTi alloy. Mater Sci Eng C 57:309–313. https://doi.org/10.1016/j.msec.2015.07.067.

91. Hamilton R, Palmer T, Bimber B (2015) Spatial characterization of the thermal-induced phase transformation throughout as-deposited additive manufactured NiTi bulk builds. Scr Mater 101:56–59. https://doi.org/10.1016/j.scriptamat.2015.01.018.

92. Hamilton R, Bimber B, Palmer T (2018) Correlating microstructure and superelasticity of directed energy deposition additive manufactured Ni-rich NiTi alloys. J Alloy Compd 739:712–722. https://doi.org/10.1016/j.jallcom.2017.12.270.

93. Bimber B, Hamilton R, Keist J, Palmer T (2016) Anisotropic microstructure and superelasticity of additive manufactured NiTi alloy bulk builds using laser directed energy deposition. Mater Sci Eng A 674:125–134. https://doi.org/10.1016/j.msea.2016.07.059.

94. Hamilton R, Bimber B, Taheri AM, Elahinia M (2017) Multi-scale shape memory effect recovery in NiTi alloys additive manufactured by selective laser melting and laser directed energy deposition. J Mater Process Technol 250:55–64. https://doi.org/10.1016/j.jmatprotec.2017.06.027.

95. Shiva S, Palani I, Mishra S, Paul C, Kukreja L (2015) Investigations on the influence of composition in the development of Ni–Ti shape memory alloy using laser based additive manufacturing. Opt Laser Technol 69:44–51. https://doi.org/10.1016/j.optlastec.2014.12.014.

96. Baran A, Polanski M (2018) Microstructure and properties of LENS (laser engineered net shaping) manufactured Ni-Ti shape memory alloy. J Alloy Compd 750:863–870. https://doi.org/10.1016/j.jallcom.2018.03.400.

97. Wang C, Tan X, Du Z, Chandra S, Sun Z, Lim C, Tor S, Lim C, Wong C (2019) Additive manufacturing of NiTi shape memory alloys using pre-mixed powders. J Mater Process Technol 271:152–161. https://doi.org/10.1016/j.jmatprotec.2019.03.025.

98. Shishkovsky I, Yadroitsev I, Smurov I (2012) Direct Selective Laser Melting of Nitinol Powder. Phys Procedia 39:447–454. https://doi.org/10.1016/j.phpro.2012.10.060.

99. Walker J, Haberland C, Taheri AM, Karaca H, Dean D, Elahinia M (2016) Process development and characterization of additively manufactured nickel–titanium shape memory parts. J Intel Mat Syst Str 27(19):2653–2660. https://doi.org/10.1177/1045389X16635848

100. Speirs M, Van Hooreweder B, Van Humbeeck J, Kruth J (2017) Fatigue behaviour of NiTi shape memory alloy scaffolds produced by SLM, a unit cell design comparison. J Mech Behav Biomed Mater 70:53–59. https://doi.org/10.1016/j.jmbbm.2017.01.016.

101. Walker J, Elahinia M, Haberland C (2013) An Investigation of Process Parameters on Selective Laser Melting of Nitinol. In: Proceedings of the ASME 2013 Conference on Smart Materials, Adaptive Structures and Intelligent Systems Vol 1, V001T01A007. https://doi.org/10.1115/SMASIS2013-3074.

102. Bormann T, Schumacher R, Müller B, Mertmann M, de Wild M (2012) Tailoring Selective Laser Melting Process Parameters for NiTi Implants. J Mater Eng Perform 21(12):2519–2524. https://doi.org/10.1007/s11665-012-0318-9.

103. Jahadakbar A, Shayesteh MN, Amerinatanzi A, Dean D, Karaca H, Elahinia M (2016) Finite Element Simulation and Additive Manufacturing of Stiffness-Matched NiTi Fixation Hardware for Mandibular Reconstruction Surgery. Bioengineering 3(4):36. https://doi.org/10.3390/bioengineering3040036.

104. Saedi S, Turabi A, Taheri AM, Haberland C, Karaca H, Elahinia M (2016) The influence of heat treatment on the thermomechanical response of Ni-rich NiTi alloys manufactured by selective laser melting. J Alloy Compd 677:204–210. https://doi.org/10.1016/j.jallcom.2016.03.161.

105. Saedi S, Turabi A, Andani M, Haberland C, Elahinia M, Karaca H (2016) Thermomechanical characterization of Ni-rich NiTi fabricated by selective laser melting. Smart Mater Struct 25(3):035005. https://doi.org/10.1088/0964-1726/25/3/035005.

106. Saedi S, Turabi A, Andani M, Moghaddam N, Elahinia M, Karaca H (2017) Texture, aging, and superelasticity of selective laser melting fabricated Ni-rich NiTi alloys. Mater Sci Eng A 686:1–10. https://doi.org/10.1016/j.msea.2017.01.008.

107. Saedi S, Shayesteh AN, Amerinatanzi A, Elahinia M, Karaca H (2018) On the effects of selective laser melting process parameters on microstructure and thermomechanical response of Ni-rich NiTi. Acta Mater 144:552–560. https://doi.org/10.1016/j.actamat.2017.10.072.

108. Shayesteh MN, Saedi S, Amerinatanzi A, Hinojos A, Ramazani A, Kundin J, Mills M, Karaca H, Elahinia M (2019) Achieving superelasticity in additively manufactured NiTi in compression without post-process heat treatment. Sci Rep 9(1):41. https://doi.org/10.1038/s41598-018-36641-4.

109. Li S, Hassanin H, Attallah M, Adkins N, Essa K (2016) The development of TiNi-based negative Poisson's ratio structure using selective laser melting. Acta Mater 105:75–83. https://doi.org/10.1016/j.actamat.2015.12.017.

110. Taheri AM, Saedi S, Turabi A, Karamooz M, Haberland C, Karaca H, Elahinia M (2017) Mechanical and shape memory properties of porous Ni 50.1 Ti 49.9 alloys manufactured by selective laser melting. J Mech Behav Biomed 68:224–231. https://doi.org/10.1016/j.jmbbm.2017.01.047.

111. Shayesteh MN, Saghaian S, Amerinatanzi A, Ibrahim H, Li P, Toker G, Karaca H, Elahinia M (2018) Anisotropic tensile and actuation properties of NiTi fabricated with selective laser melting. Mat Sci Eng A 724:220–230. https://doi.org/10.1016/j.msea.2018.03.072.

112. Taheri AM, Haberland C, Walker J, Karamooz M, Sadi TA, Saedi S, Rahmanian R, Karaca H, Dean D, Kadkhodaei M, Elahinia M (2016) Achieving biocompatible stiffness in NiTi through additive manufacturing. J Intel Mat Syst Str 27(19):2661–2671. https://doi.org/10.1177/1045389X16641199.

113. Elahinia M, Shayesteh MN, Amerinatanzi A, Saedi S, Toker G, Karaca H, Bigelow G, Benafan O (2018) Additive manufacturing of NiTiHf high temperature shape memory alloy. Scr Mater 145:90–94. https://doi.org/10.1016/j.scriptamat.2017.10.016

114. Sam J, Franco B, Ma J, Karaman I, Elwany A, Mabe J (2018) Tensile actuation response of additively manufactured nickel-titanium shape memory alloys. Scr Mater 146:164–168. https://doi.org/10.1016/j.scriptamat.2017.11.013.

115. Dadbakhsh S, Speirs M, Van Humbeeck J, Kruth J (2016) Laser additive manufacturing of bulk and porous shape-memory NiTi alloys: From processes to potential biomedical applications. MRS Bull 41(10):765–774. https://doi.org/10.1557/mrs.2016.209.

116. Dadbakhsh S, Vrancken B, Kruth J, Luyten J, Van Humbeeck J (2016) Texture and anisotropy in selective laser melting of NiTi alloy. Mat Sci Eng A 650:225–232. https://doi.org/10.1016/j.msea.2015.10.032.

117. Khoo Z, An J, Chua C, Shen Y, Kuo C, Liu Y (2018) Effect of Heat Treatment on Repetitively Scanned SLM NiTi Shape Memory Alloy. Materials 12(1):77. https://doi.org/10.3390/ma12010077.

118. Speirs M, Wang X, Van BS, Ahadi A, Dadbakhsh S, Kruth J, Van Humbeeck J (2016) On the Transformation Behavior of NiTi Shape-Memory Alloy Produced by SLM. Shap. Mem. Superelasticity 2(4):310–316. https://doi.org/10.1007/s40830-016-0083-y.

119. Hagemann R, Noelke C, Rau T, Kaierle S, Overmeyer L, Wesling V, Wolkers W (2015) Design, processing, and characterization of nickel titanium micro-actuators for medical implants. J Laser Appl 27(S2):S29203. https://doi.org/10.2351/1.4906381.

120. Khademzadeh S, Parvin N, Bariani P, Mazzucato F (2015) Effects of micro laser sintering process parameters on quality of nickel-titanium single tracks and thin walls. Met and Mater Int 21(6):1081–1090. https://doi.org/10.1007/s12540-015-5304-y.

121. Hayat M, Chen G, Liu N, Khan S, Tang H, Cao P (2018) Physical and Tensile Properties of NiTi Alloy by Selective Electron Beam Melting. Key Eng Mater 770:148–154. https://doi.org/10.4028/www.scientific.net/KEM.770.148.

122. Zhou Q, Hayat M, Chen G, Cai S, Qu X, Tang H, Cao P (2019) Selective electron beam melting of NiTi: Microstructure, phase transformation and mechanical properties. Mat Sci Eng A 744:290–298. https://doi.org/10.1016/j.msea.2018.12.023.

123. Lu B, Cui X, Liu E, Feng X, Dong M, Li Y, Wang H, Jin G (2018) Influence of microstructure on phase transformation behavior and mechanical properties of plasma arc deposited shape memory alloy. Mat Sci Eng A 736:130–136. https://doi.org/10.1016/j.msea.2018.08.098.

124. Lu B, Cui X, Feng X, Dong M, Li Y, Cai Z, Wang H, Jin G (2018) Direct rapid prototyping of shape memory alloy with linear superelasticity via plasma arc deposition. Vacuum 157:65–68. https://doi.org/10.1016/j.vacuum.2018.08.028.

125. Wang J, Pan Z, Yang G, Han J, Chen X, Li H (2019) Location dependence of microstructure, phase transformation temperature and mechanical properties on Ni-rich NiTi alloy fabricated by wire arc additive manufacturing. Mat Sci Eng A 749:218–222. https://doi.org/10.1016/j.msea.2019.02.029.

126. Reyes DG, Walczak M, Ramos ME, Ramos-Grez J (2017) Towards direct metal laser fabrication of Cu-based shape memory alloys. Rapid Prototyp J 23(2):329–336. https://doi.org/10.1108/RPJ-02-2016-0017.

127. Gargarella P, Kiminami C, Mazzer E, Cava R, Basilio L, Bolfarini C, Botta W, Eckert J, Gustmann T, Pauly S (2015) Phase Formation, Thermal Stability and Mechanical Properties of a Cu-Al-Ni-Mn Shape Memory Alloy Prepared by Selective Laser Melting. Mater Res 18(2):35–38. https://doi.org/10.1590/1516-1439.338914.

128. Gustmann T, Neves A, Kühn U, Gargarella P, Kiminami C, Bolfarini C, Eckert J, Pauly S (2016) Influence of processing parameters on the fabrication of a Cu-Al-Ni-Mn shape-memory alloy by selective laser melting. Addit Manuf 11:23–31. https://doi.org/10.1016/j.addma.2016.04.003

129. Gustmann T, Schwab H, Kühn U, Pauly S (2018) Selective laser remelting of an additively manufactured Cu-Al-Ni-Mn shape-memory alloy. Mater Des 153:129–138. https://doi.org/10.1016/j.matdes.2018.05.010.

130. Gustmann T, dos Santos J, Gargarella P, Kühn U, Van Humbeeck J, Pauly S (2016) Properties of Cu-Based Shape-Memory Alloys Prepared by Selective Laser Melting. Shap. Mem. Superelasticity 3(1):24–36. https://doi.org/10.1007/s40830-016-0088-6.

131. Tian J, Zhu W, Wei Q, Wen S, Li S, Song B, Shi Y (2019) Process optimization, microstructures and mechanical properties of a Cu-based shape memory alloy fabricated by selective laser melting. J Alloy Compd 785:754–764. https://doi.org/10.1016/j.jallcom.2019.01.153.

132. Niendorf T, Brenne F, Krooß P, Vollmer M, Günther J, Schwarze D, Biermann H (2016) Microstructural Evolution and Functional Properties of Fe-Mn-Al-Ni Shape Memory Alloy Processed by Selective Laser Melting. Metall Mater Trans A 47(6):2569–2573. https://doi.org/10.1007/s11661-016-3412-z.

133. Taylor S, Shah R, Dunand D (2018) Ni-Mn-Ga micro-trusses via sintering of 3D-printed inks containing elemental powders. Acta Mater 143:20–29. https://doi.org/10.1016/j.actamat.2017.10.002.

134. Taylor S, Shah R Dunand D (2019) Microstructure and porosity evolution during sintering of Ni-Mn-Ga wires printed from inks containing elemental powders. Intermetallics, 104:113–123. https://doi.org/10.1016/j.intermet.2018.10.024.

135. Caputo M, Solomon C, Nguyen P, Berkowitz A (2016) Electron Microscopy Investigation of Binder Saturation and Microstructural Defects in Functional Parts Made by Additive Manufacturing. Microsc Microanal 22(S3):1770–1771. https://doi.org/10.1017/S1431927616009697.

136. Caputo M, Berkowitz A, Armstrong A, Müllner P, Solomon C (2018) 4D printing of net shape parts made from Ni-Mn-Ga magnetic shape-memory alloys. Addit Manuf 21:579–588. https://doi.org/10.1016/j.addma.2018.03.028.

137. Caputo M, Solomon C (2017) A facile method for producing porous parts with complex geometries from ferromagnetic Ni-Mn-Ga shape memory alloys. Mater Lett 200:87–89. https://doi.org/10.1016/j.matlet.2017.04.112.

138. Mostafaei A, Kimes K, Stevens E, Toman J, Krimer Y, Ullakko K, Chmielus M (2017) Microstructural evolution and magnetic properties of binder jet additive manufactured Ni-Mn-Ga magnetic shape memory alloy foam. Acta Mater 131:482–490. https://doi.org/10.1016/j.actamat.2017.04.010.

139. Mostafaei A, Rodriguez De Vecchis P, Stevens E, Chmielus M (2018) Sintering regimes and resulting microstructure and properties of binder jet 3D printed Ni-Mn-Ga magnetic shape memory alloys. Acta Mater 154:355–364. https://doi.org/10.1016/j.actamat.2018.05.047.

140. Caputo M, Solomon C (2017) Microstructure and Chemical Composition Analysis of Additive Manufactured Ni-Mn-Ga Parts Sintered in Different Conditions. Microsc Microanal 23(S1):2078–2079. https://doi.org/10.1017/S1431927617011059.

141. Toman J, Müllner P, Chmielus M (2018) Properties of as-deposited and heat-treated Ni-Mn-Ga magnetic shape memory alloy processed by directed energy deposition. J Alloy Compd 752:455–463. https://doi.org/10.1016/j.jallcom.2018.04.059.

142. Ullakko K, Laitinen V, Saren A, Sozinov A, Musiienko D, Chmielus M, Salminen A (2018) Ni-Mn-Ga actuating elements manufactured using 3D

printing. Paper presented at the 11th European Symposium on Martensitic Transformations, Metz, 27–31 August 2018.

143. Laitinen V, Sozinov A, Saren A, Salminen A, Ullakko K (2019) Laser powder bed fusion of Ni-Mn-Ga magnetic shape memory alloy. Addit Manuf 30C: 100891. https://doi.org/10.1016/j.addma.2019.100891.

144. Nilsén F, Ituarte I, Salmi M, Partanen J, Hannula S (2019) Effect of process parameters on non-modulated Ni-Mn-Ga alloy manufactured using powder bed fusion. Addit Manuf 28:464–474. https://doi.org/10.1016/j.addma.2019.05.029.

145. Laitinen V, Salminen A, Ullakko K (2019) First investigation on processing parameters for laser powder bed fusion of Ni-Mn-Ga magnetic shape memory alloy. J Laser Appl 31(2):022303. https://doi.org/10.2351/1.5096108.

146. Laitinen V, Sozinov A, Saren A, Ullakko K (2019) Laser based 4D printing of Ni-Mn-Ga MSM alloy. In: Book of abstracts of 6th International Conference on Ferromagnetic Shape Memory Alloys p 156-157. ISBN 978-80-905962-9-0.

147. Stevens E, Toman J, Kimes K, Chernenko V, Wojcik A, Maziarz W, Chmielus M (2016) Microstructural Evaluation of Magnetocaloric Ni-Co-Mn-Sn Produced by Directed Energy Deposition. Microsc Microanal 22(S3):1774–1775. https://doi.org/10.1017/s1431927616009715.

148. Stevens E, Kimes K, Chernenko V, Wojcik A, Maziarz W, Toman J, Chmielus M (2017). Characterization of Direct Laser Deposited Magnetocaloric Ni-Co-Mn-Sn. In: Proceedings of Materials Science and Technology, p 430–432. https://doi.org/10.7449/2017mst/2017/mst_2017_430_432.

149. Stevens E, Kimes K, Chernenko V, Lazpita P, Wojcik A, Maziarz W, Chmielus M (2018) Direct Laser Deposition and Homogenization of Ni-Co-Mn-Sn Magnetocaloric Material. Microsc Microanal 24(S1):956–957. https://doi.org/10.1017/s1431927618005275.

150. Stevens E, Salazar D, Kimes K, de Vecchis R, Chernenko V, Chmielus M (2019) Additive Manufacturing of Ni-Mn-Cu-Ga: Influence of Sintering Temperature on Magnetocaloric Effect and Microstructure. Microsc Microanal 25(S2):2578–2579. https://doi.org/10.1017/S143192761901362X.

151. Ma J, Franco B, Tapia G, Karayagiz K, Johnson L, Liu J, Arroyave R, Karaman I, Elwany A (2017) Spatial Control of Functional Response in 4D-Printed Active Metallic Structures. Sci Rep 7(1):46707. https://doi.org/10.1038/srep46707.

152. Khoo Z, Teoh J, Liu Y, Chua C, Yang S, An J, Leong K, Yeong W (2015) 3D printing of smart materials: A review on recent progresses in 4D printing. Virtual Phys Prototy 10(3):103–122. https://doi.org/10.1080/17452759.2015.1097054.

153. Leist S, Zhou J (2016) Current status of 4D printing technology and the potential of light-reactive smart materials as 4D printable materials. Virtual

Phys Prototy 11(4):249–262. https://doi.org/10.1080/1745275
9.2016.1198630

154. Lee J, An J, Chua C (2017) Fundamentals and applications of 3D printing for novel materials. Appl Mater Today 7:120–133. https://doi.org/10.1016/j.apmt.2017.02.004.

155. Lee A, An J, Chua C (2017) Two-Way 4D Printing: A Review on the Reversibility of 3D-Printed Shape Memory Materials. Eng 3(5):663–674. https://doi.org/10.1016/J.ENG.2017.05.014.

156. Mitchell A, Lafont U, Hołyńska M, Semprimoschnig C (2018) Additive manufacturing — A review of 4D printing and future applications. Addit Manuf 24:606–626. https://doi.org/10.1016/j.addma.2018.10.038

157. Momeni FM. Mehdi Hassani.N S, Liu X, Ni J (2017) A review of 4D printing. Mater Des 122:42–79. https://doi.org/10.1016/j.matdes.2017.02.068.

158. Boydston A, Cao B, Nelson A, Ono R, Saha A, Schwartz J, Thrasher C (2018) Additive manufacturing with stimuli-responsive materials. J Mater Chem A 6(42):20621–20645. https://doi.org/10.1039/C8TA07716A.

159. Chang J, He J, Mao M, Zhou W, Lei Q, Li X, Li D, Chua C, Zhao X (2018) Advanced Material Strategies for Next-Generation Additive Manufacturing. Materials 11(1):166. https://doi.org/10.3390/ma11010166.

160. Kuang X, Roach D, Wu J, Hamel C, Ding Z, Wang T, Dunn M, Qi H (2018) Advances in 4D Printing: Materials and Applications. Adv Funct Mater 29(2):1805290. https://doi.org/10.1002/adfm.201805290.

161. Zhang Z, Demir K, Gu G (2019) Developments in 4D-printing: a review on current smart materials, technologies, and applications. Inter J Smart Nano Mater 10:205–224. https://doi.org/10.1080/19475411.2019.1591541.

162. Li X, Shang J, Wang Z (2017) Intelligent materials: a review of applications in 4D printing. Assembly Autom 37(2):170–185. https://doi.org/10.1108/AA-11-2015-093.

163. Oliveira J, Correia V, Castro H, Martins P, Lanceros-Mendez S (2018) Polymer-based smart materials by printing technologies: Improving application and integration. Addit Manuf 21:269–283. https://doi.org/10.1016/j.addma.2018.03.012.

164. Sossou G, Demoly F, Belkebir H, Qi H, Gomes S, Montavon G (2019) Design for 4D printing: A voxel-based modeling and simulation of smart materials. Mater Des 175:107798. https://doi.org/10.1016/j.matdes.2019.107798.

165. Zhang Z, Demir K, Gu G (2019) Developments in 4D-printing: a review on current smart materials, technologies, and applications. International Journal of Smart and Nano Materials 10(3):205–224. https://doi.org/10.1080/19475411.2019.1591541.

166. Gardan J (2018) Smart materials in additive manufacturing: state of the art and trends. Virtual Phys Prototyp 14(1):1–18. https://doi.org/10.108 0/17452759.2018.1518016.

167. Shafranek R, Millik S, Smith P, Lee C, Boydston A, Nelson A (2019) Stimuli-responsive materials in additive manufacturing. Prog Polym Sci 93:36–67. https://doi.org/10.1016/j.progpolymsci.2019.03.002.

168. Yamauchi K, Ohkata I, Tsuchiya K, Miyazaki S (2011) Shape memory and superelastic alloys: applications and technologies. Woodhead Publishing, Oxford.

169. Duerig T (2012) Shape Memory Alloys. In: ASM Handbook, Volume 23—Materials for medical devices. ASM International, Ohio, p 237–250.

170. Van Humbeeck J (1999) Non-medical applications of shape memory alloys. Mat Sci Eng A 273-275:134–148. https://doi.org/10.1016/S0921-5093(99)00293-2.

171. Elahinia M, Hashemi M, Tabesh M, Bhaduri S (2012) Manufacturing and processing of NiTi implants: A review. Prog Mater Sci 57(5):911–946. https://doi.org/10.1016/j.pmatsci.2011.11.001.

172. Elahinia M, Shayesteh MN, Taheri AM, Amerinatanzi A, Bimber B, Hamilton R (2016) Fabrication of NiTi through additive manufacturing: A review. Prog Mater Sci 83:630–663. https://doi.org/10.1016/j.pmatsci.2016.08.001.

173. Van Humbeeck J (2018) Additive Manufacturing of Shape Memory Alloys. Shap. Mem. Superelasticity 4(2):309–312. https://doi.org/10.1007/s40830-018-0174-z.

174. Wang X, Kustov S, Van Humbeeck J (2018) A Short Review on the Microstructure, Transformation Behavior and Functional Properties of NiTi Shape Memory Alloys Fabricated by Selective Laser Melting. Materials 11(9):1683. https://doi.org/10.3390/ma11091683.

175. Ullakko K, Huang J, Kantner C, O'Handley R, Kokorin V (1996) Large magnetic-field-induced strains in Ni2MnGa single crystals. Appl Phys Lett 69(13):1966–1968. https://doi.org/10.1063/1.117637.

176. Sozinov A, Lanska N, Soroka A, Zou W (2013) 12% magnetic field-induced strain in Ni-Mn-Ga-based non-modulated martensite. Appl Phys Lett 102(2):021902. https://doi.org/10.1063/1.4775677.

177. Aaltio I, Soroka A, Ge Y, Söderberg O, Hannula S (2010) High-cycle fatigue of 10M Ni–Mn–Ga magnetic shape memory alloy in reversed mechanical loading. Smart Materials and Structures 19(7):075014. https://doi.org/10.1088/0964-1726/19/7/075014.

178. Smith A, Tellinen J, Ullakko K (2014) Rapid actuation and response of Ni–Mn–Ga to magnetic-field-induced stress. Acta Mater 80:373–379. https://doi.org/10.1016/j.actamat.2014.06.054.

179. Gaitzsch U, Pötschke M, Roth S, Rellinghaus B, Schultz L (2009) A 1% magnetostrain in polycrystalline 5M Ni–Mn–Ga. Acta Mater 57(2):365–370. https://doi.org/10.1016/j.actamat.2008.09.017.

180. Chmielus M, Zhang X, Witherspoon C, Dunand D, Müllner P (2009) Giant magnetic-field-induced strains in polycrystalline Ni–Mn–Ga foams. Nat Mater 8(11):863–866. https://doi.org/10.1038/nmat2527.

181. Kok Y, Tan X, Wang P, Nai M, Loh N, Liu E, Tor S (2018) Anisotropy and heterogeneity of microstructure and mechanical properties in metal additive manufacturing: A critical review. Mater Des 139:565–586. https://doi.org/10.1016/j.matdes.2017.11.021.

182. Waske A, Dutta B, Teichert N, Weise B, Shayanfar N, Becker A, Hütten A, Hickel T (2018) Coupling Phenomena in Magnetocaloric Materials. Energy Technol 6(8):1429–1447. https://doi.org/10.1002/ente.201800163.

183. Brown G (1976) Magnetic heat pumping near room temperature. J App Phys 47(8):3673–3680. https://doi.org/10.1063/1.323176

184. Lyubina J (2017) Magnetocaloric materials for energy efficient cooling. J Phys D App Phys 50(5):053002. https://doi.org/10.1088/1361-6463/50/5/053002.

185. Weiss P, Piccard A (1917) Le phénomène magnétocalorique. J Phys Théor App 7(1):103–109. https://doi.org/10.1051/jphystap:019170070010300.

186. Franco V, Blázquez J, Ipus J, Law J, Moreno-Ramírez L, Conde A (2018) Prog Mater Sci 93:112–232. https://doi.org/10.1016/j.pmatsci.2017.10.005.

187. Yang Y, Tong C, Zhong J, Huang R, Tan W, Tan Z (2017) An effective thermal therapy against cancer using an E-jet 3D-printing method to prepare implantable magnetocaloric mats. J Biomed Mater Res B 106(5):1827–1841. https://doi.org/10.1002/jbm.b.33992.

188. Fähler S, Rößler U, Kastner O, Eckert J, Eggeler G, Emmerich H, Entel P, Müller S, Quandt E, Albe K (2011) Caloric Effects in Ferroic Materials: New Concepts for Cooling. Adv Eng Mater 14(1–2):10–19. https://doi.org/10.1002/adem.201100178.

189. Fähler S, Pecharsky V (2018) Caloric effects in ferroic materials. MRS Bull 43(4):264–268. https://doi.org/10.1557/mrs.2018.66.

190. Waske A, Gruner M, Gottschall T, Gutfleisch O (2018) Magnetocaloric materials for refrigeration near room temperature. MRS Bull 43(4):269–273. https://doi.org/10.1557/mrs.2018.69.

191. Lozano J, Capovilla M, Trevizoli P, Engelbrecht K, Bahl C, Barbosa J (2016) Development of a novel rotary magnetic refrigerator. Int J Refrig 68:187–197. https://doi.org/10.1016/j.ijrefrig.2016.04.005.

192. Benedict M, Sherif S, Beers D, Schroeder M (2016) Design and performance of a novel magnetocaloric heat pump. Sci Technol Built En 22(5):520–526. https://doi.org/10.1080/23744731.2016.1185889.

193. Park I, Kim Y, Jeong S (2013) Development of the tandem reciprocating magnetic regenerative refrigerator and numerical simulation for the dead volume effect. International Journal of Refrigeration 36(6):1741–1749. https://doi.org/10.1016/j.ijrefrig.2013.03.012.

194. Engelbrecht K, Bahl C, Nielsen K (2011) Int J Refrig 34(4):1132–1140. https://doi.org/10.1016/j.ijrefrig.2010.11.014.

195. Kolano R, Kolano-Burian A, Hreczka M, Polak M, Szynowski J, Tomaka W (2016) Magnetocaloric Cooling Device with Reciprocating Motion of the Magnetic Field Source. Acta Phys Pol A 129(6):1205–1209. https://doi.org/10.12693/aphyspola.129.1205.

196. Romero GJ, Ferreiro GR, Carbia CJ, Romero GM (2013) Experimental analysis of a reciprocating magnetic refrigeration prototype. Int J Refrig 36(4):1388–1398. https://doi.org/10.1016/j.ijrefrig.2013.01.008.

197. He X, Gong M, Zhang H, Dai W, Shen J, Wu J (2013) Design and performance of a room-temperature hybrid magnetic refrigerator combined with Stirling gas refrigeration effect. Int J Refrig 36(5):1465–1471. https://doi.org/10.1016/j.ijrefrig.2013.03.014.

198. Christiaanse T, Brück E (2014) Proof-of-Concept Static Thermomagnetic Generator Experimental Device. Metall Mater Trans 1(1):36–40. https://doi.org/10.1007/s40553-014-0006-9.

199. Gottschall T, Skokov K, Fries M, Taubel A, Radulov I, Scheibel F, Benke D, Riegg S, Gutfleisch O (2019) Making a Cool Choice: The Materials Library of Magnetic Refrigeration. Adv Energy Mater 9(34):1901322. https://doi.org/10.1002/aenm.201901322.

200. Gutfleisch O, Gottschall T, Fries M, Benke D, Radulov I, Skokov K, Wende H, Gruner M, Acet M, Entel P, Farle M (2016) Mastering hysteresis in magnetocaloric materials. Philos Trans Royal Soc A 374(2074):20150308. https://doi.org/10.1098/rsta.2015.0308.

201. Pulko B, Tušek J, Moore J, Weise B, Skokov K, Mityashkin O, Kitanovski A, Favero C, Fajfar P, Gutfleisch O, Waske A, Poredoš A (2015) Epoxy-bonded La–Fe–Co–Si magnetocaloric plates. J Magn Magn Mater 375:65–73. https://doi.org/10.1016/j.jmmm.2014.08.074.

202. Liu J, Gottschall T, Skokov K, Moore J, Gutfleisch O (2012) Giant magnetocaloric effect driven by structural transitions. Nat Mater 11(7):620–626. https://doi.org/10.1038/nmat3334.

203. Salazar-Jaramillo D, Álvarez-Alonso P, Lázpita P, Sánchez LJ, Gorría P, Blanco J, Chernenko V (2018) Magnetocaloric Effect in Specially Designed Materials. In: El-Gendy AA, Barandiarán JM, Hadimani RL (ed) Magnetic Nanostructured Materials. Elsevier, Amsterdam, p 199–244. https://doi.org/10.1016/B978-0-12-813904-2.00007-3.

204. Moore J, Klemm D, Lindackers D, Grasemann S, Träger R, Eckert J, Löber L, Scudino S, Katter M, Barcza A, Skokov K, Gutfleisch O (2013) Selective laser melting of La(Fe,Co,Si)13 geometries for magnetic refrigeration. J Appl Phys 114(4):043907. https://doi.org/10.1063/1.4816465.

205. Loh G, Pei E, Harrison D, Monzón M (2018) An overview of functionally graded additive manufacturing. Addit Manuf 23:34–44. https://doi.org/10.1016/j.addma.2018.06.023.

206. Bandyopadhyay A, Heer B (2018) Additive manufacturing of multi-material structures. Mater Sci Eng R Rep 129:1–16. https://doi.org/10.1016/j.mser.2018.04.001.

207. Pfaff A, Jäcklein M, Hoschke K, Wickert M (2018) Designed Materials by Additive Manufacturing—Impact of Exposure Strategies and Parameters on Material Characteristics of AlSi10Mg Processed by Laser Beam Melting. Metals 8(7):491. https://doi.org/10.3390/met8070491.

208. Zheng X, Smith W, Jackson J, Moran B, Cui H, Chen D, Ye J, Fang N, Rodriguez N, Weisgraber T, Spadaccini CM (2016) Multiscale metallic metamaterials. Nature Mater 15(10):1100–1106. https://doi.org/10.1038/nmat4694.

209. Mahmoud D, Elbestawi M (2017) Lattice Structures and Functionally Graded Materials Applications in Additive Manufacturing of Orthopedic Implants: A Review. J Manuf Mater Process 1(2):13. https://doi.org/10.3390/jmmp1020013.

210. Tofail S, Koumoulos E, Bandyopadhyay A, Bose S, O'Donoghue L, Charitidis C (2018) Additive manufacturing: scientific and technological challenges, market uptake and opportunities. Mater Today 21(1):22–37. https://doi.org/10.1016/j.mattod.2017.07.001.

211. Dehoff R, Kirka M, Sames W, Bilheux H, Tremsin A, Lowe L, Babu S (2014). Site specific control of crystallographic grain orientation through electron beam additive manufacturing. Mater Sci Tech 31(8):931–938. https://doi.org/10.1179/1743284714Y.0000000734.

Publication II

Laitinen, V., Salminen, A., and Ullakko, K.
First investigation on processing parameters for laser powder bed fusion of Ni-Mn-Ga magnetic shape memory alloy

First investigation on processing parameters for laser powder bed fusion of Ni-Mn-Ga magnetic shape memory alloy

Ville Laitinen,[1] (ID) Antti Salminen,[2] (ID) and Kari Ullakko[1]

AFFILIATIONS

[1]Material Physics Laboratory, Lappeenranta-Lahti University of Technology LUT, Yliopistonkatu 34, Lappeenranta 53850, Finland
[2]Laboratory of Laser Processing, Lappeenranta-Lahti University of Technology LUT, Yliopistonkatu 34, Lappeenranta 53850, Finland

Note: This paper is part of the Special Collection: Proceedings of the International Congress of Applications of Lasers & Electro-Optics (ICALEO® 2018).

ABSTRACT

The Ni-Mn-Ga alloy develops strains of several percents in an applied magnetic field. These materials have potential as high-speed actuators, valves, pumps, robots, and microgrippers. Laser powder bed fusion (L-PBF) of Ni-Mn-Ga was investigated in order to establish a preliminary processing window and to understand the effects of processing parameters on end-product composition. In the future, L-PBF could enable the production of functional near net shape Ni-Mn-Ga components on an industrial scale. A series of experiments were conducted for prealloyed Ni-Mn-Ga powder using an L-PBF setup developed in-house. Two different substrate materials, stainless steel 316L and Incoloy 825, were used in the experiments. The single track experiments show that tracks deposited on Incoloy substrates, in comparison to tracks deposited on stainless steel substrates, are wider and have shallower penetration into the substrate. In addition, the tracks deposited on the Incoloy substrates are more likely to exhibit irregular and balling morphologies. The results of the single track and hatching distance experiments were used to manufacture Ni-Mn-Ga cuboids on an Incoloy substrate. Analysis of the cuboid compositions revealed that L-PBF of Ni-Mn-Ga dilutes manganese and gallium. The relative amounts of vaporized manganese and gallium increased as the value of volumetric energy density was increased.

Key words: laser powder bed fusion, additive manufacturing, 3D printing, magnetic shape memory alloy, Ni-Mn-Ga

I. INTRODUCTION

Magnetic shape memory (MSM) alloys, such as Ni-Mn-Ga alloy, constitute a group of metal alloys that strain when exposed to a magnetic field. This straining phenomenon, the MSM effect, occurs when the martensitic twin structure of the alloy re-orientates in response to internal magnetic-field-induced stresses.[1,2] Strains of up to 6%[3] and 9.5%[4] have been observed in single crystalline Ni-Mn-Ga. In addition to the large strains, high strain accelerations of up to $1.6 \times 10^6\,\text{m/s}^2$ have been observed experimentally in Ni-Mn-Ga alloy.[5] The applications of Ni-Mn-Ga include different kinds of micro- and macroscale devices, such as sensors,[6] pumps,[7,8] and energy harvesters.[9]

Manufacturing of functional Ni-Mn-Ga elements is currently the major bottleneck of the technology. Alloy processing would improve with fine-grained polycrystalline Ni-Mn-Ga rather than single crystalline Ni-Mn-Ga, which is currently manufactured by Bridgman and Czochralski techniques. The disadvantage of polycrystalline Ni-Mn-Ga is its lack of MSM effect due to grain boundaries that create constraints that prevent twin boundary motion in the material. However, as was demonstrated by Taylor et al.,[10] strains of up to 2.0%–8.7% can be induced in foamy polycrystalline Ni-Mn-Ga by introducing pores smaller than the grain size into the material.

There exists a growing interest in using additive manufacturing to produce polycrystalline Ni-Mn-Ga components. Recent studies have demonstrated the feasibility of manufacturing polycrystalline Ni-Mn-Ga by 3D ink-printing[11] and binder jetting.[12–15] In addition, manufacturing of magnetocaloric Ni-Co-Mn-Sn by directed energy deposition has been demonstrated recently by Stevens et al.[16] In conclusion, additive manufacturing may become a viable technology for the fabrication of functional Ni-Mn-Ga parts. A literature

TABLE I. Compositions of the used materials in atomic percentage (at. %).

Material	Al	Si	Ti	Cr	Mn	Fe	Ni	Cu	Ga	Mo
Ni-Mn-Ga powder	…	…	…	…	28.5	…	49.8	…	21.7	…
316L substrate	0.7	1.1	…	20.9	1.7	68.1	7.1	…	…	0.2
Incoloy 825 substrate	1.0	0.8	1.1	26.1	0.8	32.1	34.2	1.9	…	1.8

review conducted by the authors of this study reveals that all of the previous research in the additive manufacturing of Ni-Mn-Ga has used the technologies mentioned above. The scientific literature on manufacturing of Ni-Mn-Ga by laser powder bed fusion (L-PBF) is sparse to nonexistent.

This study aims to develop a preliminary processing window for L-PBF of Ni-Mn-Ga by investigating deposition of Ni-Mn-Ga single tracks on two dissimilar substrate materials, and by finding optimal hatch distance values for the deposited tracks. The use of different kinds of substrates is an interesting topic since it may enable the manufacturing of Ni-Mn-Ga actuators on substrates that would act as the solid body of the device. In this study, the results of the single track and hatch distance experiments were utilized to manufacture solid Ni-Mn-Ga cuboids on an Incoloy substrate. The resulting compositions of the manufactured samples were investigated to clarify the effect of process parameters on end-product composition and to propose future steps in the development of the L-PBF process for the alloy.

II. EXPERIMENT

The experiments were implemented in three stages: (1) investigation of single track formation, (2) optimization of hatch distance values, and (3) fabrication of solid Ni-Mn-Ga cuboids. The experiments were conducted using an L-PBF system, which was built in-house for material development and testing purposes. The system employed an IPG ytterbium CW fiber laser (wavelength 1075 nm, maximum power 200 W) with a galvanometric scanner and focusing optics. The measured focal point diameter of the laser beam was 82 μm, and the laser beam was focused on the surface of the powder bed in all of the experiments. The laser beam had a near Gaussian power distribution. The system included a stainless steel platform with a slot for detachable substrate pieces.

The measured compositions of the Ni-Mn-Ga powder and the substrates are presented in Table I. The Ni-Mn-Ga powder was produced by gas atomization and consisted of spherical particles with a size distribution that is presented in Fig. 1. The experiments were conducted using stainless steel 316L and Incoloy 825 substrate pieces, which were cut by laser from standard prealloyed sheets. Substrates were mechanically attached, calibrated, and cleaned with acetone before each experiment. All of the experiments were conducted at room temperature with argon as a shielding gas and using a fixed powder layer thickness of 50 μm.

A. Single track experiments

The single track experiments were conducted varying laser power from 80 to 200 W in 40 W increments and scanning speed from 100 to 1000 mm/s in 100 mm/s increments. Single tracks

of 7 mm in length were manufactured in batches of 20 tracks (total of 160 samples, 80 samples for each substrate material), and a gap 1 mm wide was left between each track in order to avoid an influence between adjacent tracks. The experiments were repeated twice for each batch of parameter combinations in randomized order.

B. Hatch distance experiments

The hatch distance experiments were conducted using a constant laser power of 200 W, while varying scanning speed from 100 to 700 mm/s in 200 mm/s increments and hatch distance from 50 to 275 μm in 25 μm increments.

C. Manufacturing of Ni-Mn-Ga cuboids

The manufactured cuboid samples were $7 \times 7 \times 1 \text{ mm}^3$ and, in unlike the single track and hatch distance experiments, were manufactured only on an Incoloy 825 substrate because of the compositional similarity (nickel as a primary alloying element) between Ni-Mn-Ga and the used substrate. A bidirectional scan pattern with a 90° rotation of the scanning direction between each layer was used in the experiment.

The parameters were selected such that the cuboids would exhibit different volumetric energy densities, VED (J/mm³):

$$\text{VED} = \frac{P}{v*h*t}, \quad (1)$$

where P is the laser power (W), v is the scanning speed (mm/s), h is the hatch distance (mm), and t is the powder layer thickness (mm).[17]

The variation of VED was performed by varying the scanning speed. Three sets of parameters were selected for manufacturing
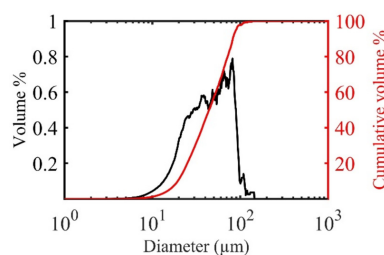

FIG. 1. Measured particle size distribution of the Ni-Mn-Ga powder produced by gas atomization. Obtained parameters from the distribution: $d_{0.1} = 19.4 \, \mu m$, $d_{0.5} = 44.1 \, \mu m$, and $d_{0.9} = 82.2 \, \mu m$.

solid Ni-Mn-Ga samples: a laser power of 200 W, a hatch distance of 100 μm, and three scanning speeds of 300, 500, and 700 mm/s. This yielded VED values of 133 J/mm^3 (v = 300 mm/s), 80 J/mm^3 (v = 500 mm/s), and 57 J/mm^3 (v = 700 mm/s).

D. Measurements

In order to obtain cross-sectional views of the single tracks, the samples were mounted in epoxy and ground with abrasive paper (grain size of 5 μm). The ground samples were consequently electropolished using a pulse-width modulated voltage of 30 V for 40 s at 253 K in an electrolyte solution containing a 3:1 volumetric ratio of ethanol and 60% HNO$_3$. The same grinding procedure was used to prepare the manufactured Ni-Mn-Ga cuboids for compositional analysis by x-ray fluorescence, which was conducted using Oxford Instruments' X-Strata 960. Absolute accuracy of the measurement was 0.3 at. %. An optical polarized light microscope was used to analyze cross sections of the single tracks and the microstructures of the manufactured cuboids.

III. RESULTS AND DISCUSSION

Single track formation and hatching distance in L-PBF are both well-understood phenomena, and therefore this section of the study aims to reflect on the selection of processing parameters for the selected alloy, Ni-Mn-Ga. As Fig. 2 shows, there exist only minor differences in the parameter combinations that produce continuous tracks between the two different substrate materials. In general, the stainless steel substrate seems to produce continuous tracks under a wider range of parameter combinations, while the Incoloy substrate produces continuous tracks within a narrower range of parameters, specifically with lower values of laser power. Analysis of the cross sections of the tracks confirms that increasing laser power or decreasing scanning speed increases the resulting track width and penetration into the substrate (Fig. 3). However, it appears that the dimensions and morphology of the deposited tracks depend strongly on the substrate material used. As can be observed from Figs. 3 and 4, single tracks that were deposited on the Incoloy substrates appear to have a greater propensity toward irregularity and balling. In addition, these tracks are wider and have shallower penetration into the substrate than the tracks deposited on the stainless steel substrates.

In the case of L-PBF, the increased width and balled morphology of the tracks often are caused by the tendency of the molten track to form spheres under insufficient substrate wetting conditions, which reduces the contact zone between the deposited track and the substrate.[18–21] The two primary factors affecting this phenomenon are the volume of the molten material in a track and the wettability of the substrate surface. The observed differences in this study may be explained by three substrate-related factors: (1) possible variations in the thickness of the deposited powder layers, (2) the possible effect of an oxide film on the Incoloy substrates, and (3) differences in thermal properties and chemical compositions of the substrates.

Because deposition of the powder layers and calibration of the substrates were carried out with detail, and because all of the samples deposited on the Incoloy substrates exhibited the same phenomenon, it is suspected that the first potential factor (variations in spread powder layer thicknesses) has only a minor effect on the observed
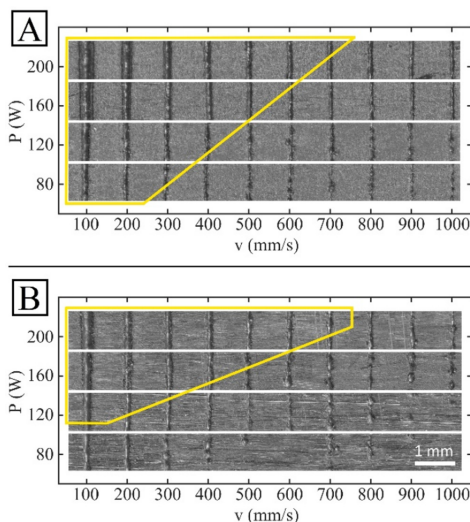

FIG. 2. Top-view of the single tracks produced on (a) stainless steel 316L substrate and (b) Incoloy 825 substrate. Parameter combinations that produce smooth continuous tracks are found within the yellow borders.

phenomenon. By deduction, it is suspected that the phenomenon is at least partly attributable to factor 2, the tendency of the Incoloy alloy to develop a protective film of oxide that might reduce the wettability of the substrate surface. However, the stainless steel develops an oxide film as well, so factor 3 (the differences in thermal and compositional substrate properties) likely contributed to the observed phenomenon. Although both of the substrate materials have the same melting range of 1645–1675 K, the observed phenomenon may be affected by the differences in heat conduction from the melt pool to the substrate. Thermal conductivity and thermal diffusivity of the Incoloy alloy (approximately 11 W/m K and 3.1×10^{-6} m^2/s at room temperature) are lower than of the stainless steel (approximately 15 W/m K and 3.8×10^{-6} m^2/s at room temperature), as calculated from Ref. 22. It is suggested that, in the case of Incoloy substrate, lower thermal diffusivity may decrease the occurring cooling and solidification rates, thus increasing the total volume of the melt pool. The increased volume of the melt pool subsequently drives the balled cross-sectional morphology of the tracks on Incoloy substrates. In addition, differences in chemical compositions of the substrates likely result in different absorptivities, phase change enthalpies and melt pool mass flows that may contribute to the observed phenomena.[19,23,24]

Of note, Fig. 3 also depicts an abrupt increase in the penetration of the tracks into the substrate with high laser power and low scanning speed. This type of abrupt increase in penetration has
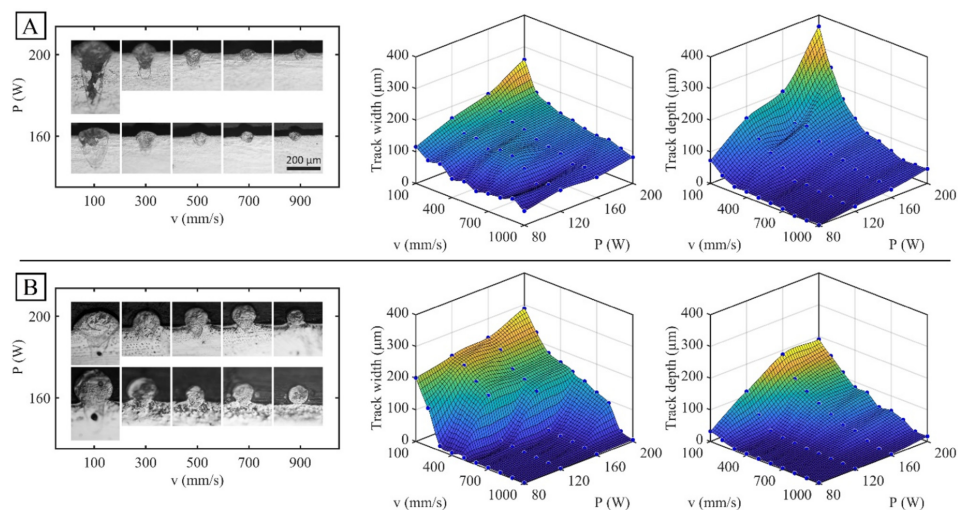
FIG. 3. Evolution of cross sections of the single tracks as a function of applied laser power and scanning speed in the setting of two substrates: (a) stainless steel 316L and (b) Incoloy 825.
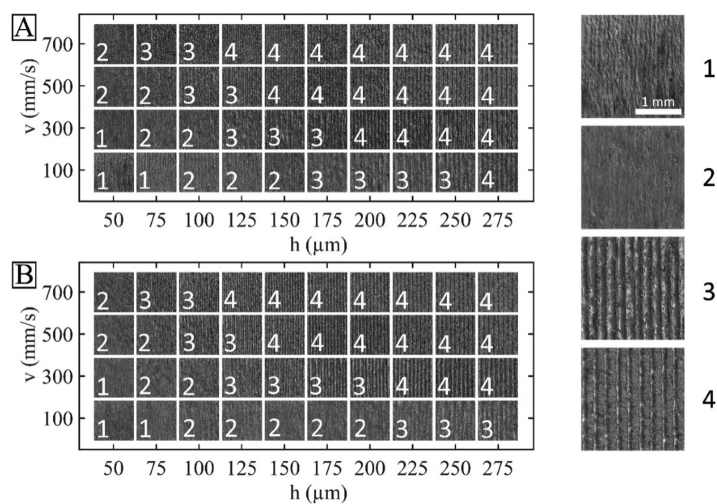

FIG. 4. Results of the hatch distance experiments on two substrates: (a) stainless steel 316L and (b) Incoloy 825. The produced surfaces were categorized as follows: (1) continuous surface with spattering and irregularity, (2) continuous surface with no apparent defects, (3) uneven continuous surface, and (4) noncontinuous surface.

been linked previously to keyhole formation in L-PBF.[25] Although keyhole formation can be useful in certain scanning strategies, such as skin-core scanning, it has also been linked to porosity and dilution. For instance, dilution of gallium has been detected in laser microprocessing and laser drilling of Ni-Mn-Ga by Biffi and Tuissi.[26,27] In the case of Ni-Mn-Ga, the composition of the end-product is critical for the MSM effect, and thus, care should be taken to avoid excessive, uncontrolled vaporization of the material. This is discussed further in the section on Ni-Mn-Ga cuboids.

A. Hatch distance

The results of the hatch distance experiments are presented in Fig. 4. The qualitative analysis of the continuity of the produced surfaces was conducted visually by dividing the surfaces into four different groups. The first group consists of continuous hatched surfaces that exhibit irregularity and spattering, likely caused by excessive heat input during the process. This type of surface was observed only with small hatch distances and low scanning speeds, as an increase in either parameter reduces the aforementioned effects and yields smooth continuous surfaces (second group). If scanning speed or hatch distance is increased further, the overlap between consecutive deposited tracks decreases and the surface becomes visibly rougher (third group). The fourth group consists of surfaces without overlap between consecutive tracks.

Increasing scanning speed while maintaining constant laser power decreases the width of the single track, which in turn decreases the amount of overlap between consecutive tracks when the hatch distance is held constant. Thus, higher scanning speeds require smaller hatch distances to form continuous surfaces. As can be observed in Fig. 3, the Incoloy substrate resulted in wider tracks than the stainless steel substrate, especially at lower scanning speeds. This concurs with the observation from Fig. 4, in which the Incoloy substrate produces continuous surfaces at greater hatch distances, in comparison to the stainless steel substrate, at lower scanning speeds (100 and 300 mm/s).

B. Ni-Mn-Ga cuboids

As was described in the experimental setup, the parameters for manufacturing Ni-Mn-Ga cuboids were selected to produce different values of VED. This parameter selection method had two implications on sample quality that are evident in Figs. 5 and 6. First, there is
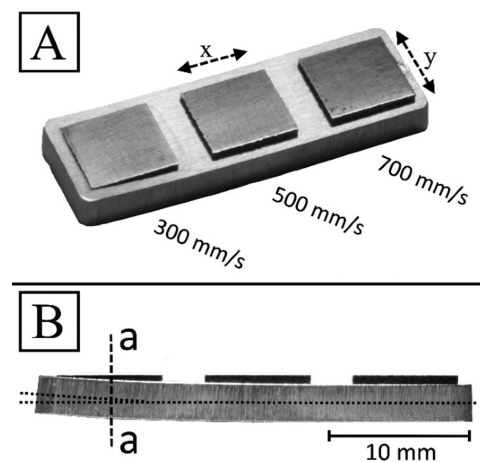

FIG. 5. (a) Manufactured Ni-Mn-Ga cuboids (top-surface prepared for the analysis) on an Incoloy substrate of size 30 × 10 × 2.5 mm³. (b) Observed bending of the substrate due to thermal stresses in the 300 mm/s sample. For the labels of x-axis, y-axis, and the a-a section line, refer to the details in Fig. 7.
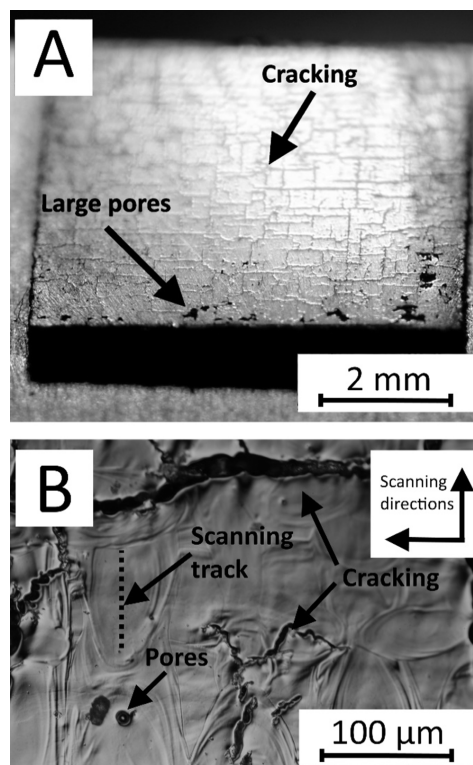

FIG. 6. Micro- and macroscale cracks and porosity in the 700 mm/s sample. (a) Cracks on the surface of the sample. (b) Microscale cracks and porosity.

increased porosity of the sample manufactured at a scanning speed of 700 mm/s (VED = 57 J/mm^3). This is unsurprising given that the laser power and scanning speed produce a track with a width of 111 μm, thus providing only 11% overlap between adjacent tracks when a hatch distance of 100 μm is used. However, this value for track width was obtained from the first layer deposited on the Incoloy substrate, and it may not apply for the consecutive layers. The relative densities of the manufactured cuboids were measured using optical measurement (area fraction of pores and cracks) conducted on pictures obtained with the optical light microscope. The measured relative densities of the samples were 96.8% (300 mm/s sample), 94.9% (500 mm/s sample), and 93.5% (700 mm/s sample).

Based on the microscopic analysis, Ni-Mn-Ga clearly has a tendency to form micro- and macroscale cracks and pores during the L-PBF process. Figure 6 shows that these cracks are narrow, long, oriented along the scanning directions, and in the z-direction of the samples. In fact, the morphology of the cracks closely resembles the cracks observed in Ref. 28. It is likely that the rapid solidification of the material during the L-PBF process induces excessive stresses in the solidifying tracks, thus causing crack formation. Besides the processing parameters used, cracking susceptibility is also affected by the composition of the processed material. Since the

composition cannot be changed for reasons related to the MSM effect, future efforts should be aimed toward reducing cracking susceptibility of the alloy with alternative approaches, such as different scanning strategies with lower values of VED (Refs. 28 and 29) or the usage of substrate preheating.[30] However, this matter, along with the characterization of the resulting microstructures and material properties, requires further research.

The second observation that can be made from Fig. 5(b) is the clear bending of the substrate under the sample manufactured with a scanning speed of 300 mm/s (VED = 133 J/mm^3). In the case of a thin substrate plate, the high thermal expansion and subsequent contraction of the solidifying molten material results in excessive thermal stresses that cause the substrate to bend. On the bent section of the substrate, less powder accumulates during the L-PBF process. With less added material, the bent surface is subjected to a larger amount of repetitive scans, which has caused greater dilution of gallium in bent section of the sample manufactured with a scanning speed of 300 mm/s in comparison to the samples manufactured with higher scanning speeds.

The compositions of the cuboids were measured by x-ray fluorescence analysis with absolute accuracy of 0.3 at. % from the polished surfaces of the samples using an 8×8 point grid scan
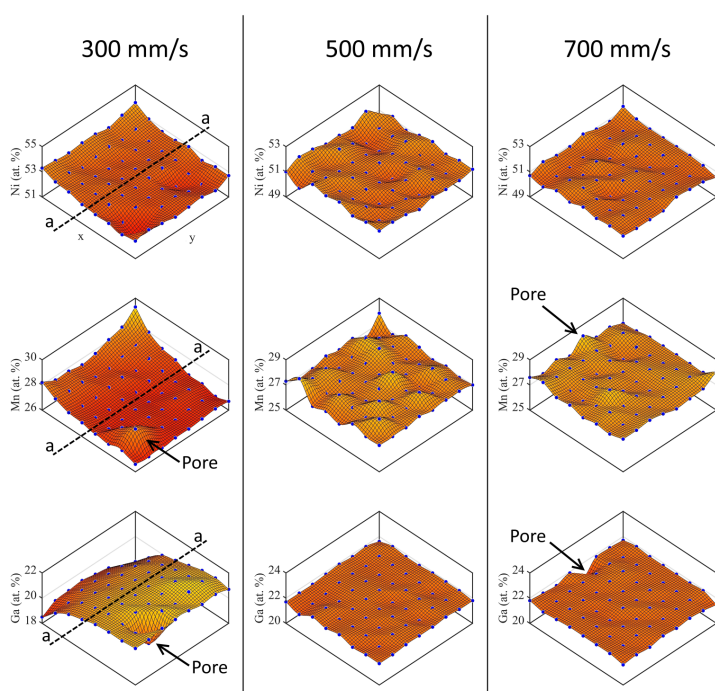

FIG. 7. Surface maps of the measured compositions at different scanning speeds. The a-a section line, the x-axis, and the y-axis correspond to those presented in Fig. 5. Arrows indicate the pores observed on the sample surfaces.

(64 total points of measurement). The distance between consecutive points of measurement along the x-axis and y-axis [Fig. 5(a)] was approximately 850 μm. Thus, the measurement covered almost the entire top-surface of each sample. As can be observed from Fig. 7, the compositions of the bulk samples manufactured with scanning speeds of 500 and 700 mm/s (VED 80 and 57 J/mm^3, respectively) are moderately homogeneous. The average compositions of these samples are Ni 51.0 at. %, Mn 27.2 at. %, and Ga 21.8 at. % for the 500 mm/s sample; and Ni 50.8 at. %, Mn 27.4 at. %, and Ga 21.8 at. % for the 700 mm/s sample. A comparison of these compositions with that of the original powder reveals a decrease in the relative amounts of manganese by 1.3 at. % (500 mm/s sample) and 1.0 at. % (700 mm/s sample) during the L-PBF process. By contrast, the relative amounts of nickel increase by 1.2 at. % (500 mm/s sample) and 1.0 at. % (700 mm/s sample), and the relative amount of gallium increases by 0.1 at. % in both of the samples.

The increase in the relative amount of gallium is much smaller than the increase in the relative amount of nickel. This indicates that besides the loss of manganese, some gallium is lost during the L-PBF process. This is not an unexpected result since the absolute boiling point of gallium is 2477 K, which is only 143 K above the absolute boiling point of manganese (2334 K).[31] It is likely that the high intensity of the laser beam increases the peak temperatures above the boiling points of these alloying elements. The boiling point of nickel is 3186 K,[31] so it is not likely that nickel will be lost without considerable loss of manganese and gallium.

However, as can be observed from Fig. 7, the sample manufactured with a scanning speed of 300 mm/s (VED = 133 J/mm^3) exhibits considerable loss of gallium compared to the two other samples. The 300 mm/s sample (measured from the leveled section) has an average composition of Ni 52.2 at. %, Mn 26.9 at. %, and Ga 20.9 at. %. In comparison to the powder, this represents a 2.4 at. % increase in the relative amount of nickel, while the relative amounts of manganese and gallium decrease by 1.6 and 0.8 at. %, respectively. The increased loss of gallium in the 300 mm/s sample is likely influenced by the keyhole formation in the deposition of the tracks; based on Fig. 3, the track penetration increases rapidly when the scanning speed falls below 300 mm/s (constant laser power of 200 W). The dilution of gallium increases in the bent section of the sample, indicating that the repetitive scanning of the material with high energy densities should be avoided.

In general, dilution in L-PBF is a moderately well-understood phenomenon,[32] and in fact, the majority of the commercial materials are prealloyed in order to produce certain compositions with predetermined sets of parameters. However, the average compositions measured from the samples manufactured with scanning speeds of 500 and 700 mm/s approximated the target composition recommended for manufacturing functional Ni-Mn-Ga elements (Ni 50 at. %, Mn 28 at. %, and Ga 22 at. %, as reported by Saren and Ullakko.[33] However, it must be noted that this study evaluated the material on a large scale and did not investigate possible variations of composition[34] on the scale of single tracks.

IV. CONCLUSION

This study investigated L-PBF of Ni-Mn-Ga powder produced by gas atomization with the aims to establish a preliminary understanding about the suitability of Ni-Mn-Ga for L-PBF and to map the effects of processing parameters on end-product composition. The following conclusions can be drawn from the results, analysis, and discussion presented in this study:

The used substrate material has an effect on resulting morphologies and dimensions of the single tracks. Two different substrate materials, stainless steel 316L and Incoloy 825, were investigated in this study. It was found that depositing tracks on Incoloy substrates results in wider tracks with shallower penetration into the substrate in comparison to the tracks deposited on the stainless steel substrates. It was also found that tracks deposited on the Incoloy substrates were more likely to exhibit irregular and balling morphologies. This phenomenon was suggested to result from the poor wettability of the Incoloy substrate, which could result from the chemical composition, thermal properties, and oxide film development of the alloy.

The processed material displayed long and narrow microscale cracks that were oriented in the build direction of the samples and most likely resulted from the rapid solidification and cooling of the material during L-PBF. To reduce the amount of cracking, this study recommends further parameter optimization, process optimization, and the possible use of a preheated substrate. Further research is required to characterize the resulting microstructures and material properties in the L-PBF of Ni-Mn-Ga.

Processing Ni-Mn-Ga by L-PBF dilutes manganese and gallium from the end-product. Increasing VED was observed to increase the relative amount of vaporized manganese and gallium. The sample with the lowest VED value of 57 J/mm^3 exhibited a drop of 1.0 at. % in the relative amount of manganese, while the sample with the highest VED value of 133 J/mm^3 exhibited drops of 1.6 and 0.8 at. % in the relative amounts of manganese and gallium. Despite the dilution, VED values of 57 and 80 J/mm^3 resulted in cuboid deposition with average compositions of Ni 51.0 at. %, Mn 27.2 at. %, and Ga 21.8 at. %, which approximate the ideal target composition of Ni 50 at. %, Mn 28 at. %, and Ga 22 at. %. It is, therefore, suggested that the dilution of manganese and gallium should be taken into account in the development of the prealloyed powders in the future. Further research is required in order to map compositional differences and distributions of alloying elements on a smaller scale.

REFERENCES

[1] K. Ullakko, "Magnetically controlled shape memory alloys: A new class of actuator materials," J. Mater. Eng. Perform. **5**, 405–409 (1996).

[2] K. Ullakko, J. Huang, C. Kantner, R. O'Handley, and V. Kokorin, "Large magnetic-field-induced strains in Ni2MnGa single crystals," Appl. Phys. Lett. **69**, 1966–1968 (1996).

[3] S. Murray, M. Marioni, S. Allen, R. O'Handley, and T. Lograsso, "6% magnetic-field-induced strain by twin-boundary motion in ferromagnetic Ni–Mn–Ga," Appl. Phys. Lett. **77**, 886–888 (2000).

[4] A. Sozinov, A. Likhachev, N. Lanska, and K. Ullakko, "Giant magnetic-field-induced strain in Ni-Mn-Ga seven-layered martensitic phase," Appl. Phys. Lett. **80**, 1746–1748 (2002).

[5]A. Smith, J. Tellinen, and K. Ullakko, "Rapid actuation and response of Ni–Mn–Ga to magnetic-field-induced stress," Acta Mater. **80**, 373–379 (2014).

[6]A. Hobza, C. Patrick, K. Ullakko, N. Rafla, P. Lindquist, and P. Müllner, "Sensing strain with Ni-Mn-Ga," Sens. Actuators A **269**, 137–144 (2018).

[7]K. Ullakko, L. Wendell, A. Smith, P. Müllner, and G. Hampikian, "A magnetic shape memory micropump: Contact-free, and compatible with PCR and human DNA profiling," Smart Mater. Struct. **21**, 115020 (2012).

[8]A. Smith, A. Saren, J. Järvinen, and K. Ullakko, "Characterization of a high-resolution solid-state micropump that can be integrated into microfluidic systems," Microfluid. Nanofluid. **18**, 1255–1263 (2015).

[9]A. Saren, D. Musiienko, A. Smith, J. Tellinen, and K. Ullakko, "Modeling and design of a vibration energy harvester using the magnetic shape memory effect," Smart Mater. Struct. **24**, 095002 (2015).

[10]M. Chmielus, X. Zhang, C. Witherspoon, D. Dunand, and P. Müllner, "Giant magnetic-field-induced strains in polycrystalline Ni–Mn–Ga foams," Nat. Mater. **8**, 863–866 (2009).

[11]S. L. Taylor, R. N. Shah, and D. C. Dunand, "Ni-Mn-Ga micro-trusses via sintering of 3d-printed inks containing elemental powders," Acta Mater. **143**, 20–29 (2017).

[12]A. Mostafaei, K. Kimes, E. Stevens, J. Toman, Y. Krimer, K. Ullakko, and M. Chmielus, "Microstructural evolution and magnetic properties of binder jet additive manufactured Ni-Mn-Ga magnetic shape memory alloy foam," Acta Mater. **131**, 482–490 (2017).

[13]M. Caputo and C. Solomon, "A facile method for producing porous parts with complex geometries from ferromagnetic Ni-Mn-Ga shape memory alloys," Mater. Lett. **200**, 87–89 (2017).

[14]M. Caputo, A. Berkowitz, A. Armstrong, P. Müllner, and C. Solomon, "4D printing of net shape parts made from Ni-Mn-Ga magnetic shape-memory alloys," Addit. Manuf. **21**, 579–588 (2018).

[15]A. Mostafaei, P. Rodriguez, E. Stevens, and, M. Chmielus, "Sintering regimes and resulting microstructure and properties of binder jet 3D printed Ni-Mn-Ga magnetic shape memory alloys," Acta Mater. **154**, 355–364 (2018).

[16]E. Stevens, J. Toman, K. Kimes, V. Chernenko, A. Wojcik, W. Maziarz, and M. Chmielus, "Microstructural evaluation of magnetocaloric Ni-Co-Mn-Sn produced by directed energy deposition," Microsc. Microanal. **22**, 1774–1775 (2016).

[17]I. Gibson, D. Rosen, and B. Stucker, *Additive Manufacturing Technologies: 3D Printing, Rapid Prototyping, and Direct Digital Manufacturing* (Springer, New York, 2015), p. 498.

[18]I. Yadroitsev and I. Smurov, "Selective laser melting technology: From the single laser melted track stability to 3D parts of complex shape," Phys. Procedia **5**, 551–560 (2010).

[19]I. Yadroitsev, P. Krakhmalev, I. Yadroitsava, S. Johansson, and I. Smurov, "Energy input effect on morphology and microstructure of selective laser melting single track from metallic powder," J. Mater. Process. Technol. **213**, 606–613 (2013).

[20]J. Kruth, L. Froyen, J. Van Vaerenbergh, P. Mercelis, M. Rombouts, and B. Lauwers, "Selective laser melting of iron-based powder," J. Mater. Process. Technol. **149**, 616–622 (2004).

[21]D. Gu and Y. Shen, "Balling phenomena in direct laser sintering of stainless steel powder: Metallurgical mechanisms and control methods," Mater. Des. **30**, 2903–2910 (2009).

[22]F. Cverna and S. D. Bagdade, *ASM Ready Reference: Thermal Properties of Metals (Materials Data Series)* (ASM International, Materials Park, OH, 2002).

[23]A. Gusarov, I. Yadroitsev, P. Bertrand, and I. Smurov, "Model of radiation and heat transfer in laser-powder interaction zone at selective laser melting," J. Heat Transfer **131**, 072101 (2009).

[24]Y. Li, K. Zhou, S. Tor, C. Chua, and K. Leong, "Heat transfer and phase transition in the selective laser melting process," Int. J. Heat Mass Transfer **108**, 2408–2416 (2017).

[25]W. King, H. Barth, V. Castillo, G. Gallegos, J. Gibbs, D. Hahn, C. Kamath, and A. Rubenchik, "Observation of keyhole-mode laser melting in laser powder-bed fusion additive manufacturing," J. Mater. Process. Technol. **214**, 2915–2925 (2014).

[26]C. Biffi and A. Tuissi, "Fiber laser drilling of Ni46Mn27Ga27 ferromagnetic shape memory alloy," Opt. Laser Technol. **63**, 1–7 (2014).

[27]C. Biffi and A. Tuissi, "Micro-processing of NiMnGa shape memory alloy by using a nanosecond fiber laser," Opt. Laser Technol. **78**, 42–49 (2016).

[28]A. Spierings, C. Leinenbach, C. Kenel, and K. Wegener, "Processing of metal-diamond-composites using selective laser melting," Rapid Prototyping J. **21**, 130–136 (2018).

[29]S. Catchpole-Smith, N. Aboulkhair, L. Parry, C. Tuck, I. Ashcroft, and A. Clare, "Fractal scan strategies for selective laser melting of "unweldable" nickel superalloys," Addit. Manuf. **15**, 113–122 (2017).

[30]K. Kempen, B. Vrancken, L. Thijs, S. Buls, J. Van Humbeeck, and J. P. Kruth, in Proceedings of the Solid Freeform Fabrication Symposium, Austin, TX, 12–14 August 2013.

[31]W. Haynes, D. Lide, and T. Bruno, *CRC Handbook of Chemistry and Physics*, 97th ed. (Taylor & Francis Group, Boca Raton, FL, 2017), p. 5652.

[32]S. Das, "Physical aspects of process control in selective laser sintering of metals," Adv. Eng. Mater. **5**, 701–711 (2003).

[33]A. Saren and K. Ullakko, "Dynamic twinning stress and viscous-like damping of twin boundary motion in magnetic shape memory alloy Ni-Mn-Ga," Scr. Mater. **139**, 126–129 (2017).

[34]Y. Guo, L. Jia, B. Kong, N. Wang, and H. Zhang, "Single track and single layer formation in selective laser melting of niobium solid solution alloy," Chin. J. Aeronaut. **31**, 860–866 (2018).

Meet the Authors

Ville Laitinen is a Junior Researcher and a doctoral student at the Material Physics Laboratory of Lappeenranta-Lahti University of Technology, where the majority of his research focuses on laser additive manufacturing of magnetic shape memory alloys, such as the Ni-Mn-Ga alloy. He previously graduated from Lappeenranta-Lahti University of Technology with a specialization in laser materials processing and additive manufacturing.

Antti Salminen is the head of the research group on laser materials processing and additive manufacturing at Lappeenranta-Lahti University of Technology. He is an expert in the manufacturing and design of products with laser-based processes and has more than 200 publications in the field. He has been working on R&D&I of laser materials processing in several national, Nordic, and European research projects in collaboration with the industry. He is a member of the scientific board of Photonics Finland, a board member of the Finnish AM society (FIRPA), vice-chair of the board of Turku Future Technologies, and chair of National Laser Users Club.

Kari Ullakko is the head of the Material Physics Laboratory at Lappeenranta-Lahti University of Technology. He has worked with several universities and companies in various countries and has led a number of international research teams and projects in the Finland, EU, and USA with total funding of over 23×10^6 euros. He has authored over 270 publications and invented 14 patents. His discovery of the magnetic shape memory effect has created a new field of material science, engineering, and technology. His first paper in this field has been cited over 2600 times. He founded two high technology companies in 1997 and 2015.

Publication III

Laitinen, V., Sozinov, A., Saren, A., Salminen, A., and Ullakko, K.
Laser powder bed fusion of Ni-Mn-Ga magnetic shape memory alloy
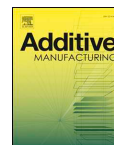
Full Length Article

Laser powder bed fusion of Ni-Mn-Ga magnetic shape memory alloy

Ville Laitinen[a,*], Alexei Sozinov[a], Andrey Saren[a], Antti Salminen[b], Kari Ullakko[a,*]

[a] *Material Physics Laboratory, Lappeenranta-Lahti University of Technology LUT, Yliopistonkatu 34, 53850, Lappeenranta, Finland*
[b] *Laboratory of Laser Processing, Lappeenranta-Lahti University of Technology LUT, Yliopistonkatu 34, 53850, Lappeenranta, Finland*

ABSTRACT

Additive manufacturing (AM) has gone through major developments in the past decade, enabling the rapid manufacture of complex geometries from traditional engineering materials. This study aims to facilitate the development and additive manufacturing of a new generation of fast and simple digital components with integrated magnetic shape memory (MSM) alloy sections that can be actuated by an external magnetic field. Here, we employ a systematic design of experiments (DoE) approach for investigating laser powder bed fusion (L-PBF) of a Ni-Mn-Ga based MSM alloy. The effects of the applied process parameters on the chemical composition and relative density are determined, and detailed investigations are conducted on the microstructural properties of the as-deposited material obtained using optimized parameters. The results show that although the L-PBF of Ni-Mn-Ga is characterized by an ever-present loss of Mn, deposition of Ni-Mn-Ga with a high relative density of 98.3% and a minimal loss of Mn at ∼1.1 at.% is feasible. The material produced in this manner was compositionally near homogenous and, in as-deposited condition, consisted of a mixture of 14 M and non-modulated (NM) martensites. However, combined measurements by the low-field ac magnetic susceptibility method (LFMS) and DSC revealed that the phase transformation of the as-deposited material from martensite to austenite, and vice versa, was broad and occurred in a paramagnetic state. Inspection by SEM revealed a layered microstructure with a stripe-like surface relief that originated from the presence of martensitic twins within the sample. Additionally, AFM and MFM measurements showed that in as-deposited Ni-Mn-Ga, there exists a weak MFM contrast that can be attributed to the twinned martensite having magnetic anisotropy. Overall, L-PBF shows high potential for the production of functional Ni-Mn-Ga based MSM alloys.

1. Introduction

Magnetic shape memory (MSM) alloys are a class of materials that produce stresses and strains when exposed to a magnetic field [1,2]. The Ni-Mn-Ga system is one of the most studied MSM materials. In contrast to the competing giant magnetostrictive materials, which can only strain up to 0.1% [3], single-crystalline Ni-Mn-Ga has been shown to develop strains of 12% [4] and high strain accelerations of 1.6×10^6 m/s^2 [5]. In addition, the fatigue life of the alloy can exceed 2×10^9 cycles [6]. For these reasons, MSM alloys have a high potential for replacing traditional mechanisms and piezoelectric materials in small devices such as fast microactuators [7,8], pumps for the precise dosing of liquids [9–12], sensors [13], and devices for generating energy from mechanical vibrations [14,15]. In addition to single-crystalline Ni-Mn-Ga, foamy polycrystalline Ni-Mn-Ga has been shown to exhibit up to 8.7% recoverable strains [16], thus overcoming grain boundary constraints that typically limit magnetic-field-induced strain (MFIS) in bulk polycrystalline Ni-Mn-Ga. From a manufacturing perspective, foamy polycrystalline Ni-Mn-Ga offers greater feasibility as it can be manufactured using replication casting [16], spark plasma sintering [17] or directional solidification [18]. In addition, additive manufacturing (AM) of near net shape polycrystalline Ni-Mn-Ga parts with controlled porosity has recently attracted interest, as it could enable manufacturing of foam-like structures with complex geometries and fewer limitations on the size of the manufactured object. Therefore, AM could facilitate the development of a new generation of fast and simple digital components by allowing manufacturing of special components integrating MSM alloy sections that can be actuated by an external magnetic field.

Common approaches to the additive manufacturing of Ni-Mn-Ga have focused on 3D ink printing [19,20] using inks with elemental powders or binder jetting [21–27] using pre-alloyed Ni-Mn-Ga pow-

---

ders. Although these processes have proven feasible for producing complex geometries, the binders they use affect the chemical integrity of the manufactured samples as the crystal structure of Ni-Mn-Ga is highly susceptible to compositional variation and impurities [28–30]. Alternatively, the use of binders can be avoided by using additive manufacturing processes based on melting the material, such as laser additive manufacturing (LAM). Previous work on laser additive manufacturing of Ni-Mn-Ga is limited to a few investigations into manufacturing polycrystalline material from pre-alloyed Ni-Mn-Ga powders using a laser based directed energy deposition (L-DED) process [31] and laser powder bed fusion (L-PBF) [32–34]. Both of the aforementioned LAM processes are in principle quite similar. The fundamental difference is that L-DED deposits material layer-by-layer using a laser beam and a dynamical powder or wire feed, while L-PBF is based on selective laser melting of a pre-spread powder layers. In general, L-PBF allows the realization of more complex geometries than L-DED, facilitating greater geometrical design freedom with MSM alloys. However, L-PBF is also characterized by a rapid heating and cooling of the processed material. Previous research on manufacturing Ni-Mn-Ga using L-DED [31], L-PBF [34] and other rapid cooling processes, such as melt spinning [35,36] or gas atomization [37], implies that the material properties, such as the microstructure, compositional homogeneity and magnetic properties, are impacted by this rapid cooling. Although the initial material properties can be retained to some extent through post-process annealing [32,34], it is important to understand the processing conditions and their effect on the properties of the processed material in as-deposited condition.

From the perspective of process development, the ability to control composition, microstructure and porosity is essential for obtaining MFIS in polycrystalline Ni-Mn-Ga. Although porous material can be easily produced in L-PBF as a defect, the morphology, size and distribution of such pores are nearly uncontrollable. Therefore, the ability to obtain a fully dense material is fundamental to avoid possible issues with mechanical properties, such as breaking of the tensile rods during sample preparation in [34]. Hence, process development for L-PBF of Ni-Mn-Ga should strive towards production of material with a high relative density and subsequent introduction of a foam-like structure with controlled porosity, for example, in a form of a fine lattice structure [32,39]. Previous investigations on the L-PBF of Ni-Mn-Ga have demonstrated the feasibility of obtaining 93.5–96.8% [33] and 88.5–92.9% [34] densities for the as-deposited material. However, the aforementioned studies show that some Mn and Ga may be lost in the process and that increasing the relative density may come at the cost of increased Mn loss. In the case of Ni-Mn-Ga, loss of Mn during the L-PBF process is expected because of the high vapor pressure and low boiling temperature [38] of Mn in comparison to the other elements in the alloy.

For these reasons, systematic experimental research is of paramount importance to understand the laser–material interactions in the L-PBF of Ni-Mn-Ga and the effects of the process parameters on the properties of the material in as-deposited condition. The aim of this study is to employ a series of Box–Behnken based experimental designs to determine the effects of the process parameters on the composition and relative density of Ni-Mn-Ga deposited by L-PBF and to identify the optimal processing conditions for obtaining high-density samples with minimal Mn loss. Besides process optimization, this study aims to determine whether L-PBF can produce polycrystalline Ni-Mn-Ga with appropriate properties in as-deposited condition to later obtain MFIS in post-process heat-treated material. Additionally, this study aims to identify some of the required post-processing steps for the as-deposited material. For this purpose, the optimized process parameters are subsequently used for the deposition of a series of Ni-Mn-Ga samples on a compositionally similar Ni-Mn-Ga substrate, and detailed investigations are conducted on the compositional, microstructural and crystal structures of the material in as-deposited condition.

2. Material and methods

2.1. Laser powder bed fusion system

All samples were manufactured using an in-house built L-PBF system that utilizes an IPG single mode ytterbium fiber laser (λ = 1075 nm, maximum P_{avg} = 200 W) as a primary heat source for melting. Measurement using a Primes MicroSpotMonitor showed that the laser produced a beam with a near Gaussian power distribution, a focal point diameter of ~82 μm, a Rayleigh length of 3.24 mm, and a beam parameter product of 0.53 mm mrad. The system was equipped with a semi-automated build platform system with a slot for detachable substrate pieces. Repeatability of the powder layer deposition from patch to patch during the experiments was ensured by a delicate mechanical calibration of the re-coater blade of the system with each substrate before the sample deposition.

2.2. Ni-Mn-Ga powder

The used Ni-Mn-Ga powder was prepared by gas atomization in an inert argon atmosphere. The volume-weighted particle size distribution ($d_{0.1}$ = 19.4 μm, $d_{0.5}$ = 44.1 μm, and $d_{0.9}$ = 82.2 μm), as shown in Fig. 1a, was determined for the powder using the automated optical particle analyzer Morphologi G3S by Malvern Panalytical Ltd. The powder was further evaluated using a Scanning Electron Microscope (SEM) Hitachi SU3500. As shown in Fig. 1b, the powder consisted mainly of spherical particles, although some irregularly shaped satellites and spatters were observed within the powder. The powder composition, as shown in Table 1, was measured with an absolute accuracy of 0.3 at.% using the X-ray fluorescence (XRF) analyzer X-Strata 960 (Oxford Instruments) and a reference sample of known composition. Although composition of the initial powder corresponds to five-layered modulated (tetragonal, 10 M) martensite structure, X-ray diffraction (XRD) of the powder showed mostly an austenitic structure (cubic, Heusler type of order) with two additional low intensity peaks originating from the 10 M martensite at angles of 50.26° and 52.73°. Additionally, measurements by differential scanning calorimetry (DSC) and low-field ac magnetic susceptibility method (LFMS) confirmed that
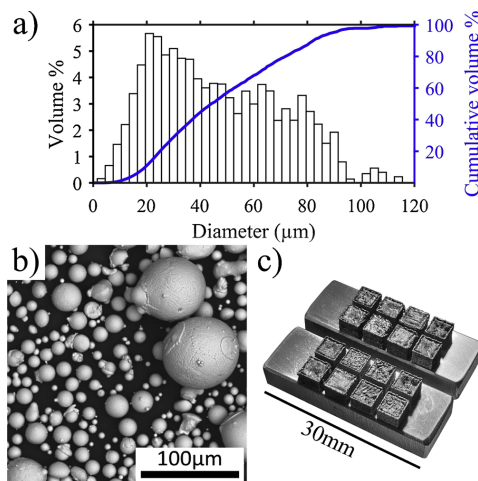

Fig. 1. (a) Particle size distribution of the used Ni-Mn-Ga powder; (b) SEM image of the powder; (c) two patches of the deposited samples on stainless steel substrates.

Table 1
Compositions of the used powder and substrates. All values arepresented in at. %.

Sample	Si	Cr	Mn	Fe	Ni	Ga	Mo
Ni-Mn-Ga powder	–	–	28.5	–	49.8	21.7	–
316 L substrates	1.0	19.0	1.7	68.6	9.6	–	0.2
Ni-Mn-Ga substrate	–	–	26.0	–	50.1	23.9	–

Table 2
Summary of the used process parameters.

Parameter	Series 1	Series 2	Optimized samples
Powder layer thickness (μm)	60	60	60
Laser power (W)	50, 85, 120	100, 150, 200	200
Scanning speed (mm/s)	50, 125, 200	150, 300, 450	450
Hatch distance (μm)	50, 75, 100	50, 75, 100	100
Volume energy density (J/mm^3)	56-567	49-333	74

the powder was austenitic at ambient temperature. Corresponding observations about gas atomization have been reported in [37].

2.3. Design of the experiments

The process parameters used in this study are summarized in Table 2. All samples were deposited at ambient temperature without substrate preheating and in an inert argon atmosphere using a constant powder layer thickness (t, mm) of 60 μm and a bidirectional scanning strategy with a 60° turn of the scanning direction from layer-to-layer. The hatched region of each sample was surrounded by a single contour scan with a 90% overlap with the hatched area. The same laser and scanning parameters were used for both hatched and contour scans of the samples. All deposited samples were cuboids with the dimensions $3.5 \times 3.5 \times 3.5$ mm^3. The cuboids were orientated on the substrate in two rows so that the x–y hatch directions of the L-PBF system were aligned with the side faces of the cuboids. The laser beam was focused on the surface of the powder bed during sample deposition.

Selection of the process parameters for initial process optimization was carried out using two partially overlapping Box–Behnken based experimental designs (series 1 and 2) with three predetermined levels for each of the three varied parameters: laser power (P, W), scanning speed (v, mm/s), and hatch distance (h, mm). The volume energy density (*VED*) of the deposited samples was calculated using Eq. 1 and ranged from 49 to 567 J/mm^3.

$$\text{VED} = \frac{P}{v*h*t} \tag{1}$$

The initial samples (Fig. 1c) were deposited on austenitic 316 L stainless steel substrates that were prepared from a cold rolled sheet by laser cutting and grinding to the final dimensions of $10 \times 30 \times 5$ mm^3. Using stainless steel as a substrate material provided a cost-effective approach for the initial parameter optimization. The composition of the 316 L substrates, as shown in Table 1, was measured by energy dispersive spectroscopy (EDS) using a Hitachi SU3500 SEM with a relative accuracy of 5%. The composition of the 316 L substrates was within the limits set by standardization. The samples were deposited in patches of eight samples on four substrates using a randomized sample order. Some parameter combinations were repeated to allow an estimation of the sample deposition reliability. A 1.2 mm wide gap was left between each sample. To minimize the thermal interaction between samples during deposition, a short delay of 60 s was set between melting the same layer of each sample.

In order to minimize the possible influence of alloying elements of

the substrate on sample quality, a single patch of four samples was deposited on an austenitic single-crystalline Ni-Mn-Ga substrate using optimized parameters obtained from the initial experiments on stainless steel substrates. The Ni-Mn-Ga substrate was a disk (Ø 22 mm, thickness ~4.1 mm) cut from an oriented single-crystalline bar prepared by AdaptaMat Ltd. The composition of the Ni-Mn-Ga substrate, shown in Table 1, was measured using the aforementioned XRF analyzer. A 5 mm gap was left between each sample to minimize thermal interaction between samples during deposition.

2.4. Sample preparation and analysis

The samples deposited on stainless steel substrates were first cut perpendicular to the build direction from a height of ~2.5 mm in build direction using a high precision wire saw (Princeton Scientific Corporation, WS2). The samples were consecutively ground incrementally using SiC abrasives and then mechanically polished using napless cloth and diamond paste with 3 and 0.04 μm grain sizes. The relative density of each deposited sample was determined optically by measuring the area fraction of pores in the polished sections of the samples using a customized optical microscope (Zeiss Axio Scope.A1) in combination with the open source image processing software ImageJ. The contour scan area of each sample, ~200 μm from the sample edge toward the center of the sample, was ignored in the measurement. The results were averaged from three consecutive cycles of sample preparation and measurement. Between each measurement, ~0.5 mm of material was removed in the build direction of the sample. Although sectioning and inspection of the samples along build direction revealed minor layering of the lack-of fusion pores on inter-layer boundaries, these pores were generally large, up to several hundred μm in diameter, and often spanned across multiple deposition layers. The inspection did not reveal clear layering of the spherical gas pores. Thus, the porosity measurements were considered representative.

The overall compositions of the samples were determined by averaging the results of the XRF measurements (6×6 grid) obtained from polished sections of the sample top surfaces at a height of ~2.5 mm from the substrate surface in build direction of the sample. An inspection of the sample-substrate interface by EDS confirmed that melting of the substrate had occurred and that there was compositional mixing between the stainless steel substrates and the deposited samples. However, the samples with the largest amount of compositional mixing showed only minor amounts of chromium and iron propagated at a length of ~300 μm from the sample–substrate interface in the build direction of the sample, thus the compositional mixing was limited to the first few layers of the sample. Therefore, compositional mixing between the stainless steel substrates and the deposited samples was ruled out as a potential source of error in the XRF measurements. The relative accuracy of the EDS measurement from point to point was ~1%.

Response surface methodology was used in combination with analysis of variance (ANOVA) for the approximation and visualization of the effects of the varied process parameters on the relative density and composition of the as-deposited samples. Mn content (at.%) of the samples was used as a performance variable to represent composition during modeling. A quadratic (2nd degree) model was used for both relative density and Mn content to avoid overfitting. A cut-off value for the statistical significance of the results was determined, whereby factors with a p-value < 0.01 were considered statistically significant and the factors with a p-value ≥0.01 were considered statistically insignificant.

The samples manufactured on the Ni-Mn-Ga substrate were first separated from the substrate by the high precision wire saw and then ground incrementally using SiC abrasives. The samples were subsequently electropolished using a constant voltage of 12 V at 253 K in an electrolyte solution containing a 3:1 volumetric ratio of ethanol to 60% HNO$_3$. The relative densities of the deposited samples were determined

using the aforementioned optical measurement technique, whereas the overall composition and homogeneity of each sample were evaluated using EDS and XRF. Differential scanning calorimetry (DSC) was conducted using a PerkinElmer DSC4000 with a measurement temperature range of 303–393 K to determine the phase transformation and Curie temperatures of the L-PBF sample, the initial powder and the Ni-Mn-Ga substrate. The DSC measurement was complemented with the low-field ac magnetic susceptibility method (LFMS) to confirm the Curie temperatures of the aforementioned samples. The LFMS measurement was conducted with a temperature range of ∼303–393 K using an in-house developed setup. The XRD analysis of the samples and the initial powder was implemented using a PANalytical Empyrean diffractometer (Co tube, λ = 0.17890 nm) equipped with a hybrid monochromator, a PIXcel3D-Medipix3 detector, and a heating stage. Microstructural analysis of the samples was implemented using optical microscopy and SEM. The volume-weighted distribution and average grain size of a sample was determined with the linear intercept method using a MATLAB-based program originally developed in [40] by first manually tracing the grain boundaries from the obtained SEM images. Atomic force microscopy (AFM) and magnetic force microscopy (MFM) measurements were implemented using a Park Systems XE7 for the characterization of the observed martensitic twins within the as-deposited samples.

3. Results and discussion

The used combinations of the process parameters in series 1 and 2 with the corresponding relative densities and average compositions are shown in Table 3, whereby the error shown represents the standard deviation of the measurement of each sample. As can be observed from the ANOVA in Table 4, both fitted quadratic polynomial models are statistically significant (p < 0.01) and can thus provide an adequate approximation within the applied range of variables. Additionally, the relatively high correlation coefficients obtained for each of the models for relative density ($R^2 = 0.855$, $R^2_{pred} = 0.669$, $RMSE = 2.86$) and Mn content ($R^2 = 0.927$, $R^2_{pred} = 0.786$, $RMSE = 0.82$) indicate moderate consistency between the experimental and predicted values. It is

expected that the accuracy of each model is limited to the area between the samples due to the used experimental design and the simple quadratic polynomial fit. However, as the models were only intended for the initial parameter optimization and to study the effects of the applied process parameters, this was considered a sufficient approximation to the made observations and provided a good basis for further process optimization using the aforementioned L-PBF system. The contour plots of the two fitted models in Fig. 2 show the effects of applied laser power, scanning speed and hatch distance on the relative density and Mn content of the as-deposited samples.

An inspection of the contour plots of relative density in Fig. 2 reveals that for each used value of hatch distance, there exists a clear area of optimum processing conditions where the highest relative densities are achieved. Additionally, the morphology of the observed pores within the samples appears to be affected by their position relative to this area of high relative density. Examples of observed sample sections with different porosities are presented in Fig. 3. Based on previous scientific literature on the topic [41–46], the consolidation of powder and the consequent densification of the deposited sample in L-PBF can be simplified as follows. At optimal *VED* conditions, the highest relative densities are achieved through the optimal combination of the formation of single tracks with sufficient penetration into the underlying material and the stacking of the consecutive adjacent tracks. A variation of the process parameters from optimum toward low *VED* conditions leads to the formation of lack-of-fusion pores with irregular morphologies through an incomplete or non-existent connection of the produced tracks to consecutive tracks or layers. Additionally, balling and other phenomena connected to the instability of single track formation likely contribute to pore formation. If the process parameters are varied from the optimum toward high *VED* conditions, the density of the sample begins to decrease due to the formation of spherical gas pores as excessive laser power with a low scanning speed may shift the process from conduction mode melting to keyhole melting [41,42].

The described evolution of the processing conditions is clearly observable in Fig. 2. Here, the samples with irregular pores are primarily located at the bottom right side and the samples with spherical pores are located at the top left side along the scanning speed–laser power

Table 3

Relative compositions and densities of the as-deposited samples. Presented errors correspond to standard deviations of the measurements.

Sample							
h (µm)	P (W)	v (mm/s)	VED (J/mm³)	Ni (at.%)	Mn (at.%)	Ga (at.%)	Density (%)
50	50	125	133	51.6 ± 0.71	27.1 ± 0.85	21.2 ± 0.30	75.2 ± 4.8
50	85	50	567	64.6 ± 2.67	19.1 ± 3.93	16.3 ± 1.55	86.2 ± 2.8
50	85	200	142	51.2 ± 1.01	27.4 ± 1.29	21.3 ± 0.42	87.7 ± 1.6
50	100	300	111	51.9 ± 1.33	26.7 ± 1.68	21.4 ± 0.54	79.4 ± 2.1
50	120	125	320	58.7 ± 1.50	21.0 ± 2.51	20.3 ± 1.13	95.2 ± 0.9
50	150	150	333	59.1 ± 0.83	19.9 ± 0.83	21.0 ± 0.20	92.7 ± 2.1
50	150	450	111	51.7 ± 0.44	26.5 ± 0.48	21.9 ± 0.11	93.7 ± 0.4
50	200	300	222	56.8 ± 0.81	21.8 ± 0.78	21.4 ± 0.08	96.2 ± 0.5
75	50	50	222	52.7 ± 0.92	26.6 ± 1.21	20.8 ± 0.60	81.0 ± 3.2
75	50	200	56	50.3 ± 0.29	27.9 ± 0.42	21.8 ± 0.17	72.6 ± 5.2
75	85	125	151	52.6 ± 1.50	26.3 ± 1.58	21.2 ± 0.50	91.2 ± 1.5
75	100	150	148	53.6 ± 1.24	25.0 ± 1.33	21.4 ± 0.24	94.9 ± 0.6
75	100	450	49	50.8 ± 0.38	27.4 ± 0.38	21.8 ± 0.10	83.1 ± 3.7
75	120	50	533	64.2 ± 1.71	17.2 ± 2.06	18.6 ± 1.09	92.6 ± 0.5
75	120	200	133	52.5 ± 0.67	26.1 ± 0.70	21.4 ± 0.14	97.8 ± 0.3
75	150	300	111	51.9 ± 0.86	26.4 ± 0.99	21.7 ± 0.24	91.8 ± 2.4
75	200	150	296	58.3 ± 1.00	20.6 ± 0.96	21.0 ± 0.13	93.7 ± 0.9
75	200	450	99	51.6 ± 0.44	26.7 ± 0.49	21.7 ± 0.12	98.7 ± 0.5
100	50	125	67	50.0 ± 0.62	28.0 ± 0.59	22.0 ± 0.58	76.0 ± 2.7
100	85	50	283	56.2 ± 1.96	24.4 ± 2.96	19.4 ± 1.24	93.5 ± 0.9
100	85	200	71	50.3 ± 0.56	28.1 ± 0.71	21.6 ± 0.30	93.9 ± 2.3
100	100	300	56	50.8 ± 0.43	27.4 ± 0.41	21.8 ± 0.13	84.2 ± 1.8
100	120	125	160	53.7 ± 1.18	25.4 ± 1.35	20.9 ± 0.44	96.8 ± 0.6
100	150	150	167	53.4 ± 0.77	25.2 ± 0.89	21.4 ± 0.26	94.2 ± 1.1
100	150	450	56	50.6 ± 0.24	27.6 ± 0.27	21.8 ± 0.09	94.8 ± 1.1
100	200	300	111	51.7 ± 0.58	26.7 ± 0.75	21.6 ± 0.19	98.5 ± 0.3

Table 4
ANOVA for the quadratic polynomial models of relative density and Mn content.

Source	Relative density (%)					Mn content (at.%)				
	DF	Adj SS	Adj MS	F-value	P-value	DF	Adj SS	Adj MS	F-value	P-value
Model	9	1257.04	139.67	10.49	0.000	9	223.485	24.832	22.73	0.000
P	1	1024.75	1024.75	76.93	0.000	1	62.910	62.910	57.58	0.000
h	1	32.37	32.37	2.43	0.139	1	25.094	25.094	22.97	0.000
v	1	97.48	97.48	7.32	0.016	1	119.637	119.637	109.50	0.000
P^2	1	314.14	314.14	23.58	0.000	1	0.187	0.187	0.17	0.685
h^2	1	8.07	8.07	0.61	0.448	1	0.260	0.260	0.24	0.632
v^2	1	12.57	12.57	0.94	0.346	1	29.358	29.358	26.87	0.000
$P*h$	1	1.20	1.20	0.09	0.768	1	12.374	12.374	11.33	0.004
$P*v$	1	116.81	116.81	8.77	0.009	1	10.756	10.756	9.85	0.006
$h*v$	1	0.39	0.39	0.03	0.866	1	12.088	12.088	11.06	0.004
Error	16	213.12	13.32	–	–	16	17.481	1.093	–	–
Total	25	1470.16	–	–	–	25	240.965	–	–	–

axis in comparison to the area of high relative density. Additionally, there exist samples at intermediate positions with low values of scanning speed that possess pores of both morphologies, which implies the presence of imbalanced processing conditions, whereby keyhole melting occurs alongside single track instability or the poor stacking of consecutive tracks. In this study, the observed lack-of-fusion pores were up to several hundred μm in diameter, whereas the observed spherical pores were noticeably smaller, generally < 70 μm in diameter. Thus, the larger standard deviation of relative density in the lower-density samples was suspected to attribute to the highly irregular morphology of the lack-of-fusion pores. The lack of high relative density samples at low laser power and scanning speed values implies that the parameter spacing of these values in the used experimental design may have been too large in this region. Taking additional samples into account and possibly using narrower spacing between the parameter levels in this region could improve the accuracy and extent of the model. Additionally, minor amounts of cracks were observed in some of the samples, which was expected based on the previous research by [33]. However, the cracking was not observed with the optimized parameters and is thus not addressed further in this study. Further research on the topic is required.

Although there appears to be an overall exchange between the increasing relative density and the decrease of the fraction of Mn, the effects of the applied process parameters on relative density and Mn content are remarkably different. It can be observed from the contour plots of Mn content in Fig. 2 that the marked levels of *VED* are almost parallel with the contour lines of Mn content, which implies that *VED* may be used as an explanatory parameter for composition in the present L-PBF system. However, Fig. 2 shows that *VED* generally does not provide a sufficient approximation of the resulting relative density of a sample. This is expected because *VED* is essentially a thermodynamic parameter that does not describe well the complex physical phenomena connected with densification in L-PBF. An inspection of the p-values in Table 4 reveals that the statistically significant parameters (in order of significance) for relative density were P, P^2, $P*v$ and v, whereas the statistically significant parameters for Mn content were v, P, v^2, h, $P*h$, $h*v$, and $P*v$. Thus, it appears that relative density is mainly affected by the applied laser power and its product with scanning speed, whereas Mn content is significantly influenced by most of the applied parameters. This confirms the previous statement about *VED*. In particular, applied hatch distance had a relatively large impact on Mn content, whereas it appeared to have only an imperceptible impact on relative density. In fact, the effect of hatch distance is noticeable in Fig. 2 as a shift of the area of high relative density towards lower values of scanning speed when hatch distance is increased. This is expected because larger values of hatch distance require wider tracks to obtain a sufficient overlap from track to track. Track width is primarily influenced by the applied laser power and scanning speed, which explains the

significance of these parameters on the formation of relative density in L-PBF.

Fig. 4 shows that the samples with low values of *VED* are compositionally close to the initial powder, exhibiting only a ~0.5-1.0 at.% decrease in the fraction of Mn, and overall the Mn content appears to saturate towards the Mn content of the initial powder when *VED* is decreased. The slight decrease of Mn content with *VED* values under ~50 J/mm³ in Fig. 2 occurs due to the model inaccuracy, as this value represents the samples with the lowest *VED* in this study. However, Fig. 4 shows a distinctive decrease in the fraction of Mn, while a corresponding increase in the fraction of Ni can be observed simultaneously when *VED* is increased above ~75-100 J/mm³. Additionally, a decrease in the fraction of Ga is observed when *VED* is increased above ~200-250 J/mm³. The presented evolution of the composition is in good agreement with the results presented in previous studies [33,34] and is linked to the vaporization of Mn and Ga during the L-PBF process. A second observation that can be made from Table 3 and Fig. 4 is that the standard deviation of the measured composition increases toward the high *VED* samples. As supported by previous observations [47], the reason for the observed phenomenon may be connected to localized segregation or a selective vaporization of certain elements on a small scale when *VED* is increased. However, the low *VED* samples near ~50 J/mm³ exhibited standard deviations of the composition within the approximate range of the accuracy of the measurement. These results suggest that, with the present L-PBF system, high-density Ni-Mn-Ga samples can be deposited with minimal loss of Mn by avoiding combinations of process parameters that produce *VED* values above ~75 J/mm³. However, a minimum amount of ~0.5-2.0 at.% of Mn was lost with all parameter combinations, which implies that an over-alloying of Mn into the initial powder is required to counteract the vaporization of Mn during the L-PBF process.

As determined from the fit presented in Fig. 2, the highest relative density of a sample within the area covered by the model is obtained with a minimal value of *VED* by using a hatch distance of 100 μm, a scanning speed of 450 mm/s and a laser power of 200 W. The L-PBF samples deposited on the Ni-Mn-Ga substrate using the aforementioned combination of process parameters were 98.3% dense and had an overall composition of 50.9 at.% Ni, 27.4 at.% Mn, and 21.7 at.% Ga in as-deposited condition. Thus, the samples exhibited a 1.1 at.% decrease in the fraction of Mn and a corresponding increase in the fraction of Ni in comparison to the initial powder. The fraction of Ga remained the same compared to the initial powder, as expected based on the samples deposited on the stainless steel substrates. An EDS analysis of a sample was carried out to determine whether any segregation or scattering of the chemical elements had occurred. Fig. 5 shows the image result of an area scan based EDS measurement of a sample deposited on the Ni-Mn-Ga substrate obtained from a section along the build direction of the sample. Although the figure features a boundary separating two
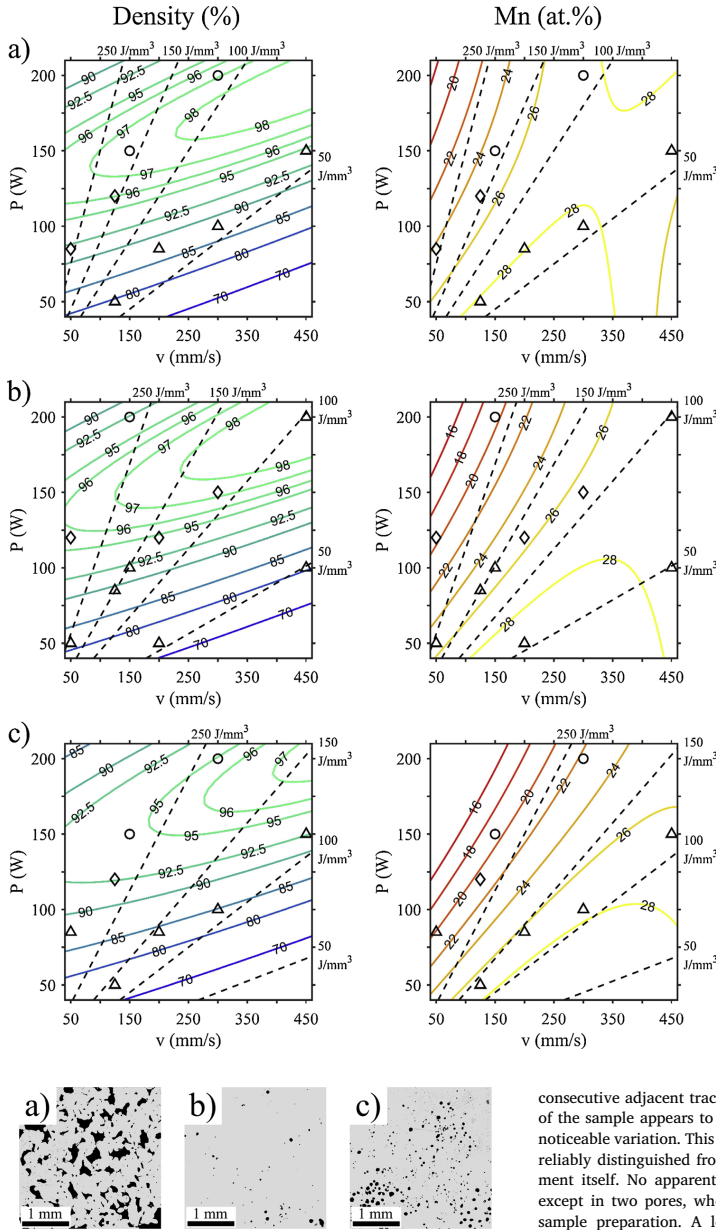
Fig. 2. Effect of applied laser power and scanning speed on relative density ($R^2 = 0.855$, $R^2_{pred} = 0.669$, $RMSE = 2.86$) and Mn content ($R^2 = 0.927$, $R^2_{pred} = 0.786$, $RMSE = 0.82$) of as-deposited Ni-Mn-Ga samples. (a) $h = 100\,\mu m$; (b) $h = 75\,\mu m$; (c) and $h = 50\,\mu m$. For reference, locations of four selected *VED* levels has been marked using black dashed lines. Sample locations have been marked with symbols that correspond to the type of porosity observed within the sample: ○ gas porosity, △ irregular shaped lack-of-fusion pores, and ◇ combination of the two. For reference, see Fig. 3.

Fig. 3. Examples of sample sections with different porosities observed by optical microscope. (a) a sample with irregular shaped lack-of-fusion pores ($P = 50$ W, $v = 125$ mm/s, $h = 100\,\mu m$); (b) a high-density sample with a low amount of gas pores ($P = 200$ W, $v = 300$ mm/s, $h = 100\,\mu m$); (c) a lower density sample with an increased amount of gas pores ($P = 150$ W, $v = 150$ mm/s, $h = 50\,\mu m$).

consecutive adjacent tracks and the underlying layer, the composition of the sample appears to be moderately homogenous with only minor noticeable variation. This detected variation is so small that it cannot be reliably distinguished from the noise and uncertainty of the measurement itself. No apparent oxidation is observable within the section, except in two pores, whereby the oxygen likely originated from the sample preparation. A low amount of apparent element scattering within the as-deposited sample is considered beneficial for obtaining a homogenous material after compositional ordering heat-treatment.

Fig. 6 shows the results of the DSC and LFMS measurements of an L-PBF sample. For reference, the measurements were also carried out on the initial powder and the Ni-Mn-Ga substrate. The phase transformation and Curie temperatures of the samples were determined from the
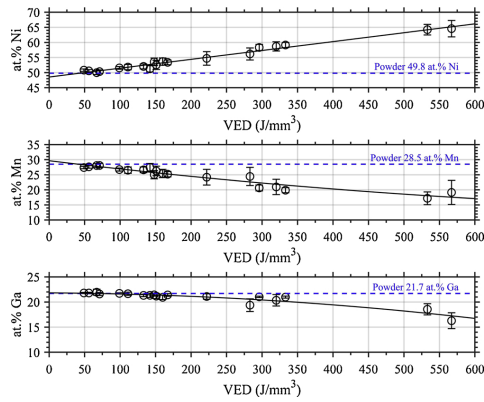
Fig. 4. Effect of the applied *VED* on chemical composition averaged from XRF measurements on ground and polished top-surfaces of as-deposited Ni-Mn-Ga samples.
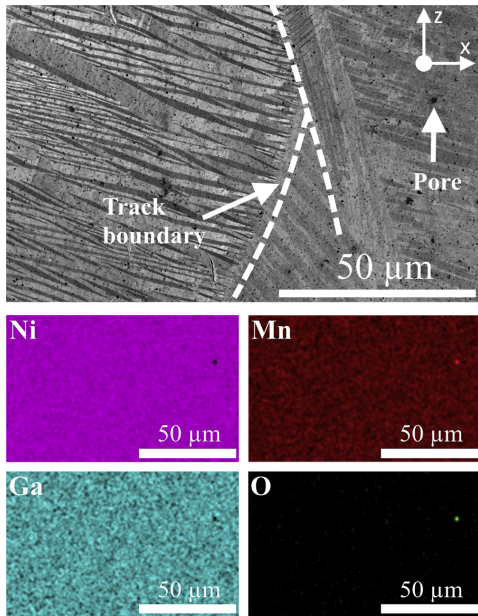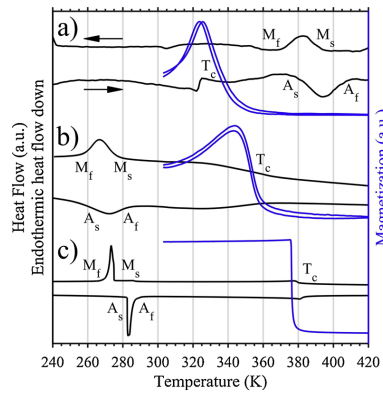

Fig. 6. DSC (heat flow versus temperature) and LFMS (magnetization versus temperature) curves obtained for: (a) a sample deposited by L-PBF; (b) initial Ni-Mn-Ga powder; (c) a single-crystalline Ni-Mn-Ga used as a substrate.

Fig. 5. EDS image of a section along the build direction of an L-PBF sample as-deposited on a compositionally similar Ni-Mn-Ga substrate.

obtained curves and are further summarized in Table 5. Although previous research [34] on the L-PBF of Ni-Mn-Ga reported the paramagnetic behavior of as-deposited material, the samples deposited by L-PBF in this study showed a clear ferromagnetic behavior during measurement by LFMS. This difference in magnetic behavior may be linked to the notable compositional difference between the used Ni-Mn-Ga alloys in [34] and this study or other differences in the processing conditions. However, LFMS signals obtained from both the initial powder and the L-PBF sample implies an inferior magnetization

compared to the single-crystalline Ni-Mn-Ga used as a substrate. For the sample deposited by L-PBF, the transformation from martensite to austenite, and vice versa, occurred in a paramagnetic state. Additionally, the transformation and Curie temperatures for both the initial powder and the L-PBF sample were broad, in the range of ~ 20-30 K, and there exists a large deviation from previously reported values [28] for a similar alloy composition. A difference in transformation and Curie temperatures between the initial powder and the L-PBF sample was expected because the as-deposited sample exhibited a loss of Mn in comparison to the initial powder. Additionally, the powder exhibited austenitic structure of the crystal lattice at ambient temperature due to the residual internal stresses created by the gas atomization process [37]. It has been previously suggested for the Ni-Mn-Ga alloy deposited by LAM [31,34] that the shift and broadening of the main transformation peaks could correspond to minor compositional variations, lattice strains, or the presence of multiple phases or martensite structures. It is expected that the initial powder and the L-PBF sample would recover more typical values for transformation and Curie temperatures after compositional and structural ordering heat-treatments [32,34,37]. However, the results of the DSC and LFMS measurements imply that the as-deposited sample was almost fully martensitic at ambient temperature. Measurements by SEM and XRD later confirmed this observation.

Fig. 7 shows the X-ray diffractograms and identified peaks obtained from a sample as deposited by L-PBF, with a diffractogram obtained from the initial Ni-Mn-Ga powder presented for reference. To increase ration of peak intensities to background level, scanning line mode of 2D detectors and low background single-crystal Si-111 were used to record the pattern for of the L-PBF sample at 298 K. The diffraction pattern originating from the Si-111 holder is presented in Fig. 7 also, and the peaks originating from it were disregarded in the analysis of the diffraction of the L-PBF sample. Approximate lattice parameters were determined for the identified phases in both the initial powder and the L-PBF sample and are presented in Table 6. After a detailed inspection of the obtained diffractions from the L-PBF sample at 298 K and 433 K, it can be concluded with high confidence that the crystal structure of the as-deposited L-PBF sample at ambient temperature was a mixture of 14 M and NM martensites, as supported by the following arguments. At 433 K, the L-PBF sample exhibits an austenitic crystal structure – compare the diffractions obtained for the initial powder and the L-PBF sample at 433 K. When the sample is cooled to 298 K, the corresponding austenite peaks disappear and a new pattern emerges. Therefore, diffraction peaks from the L-PBF sample at 298 K must originate from one

Table 5

Phase transformation and Curie temperatures of an as-deposited L-PBF sample, the initial powder and the Ni-Mn-Ga substrate, as measured by LFMS* and DSC.

Sample	T_c (K)	A_s (K)	A_{peak} (K)	A_f (K)	M_s (K)	M_{peak} (K)	M_f (K)
SG substrate	376*, 380	282	283	287	275	273	270
Powder	345-359*	260	271	284	278	267	259
L-PBF sample	325-346*	376	393	408	395	390	370

or several martensite phases. For the sample at 298 K, the observed peaks at small angles of 30-40° indicate the orthorhombic structure of 14 M martensite. After deduction of the peaks associated with the 14 M structure, a consideration of the additional peaks provides a very reasonable correspondence with the non-modulated (NM) martensite structure. Some additional peaks that were present but were not identified may be connected to the modulation of 14 M martensite. Additionally, the broadening of the diffraction lines and abnormally low intensity of the diffraction obtained from the L-PBF sample implies the presence of a localized variation of lattice parameters, possibly due to compositional variation and internal stresses in the as-deposited material [48].

Fig. 8 shows two SEM images, one perpendicular to the build direction and another along the build direction of the sample, obtained from a ground and electropolished L-PBF sample manufactured on the Ni-Mn-Ga substrate. Overall, the observed structure is typical of materials processed by L-PBF, featuring the clearly distinguishable boundaries and profiles of each deposited track. The volume-weighted average grain size of the L-PBF sample was determined as 16.6 µm, and the measured grain size distribution is shown in Fig. 9. The measured grain size is small but within the range typical for the L-PBF process. No apparent L-PBF process related cracking was observed within the

Table 6

Approximate lattice parameters obtained for the initial powder and an as-deposited L-PBF sample.

Sample	Phase	a_0 (nm)	a_M (nm)	b_M (nm)	c_M (nm)	γ_M (°)
Powder 298 K	Austenite	0.5830	–	–	–	–
L-PBF sample 298 K	NM	–	0.538	0.538	0.665	–
	14 M	–	0.6207	0.5817	0.5520	90.5
L-PBF sample 433 K	Austenite	0.5838	–	–	–	–

samples deposited using the optimized parameters. As is apparent in the image, L-PBF did not produce a dendritic cooling structure; instead, there exists a parallel stripe-like surface relief throughout the L-PBF sample. Typically, this kind of striping with contrasting areas is linked to martensitic twin variants in Ni-Mn-Ga based alloys. As the results from the DSC/LFMS and XRD measurements indicated that the as-deposited sample was martensitic at ambient temperature, it is concluded that the stripe-like surface relief observed within the L-PBF sample must originate from twin variants. The orientation of the twins appears to vary from grain to grain, and in some areas, the twins are more pronounced because of a larger width of ~5 µm; for reference, see the SEM image with larger magnification in Fig. 5. Additionally, some of the
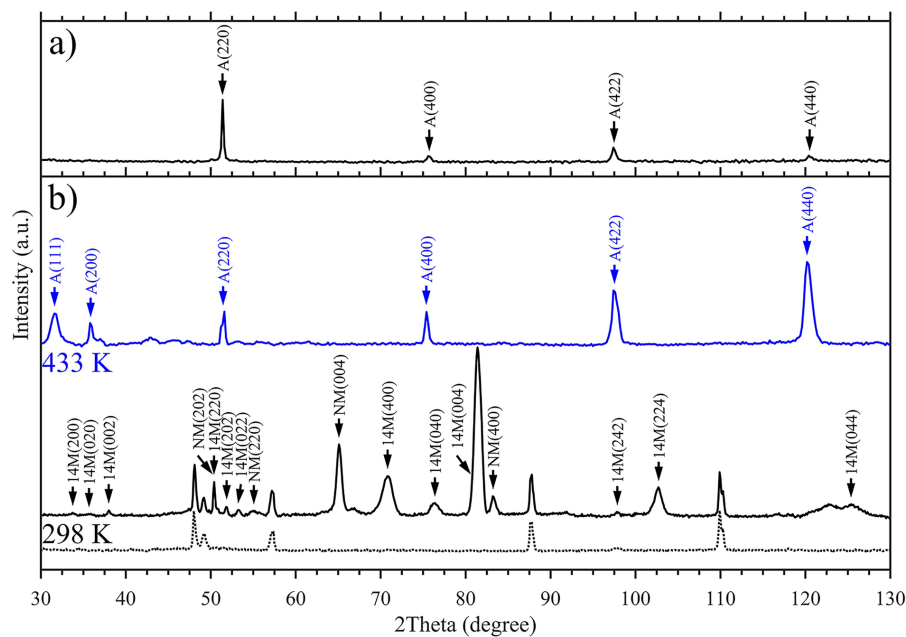

Fig. 7. XRD patterns obtained from: (a) the initial Ni-Mn-Ga powder at 298 K; (b) an as-deposited L-PBF sample at 298 K and 433 K. Diffraction pattern of the Si-holder used during the XRD measurement of the L-PBF sample at 298 K has been marked with a dotted line. Recognized peaks and peak indexes for austenite (A), non-modulated martensite (NM) and orthorhombic martensite phase (14 M) have been marked with arrows.
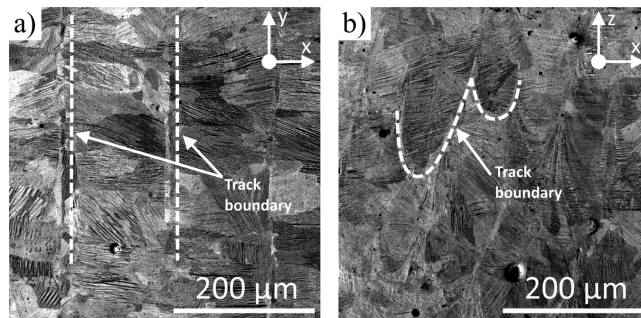
Fig. 8. SEM images of the microstructure obtained from: (a) a section of a sample perpendicular to the build direction; (b) a section of a sample along the build direction.
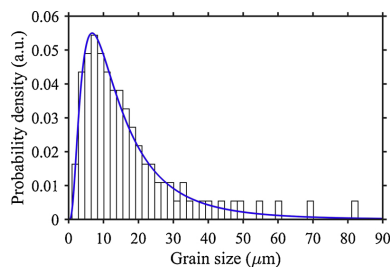

Fig. 9. The grain size distribution measured from multiple sections of a sample along the build direction.

observed twins cross the boundaries between adjacent tracks and consecutive deposition layers.

A series of AFM and MFM measurements was conducted for the L-PBF samples in as-deposited condition to investigate magnetic properties of the observed twins. To make a comparison, a heat-treated and electropolished single-crystalline sample with 10 M martensite structure (40° $Ni_{50}Mn_{28.5}Ga_{21.5}$ alloy by AdaptaMat Ltd.) was heated to ~ 353 K and then cooled to ambient temperature to create a random twin structure. Fig. 10a shows AFM and MFM images of the 10 M sample capturing two variants with a- and c-axes perpendicular to the plane of view and twin variant widths as low as ~ 1-2μm. Where the c-axis is perpendicular to the image plane, we can see a characteristic picture of the branched magnetic domains in the 10 M martensite. On this scale, a clear MFM contrast between the different twin variants is observable, and the twin boundaries appear as clearly distinguishable straight lines. Fig. 10b shows AFM and MFM images of the 10 M martensite sample with the c-axis oriented in the plane of view but rotated by ~ 90 degrees in the neighboring variants. Although the MFM image confirms the in-plane orientation of the c-axis in both variants, a slight relief visible in the AFM image indicates that the sample was not cut exactly along {001} planes. Nevertheless, the MFM phase signal provides enough contrast to differentiate between the variants with a width as low as $\sim 1 \mu$m.

The MFM scans of sections of the L-PBF sample, as presented in Fig. 10c–d, show very small stripes, down to fractions of a micrometer in width, with magnetic anisotropy that is much weaker compared to the heat-treated 10 M martensite sample. Additionally, for the 10 M martensite sample, the twin boundaries are always straight lines with a clear contrast, and a labyrinth-like domain structure is observable in the areas where the c-axis is mainly perpendicular to the plane of view. Meanwhile, for the LPBF sample, the domain boundaries and the

domains themselves are visibly less pronounced. Additionally, with the L-PBF samples, there exists a minor variation between the MFM contrasts from measurement to measurement, possibly due to compositional variation or internal stresses in the as-deposited material. Alternatively, the observed variation could be linked to the differences in MFM contrast between different variants at different angles – compare with the two MFM images obtained for the 10 M martensite sample. As the orientation of the grains in the L-PBF sample was not inspected in this study, no conclusive evidence on the effect of grain orientation on MFM contrast can be presented for the L-PBF samples. Thus, the overall conclusion can be made that in the L-PBF sample in as-processed condition, there exists a weak MFM contrast that can be attributed to the twinned martensite having magnetic anisotropy. The MFM contrast was visible in all scans, which was considered generally beneficial for obtaining a stronger MFM contrast and MFIS promoting properties after post-process heat-treatment.

4. Conclusion

This study concentrated on development of an L-PBF process for production of a Ni-Mn-Ga based MSM alloy with a high relative density and controlled composition. A series of cuboids was deposited on stainless steel substrates using gas atomized Ni-Mn-Ga powder and an in-house developed L-PBF system. Response surface methodology and analysis of variance (ANOVA) were used to determine the effects of the varied process parameters on composition and relative density of the as-deposited material. The results show that the L-PBF of Ni-Mn-Ga is characterized by the loss of Mn and the corresponding concentration of Ni. For this reason, future applications using this method will require a minor over-alloying of Mn into the initial powder to counteract the observed loss. Increasing *VED* increased Mn loss, especially for values above ~ 75–100 J/mm^3, whereas an increase in the loss of Ga was observed when *VED* was increased above ~ 200–250 J/mm^3. Additionally, the results revealed highly dissimilar effects of the applied process parameters on the composition and relative density of the as-deposited material, with a clear optimum where high relative density material could be produced with minimal loss of Mn.

For studying the properties of the as-deposited material, the optimized parameters were used for manufacturing samples on a Ni-Mn-Ga substrate compositionally similar to the used powder. The produced material was 98.3% dense and compositionally near homogenous, exhibiting a ~ 1.1 at.% loss of Mn in comparison to the initial powder. DSC and LFMS measurements indicated that the as-deposited material was martensitic at ambient temperature. Phase transformations of the material from martensite to austenite, and vice versa, were broad and occurred in a paramagnetic state. XRD confirmed that the as-deposited material consisted of a mixture of 14 M and NM martensites at ambient
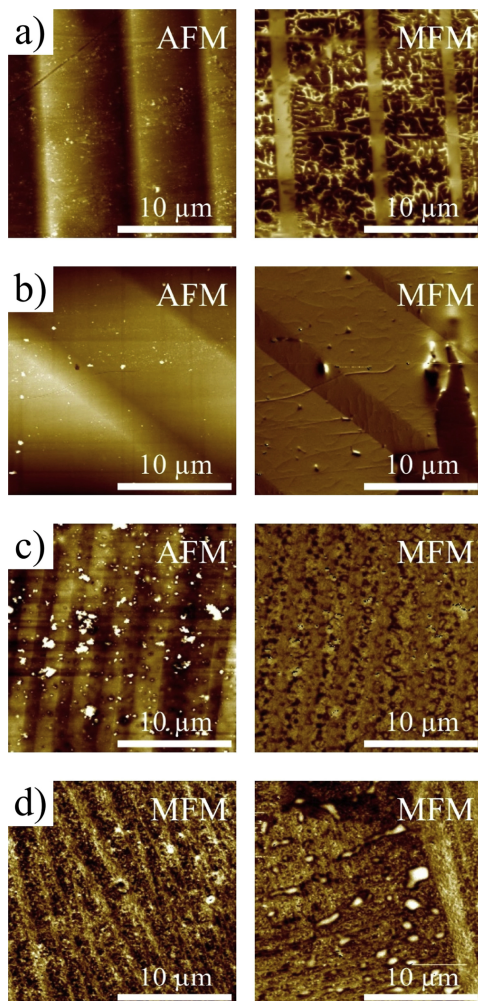
Fig. 10. AFM and MFM images obtained from: (a) a section of a single-crystalline 10 M martensite reference sample showing two variant microstructure with a- and c-axes perpendicular to plane of view; (b) a section of the 10 M sample with c-axis oriented in the plane of view; (c–d) multiple sections of an L-PBF sample perpendicular to the build direction.

temperature. Inspection of the sample using SEM showed a typical layered microstructure of material deposited using L-PBF, and revealed a stripe-like surface relief connected to the martensitic twins in Ni-Mn-Ga based alloys. Some of the twins were observed to cross the boundaries between adjacent tracks and consecutive deposition layers. Inspection of the observed twins using AFM and MFM showed that there exists a weak MFM contrast in as-deposited Ni-Mn-Ga that can be attributed to magnetic anisotropy of the twinned martensite. However, the MFM contrast obtained from the L-PBF samples was weaker than in the single crystalline 10 M martensite sample that was used as a reference. The weak MFM contrast and the observed broadening of the

XRD and main phase transformation peaks are likely result from minor variations of the composition and the internal stresses related to the rapid cooling of the deposited material during the L-PBF process.

Future experiments are planned for optimization of the process towards manufacturing of foam like materials, such as different types of fine lattice structures, which could exhibit fewer grain boundary constraints and could potentially develop a high MFIS. Although L-PBF shows high potential for the production of functional Ni-Mn-Ga based MSM alloys, the results of this study indicate that future research on post-process heat-treatments is required for obtaining sufficient magnetic properties for MFIS to occur.

Acknowledgements

References

[1] K. Ullakko, Magnetically controlled shape memory alloys: a new class of actuator materials, J. Mater. Eng. Perform. 5 (1996) 405, https://doi.org/10.1007/BF02649344.

[2] K. Ullakko, J.K. Huang, C. Kantner, R.C. O'Handley, V.V. Kokorin, Large magnetic-field-induced strains in Ni2MnGa single crystals, Appl. Phys. Lett. 69 (1996) 1966, https://doi.org/10.1063/1.117637.

[3] G. Engdahl, Handbook of Giant Magnetostrictive Materials, Academic Press, San Diego, 2000 ISBN 0-12-238640-X.

[4] A. Sozinov, N. Lanska, A. Soroka, W. Zou, 12% magnetic field-induced strain in Ni-Mn-Ga-based non-modulated martensite, Appl. Phys. Lett. 102 (2013) 021902, , https://doi.org/10.1063/1.4775677.

[5] A. Smith, J. Tellinen, K. Ullakko, Rapid actuation and response of Ni–Mn–Ga to magnetic-field-induced stress, Acta Mater. 80 (2014) 373–379, https://doi.org/10.1016/j.actamat.2014.06.054.

[6] I. Aaltio, A. Soroka, Y. Ge, O. Söderberg, S.P. Hannula, High-cycle fatigue of 10M Ni-Mn-Ga magnetic shape memory alloy in reversed mechanical loading, Smart Mater. Struct. 19 (2010) 075014, , https://doi.org/10.1088/0964-1726/19/7/075014.

[7] D. Musiienko, L. Straka, L. Klimša, A. Saren, A. Sozinov, O. Heczko, K. Ullakko, Giant magnetic-field-induced strain in Ni-Mn-Ga micropillars, Scr. Mater. 150 (2018) 173–176, https://doi.org/10.1016/j.scriptamat.2018.03.020.

[8] D. Musiienko, A. Saren, L. Straka, M. Vronka, J. Kopeček, O. Heczko, A. Sozinov, K. Ullakko, Ultrafast actuation of Ni-Mn-Ga micropillars by pulsed magnetic field, Scr. Mater. 162 (2019) 482–485, https://doi.org/10.1016/j.scriptamat.2018.12.009.

[9] K. Ullakko, L. Wendell, A. Smith, P. Müllner, G. Hampikian, A magnetic shape memory micropump: contact-free, and compatible with PCR and human DNA profiling, Smart Mater. Struct. 21 (2012) 115020, , https://doi.org/10.1088/0964-1726/21/11/115020.

[10] A. Smith, A. Saren, J. Järvinen, K. Ullakko, Characterization of a high-resolution solid-state micropump that can be integrated into microfluidic systems, Microfluid. Nanofluid. 18 (2015) 1255–1263, https://doi.org/10.1007/s10404-014-1524-6.

[11] S. Barker, E. Rhoads, P. Lindquist, M. Vreugdenhil, P. Müllner, Magnetic shape memory micropump for submicroliter intracranial drug delivery in rats, Am. J. Respir. Med. 10 (2016) 041009, , https://doi.org/10.1115/1.4034576.

[12] A. Saren, A. Smith, K. Ullakko, Integratable magnetic shape memory micropump for high-pressure, precision microfluidic applications, Microfluid. Nanofluid. 22 (2018) 38, https://doi.org/10.1007/s10404-018-2058-0.

[13] A. Hobza, C. Patrick, K. Ullakko, N. Rafla, P. Lindquist, P. Müllner, Sensing strain with Ni-Mn-Ga, Sens. Actuators A Phys. 269 (2018) 137–144, https://doi.org/10.1016/j.sna.2017.11.002.

[14] A. Saren, D. Musiienko, A. Smith, J. Tellinen, K. Ullakko, Modeling and design of a vibration energy harvester using the magnetic shape memory effect, Smart Mater. Struct. 24 (2015) 095002, , https://doi.org/10.1088/0964-1726/24/9/095002.

[15] P. Lindquist, T. Hobza, C. Patrick, P. Müllner, Efficiency of energy harvesting in Ni–Mn–Ga shape memory alloys, Shap. Mem. Superelasticity 4 (2018) 93–101, https://doi.org/10.1007/s40830-018-0158-z.

[16] M. Chmielus, X.X. Zhang, C. Witherspoon, D.C. Dunand, P. Müllner, Giant magnetic-field-induced strains in polycrystalline Ni–Mn–Ga foams, Nat. Mater. 8 (2009) 863–866, https://doi.org/10.1038/nmat2527.

[17] F. Nilsén, J. Lehtonen, Y. Ge, I. Aaltio, S.P. Hannula, Highly porous spark plasma sintered Ni-Mn-Ga structures, Scr. Mater. 139 (2017) 148–151, https://doi.org/10.1016/j.scriptamat.2017.06.040.

[18] P. Zheng, N. Kucza, Z. Wang, P. Müllner, D. Dunand, Effect of directional solidification on texture and magnetic-field-induced strain in Ni–Mn–Ga foams with coarse grains, Acta Mater. 86 (2015) 95–101, https://doi.org/10.1016/j.actamat.2014.12.005.

[19] S. Taylor, R. Shah, D. Dunand, Ni-Mn-Ga micro-trusses via sintering of 3D-printed

inks containing elemental powders, Acta Mater. 143 (2017) 20–29, https://doi.org/10.1016/j.actamat.2017.10.002.

[20] S. Taylor, R. Shah, D. Dunand, Microstructure and porosity evolution during sintering of Ni-Mn-Ga wires printed from inks containing elemental powders, Intermetallics 104 (2019) 113–123, https://doi.org/10.1016/j.intermet.2018.10.024.

[21] M. Caputo, M. Krizner, C.V. Solomon, Investigation of 3d printing parameters of shape memory alloy powders, Materials Science & Technology, Columbus (October) (2015) 4–8.

[22] M. Caputo, C.V. Solomon, P.-K. Nguyen, A.E. Berkowitz, Electron microscopy investigation of binder saturation and microstructural defects in functional parts made by additive manufacturing, Microsc. Microanal. 22 (2016) 1770–1771, https://doi.org/10.1017/S1431927616009697.

[23] A. Mostafaei, K. Kimes, E. Stevens, J. Toman, Y. Krimer, K. Ullakko, M. Chmielus, Microstructural evolution and magnetic properties of binder jet additive manufactured Ni-Mn-Ga magnetic shape memory alloy foam, Acta Mater. 131 (2017) 482–490, https://doi.org/10.1016/j.actamat.2017.04.010.

[24] M. Caputo, C.V. Solomon, Microstructure and chemical composition analysis of additive manufactured Ni-Mn-Ga parts sintered in different conditions, Microsc. Microanal. 23 (2017) 2078–2079, https://doi.org/10.1017/S1431927617011059.

[25] M. Caputo, C.V. Solomon, A facile method for producing porous parts with complex geometries from ferromagnetic Ni-Mn-Ga shape memory alloys, Mater. Letters 200 (2017) 87–89, https://doi.org/10.1016/j.matlet.2017.04.112.

[26] M. Caputo, A. Berkowitz, A. Armstrong, P. Müllner, C.V. Solomon, 4D printing of net shape parts made from Ni-Mn-Ga magnetic shape-memory alloys, Addit. Manuf. 21 (2018) 579–588, https://doi.org/10.1016/j.addma.2018.03.028.

[27] A. Mostafaei, P. Rodriguez, E. Stevens, M. Chmielus, Sintering regimes and resulting microstructure and properties of binder jet 3D printed Ni-Mn-Ga magnetic shape memory alloys, Acta Mater. 154 (2018) 355–364, https://doi.org/10.1016/j.actamat.2018.05.047.

[28] N. Lanska, O. Soderberg, A. Sozinov, Y. Ge, K. Ullakko, V.K. Lindroos, Composition and temperature dependence of the crystal structure of Ni–Mn–Ga alloys, J. Appl. Phys. 95 (2004) 8074–8078, https://doi.org/10.1063/1.1748860.

[29] O. Heczko, L. Straka, Compositional dependence of structure, magnetization and magnetic anisotropy in Ni–Mn–Ga magnetic shape memory alloys, J. Magn. Magn. Mater. 272–276 (2004) 2045–2046, https://doi.org/10.1016/j.jmmm.2003.12.819.

[30] M. Richard, J. Feuchtwanger, D. Schlagel, T. Lograsso, S. Allen, R. O'Handley, Crystal structure and transformation behavior of Ni–Mn–Ga martensites, Scr. Mater. 54 (2006) 1797–1801, https://doi.org/10.1016/j.scriptamat.2006.01.033.

[31] J. Toman, P. Müllner, M. Chmielus, Properties of as-deposited and heat-treated Ni-Mn-Ga magnetic shape memory alloy processed by directed energy deposition, J. Alloys. Compd. 752 (2018) 455–463, https://doi.org/10.1016/j.jallcom.2018.04.059.

[32] K. Ullakko, V. Laitinen, A. Saren, A. Sozinov, D. Musiienko, M. Chmielus, A. Salminen, Ni-Mn-Ga actuating elements manufactured using 3D printing, 11th European Symposium on Martensitic Transformations, Metz, (2018), pp. 27–31. August.

[33] V. Laitinen, A. Salminen, K. Ullakko, First investigation on processing parameters for laser powder bed fusion of Ni-Mn-Ga magnetic shape memory alloy, J. Laser Appl. 31 (2019) 022303, , https://doi.org/10.2351/1.5096108.

[34] F. Nilsén, I. Ituarte, M. Salmi, J. Partanen, S. Hannula, Effect of process parameters on non-modulated Ni-Mn-Ga alloy manufactured using powder bed fusion, Addit. Manuf. 28 (2019) 464–474, https://doi.org/10.1016/j.addma.2019.05.029.

[35] F. Albertini, S. Besseghini, A. Paoluzi, L. Pareti, M. Pasquale, F. Passaretti, C. Sasso, A. Stantero, E. Villa, Structural, magnetic and anisotropic properties of Ni2MnGa melt-spun ribbons, J. Magn. Magn. Mater. 242-245 (2002) 1421–1424, https://doi.org/10.1016/S0304-8853(01)00992-1.

[36] J. Wang, C. Jiang, R. Techapiesancharoenkij, D. Bono, S.M. Allen, R.C. O'Handley, Microstructure and magnetic properties of melt spinning Ni-Mn-Ga, Intermetallics 32 (2013) 151–155, https://doi.org/10.1016/j.intermet.2012.08.021.

[37] F. Nilsén, I. Aaltio, Y. Ge, T. Lindroos, S. Hannula, Characterization of gas atomized Ni-Mn-Ga powders, Mater. Today Proc. 2 (2015) S879–S882, https://doi.org/10.1016/j.matpr.2015.07.422.

[38] ASM Handbook Committee, Heat Treating vol. 4, ASM International, 1991 ISBN 0-87170-379-3.

[39] S. Ghouse, S. Babu, R. Van Arkel, K. Nai, P. Hooper, J. Jeffers, The influence of laser parameters and scanning strategies on the mechanical properties of a stochastic porous material, Mater. Des. 131 (2017) 498–508, https://doi.org/10.1016/j.matdes.2017.06.041.

[40] P. Lehto, H. Remes, T. Saukkonen, H. Hänninen, J. Romanoff, Influence of grain size distribution on the Hall–Petch relationship of welded structural steel, Mater. Sci. Eng. A 592 (2014) 28–39, https://doi.org/10.1016/j.msea.2013.10.094.

[41] W. King, H. Barth, V. Castillo, G. Gallegos, J. Gibbs, D. Hahn, C. Kamath, A. Rubenchik, Observation of keyhole-mode laser melting in laser powder-bed fusion additive manufacturing, J. Mater. Process. Technol. 214 (2014) 2915–2925, https://doi.org/10.1016/j.jmatprotec.2014.06.005.

[42] C. Kamath, B. El-dasher, G. Gallegos, W. King, A. Sisto, Density of additively-manufactured, 316L SS parts using laser powder-bed fusion at powers up to 400 W, Int. J. Adv. Manuf. Technol. 74 (2014) 65–78, https://doi.org/10.1007/s00170-014-5954-9.

[43] N. Aboulkhair, N. Everitt, I. Ashcroft, C. Tuck, Reducing porosity in AlSi10Mg parts processed by selective laser melting, Addit. Manuf. 1-4 (2014) 77–86, https://doi.org/10.1016/j.addma.2014.10.001.

[44] Q. Jia, D. Gu, Selective laser melting additive manufacturing of Inconel 718 superalloy parts: densification, microstructure and properties, J. Alloys. Compd. 585 (2014) 713–721, https://doi.org/10.1016/j.jallcom.2013.09.171.

[45] G. Kasperovich, J. Haubrich, J. Gussone, G. Requena, Correlation between porosity and processing parameters in TiAl6V4 produced by selective laser melting, Mater. Design 105 (2016) 160–170, https://doi.org/10.1016/j.matdes.2016.05.070.

[46] B. Zhang, Y. Li, Q. Bai, Defect formation mechanisms in selective laser melting: a review, Chin. J. Mech. Eng. 30 (2017) 515–527, https://doi.org/10.1007/s10033-017-0121-5.

[47] H. Schönrath, M. Spasova, S. Kilian, R. Meckenstock, G. Witt, J. Sehrt, M. Farle, Additive manufacturing of soft magnetic permalloy from Fe and Ni powders: control of magnetic anisotropy, J. Magn. Magn. Mater. 478 (2019) 274–278, https://doi.org/10.1016/j.jmmm.2018.11.084.

[48] R. Pokharel, L. Balogh, D. Brown, B. Clausen, G. Gray, V. Livescu, S. Vogel, S. Takajo, Signatures of the unique microstructure of additively manufactured steel observed via diffraction, Scr. Mater. 155 (2018) 16–20, https://doi.org/10.1016/j.scriptamat.2018.06.008.
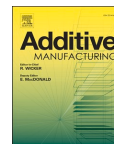
Publication IV

Laitinen, V., Sozinov, A., Saren, A., Chmielus, M., and Ullakko, K.
Characterization of as-built and heat-treated Ni-Mn-Ga magnetic shape memory alloy manufactured via laser powder bed fusion

Research Paper

Characterization of as-built and heat-treated Ni-Mn-Ga magnetic shape memory alloy manufactured via laser powder bed fusion

Ville Laitinen [a],[*], Alexei Sozinov [a], Andrey Saren [a], Markus Chmielus [b], Kari Ullakko [a],[*]

[a] Material Physics Laboratory, Lappeenranta-Lahti University of Technology LUT, Lappeenranta 53850, Finland
[b] Department of Mechanical Engineering and Materials Science, University of Pittsburgh, Pittsburgh, PA 15261, USA

ARTICLE INFO

ABSTRACT

Magnetic shape memory (MSM) alloys have a high potential as an emerging class of actuator materials for a new generation of fast and simple digital components. In this study, the MSM alloy $Ni_{50.5}Mn_{27.5}Ga_{22.0}$ was built via laser powder bed fusion (L-PBF) using gas atomized powder doped with excess Mn to compensate for the expected evaporation of Mn during L-PBF. The built samples were subjected to stepwise chemical homogenization and atomic ordering heat treatments. The experiments followed a systematic experimental design, using temperature and the duration of the homogenization treatment as the varied parameters. Overall, the produced samples showed only a minor variation in relative density (average density ~98.4%) and chemical composition from sample to sample. The as-built material showed broad austenite-martensite transformation and low saturation magnetization. The crystal structure of the as-built material at ambient temperature was a mixture of seven-layered modulated orthorhombic (14 M) and five-layered modulated tetragonal (10 M) martensites. Notably, ordering heat treatment at 800 °C for 4 h without homogenization at a higher temperature was enough to obtain narrow austenite-14 M martensite transformation, Curie temperature, and saturation magnetization typical for bulk samples of the same composition. Additionally, homogenization at 1080 °C stabilized the single-phase 14 M martensite structure at ambient temperature and resulted in considerable grain growth for homogenization times above 12 h. The results show that post-process heat treatment can considerably improve the magneto-structural properties of Ni-Mn-Ga built via L-PBF.

1. Introduction

Magnetic shape memory (MSM) alloys are a group of functional materials characterized by a coupling between the structural and magnetic orders of the material [1,2]. These materials can develop large reversible magnetic-field-induced strains (MFIS) when, in response to magnetic-field-induced stress, crystallographic domains (twin variants) of the martensitic phase are rearranged. Oriented Ni-Mn-Ga single crystals exhibit the largest MFIS: up to ~6% [3] for five-layered modulated tetragonal (10 M) martensite and up to ~9.5% [4] for seven-layered modulated orthorhombic (14 M) martensite. Non-modulated tetragonal (NM) martensite does not typically exhibit large MFIS [5,6], although 12% MFIS has been obtained in a doped alloy exhibiting an NM structure [7]. MSM alloys are emerging as a promising class of actuator materials for devices requiring a high response frequency, a large reversible strain, and high energy efficiency. Examples of such devices include microactuators [8,9], microfluidic pumps

[10–13], energy conversion devices [14,15], and sensors [16].

Large MFIS in Ni-Mn-Ga is almost exclusively achieved in oriented single crystals (SC). The motion of twin boundaries is significantly hindered by the grain boundaries, and thus, polycrystalline MSM alloys do not generally develop any MFIS. However, polycrystalline Ni-Mn-Ga has been shown to develop moderate MFIS when grain boundary constraints are sufficiently reduced, for example, by increasing porosity [17–20] or by introducing a strong crystallographic texture [21–24]. Ni-Mn-Ga based polycrystalline foams have been shown to develop up to 8.7% MFIS [17], whereas bulk polycrystalline Ni-Mn-Ga with a strong crystallographic texture has been shown to exhibit up to 4% [21]. Improving the manufacturability of functional Ni-Mn-Ga based devices is the primary motivation for using polycrystalline material instead of SCs.

For this reason, in recent years, additive manufacturing (AM) has attracted increasing interest as a promising method for manufacturing near net shape parts with complex geometries and tailored porosities.

The majority of AM research on Ni-Mn-Ga has focused on binder-based processes, such as 3D ink printing [25,26] and binder jetting of Ni-Mn-Ga [27–33] and Ni-Mn(Cu)-Ga metamagnetic materials [34]. Additionally, a few investigations have recently been published relating to the laser-based directed energy deposition (L-DED) of Ni-Mn-Ga [35] and magnetocaloric Ni-Co-Mn-Sn [36,37] as well as the laser powder bed fusion (L-PBF) of Ni-Mn-Ga [38–42]. Laser additive manufacturing (LAM) effectively circumvents the use of binder materials. This is considered beneficial because the magneto-structural properties and MFIS in Ni-Mn-Ga are highly dependent on chemical composition [43–49] and atomic ordering [50–61]. However, these properties are influenced by L-PBF processing conditions.

Previous L-PBF of Ni-Mn-Ga investigations [38–42] revealed some of the complex interactions between the applied process parameters and the resulting material properties. Foremost, these studies have demonstrated the feasibility of L-PBF for manufacturing three-dimensional geometries with high relative densities from Ni-Mn-Ga, with reported values of 88.5–92.9% [40], 93.5–96.8% [39], and 72.6–98.7% [42]. The non-equilibrium conditions and rapid heating/cooling during layer-by-layer melting in L-PBF have been shown to significantly affect the composition, as well as the resulting phase constitution and magneto-structural properties of the built Ni-Mn-Ga, through the selective evaporation of Mn and quenched-in stresses and atomic disorder [40,42]. Additionally, previous investigations [38,40] indicated that some of the initial composition-dependent material properties can to a large extent be retained via post-process heat treatment. However, the scientific literature lacks systematic parametric studies on the effects that heat treatment parameters have on the properties of Ni-Mn-Ga built using L-PBF. For comparison, studies [27–33] on the binder jetting of Ni-Mn-Ga exclusively discuss high-temperature sintering as a post-processing step to achieve the final part from the green part.

Upon cooling, Ni-Mn-Ga MSM alloys undergo a phase transition sequence, namely liquid → disordered cubic B2' → ordered cubic L2$_1$ (austenite) → low-symmetric martensite. Subsequently, the magneto-structural properties of Ni-Mn-Ga martensites are correlated with the magneto-structural properties of the cubic L2$_1$ parent phase. In principle, the heat treatment of Ni-Mn-Ga alloys is a two-step process, including chemical homogenization and/or atomic ordering treatments. The aim of the homogenization treatment is to evenly distribute the alloy atoms within the material. The typical homogenization treatment of Ni-Mn-Ga is carried out at ~1000 °C for ≤ 24 h [54,61], which is generally considered enough to achieve an even distribution of SC material elements that are typically near-homogenous in their initial state. However, in comparison to conventionally manufactured samples, polycrystalline Ni-Mn-Ga built via L-PBF is expected to be less homogenous [41,43]. Hence, it may be beneficial to strive for higher temperatures below the solidus temperature to increase diffusion. The aim of the ordering treatment is to increase the atomic order degree of the L2$_1$ structure, which enhances the stability of martensite, martensitic transformations, and magneto-structural properties. The highest degree of long-range atomic ordering can be achieved by treating the material slightly above the L2$_1$ to B2' transition temperature and then slowly cooling the sample over the transition to ambient temperature. In the cited literature, heat treatment below the ordering temperature and fast quenching have both been shown to decrease long-range ordering.

This work aims to experimentally determine the effects of the heat treatment parameters on the properties of Ni-Mn-Ga built via L-PBF. For this purpose, L-PBF was used to manufacture samples from gas atomized Ni-Mn-Ga powder, while the built samples were subjected to heat treatments for chemical homogenization and atomic ordering. Detailed investigations were conducted on the composition, microstructure, and magneto-structural properties of the built material in both as-built and heat-treated conditions. This study aims to determine whether heat treatment can improve the magneto-structural properties of Ni-Mn-Ga built via L-PBF. The aim is to identify optimal heat treatment conditions for the improvement of functional properties, which is critical for

achieving large MFIS in Ni-Mn-Ga manufactured via L-PBF.

2. Material and methods

2.1. Ni-Mn-Ga powder

A pre-alloyed powder with a nominal composition of Ni$_{49.7}$Mn$_{29.1}$Ga$_{21.2}$ was prepared using an argon gas atomization process. The powder was pre-alloyed with excess Mn in comparison to the approximate target composition of ~Ni$_{50.5}$Mn$_{27.7}$Ga$_{21.8}$ to compensate for the expected evaporation of Mn during L-PBF. The powder composition was determined using an Oxford Instruments X-Strata 960 X-ray fluorescence analyzer (XRF) calibrated with a Ni-Mn-Ga reference sample of known composition. The absolute accuracy of the measurement was 0.3 at%. The powder was mechanically sieved to obtain a particle size of < 80 μm. The volume-weighted particle size distribution ($d_{0.1}$=8.8 μm, $d_{0.5}$=21.6 μm, and $d_{0.9}$=63.5 μm) of the sieved powder was measured using a Malvern Panalytical Morphologi G3S. As can be observed from Fig. 1a, the measured patch of powder was largely dominated by small Ø< 30 μm particles. Analysis using a Hitachi SU3500 scanning electron microscope (SEM), as shown in Fig. 1b, confirmed that the powder particles possessed a highly spherical morphology, with only a minor amount of irregularly shaped particles present within the analyzed patch.

2.2. Laser powder bed fusion

All samples were built using an in-house built L-PBF testbed system with a modular build chamber and a semi-automated recoater-build platform setup. The system was equipped with an IPG YLS-200-SM-WC continuous-wave single-mode ytterbium fiber laser ($\lambda = 1075$ nm, maximum $P_{avg} = 200$ W), producing a laser beam with near-Gaussian power distribution, a ~82 μm focal point diameter, a Rayleigh length of 3.24 mm, and a beam parameter product of 0.53 mm mrad. Both the laser and the scan head (SCANLAB intelliSCAN 10) were controlled
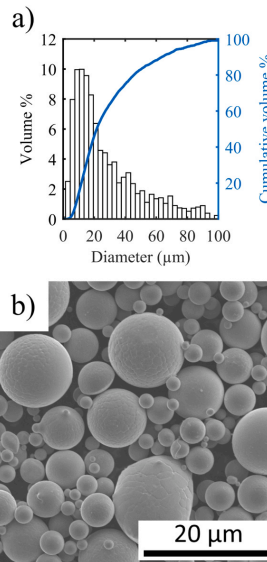

Fig. 1. (a) Volume-weighted particle size distribution of the used Ni-Mn-Ga powder; (b) SEM image of the powder.

externally using SCAPS SAMLight scanner software with 3D functionality.

The applied L-PBF process parameters (summarized in Table 1) were selected and adjusted to obtain the target composition based on previous L-PBF process optimization, as performed in [42]. All samples were built at ambient temperature without substrate preheating in a high-purity argon atmosphere. The laser beam was focused on the surface of the powder bed during sample manufacturing. The hatched region of each sample was melted using a bidirectional scanning strategy with a 60° turn of the scanning direction from layer to layer. The edge of each sample was melted with a single contour scan and a ~90% overlap with the hatched area. The same combination of process parameters was used for both hatched and contour scans. All built samples were 5x5x 5 mm³ cuboids, orientated on the substrate in a 3×3 matrix so that the side faces of the cuboids were aligned at a 45° angle compared to the x-y hatch directions of the applied L-PBF system. This specific sample orientation was chosen to enable a smooth operation of the recoater blade along the x-direction of the platform as well as to minimize the risk of recoater collision with the built samples. To minimize thermal interaction between samples during manufacture, a 5 mm gap was left between each sample. The samples were built in two patches of nine samples on high-purity (>99.5%) Ni substrates (Ø 45 mm, thickness ~6.3 mm). High-purity Ni was selected as the substrate material to ensure chemical combability and to minimize the possible contamination of the built Ni-Mn-Ga by elements in the substrate. Fig. 2 shows a single patch of built Ni-Mn-Ga samples on a high-purity Ni substrate.

2.3. Heat treatment

All samples were heat-treated using an in-house developed system based on an MTI OTF-1200X furnace. The system holds a temperature ± 1 °C from the set-point temperature within the active length of the main tube. After manufacturing via L-PBF, the samples were removed from the Ni substrates using a Princeton Scientific Corporation WS2 high-precision wire saw. Before heat treatment, each sample was cleaned in a beaker filled with acetone to remove possible surface contaminants and then washed with 2-propanol in an ultrasonic bath to remove any remaining contaminated acetone. Each sample was placed on a high-purity alumina boat with a titanium oxygen-getter. The alumina boat and its contents were placed inside the main tube of the heat treatment system, which was then sealed and subsequently vacated using a Pfeiffer vacuum HiCube 80 Eco turbopump. The exact pressure within the main tube was monitored using an Oerlikon Leybold Vacuum PTR 90 N vacuum meter. The system was then pumped until a high vacuum was achieved, after which it was flooded with pure argon to prevent Mn evaporation, which can occur during heat treatment in a vacuum. The argon pressure within the main tube of the system was adjusted to ~300 mbar at ambient temperature, thus taking into consideration the thermal expansion of argon and the resulting increase of pressure during the heat treatment sequence.

The solidus temperature (~1110 °C) and L2$_1$→B2' transition temperature (~765 °C), corresponding to the composition of the as-built material, were approximated based on the available literature [51,57] and used to determine the corresponding critical temperatures for the heat treatment. Each sample was first homogenized at a higher temperature – according to the heat treatment parameters presented in

Table 1
Summary of the used L-PBF process parameters.

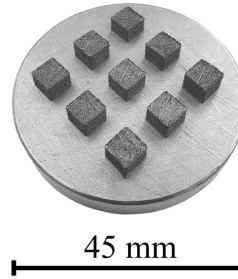| Parameter	Value
Powder layer thickness, t (μm)	60
Laser power, P (W)	200
Scanning speed, v (mm/s)	750
Hatch distance, h (μm)	100
Volume energy density, VED (J/mm³)	44.4

Fig. 2. A patch of nine Ni-Mn-Ga samples built on a high-purity Ni substrate using L-PBF.

Table 2
Summary of the used heat treatment parameters.

Parameter	Value
Heating rate 20 °C → T_h (°C/h)	250
Homogenization temperature, T_h (°C)	1000, 1040, 1080
Homogenization time, t_o (h)	6, 12, 24
Cooling rate T_h → T_o (°C/h)	100
Ordering temperature, T_o (°C)	800
Ordering time, t_o (h)	4
Cooling rate T_o → 20 °C (°C/h)	Furnace cooling

Tables 2 and 3 – which was then decreased for the ordering treatment. Subsequently, the samples were furnace-cooled to ambient temperature. The samples were heat-treated in a randomized sample order and some treatments were repeated for secondary samples to allow for reliability estimation. Additionally, two reference samples – one without heat treatment (S$_1$) and one with the ordering treatment without prior homogenization (S$_2$) – were produced to facilitate a comparison. An initial inspection (composition, martensitic transformation, and crystal structure) of the as-built samples showed only minor variations from sample to sample; therefore, sample S$_1$ can be considered as representative of all as-built samples in this study.

2.4. Sample preparation and analysis

The samples were ground incrementally using SiC abrasives, then polished mechanically using a napless cloth and diamond paste with a 3 μm grain size. The relative densities of all samples were determined optically using a customized Zeiss Axio Scope.A1 optical microscope and the ImageJ image processing software. The results were obtained by averaging the area fraction of pores measured from three consecutive layers on the top surface of each sample (~0.25 mm material removal in the build direction between each layer). For further characterization, the samples were electropolished with a constant voltage of 12 V at − 20 °C using an in-house developed polishing device. The electropolishing solution was a mixture of a 3:1 volumetric ratio of ethanol to 60% HNO$_3$. The chemical compositions of the samples were determined from sample top surfaces by averaging 16 measurements (4×4 grid scan of full surface) obtained using an Oxford Instruments X-Strata 960 XRF with a Ø 300 μm collimator. The microstructure of each sample was imaged with a Hitachi SU3500 SEM and a polarized Zeiss Axio Scope.A1 optical microscope. Grain sizes were determined from the obtained SEM images with a linear intercept method using a combination of the ImageJ software package and the MATLAB-based program originally developed in [62]. Magnetic force microscopy (MFM) using a Park Systems XE7 was used for the magnetostructural characterization of the observed martensitic twins. The crystal structures of the samples were studied using a PANalytical Empyrean 3 diffractometer (Cu tube,

Table 3

Chemical compositions, relative densities, and average grain sizes of the manufactured samples. Presented errors correspond to standard measurement deviations.

| Sample | HT parameters | | | | Composition | | | | Density (%) | Average grain size (µm) |
	T_h (°C)	t_h (h)	T_o (°C)	t_o (h)	Ni (at%)	Mn (at%)	Ga (at%)	e/a (-)		
S_1	–	–	–	–	50.47 ± 0.20	27.50 ± 0.32	22.03 ± 0.24	7.65	98.6 ± 0.33	13.5 ± 3.5
S_2	–	–	800	4	50.66 ± 0.29	27.27 ± 0.29	22.06 ± 0.14	7.63	98.2 ± 0.24	22.2 ± 6.2
S_3	1000	6	800	4	50.57 ± 0.22	27.36 ± 0.28	22.07 ± 0.15	7.64	98.4 ± 0.41	22.1 ± 5.8
S_4	1000	12	800	4	50.62 ± 0.15	27.46 ± 0.27	21.92 ± 0.14	7.63	97.9 ± 0.26	24.2 ± 7.4
S_5	1000	24	800	4	50.76 ± 0.27	27.22 ± 0.30	22.02 ± 0.15	7.64	98.3 ± 0.25	34.8 ± 9.9
S_6	1040	6	800	4	50.52 ± 0.26	27.70 ± 0.31	21.78 ± 0.24	7.64	98.4 ± 0.31	23.2 ± 6.9
S_7	1040	12	800	4	50.57 ± 0.19	27.54 ± 0.26	21.89 ± 0.13	7.64	98.8 ± 0.15	24.5 ± 7.2
S_8	1040	24	800	4	50.78 ± 0.08	27.08 ± 0.17	22.14 ± 0.13	7.64	98.2 ± 0.26	38.0 ± 10.8
S_9	1080	6	800	4	50.60 ± 0.21	27.40 ± 0.25	22.00 ± 0.14	7.64	98.1 ± 0.40	25.4 ± 7.5
S_{10}	1080	12	800	4	50.66 ± 0.18	27.34 ± 0.08	22.00 ± 0.15	7.64	98.2 ± 0.35	55.5 ± 14.8
S_{11}	1080	24	800	4	50.72 ± 0.10	27.21 ± 0.09	22.07 ± 0.09	7.64	98.8 ± 0.24	66.2 ± 16.7

$\lambda = 0.15406$ nm) equipped with poly-capillary optics, a PIXcel3D-Medipix3 detector, and a Si-510 zero background holder. A generator voltage of 45 kV and a current of 40 mA were applied, while the scans were performed over a 2θ range of 24–140°. Additionally, a heating stage was used to inspect the samples in the cubic phase above the martensite transformation temperature. The lattice parameters were refined using the Bruker TOPAS software. The phase transformation and Curie temperatures of each sample were determined using an in-house developed low-field AC magnetic susceptibility (LFMS) device. In addition, differential scanning calorimetry (DSC) using a TA Instruments DSC250 with an autosampler and an RCS90 two-stage refrigeration system was used to determine the phase transformation temperatures of the as-built sample and selected HT samples. The saturation magnetization of each sample was measured using a LakeShore model 7407 vibrating sample magnetometer (VSM), applying a field of up to 1.2 T. Each sample was secured to the VSM sample holder using Teflon tape.

3. Results and discussion

Table 3 summarizes the used heat treatment parameter combinations, together with the corresponding chemical compositions, relative densities, and average grain sizes. The shown errors correspond to the standard measurement deviations. Table 4 presents the analysis of variance (ANOVA) tables for relative density, Mn content, average grain size, and the width of austenite-14 M martensite transformation (ΔT_M), including homogenization temperature (T_h) and time (t_h) as continuous predictors. In the analysis, factors with a p-value < 0.05 were considered statistically significant, whereas those exceeding this threshold

were considered statistically insignificant. Special consideration should be taken when interpreting the p-values due to the relatively small sample size used in this study.

Overall, L-PBF demonstrated high repeatability for manufacturing high-density polycrystalline Ni-Mn-Ga with a consistent and predictable composition. All samples were highly dense (average ~98.4%) with only a minor variation of density observed from sample to sample. Additionally, the standard deviations of density were small, in the range of ± 0.15–0.41% for all samples. Considerable density changes were not expected during the heat treatment because the density of the as-built samples was relatively high. The ANOVA in Table 4 does not show any dependency between the applied homogenization treatment and observed density.

The average composition of the as-built samples was $Ni_{50.5}Mn_{27.5}Ga_{22.0}$, thus exhibiting an average of ~1.6 at% loss of Mn in comparison to the initial powder. Consequently, the fractions of Ni and Ga each increased by ~0.8 at%. The obtained composition shows a slight deviation from the initial target composition, with a slightly larger amount (0.2 at%) of Ga and an equally lower amount of Mn. The amount of Ni in the as-built samples was approximately within expectations. Using a relatively low value of *VED* (44.4 J/mm³) in comparison to [42] likely resulted in a reduced evaporation of Ga during L-PBF, which explains this observation. Additionally, the values in Table 3 and Fig. 3 show a slight trend of decreasing Mn content from samples $S_{3\rightarrow5}$, $S_{6\rightarrow8}$, and $S_{9\rightarrow11}$. This implies that increasing the homogenization time may have resulted in increased Mn evaporation during the heat treatment. However, the ANOVA for Mn content in Table 4 shows that the applied heat treatment parameters were not statistically significant for Mn

Table 4

ANOVA tables for relative density, Mn content, average grain size, and the width of austenite-14 M martensite transformation (ΔT_M), including homogenization temperature (T_h) and time (t_h) as continuous predictors.

| Source | Relative density (%) | | | | | Mn content (at%) | | | | |
	DF	Adj SS	Adj MS	F-value	P-value	DF	Adj SS	Adj MS	F-value	P-value
T_h	1	0.063	0.063	0.43	0.558	1	0.001	0.001	0.05	0.832
t_h	1	0.027	0.027	0.18	0.699	1	0.151	0.151	5.89	0.094
T_h^2	1	0.067	0.067	0.46	0.547	1	0.024	0.024	0.92	0.408
t_h^2	1	0.004	0.004	0.03	0.882	1	0.008	0.008	0.30	0.620
$T_h^*t_h$	1	0.138	0.138	0.94	0.404	1	0.000	0.000	0.01	0.935
Error	3	0.440	0.147	–	–	3	0.077	0.026	–	–
Total	8	0.722	–	–	–	8	0.280	–	–	–
Source	Average grain size (µm)					ΔT_M (°C)				
	DF	Adj SS	Adj MS	F-value	P-value	DF	Adj SS	Adj MS	F-value	P-value
T_h	1	803.610	803.610	12.38	0.039	1	16.822	16.822	113.47	0.002
t_h	1	776.410	776.410	11.96	0.041	1	3.760	3.760	25.36	0.015
T_h^2	1	180.620	180.620	2.78	0.194	1	0.020	0.020	0.13	0.738
t_h^2	1	24.510	24.510	0.38	0.582	1	0.372	0.372	2.51	0.212
$T_h^*t_h$	1	150.690	150.690	2.32	0.225	1	0.012	0.012	0.08	0.795
Error	3	194.770	64.920	–	–	3	0.445	0.148	–	–
Total	8	2029.410	–	–	–	8	21.300	–	–	–
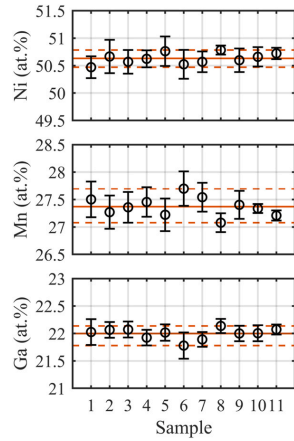
Fig. 3. Compositions of the studied samples. The solid line indicates the average value of all samples combined, while the dashed lines indicate the minimum and maximum values.

content. Overall, the observed differences in the average sample compositions were insignificant and not likely to impact on the magneto-structural properties of the samples. The XRF measurements did not reveal any distinct change of composition within each sample. Deviations of composition within the size scales smaller than the diameter of the used collimator (300 µm) were undetectable in each measurement. However, [42] showed that as-built material is overall homogenous also in smaller size scales. Foremost, all samples exhibited standard deviations of the measured compositions approximately within the accuracy of the measurement (0.3 at%). The standard deviations of the measured compositions are smaller in samples with longer homogenization times or higher homogenization temperatures, implying a chemical homogeneity increase.

Fig. 4 shows SEM images perpendicular to the build direction obtained from sections of the as-built sample (S_1) and the selected heat-treated samples (S_2, S_6, and S_{11}). The boundaries between adjacent laser scanning tracks are marked with red dotted lines. The presented SEM images were obtained with relatively low magnifications of 200x and 400x using a backscattered electron detector and a relatively low acceleration voltage of 3 kV to increase the channeling contrast. This approach provided a high grain contrast but was not ideal for observing individual twins that were generally too narrow to be imaged using the obtained pixel resolution. Polarized light microscopy was later used to observe the martensitic twins within the samples.

The microstructure of the as-built samples was highly anisotropic, as expected for a material built via L-PBF. The SEM image in Fig. 4 shows
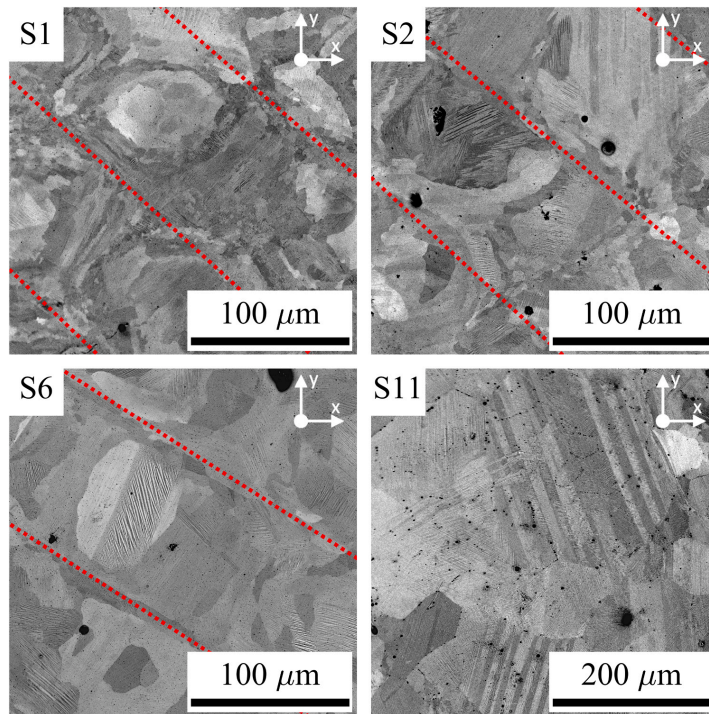

Fig. 4. SEM images of the microstructures in sections perpendicular to the build direction obtained from the as-built sample (S_1), the ordered sample (S_2), the sample homogenized at 1040 °C for 6 h (S_6), and the sample homogenized at 1080 °C for 24 h (S_{11}). The dotted lines indicate observed boundaries between adjacent laser-scanning tracks.

that the as-built sample, S_1, exhibited a columnar grain texture. This is a texture that develops when columnar grains grow along the normal direction to the edge of melt pools induced by the large directional thermal gradients during manufacturing via L-PBF. Additionally, finer grains were located between the relatively larger columnar grains at boundaries between adjacent laser-scanning tracks. Consequently, the microstructure exhibits clearly distinguishable boundaries between each laser scan track. The L-PBF did not produce a dendritic cooling structure, which is considered beneficial for obtaining typical magneto-structural properties after heat treatment. Overall, the grains formed during the solidification in L-PBF were relatively small, with an average grain size of 13.5 µm. This observation is in good agreement with the values previously reported in [42]. Some intergranular cracking was observed within the built samples, which was expected based on previous research. The location, size, number and distribution of the observed cracks appeared to be random. Overall, Ni-Mn-Ga based MSM alloys are extremely brittle because of their low deformability [63]. The previously built layers undergo repetitive heating/cooling through martensitic transformation, which may generate stresses that contribute to the cracking phenomenon. Additionally, some of the cracks may appear during sample preparation (e.g. during cutting or grinding). Therefore, future efforts should be placed towards systematic analysis of the cracking phenomenon using micro-computed tomography.

It is particularly clear that during the homogenization treatment at 1080 °C for 24 h, sample S_{11} underwent considerable recrystallization. As a result, the boundaries between adjacent laser-scanning tracks are no longer observable with this sample and the observed structure shows predominantly large equiaxed grains. Additionally, the observed change from the primary columnar grains of the as-built sample S_1 to the equiaxed grains of sample S_{11} is gradual – as seen when comparing the SEM images of different samples in Fig. 4. Consequently, all heat-treated samples exhibited grain growth in comparison to the as-built material. Table 3 and Fig. 5 show the volume-weighted average grain sizes of the built samples. The observed grain growth was overall equal throughout the volume of each sample, although some singular larger grains formed near the edges of these samples. Homogenization treatments at 1000 °C and 1040 °C for 6–12 h resulted in only negligible grain growth, whereas the samples homogenized for 24 h showed a larger average grain size increase. A significant average grain size increase was observed with the samples that were homogenized at 1080 °C for 12 and 24 h. For example, the heat-treated sample S_{11} exhibited a large quantity of grains exceeding 300 µm in diameter – see the SEM image in Fig. 4 and the polarized light optical image in Fig. 6. Indeed, the ANOVA in Table 4 shows a statistically significant dependency between the observed grain size and the applied homogenization temperature and time. It is expected that homogenization temperatures below 1080 °C would require considerably longer treatment times in order to increase diffusion and achieve a significant average grain size increase. Obtaining a large grain size is considered beneficial for the manufacturing of bamboo-grained Ni-Mn-Ga structures, in which neighboring grains are

less constrained and pose fewer obstacles to twin boundary motion. Future efforts should be aimed at alloying Ni-Mn-Ga with additive elements to enhance grain growth.

All as-built and heat-treated samples exhibited microstructures with martensitic twins. These twins were thermally induced during martensitic transformation when the material cooled following L-PBF or heat treatment. A previous study by [42] showed that as-built Ni-Mn-Ga exhibits twinned martensite with weak magnetic anisotropy. Based on the observation using a polarized light microscope, a few areas of sample S_{11} with the largest features attributed to the twins were chosen for AFM/MFM scanning. Fig. 6 shows an example optical image of the sample surface with the MFM images obtained from specified locations outlined with white squares. The optical image was obtained with a long exposure as the overall contrast of the twins was less pronounced in comparison to standard Ni-Mn-Ga single crystalline samples. In this image, very thin stripes are visible (at the limit of optical resolution), in full agreement with the obtained MFM images. The orientation of the twins appears to vary from grain to grain. In some areas, no stripes could be observed, which is possibly due to the thickness of the twins being under the optical resolution limit. The presented MFM images demonstrate contrast complexity, revealing thick bands that correspond to the optical polarized light contrast and thinner bands with thicknesses down to the nanoscale. Thus, the thicker bands are composed of very narrow bands. This explains the unusually weak contrast obtained for the optical images. Some of the observed variations could also be linked to the MFM contrast differences between different variants at different angles depending on the localized crystalline orientation of each grain. Additionally, the MFM image obtained from A1 shows visible signs of branching in the central band. The observed twin structure is consistent with polycrystalline Ni-Mn-Ga 14 M martensites [64], which was also confirmed by XRD measurement. Overall, homogenization at 1080 °C for 24 h drastically improved the contrast obtained with magnetic force microscopy in comparison to the as-built material in [42].

Fig. 7 shows the X-ray diffractograms obtained for each sample. The identified peaks have been indexed with respect to the coordinate system of the parent cubic phase (austenite). The unindexed diffraction peaks originate from the modulated superstructure. The recorded diffraction peaks were used to determine the average lattice parameters shown in Table 5, whereby the presented constants correspond to the seven-layered modulated orthorhombic (14 M) and five-layered modulated tetragonal (10 M) martensites in the coordinate system of the parent cubic phase. Only the main diffraction peaks were considered in calculating the lattice parameters.

All samples were first inspected at 100 °C, where they exhibited an austenitic crystal structure. All diffraction peaks from each sample at ambient temperature must, therefore, have originated from one or several martensite phases. A large majority of the observed peaks correspond with the orthorhombic structure of 14 M martensite, whereas the consideration of the additional peaks provides a very reasonable correspondence with the 10 M martensite. Therefore, it can be said with high confidence that the as-built sample S_1 showed a mixed crystal structure of 14 M and 10 M martensites. The intensity of the 10 M peaks at the angles of ~62.0° and ~62.5° is moderately high with both samples S_1 and S_2 but is considerably reduced with all homogenized samples. As a result, the lattice parameters of the 10 M martensite could only be obtained for the samples $S_{1\rightarrow5}$. After homogenization at 1080 °C for 12–24 h, the samples showed only the diffraction peaks originating from 14 M martensite at ambient temperature. The electron concentration values in Table 3 show that all samples are distant from compositions (e/a≈7.7) that are more likely to exhibit co-existing martensite phases at ambient temperature [43]. Therefore, the presence of the 10 M phase in the as-built samples must relate to the inhomogeneity of the chemical composition typically present in the anisotropic microstructures developed during L-PBF. Homogenization at elevated temperatures above 1040 °C leads to chemical homogenization, which increases the stability of the 14 M martensite at the cost of
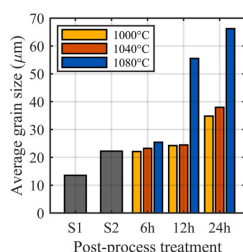

Fig. 5. Average grain sizes of the samples as measured from multiple sections of each sample perpendicular to the build direction.
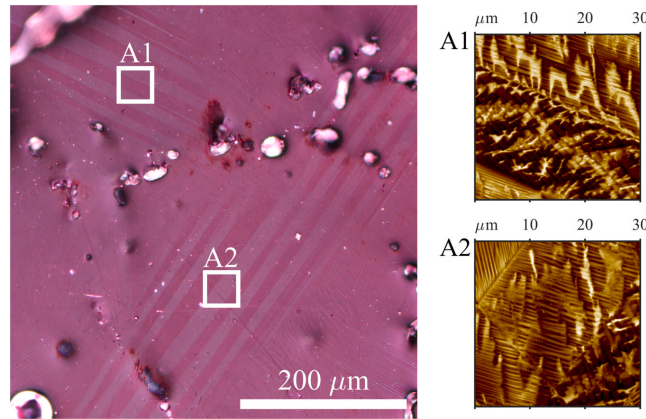
Fig. 6. Optical image with polarized light contrast of the L-PBF sample S₁₁ homogenized at 1080 ℃ for 24 h (left). The image was taken perpendicular to the build direction. Areas A1 and A2 correspond to the locations of the two MFM scans shown on the right.
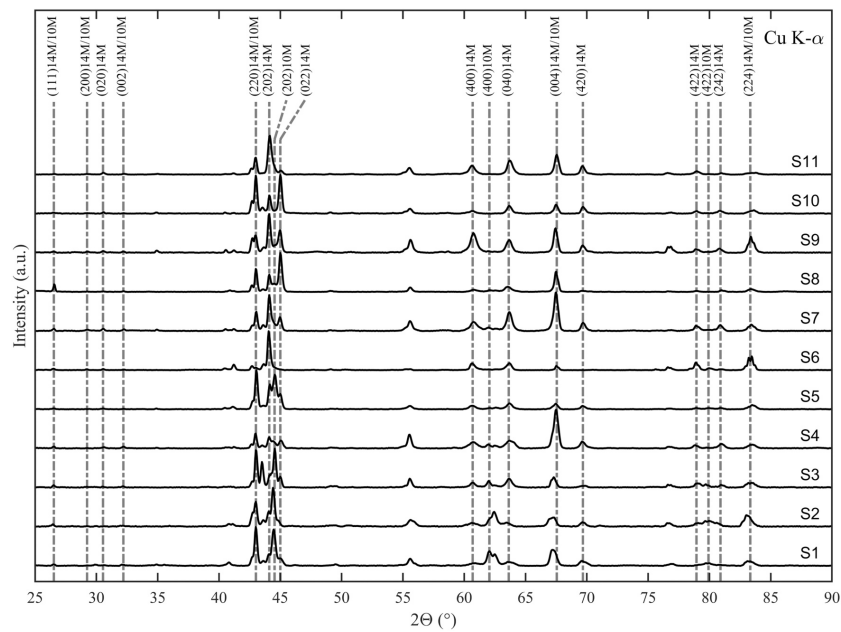

Fig. 7. XRD patterns obtained for each sample recorded at ambient temperature. Intensities have been scaled and the baseline is offset. Recognized peaks of the 14 M and 10 M martensites are marked with gray dashed lines and indexed with respect to the coordinate system of the parent austenite unit cell.

the 10 M martensite. Overall, the samples showed very little lattice parameter variation from sample to sample, which was expected based on the consistency of average compositions from sample to sample observed via XRF.

Additionally, the variation and distribution of peak intensities within the measured samples suggest the presence of a crystallographic texture. However, a more thorough analysis of the crystallographic texture is not feasible here due to the complex nature of the diffraction patterns produced by modulated Ni-Mn-Ga martensites. Future efforts, therefore, should be focused on a systematic analysis of the crystallographic texture using the austenite cubic phase as well as other methods, such as electron backscatter diffraction (EBSD). This is considered important because the occurrence of MFIS in polycrystalline material is enhanced by increasing texture [21–24].

Table 5

Lattice parameters obtained for each sample corresponding to the 14 M and 10 M martensites. All lattice constants are presented in the cubic coordinate system with an approximate accuracy of ± 0.005 Å and ± 0.01°.

| Sample | 14 M | | | | | | 10 M | | | | |
	a (Å)	b (Å)	c (Å)	γ (°)	Vol (Å³)	c/a (-)	a, b (Å)	c (Å)	γ (°)	Vol (Å³)	c/a (-)
S_1	6.102	5.851	5.551	90.47	198.18	0.910	5.972	5.569	90.32	198.61	0.933
S_2	6.103	5.849	5.552	90.48	198.18	0.910	5.979	5.567	90.34	199.01	0.931
S_3	6.099	5.852	5.555	90.53	198.26	0.911	5.983	5.556	90.29	198.88	0.929
S_4	6.103	5.848	5.552	90.50	198.15	0.910	5.984	5.571	90.34	199.48	0.931
S_5	6.102	5.849	5.548	90.51	198.00	0.909	5.978	5.546	90.32	198.19	0.928
S_6	6.105	5.850	5.551	90.51	198.24	0.909	–	–	–	–	–
S_7	6.094	5.852	5.553	90.49	198.02	0.911	–	–	–	–	–
S_8	6.102	5.851	5.548	90.46	198.07	0.909	–	–	–	–	–
S_9	6.110	5.847	5.552	90.51	198.34	0.909	–	–	–	–	–
S_{10}	6.099	5.852	5.554	90.50	198.22	0.911	–	–	–	–	–
S_{11}	6.101	5.845	5.548	90.52	197.84	0.909	–	–	–	–	–

Fig. 8 shows the results of the DSC and LFMS measurements for the as-built sample S_1 and the heat-treated sample S_{11}. The phase transformation and Curie temperatures obtained for each sample are summarized in Table 6. Two phase transformations are observed upon heating: the first-order structural transformation from 14 M martensite to cubic, and the second-order phase transformation from cubic ferromagnetic to cubic paramagnetic. The reverse transformations are observed upon cooling. A measurement using DSC showed that the martensitic transformation of the as-built sample was broad (~40 ℃), with a partially overlapped ambient temperature upon cooling. This implies that small amounts of the cubic phase may be present within the sample at ambient temperature. However, the cubic phase was not observed in XRD measurements at ambient temperature. Both the martensitic transformation and Curie temperatures (T_C) obtained for the as-built sample deviate from the values in the cited literature for a similar alloy composition, which was expected based on the previous study by [42].

Notably, all heat-treated samples, including sample S_2 with ordering treatment at 800 ℃ for 4 h without homogenization at a higher temperature, showed a recovery of the typical (with respect to chemical

Table 6

The martensitic transformation temperatures and magnetic properties of the studied samples.

| Sample | Martensitic transformation | | | | Magnetic properties | | |
	T_{AS} (℃)	T_{AF} (℃)	T_{MS} (℃)	T_{MF} (℃)	T_C (℃)	M_S (Am²/kg)	H_C (mT)
S_1	22	64	57	16	73–90	25	31
S_2	46	58	54	42	90	69	8
S_3	49	62	58	45	89	68	5
S_4	46	57	54	43	90	67	5
S_5	46	57	54	42	89	67	4
S_6	50	60	57	46	89	68	5
S_7	50	60	57	47	89	67	4
S_8	51	60	57	48	89	68	4
S_9	49	58	54	45	90	68	4
S_{10}	47	56	52	44	90	68	4
S_{11}	48	56	52	45	92	68	4

composition) magneto-structural properties and reversible martensitic transformations with narrow temperature hysteresis. Ordering treatment alone is not expected to induce a large increase in the homogeneity of the as-built material, which implies that the untypical magneto-structural properties of as-built Ni-Mn-Ga are mostly related to the atomic disorder and quenched-in stress from the L-PBF process. All heat-treated samples exhibited a similar martensitic transformation (average $T_{AS}≈48$ ℃, variation within ~5 ℃) and Curie temperatures (average $T_C≈90$ ℃, variation within ~3 ℃), with only a small variation from sample to sample. The observed differences are suggested to originate from these small composition variations. Achieving martensitic transformation right above ambient temperature is considered promising for achieving low twinning stress. For all heat-treated samples, the temperature hysteresis of martensitic transformation was in the range of 3–5 ℃. Additionally, Fig. 9 shows that increasing the homogenization temperature or time resulted in a decreased width of the austenite-14 M
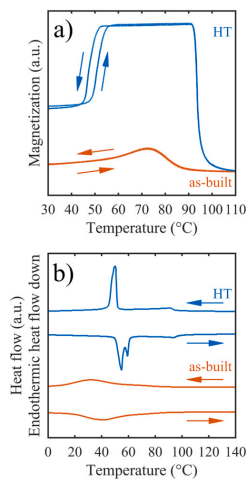
Fig. 8. Martensitic transformation and Curie temperatures obtained for a heat-treated sample (S_{11}) and the as-built sample (S_1): (a) LFMS (magnetization versus temperature); (b) DSC (heat flow versus temperature). All curves have been normalized against sample masses, with the magnetization of paramagnetic austenite as the zero-magnetization level for LFMS measurement.
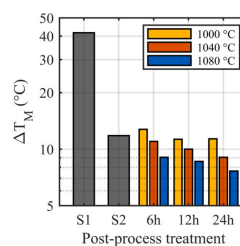
Fig. 9. Variation of the width of the martensitic transformation (ΔT_M) from sample to sample.

martensite transformation (ΔT_M). Additionally, the ANOVA in Table 4 confirms that both applied parameters were statistically significant for ΔT_M. This change is likely attributed to the general increase of the homogeneity of the heat-treated material in comparison to the as-built material and the dissolving of the 10 M martensite, as observed earlier via XRD measurements. However, 14 M martensite has been shown to exhibit broader transitions compared to 10 M martensite [65], which may limit a further reduction of ΔT_M. Additionally, the observed transitions are wider in comparison to the transitions observed in conventional Ni-Mn-Ga single crystals.

As can be observed from Fig. 8b, upon heating, the DSC measurement of the heat-treated sample S_{11} showed two transformation peaks, with the same observation being made over multiple measurement repetitions. The observed peak splitting may relate to intermartensitic transformation in Ni-Mn-Ga. For this purpose, the section of S_{11} used in the DSC measurement was re-polished and subjected to stepwise in-situ XRD measurement with heating and cooling of the sample over martensitic transformation. The X-ray diffractograms obtained from $2\Theta= 60$–$70°$ are shown in Fig. 10. At 46 °C, the sample exhibited a diffraction pattern typical for a 14 M structure. Upon heating (Fig. 10a) the diffraction pattern changed as the 14 M structure was transformed into a cubic $L2_1$ structure. Upon cooling, a reverse change was observed (Fig. 10b). The transformations in diffraction patterns were observed at 53–55 °C upon heating and at 53–51 °C upon cooling. The observed changes occurred in the temperature range of ~2 °C, which is considerably narrower in comparison to ΔT_M measured using LFMS or DSC. This was expected because martensitic transformation does not occur simultaneously throughout the sample, and XRD reveals structural changes in a thin layer on the sample surface, whereas LFMS and DSC obtain information from the whole sample volume. Overall, the diffraction data revealed the absence of intermediate phases during martensitic and reverse martensitic transformations. Therefore, the observed splitting of the transformation peak upon heating in DSC measurements may be related to the presence of structural defects such as pores or cracks. The observed anomaly was not observed upon cooling, which supports this argument.
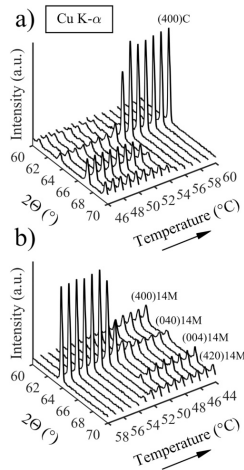
The additional LFMS curve comparison in Fig. 8a shows that the as-built sample S_1 has inferior magnetization to the heat-treated samples. The applied LFMS setup could only provide qualitative information about magnetization and, therefore, VSM was used to measure the magnetization of each sample as a function of magnetic field strength. Fig. 11 presents the results of VSM measurement for the as-built sample S_1 and the heat-treated sample S_{11}. The same hysteresis loops were obtained for all samples. The saturation magnetizations (M_S) and coercive fields (H_C) determined for each sample are summarized in Table 6. The measured saturation magnetization of the as-built sample was small (25 Am^2/kg), whereas the saturation magnetizations (average ~68 Am^2/kg) for the heat-treated samples were nearly identical to the saturation magnetizations previously reported in the scientific literature for Ni-Mn-Ga with the same electron concentrations [47]. Hence, there was a clear increase of nearly ~170% in the magnetization of all heat-treated samples in comparison to the as-built sample. Overall, with the heat-treated samples, the variation of saturation magnetization between the samples was small (approximately ± 1 Am^2/kg), which was expected because all samples exhibited mostly the same crystal structure and were equally dense. The larger grain size obtained for the samples homogenized at 1080 °C for 12–24 h did not seem to influence the observed saturation magnetizations. The coercive field of the as-built sample S_1 ($H_C \approx 31$ mT) was relatively high compared to the ordered sample S_2 ($H_C \approx 8$ mT) and the homogenized samples $S_{3 \to 11}$ ($H_C \approx 4$–5 mT). A previous investigation into the L-DED of Ni-Mn-Ga [35] suggested that the observed coercive field decrease after heat treatment may relate to the decrease in the number of magnetic domain pinning sites, such as defects and grain boundaries, in comparison to the as-built material. The saturation field for all heat-treated samples was in the approximate range of 0.6–0.8 T, which is within the expected values for polycrystalline Ni-Mn-Ga 14 M martensites.

4. Conclusion

In this study, a Ni-Mn-Ga magnetic shape memory (MSM) alloy was built via laser powder bed fusion (L-PBF). The built samples were subjected to stepwise chemical homogenization and atomic ordering heat treatments. The experiments were implemented following a systematic experimental design using the temperature and duration of the homogenization treatment as the varied parameters.

All produced samples were highly dense (average ~98.4%) with the average composition of the as-built samples at $Ni_{50.5}Mn_{27.5}Ga_{22.0}$. The samples showed only a minor variation of relative density and chemical composition from sample to sample. The as-built material showed a broad austenite-martensite transformation and low saturation magnetization. The crystal structure of the as-built material at ambient temperature was a mixture of seven-layered modulated orthorhombic (14 M) and five-layered modulated tetragonal (10 M) martensites.

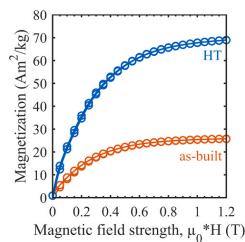Notably, ordering heat treatment at 800 °C for 4 h without

Fig. 10. Martensitic transformation of a heat-treated sample (S_{11}) imaged through the evolution of the obtained XRD patterns as a function of the applied measurement temperature. Intensities have been scaled and the baseline is used as an offset for each measurement. Recognized peaks are indexed with respect to the coordinate system of the austenite unit cell. (a) Heating from 46 to 60 °C; (b) cooling from 58 to 44 °C.

Fig. 11. The VSM magnetization curves obtained for a heat-treated sample (S_{11}) and the as-built sample (S_1).

homogenization at higher temperature was enough to obtain the narrow austenite-14 M martensite transformation, Curie temperature, and saturation magnetization typical for bulk samples of the same composition. This suggests that the atomic disorder and quenched-in stress from the L-PBF process are the primary factors influencing the untypical magneto-structural properties of the as-built Ni-Mn-Ga. Finally, homogenization at 1080 °C stabilized the 14 M martensite structure at ambient temperature and resulted in considerable grain growth for homogenization times above 12 h.

Overall, the results show that post-process heat treatment can considerably improve the magneto-structural properties of Ni-Mn-Ga built via L-PBF. However, the bulk samples produced in this study exhibit grain boundary constraints that hinder the development of macroscopic magnetic-field-induced strains. Therefore, future efforts should be placed on systematic development of the L-PBF process towards manufacturing of foam-like (bamboo-grained) lattice structures with enhanced crystallographic texture.

Declaration of Competing Interest

The authors declare that they have no known competing financial interests or personal relationships that could have appeared to influence the work reported in this paper.

Acknowledgments

References

[1] K. Ullakko, J. Huang, C. Kantner, R. O'Handley, V.V. Kokorin, Large magnetic-field-induced strains in Ni2MnGa single crystals, Appl. Phys. Lett. 69 (1996) 1966–1968, https://doi.org/10.1063/1.117637.

[2] K. Ullakko, J. Huang, V. Kokorin, R. O'Handley, Magnetically controlled shape memory effect in Ni2MnGa intermetallics, Scr. Mater. 36 (1997) 1133–1138, https://doi.org/10.1016/S1359-6462(96)00483-6.

[3] S. Murray, M. Marioni, S. Allen, R. O'Handley, T. Lograsso, 6% magnetic-field-induced strain by twin-boundary motion in ferromagnetic Ni–Mn–Ga, Appl. Phys. Lett. 77 (2000) 886–888, https://doi.org/10.1063/1.1306635.

[4] A. Sozinov, A. Likhachev, N. Lanska, K. Ullakko, Giant magnetic-field-induced strain in NiMnGa seven-layered martensitic phase, Appl. Phys. Lett. 80 (2002) 1746–1748, https://doi.org/10.1063/1.1458075.

[5] A. Likhachev, A. Sozinov, K. Ullakko, Modeling the strain response, magneto-mechanical cycling under the external stress, work output and energy losses in Ni–Mn–Ga, Mech. Mater. 38 (2006) 551–563, https://doi.org/10.1016/j.mechmat.2005.05.022.

[6] V. Chernenko, M. Chmielus, P. Müllner, Large magnetic-field-induced strains in Ni–Mn–Ga nonmodulated martensite, Appl. Phys. Lett. 95 (2009) 104103, https://doi.org/10.1063/1.3227661.

[7] A. Sozinov, N. Lanska, A. Soroka, W. Zou, 12% magnetic field-induced strain in Ni-Mn-Ga-based non-modulated martensite, Appl. Phys. Lett. 102 (2013), 021902, https://doi.org/10.1063/1.4775677.

[8] D. Musiienko, L. Straka, L. Klimša, A. Saren, A. Sozinov, O. Heczko, K. Ullakko, Giant magnetic-field-induced strain in Ni-Mn-Ga micropillars, Scr. Mater. 150 (2018) 173–176, https://doi.org/10.1016/j.scriptamat.2018.03.020.

[9] D. Musiienko, A. Saren, L. Straka, M. Vronka, J. Kopeček, O. Heczko, A. Sozinov, K. Ullakko, Ultrafast actuation of Ni-Mn-Ga micropillars by pulsed magnetic field, Scr. Mater. 162 (2019) 482–485, https://doi.org/10.1016/j.scriptamat.2018.12.009.

[10] K. Ullakko, L. Wendell, A. Smith, P. Müllner, G. Hampikian, A magnetic shape memory micropump: contact-free, and compatible with PCR and human DNA profiling, Smart Mater. Struct. 21 (2012), 115020, https://doi.org/10.1088/0964-1726/21/11/115020.

[11] A. Smith, A. Saren, J. Järvinen, K. Ullakko, Characterization of a high-resolution solid-state micropump that can be integrated into microfluidic systems, Microfluid. Nanofluid. 18 (2015) 1255–1263, https://doi.org/10.1007/s10404-014-1524-6.

[12] S. Barker, E. Rhoads, P. Lindquist, M. Vreugdenhil, P. Müllner, Magnetic shape memory micropump for submicroliter intracranial drug delivery in rats, J. Med. Devices 10 (2016), 041009, https://doi.org/10.1115/1.4034576.

[13] A. Saren, A. Smith, K. Ullakko, Integratable magnetic shape memory micropump for high-pressure, precision microfluidic applications, Microfluid. Nanofluid. 22 (2018) 38, https://doi.org/10.1007/s10404-018-2058-0.

[14] A. Saren, D. Musiienko, A. Smith, J. Tellinen, K. Ullakko, Modeling and design of a vibration energy harvester using the magnetic shape memory effect, Smart Mater. Struct. 24 (2015), 095002, https://doi.org/10.1088/0964-1726/24/9/095002.

[15] P. Lindquist, T. Hobza, C. Patrick, P. Müllner, Efficiency of energy harvesting in Ni–Mn–Ga shape memory alloys, Shap. Mem. Superelasticity 4 (2018) 93–101, https://doi.org/10.1007/s40830-018-0158-z.

[16] A. Hobza, C. Patrick, K. Ullakko, N. Rafla, P. Lindquist, P. Müllner, Sensing strain with Ni-Mn-Ga, Sens. Actuators A 269 (2018) 137–144, https://doi.org/10.1016/j.sna.2017.11.002.

[17] M. Chmielus, X. Zhang, C. Witherspoon, D. Dunand, P. Müllner, Giant magnetic-field-induced strains in polycrystalline Ni–Mn–Ga foams, Nat. Mater. 8 (2009) 863–866, https://doi.org/10.1038/nmat2527.

[18] X. Zhang, C. Witherspoon, P. Müllner, D. Dunand, Effect of pore architecture on magnetic-field-induced strain in polycrystalline Ni–Mn–Ga, Acta Mater. 59 (2011) 2229–2239, https://doi.org/10.1016/j.actamat.2010.12.026.

[19] P. Zheng, N. Kucza, Z. Wang, P. Müllner, D. Dunand, Effect of directional solidification on texture and magnetic-field-induced strain in Ni–Mn–Ga foams with coarse grains, Acta Mater. 86 (2015) 95–101, https://doi.org/10.1016/j.actamat.2014.12.005.

[20] C. Witherspoon, P. Zheng, M. Chmielus, D. Dunand, P. Müllner, Effect of porosity on the magneto-mechanical behavior of polycrystalline magnetic shape-memory Ni–Mn–Ga foams, Acta Mater. 92 (2015) 64–71, https://doi.org/10.1016/j.actamat.2015.03.038.

[21] K. Ullakko, Y. Ezer, A. Sozinov, G. Kimmel, P. Yakovenko, V. Lindroos, Magnetic-field-induced strains in polycrystalline Ni-Mn-Ga at room temperature, Scr. Mater. 44 (2001) 475–480, https://doi.org/10.1016/S1359-6462(00)00610-2.

[22] U. Gaitzsch, M. Pötschke, S. Roth, B. Rellinghaus, L. Schultz, A 1% magnetostrain in polycrystalline 5M Ni–Mn–Ga, Acta Mater. 57 (2009) 365–370, https://doi.org/10.1016/j.actamat.2008.09.017.

[23] C. Hürrich, S. Roth, H. Wendrock, M. Pötschke, D. Cong, B. Rellinghaus, L. Schultz, Influence of grain size and training temperature on strain of polycrystalline Ni50Mn29Ga21samples, J. Phys. Conf. Ser. 303 (2011), 012080, https://doi.org/10.1088/1742-6596/303/1/012080.

[24] U. Gaitzsch, J. Romberg, M. Pötschke, S. Roth, P. Müllner, Stable magnetic-field-induced strain above 1% in polycrystalline Ni–Mn–Ga, Scr. Mater. 65 (2011) 679–682, https://doi.org/10.1016/j.scriptamat.2011.07.011.

[25] S. Taylor, R. Shah, D. Dunand, Ni-Mn-Ga micro-trusses via sintering of 3D-printed inks containing elemental powders, Acta Mater. 143 (2017) 20–29, https://doi.org/10.1016/j.actamat.2017.10.002.

[26] S. Taylor, R. Shah, D. Dunand, Microstructure and porosity evolution during sintering of Ni-Mn-Ga wires printed from inks containing elemental powders, Intermetallics 104 (2019) 113–123, https://doi.org/10.1016/j.intermet.2018.10.024.

[27] M. Caputo, C.V. Solomon, P.-K. Nguyen, A.E. Berkowitz, Electron microscopy investigation of binder saturation and microstructural defects in functional parts made by additive manufacturing, Microsc. Microanal. 22 (2016) 1770–1771, https://doi.org/10.1017/S1431927616009697.

[28] A. Mostafaei, K. Kimes, E. Stevens, J. Toman, Y. Krimer, K. Ullakko, M. Chmielus, Microstructural evolution and magnetic properties of binder jet additive manufactured Ni-Mn-Ga magnetic shape memory alloy foam, Acta Mater. 131 (2017) 482–490, https://doi.org/10.1016/j.actamat.2017.04.010.

[29] M. Caputo, C.V. Solomon, Microstructure and chemical composition analysis of additive manufactured Ni-Mn-Ga parts sintered in different conditions, Microsc. Microanal. 23 (2017) 2078–2079, https://doi.org/10.1017/S1431927617011059.

[30] M. Caputo, C.V. Solomon, A facile method for producing porous parts with complex geometries from ferromagnetic Ni-Mn-Ga shape memory alloys, Mater. Lett. 200 (2017) 87–89, https://doi.org/10.1016/j.matlet.2017.04.112.

[31] M. Caputo, A. Berkowitz, A. Armstrong, P. Müllner, C.V. Solomon, 4D printing of net shape parts made from Ni-Mn-Ga magnetic shape-memory alloys, Addit. Manuf. 21 (2018) 579–588, https://doi.org/10.1016/j.addma.2018.03.028.

[32] A. Mostafaei, P. Rodriguez, E. Stevens, M. Chmielus, Sintering regimes and resulting microstructure and properties of binder jet 3D printed Ni-Mn-Ga magnetic shape memory alloys, Acta Mater. 154 (2018) 355–364, https://doi.org/10.1016/j.actamat.2018.05.047.

[33] M. Caputo, D. Waryoba, C. Solomon, Sintering effects on additive manufactured Ni–Mn–Ga shape memory alloys: a microstructure and thermal analysis, J. Mater. Sci. 55 (2020) 5311–5321, https://doi.org/10.1007/s10853-020-04352-9.

[34] E. Stevens, K. Kimes, A. Mostafaei, D. Salazar, R. Rodriguez, A. Acierno, P. Lázpita, V. Chernenko, M. Chmielus, Mastering a 1.2 K hysteresis for martensitic para-ferromagnetic partial transformation in Ni-Mn(Cu)-Ga magnetocaloric material via binder jet 3D printing, Addit. Manuf. (2020), 101560, https://doi.org/10.1016/j.addma.2020.101560.

[35] J. Toman, P. Müllner, M. Chmielus, Properties of as-deposited and heat-treated Ni-Mn-Ga magnetic shape memory alloy processed by directed energy deposition, J. Alloy. Compd. 752 (2018) 455–463, https://doi.org/10.1016/j.jallcom.2018.04.059.

[36] E. Stevens, J. Toman, K. Kimes, V. Chernenko, A. Wojcik, W. Maziarz, M. Chmielus, Microstructural evaluation of magnetocaloric Ni-Co-Mn-Sn produced by directed energy deposition, Microsc. Microanal. 22 (2016) 1774–1775, https://doi.org/10.1017/S1431927616009715.

[37] E. Stevens, K. Kimes, V. Chernenko, P. Lazpita, A. Wojcik, W. Maziarz, M. Chmielus, Direct laser deposition and homogenization of Ni-Co-Mn-Sn

magnetocaloric material, Microsc. Microanal. 24 (2018) 956–957, https://doi.org/10.1017/S1431927618005275.

[38] K. Ullakko, V. Laitinen, A. Saren, A. Sozinov, D. Musiienko, M. Chmielus, A. Salminen, Ni-Mn-Ga actuating elements manufactured using 3D printing, 11th European Symposium on Martensitic Transformations, Metz, 27–31 August 2018.

[39] V. Laitinen, A. Salminen, K. Ullakko, First investigation on processing parameters for laser powder bed fusion of Ni-Mn-Ga magnetic shape memory alloy, J. Laser Appl. 31 (2019), 022303, https://doi.org/10.2351/1.5096108.

[40] F. Nilsén, I. Ituarte, M. Salmi, J. Partanen, S. Hannula, Effect of process parameters on non-modulated Ni-Mn-Ga alloy manufactured using powder bed fusion, Addit. Manuf. 28 (2019) 464–474, https://doi.org/10.1016/j.addma.2019.05.029.

[41] V. Laitinen, A. Sozinov, A. Saren, A. Salminen, K. Ullakko, Laser based 4D printing of Ni-Mn-Ga MSM alloy, The 6th International Conference on Ferromagnetic Shape Memory Alloys: book of abstracts (2019) 156–157. ISBN 978-80-905962-9-0.

[42] V. Laitinen, A. Sozinov, A. Saren, A. Salminen, K. Ullakko, Laser powder bed fusion of Ni-Mn-Ga magnetic shape memory alloy, Addit. Manuf. 30 (2019), 100891, https://doi.org/10.1016/j.addma.2019.100891.

[43] V. Chernenko, Compositional instability of β-phase in Ni-Mn-Ga alloys, Scr. Mater. 40 (1999) 523–527, https://doi.org/10.1016/S1359-6462(98)00494-1.

[44] X. Jin, M. Marioni, D. Bono, S. Allen, R. O'Handley, T. Hsu, Empirical mapping of Ni–Mn–Ga properties with composition and valence electron concentration, J. Appl. Phys. 91 (2002) 8222, https://doi.org/10.1063/1.1453943.

[45] I. Takeuchi, O. Famodu, J. Read, M. Aronova, K. Chang, C. Craciunescu, S. Lofland, M. Wuttig, F. Wellstood, L. Knauss, A. Orozco, Identification of novel compositions of ferromagnetic shape-memory alloys using composition spreads, Nat. Mater. 2 (2003) 180–184, https://doi.org/10.1038/nmat829.

[46] N. Lanska, O. Soderberg, A. Sozinov, Y. Ge, K. Ullakko, V.K. Lindroos, Composition and temperature dependence of the crystal structure of Ni–Mn–Ga alloys, J. Appl. Phys. 95 (2004) 8074–8078, https://doi.org/10.1063/1.1748860.

[47] O. Heczko, L. Straka, Compositional dependence of structure, magnetization and magnetic anisotropy in Ni–Mn–Ga magnetic shape memory alloys, J. Magn. Magn. Mater. 272–276 (2004) 2045–2046, https://doi.org/10.1016/j.jmmm.2003.12.819.

[48] M. Richard, J. Feuchtwanger, D. Schlagel, T. Lograsso, S. Allen, R. O'Handley, Crystal structure and transformation behavior of Ni–Mn–Ga martensites, Scr. Mater. 54 (2006) 1797–1801, https://doi.org/10.1016/j.scriptamat.2006.01.033.

[49] S. Yang, C. Wang, X. Liu, Phase equilibria and composition dependence of martensitic transformation in Ni–Mn–Ga ternary system, Intermetallics 25 (2012) 101–108, https://doi.org/10.1016/j.intermet.2011.12.009.

[50] R. Overholser, M. Wuttig, D. Neumann, Chemical ordering in Ni-Mn-Ga Heusler alloys, Scr. Mater. 40 (1999) 1095–1102, https://doi.org/10.1016/S1359-6462(99)00080-9.

[51] D. Schlagel, Y. Wu, W. Zhang, T. Lograsso, Chemical segregation during bulk single crystal preparation of Ni–Mn–Ga ferromagnetic shape memory alloys, J. Alloy. Compd. 312 (2000) 77–85, https://doi.org/10.1016/S0925-8388(00)01161-0.

[52] M. Kreissl, K. Neumann, T. Stephens, K. Ziebeck, The influence of atomic order on the magnetic and structural properties of the ferromagnetic shape memory compound Ni2MnGa, J. Phys. Condens. Matter 15 (2003) 3831–3839, https://doi.org/10.1088/0953-8984/15/22/317.

[53] U. Gaitzsch, S. Roth, B. Rellinghaus, L. Schultz, Adjusting the crystal structure of NiMnGa shape memory ferromagnets, J. Magn. Magn. Mater. 305 (2006) 275–277, https://doi.org/10.1016/j.jmmm.2006.01.017.

[54] T. Goryczka, M. Gigla, H. Morawiec, Effect of quenching on martensitic transformation course in non-stoichiometric NiMnGa alloy, Int. J. Appl. Electromagn. Mech. 23 (2006) 81–88, https://doi.org/10.3233/JAE-2006-726.

[55] V. Sánchez-Alarcos, V. Recarte, J. Pérez-Landazábal, G. Cuello, Correlation between atomic order and the characteristics of the structural and magnetic transformations in Ni–Mn–Ga shape memory alloys, Acta Mater. 55 (2007) 3883–3889, https://doi.org/10.1016/j.actamat.2007.03.001.

[56] C. Segui, J. Pons, E. Cesari, Effect of atomic ordering on the phase transformations in Ni–Mn–Ga shape memory alloys, Acta Mater. 55 (2007) 1649–1655, https://doi.org/10.1016/j.actamat.2006.10.025.

[57] I. Aaltio, O. Söderberg, M. Friman, I. Glavatskyy, Y. Ge, N. Glavatska, S.-P. Hannula, Determining the liquidus and ordering temperatures of the ternary Ni-Mn-Ga and quaternary Ni-Mn-Ga-Fe/Cu alloys, 8th European Symposium on Martensitic Transformations, 2009 04001. https://doi.org/10.1051/esomat/200904001.

[58] A. Backen, R. Niemann, S. Kaufmann, J. Buschbeck, L. Schultz, S. Fähler, The effect of post annealing on structure, microstructure and magnetic prop erties of thin Ni-Mn-Ga films, 8th European Symposium on Martensitic Transformations, 2009 04002. https://doi.org/10.1051/esomat/200904002.

[59] B. Ingale, R. Gopalan, M. Rajasekhar, S. Ram, Studies on ordering temperature and martensite stabilization in Ni55Mn20−xGa25+x alloys, J. Alloy. Compd. 475 (2009) 276–280, https://doi.org/10.1016/j.jallcom.2008.08.004.

[60] M. Qian, X. Zhang, L. Wei, L. Geng, H. Peng, Effect of chemical ordering annealing on martensitic transformation and superelasticity in polycrystalline Ni–Mn–Ga microwires, J. Alloy. Compd. 645 (2015) 335–343. https://doi.org/10.1016/j.jallcom.2015.05.118.

[61] L. Straka, L. Fekete, M. Rameš, E. Belas, O. Heczko, Magnetic coercivity control by heat treatment in Heusler Ni–Mn–Ga(–B) single crystals, Acta Mater. 169 (2019) 109–121, https://doi.org/10.1016/j.actamat.2019.02.045.

[62] P. Lehto, H. Remes, T. Saukkonen, H. Hänninen, J. Romanoff, Influence of grain size distribution on the Hall–Petch relationship of welded structural steel, Mater. Sci. Eng. A 592 (2014) 28–39, https://doi.org/10.1016/j.msea.2013.10.094.

[63] L. Wei, X. Zhang, M. Qian, P. Martin, L. Geng, T. Scott, H. Peng, Compressive deformation of polycrystalline Ni-Mn-Ga alloys near chemical ordering transition temperature, Mater. Des. 142 (2018) 329–339, https://doi.org/10.1016/j.matdes.2018.01.048.

[64] Z. Li, Y. Jiang, Z. Li, Y. Yang, B. Yang, Y. Zhang, C. Esling, X. Zhao, L. Zuo, Texture inheritance from austenite to 7 M martensite in Ni–Mn–Ga melt-spun ribbons, Results Phys. 6 (2016) 428–433, https://doi.org/10.1016/j.rinp.2016.07.012.

[65] M. Richard, J. Feuchtwanger, S. Allen, R. O'handley, P. Lázpita, J. Barandiaran, Martensite transformation in Ni-Mn-Ga ferromagnetic shape-memory alloys, Metall. Mater. Trans. A 38 (2007) 777–780, https://doi.org/10.1007/s11661-007-9097-6.

Publication V

Laitinen, V., Saren, A., Sozinov, A., and Ullakko, K.
Giant 5.8% magnetic-field-induced strain in additive manufactured Ni-Mn-Ga magnetic shape memory alloy

Giant 5.8% magnetic-field-induced strain in additive manufactured Ni-Mn-Ga magnetic shape memory alloy

Ville Laitinen*, Andrey Saren, Alexei Sozinov, Kari Ullakko*

Material Physics Laboratory, Lappeenranta-Lahti University of Technology LUT, Lappeenranta 53850, Finland

ABSTRACT

Laser powder bed fusion (L-PBF) additive manufacturing process was employed to manufacture polycrystalline Ni-Mn-Ga samples. The samples were heat-treated for chemical homogenization and grain growth. It is demonstrated that the chemical composition, resulting martensitic crystal structures, and phase transformation temperatures of the L-PBF-built Ni-Mn-Ga can be precisely changed in-situ by controlling the selective evaporation of Mn through adjusting the process parameters. Subsequently, repeatable and fully reversible magnetic-field-induced strain of 5.8% was measured in a single crystalline grain of an additive manufactured polycrystalline Ni-Mn-Ga sample exhibiting a 10M martensitic structure at ambient temperature. The results indicate that L-PBF can be used to manufacture Ni-Mn-Ga devices containing active parts that can be strained by an external magnetic field.

© 2021 The Authors. Published by Elsevier Ltd on behalf of Acta Materialia Inc.
This is an open access article under the CC BY license (http://creativecommons.org/licenses/by/4.0/)

The magnetic shape memory (MSM) alloy Ni-Mn-Ga can develop giant reversible magnetic-field-induced strains (MFIS), when the twin variants of the low-symmetry martensitic phase are reoriented by twin boundary (TB) motion in response to an applied magnetic field [1–5]. This makes Ni-Mn-Ga a promising actuator material for microscale actuators, sensors, pumps, and energy conversion devices [6–12]. The maximum possible MFIS, which is determined by the crystallographic structure, reaches values of 6-12% and has been achieved almost exclusively in single crystals [3–5]. As the grain boundaries significantly hinder TB motion, fine-grained randomly textured polycrystalline Ni-Mn-Ga does not typically develop large MFIS [13]. However, sufficiently reducing these constraints can enable it to develop moderate MFIS, reaching ~8.7% MFIS [13] in directionally solidified Ni-Mn-Ga foam or ~1-4% MFIS [14–18] in coarse-grained bulk polycrystalline Ni-Mn-Ga with a strong crystallographic texture. Drawbacks of conventionally manufactured single crystals and polycrystalline Ni-Mn-Ga include low freedom of geometry and the high cost of production, which currently limit the development of novel functional MSM devices.

Additive manufacturing (AM) has attracted increasing attention as a promising method for manufacturing polycrystalline Ni-Mn-Ga, especially due to its feasibility for incorporating complex geometries or device structures. Recent investigations have demonstrated the feasibility of laser powder bed fusion (L-PBF)

for manufacturing polycrystalline Ni-Mn-Ga with high relative densities [19–24]. The non-equilibrium conditions and rapid heating/cooling during the layer-by-layer melting in L-PBF result in the selective evaporation of Mn, which, in combination with quenched-in stresses and atomic disorder, has been shown to significantly affect the final composition, resulting phase constitution, and magneto-structural properties of the built Ni-Mn-Ga. The initial composition-dependent material properties can be retained via heat treatment [23]. A severe shortcoming of recent research is that additively manufactured Ni-Mn-Ga has shown maximum strains of only 0.01% [19,25]. The reasons for the lack of large MFIS are numerous, ranging from process-induced internal defects [26] to metallurgical characteristics, such as a lack or randomness of the crystallographic texture or the relatively small grain size [22–23]. Additionally, the polycrystalline structure formed during solidification in L-PBF is unlikely to develop large MFIS without removal of grain boundary constraints through introduction of bamboo-like grain structure and/or magneto-mechanical training [13-14,16]. In response to these shortcomings, it is shown here that L-PBF-built Ni-Mn-Ga can develop giant fully reversible MFIS, and that the Mn evaporation during the process can be used to control the MSM-related properties of the built material.

A pre-alloyed $Ni_{48.7\pm0.1}Mn_{30.7\pm0.4}Ga_{20.6\pm0.3}$ powder ($d_{0.1}$=13.7 μm, $d_{0.5}$=32.8 μm, and $d_{0.9}$=69.5 μm; oxygen content <500 ppm) with approximately 2 at.% excess Mn in comparison to the typical 10M composition was prepared via gas atomization. All samples were built using an in-house-developed L-PBF system previously described in [22–23]. Fig. 1a presents a photographic image

* Corresponding authors.
E-mail addresses: ville.laitinen@lut.fi (V. Laitinen), kari.ullakko@lut.fi (K. Ullakko).
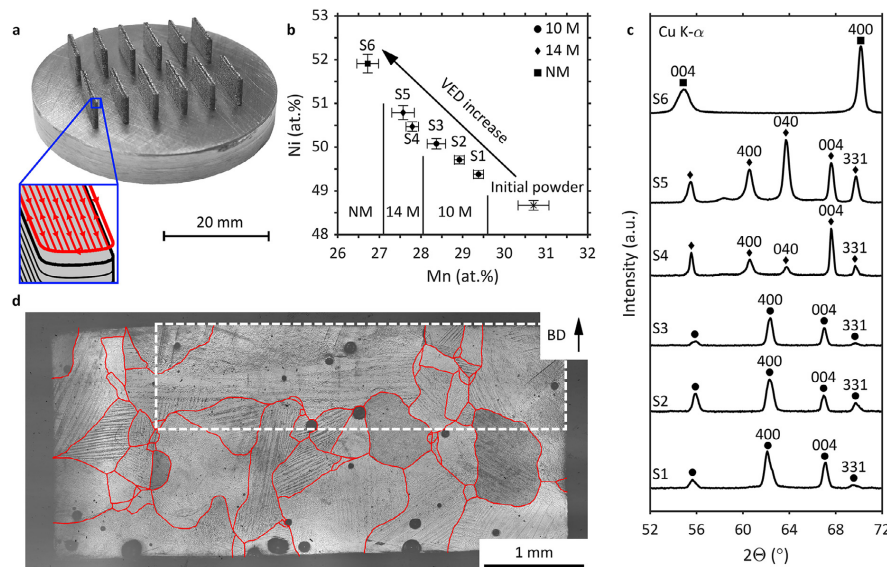
Fig. 1. Characterization of the Ni-Mn-Ga samples additively manufactured with the laser powder bed fusion process. a) Photo image of the as-built samples, S1-S12, built on a high-purity Ni substrate using different process parameters (see Table 1 for the parameters' values). Each sample has the dimensions 10 × 0.8 × 5 mm³. The inset shows the applied scanning strategy with respect to the sample geometry. b) Chemical composition (error bars correspond to standard measurement deviations) and the corresponding martensitic crystal structure at ambient temperature (295 K) for heat-treated samples S1-S6. c) A set of x-ray diffraction patterns obtained for heat-treated samples S1-S6 at 295 K. The peaks have been indexed with respect to the coordinate system of the parent austenite unit cell. The unindexed peaks originate from the modulated superstructure. d) Optical polarized light image of the heat-treated and polished sample S2 with the 10M structure revealing large single crystalline grains (outlined with red lines) with twins. BD notes the build direction. The twins are visible due to the use of polarized light contrast. The white rectangle marks the part of the sample containing the largest grain, which is further investigated in the magnetic actuation experiments.

Table 1
L-PBF process parameters and properties of the heat-treated samples.

	L-PBF process parameters			Chemical composition			Martensitic crystal structure at 295 K							Transformation temperatures		
Sample	P (W)	V (mm/s)	VED (J/mm³)	Ni (at.%, ±0.15)	Mn (at.%, ±0.15)	Ga (at.%, ±0.15)	Phase	a (Å, ±0.01)	b (Å, ±0.01)	c (Å, ±0.01)	γ (°, ±0.01)	Vol (Å³)	c/a (-)	T_A (K)	T_M (K)	T_C (K)
S1,S7	200	1300	34.2	49.38	29.38	21.25	10M	5.97	5.90	5.57	90.34	196.4	0.93	328	321	372
S2,S8	200	1000	44.4	49.71	28.92	21.37	10M	5.96	5.89	5.59	90.39	196.0	0.94	324	317	372
S3,S9	200	700	63.5	50.08	28.37	21.55	10M	5.95	5.89	5.58	90.32	195.8	0.94	323	317	369
S4,S10	190	500	84.4	50.47	27.79	21.73	14M	6.11	5.84	5.54	90.51	197.4	0.91	329	321	372
S5,S11	180	375	106.7	50.79	27.57	21.64	14M	6.11	5.84	5.54	90.47	197.5	0.91	334	330	365
S6,S12	160	250	142.2	51.91	26.72	21.37	NM	5.37	5.37	6.68	-	192.5	1.25	338	334	356

of samples S1-S12 (prior to heat treatment), which were built on a high-purity (>99.5%) Ni substrate (Ø 45 × 6.1 mm²) using the process parameters that were selected and adjusted for the excess Mn within the used powder based on the L-PBF process optimization presented in [22]. The varied L-PBF process parameters (laser power *P*; scanning speed *v*; volume energy density *VED*) and corresponding sample properties are summarized in Table 1. All samples were melted using constant hatch distance of 75 μm and powder layer thickness of 60 μm, while using a bidirectional scanning strategy without a turn in the scanning direction from layer to layer. All samples (10 × 0.8 × 5 mm³ thin walls) were built in a single patch at ambient temperature in a high-purity argon atmosphere without substrate preheating. The samples were oriented

on the substrate in a 2 × 6 matrix with ~4 mm distance between the samples so that the side faces of the walls were aligned at a 45° angle compared to the x-y hatch directions of the used L-PBF system.

After build, the samples were separated from the substrate using a Princeton Scientific Corporation WS-25 high-precision wire saw. All samples were heat treated in a single patch, using the setup previously described in [23], in an argon atmosphere at 1363 K for 24 hours with subsequent atomic ordering treatment at 1073 K for 4 hours followed by furnace cooling. Before heat treatment, the edges of each sample were cut off and ground to ensure a compatible sample size with the used alumina sample holders. Consequently, the heat-treated samples had a reduced size (~6 × 0.6 × 3

mm^3) in comparison to as-built samples. After the heat treatment, each sample was electropolished using a constant voltage of 14 V at 253 K in an electrolyte solution comprising 3 volume parts ethanol to 1 volume part 60% HNO_3.

The chemical compositions of the initial powder and L-PBF samples were determined using an Oxford Instruments X-Strata 960 X-ray fluorescence analyser with a Ø 300 μm collimator calibrated with a Ni-Mn-Ga reference sample. The L-PBF samples showed a consistent decreasing trend in the relative amount of Mn from sample to sample in comparison to the initial powder. This result is in agreement with previous studies [20–24], where it was shown that the evaporation of Mn during L-PBF increases with increasing *VED*. It is known that the crystal structure of Ni-Mn-Ga is highly composition-dependent [27], and maximum MFIS and martensite transformation temperatures can be significantly altered with small changes in chemical composition. Therefore, the composition, resulting crystal structure, and phase transformation temperatures of the built samples could be precisely changed by controlling the selective evaporation of Mn, see Fig. 1b.

The X-ray diffraction measurements were performed using a PANalytical Empyrean 3 diffractometer (Cu tube, λ=0.15406 nm) equipped with poly-capillary optics, a PIXcel3D-Medipix3 detector and a Si-510 zero background holder. The diffraction patterns of the samples are displayed in Fig 1c. Peaks belonging to the tetragonal five-layered modulated (10M), orthorhombic seven-layered modulated (14M), and non-modulated (NM) martensites are indexed with respect to the cubic coordinate system of the parent austenite. The corresponding martensite lattice parameters are summarized in Table 1. All samples exhibited a single martensite phase structure, thus implying that the applied heat treatment effectively increased the chemical homogeneity and reduced the residual stresses accumulated during the layer-by-layer melting in L-PBF. Additionally, the X-ray diffraction measurements did not detect any oxides, thus implying a low oxygen content within the built samples.

The phase transformation and Curie temperatures of each sample were determined using an in-house-developed low-field AC magnetic susceptibility device. Each sample exhibited different phase transformation temperatures, corresponding to the chemical composition and crystal structure. The increase in the martensite transformation temperature and the decrease in the Curie temperature from S1 to S6 can be attributed to the evaporation of Mn during L-PBF. The transformation widths ($T_{AS \to AF}$ and $T_{MS \to MF}$) were in the range of ∼5-7 K for samples S1-S4, ∼9 K for sample S5, and ∼11 K for sample S6. The increased width of transformation implies that samples S5 and S6 are chemically less homogenous, as also supported by the larger standard deviations of composition – see Fig. 1b. The transformation hysteresis (T_A–T_M) was in the range of 4-7 K for all samples.

Fig. 1d shows an optical polarized light image of the sample S2, in which homogenization treatment near the melting temperature ensured development of a coarse grain structure. The polarized light contrast also reveals martensitic twins spanning from few micrometres to hundreds of micrometres in width. The spherical pores visible in the figure may have formed due to gas entrapment during the manufacture via L-PBF [22,26]. In comparison to the literature, crack formation was not observed in the produced samples, possibly due to the smaller thickness of the samples, which reduces the internal stresses formed during processing via L-PBF.

Although the layer-by-layer directional cooling/solidification in L-PBF enhances the formation of a strong texture along the build direction [26], the grains are generally oriented inconveniently with respect to each other and are also constrained by grain boundaries. To investigate the magnetic field actuation of L-PBF-

built Ni-Mn-Ga, a section about 4 × 1.1 × 0.35 mm^3 in size containing a large grain, as marked in Fig. 1d, was cut out from sample S2 (10M martensite) using the wire saw. The general aim was to create a sample with so-called 'bamboo grains', wherein the sample width is smaller than the grain size. Within this structure, each grain, when unconstrained, behaves like a single crystal, allowing free motion of TBs and a large MFIS [13]. The possible surface defects caused by the cutting, which are known to inhibit TB motion and thus suppress MFIS, were removed by thorough mechanical and electropolishing. Finally, the large grain (∼1.7 × 1.1 × 0.35 mm^3) was freed from possible constraints at one end of the prepared sample, while the other end was fixed with an epoxy adhesive to a Ø 3 mm sapphire rod, which functioned as a sample holder.

In the first experiment, the section cut from sample S2 was placed at different angles in a homogeneous 0.8 T magnetic field, created by an EMU-75 electromagnet (SES Instruments Pvt. Ltd.). The field caused the active part of the sample to elongate or contract, depending on the field direction. Polarized light contrast imaging (Zeiss Axio Scope.A1) was utilized to characterize the twin variants' rearrangement and to determine the *c*-axis orientation in different parts of the sample. Fig. 2a and b present two images of the sample's front side taken after the magnetic field application perpendicular (a) and parallel (b) to the sample length. In the 10M Ni-Mn-Ga martensite, the shortest crystallographic *c*-axis is the easy magnetization axis, *i.e.*, the axis along which the cell magnetic moment is aligned, and the TBs separate the martensitic variants with a different – by around 86° – orientation of the *c*-axis. In the polarized light images, different colours visualize different orientations of the *c*-axis, which are marked according to above observations. It can be seen that a large part of the sample, measuring 1.65 mm along the sample length, was transformed during the magnetic field application. The white arrows mark the final positions of the TBs that moved during the transformation. The ∼45° inclination angle of the TBs' traces shows that the crystallographic axes are oriented almost parallel to the top facet in the transformed region. The TB motion is restricted from both sides by surface defects and/or grain boundaries, and thus TBs do not disappear after the field application.

To ensure *c*-axis orientation in the different variants, atomic/magnetic force microscopy (AFM/MFM) using a Park Systems XE7 was applied to follow the *c*-axis rotation at the TB on the top side. Fig. 2c shows an optical image taken from the top facet of the sample in its elongated state with the TB located near the free end of the sample. The red circle marks the area scanned with AFM/MFM. On this facet, the *c*-axis changes its orientation at the TB, becoming perpendicular to the sample surface in one of the neighbouring variants. This is fully supported by the MFM image displayed in Fig. 2d, in which the magnetic domain pattern, characteristic for the out-of-plane *c*-axis orientation [22], is visualized in the left variant. On the contrary, the right part of the MFM image does not show any remarkable contrast because the *c*-axis is almost parallel to the surface and the magnetic lines do not cross the sample surface. Furthermore, the sample surface kinks at the TB location due to the almost 6% difference between the longer *a* and *b*, and the shortest *c* crystallographic axes; see the 3D rendered AFM scan in Fig. 2e. Based on the scan, it follows that the kinking angle is ∼3.9°, which is in good agreement with the value of $\frac{\pi}{2} - 2\mathrm{atan}(\frac{c}{a}) = 3.7°$ calculated using the measured lattice constants. Finally, based on the TB trace inclination observed on the top surface, the *c*-axis in the right variant deviates by ∼20° from the front facet displayed in Figs. 2a and 2b.

In the next experiment, laser Doppler vibrometer (LDV) based setup, previously described in [28], was used to precisely characterize the sample's response to a pulsed magnetic field. The sam-
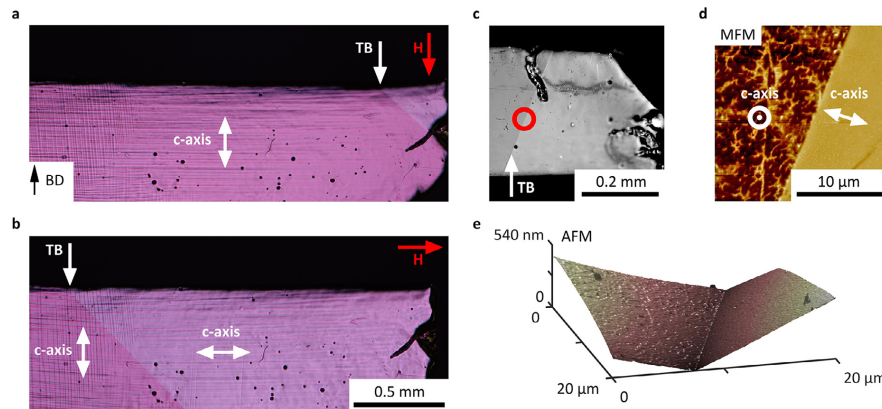
Fig. 2. a-b) Optical polarized light images of the magnetically actuated sample (front view) in its elongated (a) and contracted (b) states obtained after application of a homogeneous 0.8 T magnetic field in different directions. BD notes the build direction. The red arrows indicate the field direction. The white arrows show the final location of the observed twin boundary after the field application. The double-ended arrows show the orientation of the easy magnetization c-axis in different twin variants. c) Optical image obtained from the top side of the sample in the elongated state showing TB trace. The red circle marks the location of the AFM/MFM scan. d) MFM image revealing the change in the c-axis orientation in the adjacent twin variants at the TB site. e) 3D rendered image of the AFM scan showing a kink angle of ~3.9° at the TB site.
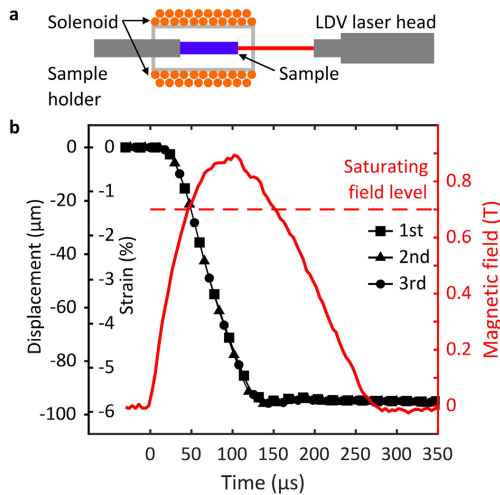

Fig. 3. a) Schematic representation of the LDV experimental setup for the pulsed magnetic field actuation of Ni-Mn-Ga. A magnetic field created inside the solenoid is applied along the length of the sample, thereby contracting it. During the magnetic field pulse, LDV measures the displacement of the free end of the sample with respect to its fixed part. b) Dependencies of the applied magnetic field (red line, right axis), and the measured displacement and strain versus time (black lines, left axis) for three sequential measurements. Before each measurement, the sample with the holder was placed in a transversal homogeneous magnetic field of 0.8 T to elongate the sample. Saturating field level refers to a typical value of the anisotropy field needed to fully magnetically saturate 10M Ni-Mn-Ga. The magnetic field was calculated from the measured solenoid current. The strain was calculated by dividing the displacement by the length (1.65 mm) of the transformed part of the sample.

ple fixed to the sapphire rod was placed inside the solenoid as depicted in Fig. 3a. In the present setup, a miniature solenoid (with an inner diameter of 4.3 mm, a length of 16.3 mm, and consisting of 140 turns of insulated copper wire 0.2 mm in diameter, wound in 2 layers) was connected to a high-voltage pulse generator (EMC, Transient 1000) in series with an additional coil (of 1.86 mH inductance and 0.83 Ohm resistance) that produced a ~250 μs current pulse providing magnetic field amplitude above the anisotropy field level of 0.7 T [29–30] to fully magnetize the sample. The vibrometer (Polytec, OFV-5000 and OFV-534) measured the displacement of the sample's free end with respect to the fixed end of the sample. The solenoid current was calculated based on the voltage drop on a wire resistor of 0.2 Ohm connected in series with the solenoid. The transient velocity and displacement signals from the LDV as well as the solenoid current were recorded using a 200 MHz oscilloscope (Metrix Scopix III OX 7204). The magnetic field was calculated from the measured current using the solenoid parameters.

Prior to each LDV measurement, the sample was placed in a homogeneous 0.8 T magnetic field, applied in the transverse direction to elongate the sample. The results of three sequential LDV measurements are presented in Fig. 3b. All measurements showed identical results: the sample contracted by 96±1 μm within ~135 μs with an average actuation speed of 0.7 m/s and a maximum speed of ~1.2 m/s. The MFIS, calculated from the measured displacement and the sample's active part length of 1.65 mm, reached a value of 5.8%, which agrees well with the transformation strain of 5.7% calculated from the lattice parameters. Notably, the measured actuation speed is comparable with the actuation speeds of ~2 m/s observed in conventionally grown single crystals of 10M Ni-Mn-Ga [28–30], indicating a low-defect crystal structure that does not hinder the TB motion in the additively manufactured sample.

It is demonstrated that the properties of the L-PBF built polycrystalline Ni-Mn-Ga can be precisely changed in-situ by controlling the selective evaporation of Mn by adjusting the applied process parameters, thereby opening up the possibility of additively manufacturing functional Ni-Mn-Ga-based MSM devices with tailored or localized (within the device itself) functional properties. It is also demonstrated that a large, mm-sized single crystalline grain,

extracted from an additively manufactured polycrystalline 10M Ni-Mn-Ga sample, exhibits a giant repeatable MFIS of 5.8%. The obtained MFIS is two orders of magnitude larger than the strains of 0.01% previously reported [19,25] for additive manufactured Ni-Mn-Ga, and is similar to that of conventionally grown single crystals exhibiting the 10M crystal structure [3]. The result demonstrates that L-PBF can produce material with MSM properties. Creation of single crystals by this or similar methods is still a challenge, but this problem has been partially solved for Ni-base single crystal superalloys [26] and therefore any principal obstacles are not seen in this way. The reported results are an important step towards the additive manufacturing of MSM devices and will permit the exploration of polycrystalline-MSM-based devices with a geometric freedom that has thus far not been possible with conventional manufacturing methods.

Author contributions

V.L. developed the manufacturing method and produced the samples and characterized their composition, microstructure, and transformation temperatures. A.Sar. carried out the MFIS characterization, LDV and AFM/MFM experiments. V.L. and A.Sar. analysed the data and wrote the first version of the manuscript (with contributions from A.Soz. and K.U.) and completed the manuscript. V.L. and K.U. conceived the initial research idea and strategy. K.U. supervised the experiments and acquired the financial support.

Declaration of Competing Interest

The authors declare that they have no known competing financial interests or personal relationships that could have appeared to influence the work reported in this paper.

Acknowledgments

References

[1] K. Ullakko, J. Huang, C. Kantner, R. O'Handley, V.V. Kokorin, Appl. Phys. Lett. 69 (1996) 1966–1968.
[2] O. Heczko, N. Scheerbaum, O. Gutfleisch, in: J. Ping Liu, E. Fullerton, O. Gutfleisch, D. Sellmyer (Eds.), Nanoscale Magnetic Materials and Applications, Springer, Boston, 2009, pp. 399–439.
[3] S. Murray, M. Marioni, S. Allen, R. O'Handley, T. Lograsso, Appl. Phys. Lett. 77 (2000) 886–888.
[4] A. Sozinov, A. Likhachev, N. Lanska, K. Ullakko, Appl. Phys. Lett. 80 (2002) 1746–1748.
[5] A. Sozinov, N. Lanska, A. Soroka, W. Zou, Appl. Phys. Lett. 102 (2013) 021902.
[6] M. Kohl, M. Gueltig, V. Pinneker, R. Yin, F. Wendler, B. Krevet, Micromachines 5 (2014) 1135–1160.
[7] A. Hubert, N. Calchand, Y.Le Gorrec, J. Gauthier, Adv. Electromagn. 1 (2012) 75–84.
[8] S. Barker, E. Rhoads, P. Lindquist, M. Vreugdenhil, P. Müllner, J. Med. Devices 10 (2016) 041009.
[9] A. Saren, A. Smith, K. Ullakko, Microfluid. Nanofluid. 22 (2018) 38.
[10] A. Armstrong, B. Karki, A. Smith, P. Müllner, Smart Mater. Struct. 30 (2021) 085001.
[11] A. Hobza, C. Patrick, K. Ullakko, N. Rafla, P. Lindquist, P. Müllner, Sens. Actuators A 269 (2018) 137–144.
[12] P. Lindquist, T. Hobza, C. Patrick, P. Müllner, Shape Mem. Superelasticity 4 (2018) 93–101.
[13] M. Chmielus, X. Zhang, C. Witherspoon, D. Dunand, P. Müllner, Nat. Mater. 8 (2009) 863–866.
[14] K. Ullakko, Y. Ezer, A. Sozinov, G. Kimmel, P. Yakovenko, V. Lindroos, Scr. Mater. 44 (2001) 475–480.
[15] U. Gaitzsch, M. Pötschke, S. Roth, B. Rellinghaus, L. Schultz, Acta Mater 57 (2009) 365–370.
[16] C. Hürrich, S. Roth, H. Wendrock, M. Pötschke, J. Phys. Conf. Series 303 (2011) 012080.
[17] U. Gaitzsch, J. Romberg, M. Pötschke, S. Roth, P. Müllner, Scr. Mater. 65 (2011) 679–682.
[18] Z. Li, Z. Li, B. Yang, X. He, W. Gan, Y. Zhang, Z. Li, Y. Zhang, C. Esling, X. Zhao, L. Zuo, Mater. Sci. Eng. A 780 (2020) 139170.
[19] K. Ullakko, V. Laitinen, A. Saren, A. Sozinov, D. Musiienko, M. Chmileus, A. Salminen, 11ᵗʰ European Symposium on Martensitic Transformations, Metz, 27-31 August 2018.
[20] V. Laitinen, A. Salminen, K. Ullakko, J. Laser Appl. 31 (2019) 022303.
[21] F. Nilsén, I. Ituarte, M. Salmi, J. Partanen, S. Hannula, Addit. Manuf. 28 (2019) 464–474.
[22] V. Laitinen, A. Sozinov, A. Saren, A. Salminen, K. Ullakko, Addit. Manuf. 30 (2019) 100891.
[23] V. Laitinen, A. Sozinov, A. Saren, M. Chmielus, K. Ullakko, Addit. Manuf. 39 (2021) 101854.
[24] W. Maziarz, P. Czaja, R. Chulist, A. Wójcik, Ł. Żrodowski, B. Morończyk, R. Wróblewski, M. Kowalczyk, Metals 11 (2021) 903.
[25] M. Caputo, A. Berkowitz, A. Armstrong, P. Müllner, C.V. Solomon, Addit. Manuf. 21 (2018) 579–588.
[26] T. DebRoy, H. Wei, J. Zuback, T. Mukherjee, J. Elmer, J. Milewski, A. Beese, A. Wilson-Heid, A. De, W. Zhang, Prog. Mater. Sci. 92 (2018) 112–224.
[27] X. Jin, M. Marioni, D. Bono, S. Allen, R. O'Handley, T. Hsu, J. Appl. Phys. 91 (2002) 8222.
[28] A. Saren, D. Musiienko, A.R. Smith, K. Ullakko, Scripta Mat 113 (2016) 154–157.
[29] A. Saren, T. Nicholls, J. Tellinen, K. Ullakko, Scripta Mat 123 (2016) 9–12.
[30] A. Saren, K. Ullakko, Scripta Mat 139 (2017) 126–129.

ACTA UNIVERSITATIS LAPPEENRANTAENSIS

957. IMMONEN, HEIKKI. Application of object-process methodology in the study of entrepreneurship programs in higher education. 2021. Diss.

958. KÄRKKÄINEN, HANNU. Analysis of theory and methodology used in determination of electric motor drive system losses and efficiency. 2021. Diss.

959. KIM, HEESOO. Effects of unbalanced magnetic pull on rotordynamics of electric machines. 2021. Diss.

960. MALYSHEVA, JULIA. Faster than real-time simulation of fluid power-driven mechatronic machines. 2021. Diss.

961. SIEVINEN, HANNA. Role of the board of directors in the strategic renewal of later-generation family firms. 2021. Diss.

962. MENDOZA MARTINEZ, CLARA. Assessment of agro-forest and industrial residues potential as an alternative energy source. 2021. Diss.

963. OYEWO, AYOBAMI SOLOMON. Transition towards decarbonised power systems for sub-Saharan Africa by 2050. 2021. Diss.

964. LAHIKAINEN, KATJA. The emergence of a university-based entrepreneurship ecosystem. 2021. Diss.

965. ZHANG, TAO. Intelligent algorithms of a redundant robot system in a future fusion reactor. 2021. Diss.

966. YANCHUKOVICH, ALEXEI. Screening the critical locations of a fatigue-loaded welded structure using the energy-based approach. 2021. Diss.

967. PETROW, HENRI. Simulation and characterization of a front-end ASIC for gaseous muon detectors. 2021. Diss.

968. DONOGHUE, ILKKA. The role of Smart Connected Product-Service Systems in creating sustainable business ecosystems. 2021. Diss.

969. PIKKARAINEN, ARI. Development of learning methodology of additive manufacturing for mechanical engineering students in higher education. 2021. Diss.

970. HOFFER GARCÉS, ALVARO ERNESTO. Submersible permanent-magnet synchronous machine with a stainless core and unequal teeth widths. 2021. Diss.

971. PENTTILÄ, SAKARI. Utilizing an artificial neural network to feedback-control gas metal arc welding process parameters. 2021. Diss.

972. KESSE, MARTIN APPIAH. Artificial intelligence : a modern approach to increasing productivity and improving weld quality in TIG welding. 2021. Diss.

973. MUSONA, JACKSON. Sustainable entrepreneurial processes in bottom-of-the-pyramid settings. 2021. Diss.

974. NYAMEKYE, PATRICIA. Life cycle cost-driven design for additive manufacturing: the frontier to sustainable manufacturing in laser-based powder bed fusion. 2021. Diss.

975. SALWIN, MARIUSZ. Design of Product-Service Systems in printing industry. 2021. Diss.

976. YU, XINXIN. Contact modelling in multibody applications. 2021. Diss.

977. EL WALI, MOHAMMAD. Sustainability of phosphorus supply chain – circular economy approach. 2021. Diss.

978. PEÑALBA-AGUIRREZABALAGA, CARMELA. Marketing-specific intellectual capital: Conceptualisation, measurement and performance. 2021. Diss.

979. TOTH, ILONA. Thriving in modern knowledge work: Personal resources and challenging job demands as drivers for engagement at work. 2021. Diss.

980. UZHEGOVA, MARIA. Responsible business practices in internationalized SMEs. 2021. Diss.

981. JAISWAL, SURAJ. Coupling multibody dynamics and hydraulic actuators for indirect Kalman filtering and real-time simulation. 2021. Diss.

982. CLAUDELIN, ANNA. Climate change mitigation potential of Finnish households through consumption changes. 2021. Diss.

983. BOZORGMEHRI, BABAK. Finite element formulations for nonlinear beam problems based on the absolute nodal coordinate formulation. 2021. Diss.

984. BOGDANOV, DMITRII. Transition towards optimal renewable energy systems for sustainable development. 2021. Diss.

985. SALTAN, ANDREY. Revealing the state of software-as-a-service pricing. 2021. Diss.

986. FÖHR, JARNO. Raw material supply and its influence on profitability and life-cycle assessment of torrefied pellet production in Finland – Experiences from pilot-scale production. 2021. Diss.

987. MORTAZAVI, SINA. Mechanisms for fostering inclusive innovation at the base of the pyramid for community empowerment - Empirical evidence from the public and private sector. 2021. Diss.

988. CAMPOSANO, JOSÉ CARLOS. Integrating information systems across organizations in the construction industry. 2021. Diss.

989. LAUKALA, TEIJA. Controlling particle morphology in the in-situ formation of precipitated calcium carbonate-fiber composites. 2021. Diss.

990. SILLMAN, JANI. Decoupling protein production from agricultural land use. 2021. Diss.

991. KHADIM, QASIM. Multibody system dynamics driven product processes. 2021. Diss.

992. ABDULKAREEM, MARIAM. Environmental sustainability of geopolymer composites. 2021. Diss.

993. FAROQUE, ANISUR. Prior experience, entrepreneurial outcomes and decision making in internationalization. 2021. Diss.

994. URBANI, MICHELE. Maintenance policies optimization in the Industry 4.0 paradigm. 2021. Diss.

LUT University